Measurement of 14 MeV neutron for triton burnup study on the Large Helical Device

Neng PU

Doctor of Philosophy

Department of Fusion Science
School of Physical Sciences
The Graduate University for Advanced Studies, SOKENDAI

2020

Abstract

The deuterium plasma experiments have been conducted since March 2017 on the Large Helical Device (LHD) to explore higher-confinement regime, to reveal isotope effects, and to enhance energetic-particle confinement study. In deuterium plasma experiments, neutrons are generated by thermal-thermal, thermal-beam, and beam-beam D-D reactions. Therefore, the neutron diagnostics preform important role not only for evaluation of the neutron yield which is the index of the fusion power, the but also for study of energetic-particle confinement. Meanwhile, the neuron measurement is key for the radiation safety.

Prior the LHD deuterium plasma experiment, the *in situ* neutron calibration experiment was performed by using an intense ^{252}Cf neutron source for the neutron flux monitor (NFM) and the neutron activation system (NAS) on the LHD in November 2016 to evaluate the accurate data of the neutron yield. To simulate a ring-shaped neutron source, we installed a railway inside the LHD vacuum vessel, where a train loaded with the ^{252}Cf source run along a typical magnetic axis position.

The NFM based on combination of ^{235}U fission chambers (FC), and ^{10}B and/or ^{3}He proportional counters are positioned at three different locations outside the LHD cryostat. Detection efficiencies for the ^{252}Cf ring source are derived by the ratio of (total counts)/(total emitted neutron number) in the continuous rotation of the neutron source. Detection efficiencies for the real plasma neutron source are derived from the measured detection efficiencies with the correction factor taking account of the deference between the ^{252}Cf ring source and the real plasma neutron source evaluated by a general-purpose Monte Carlo N-Particle code 6 (MCNP) calculations with the three-dimensional model of LHD. Finally, the uncertainty of the total neutron emission rate measurement is discussed.

At the same time, three activation capsules loaded with thirty pieces of indium (In) foil-stacked with the total mass of approximately 18 g were prepared. Each capsule placed in the irradiation end of NAS on the 8-O port was irradiated over 15 hours while the train was circulating continuously. The activation response coefficient $(9.4\pm1.2)\times10^{-8}$ of ^{115}In(n, n')^{115m}In reaction obtained from the experiment is in good agreement with results calculated by the MCNP code. The difference of between the *in situ* calibration and the MCNP calculation for the ^{252}Cf ring-shaped source case is evaluated to be 7%. It is considered that this discrepancy is caused mainly by the uncertainly of the modeling error in the MCNP calculation. Therefore, the activation response coefficients for 2.45 MeV

birth neutron and secondary 14.1 MeV neutron from deuterium plasma were evaluated from the MCNP calculation with the correction by this calibration experiment result.

In the LHD experiment, the absolute neutron yield has been measured by NAS using In foil and FC#1 of NFM. The neutron yield per shot has reached up to 7×10^{14} and 4×10^{15} in the first phase, where NBI #1, 2, and 3 used hydrogen and NBI #4 and 5 used deuterium, and in the full D-D phase, respectively. The NAS plays a role of the cross-calibration tool for NFM in the LHD deuterium campaign.

By using the activation response coefficients evaluated from the MCNP calculation with the correction by *in situ* calibration experiment, the shot-integrated total neutron yield measured by NAS on the 8-O port is across three orders of magnitude in good agreement with that by FC#1 of NFM in the first phase. The maximum relative deviations between the NAS and NFM is less than 10%. In addition to this, the activation response coefficient calculated by MCNP for the irradiation end of NAS on the 2.5-L port is cross-calibrated by the center FC#1 measurement of NFM. After the cross calibration, the neutron yields measured by NAS on the 2.5-L port agree with those by NFM.

The absolute shot-integrated 14 MeV neutron yields measured by NAS on the 8-O port with silicon (Si) foil increase with the total neutron yields, which has been performed to calibrate other 14 MeV neutron detectors on LHD experiment. Triton burnup secondary 14 MeV neutrons have been measured from a large stellarator/heliotron for the first time in the world.

Two scintillating fiber (Sci-Fi) detectors have been operated in the LHD experiment to investigate the time evolution of 14 MeV neutron for the triton burnup study. Two detectors use scintillating fibers of 1 mm diameter embedded in an Al matrix with a length of 10 cm connected to the magnetic field resistant photomultiplier. A detector with 91 fibers was developed in Los Alamos National Laboratory (LANL) and has been employed on JT-60U. The other detector with 109 fibers has been developed in National Institute for Fusion Science (NIFS). The signals are fed into a discriminator of 300 MHz bandwidth with a pulse counter module for the on-line measurement and a digitizer of 1 GHz sampling with 14 bits to acquire the pulse shape information for the off-line data analysis. The pulse height spectra (PHS) of the two Sci-Fi detectors were obtained to choose suitable threshold for discrimination of lower-energy neutrons and gamma-rays. In the low-threshold case, time evolution measurements of Sci-Fi detectors were influenced by 2.45 MeV neutrons and gamma-rays. The measurements have shown the same tendency in high-threshold case.

The PHS of the Sci-Fi detector have two components with different decay slopes in

the LHD experiment. To study the pulse height property of the Sci-Fi detector, the PHS on different energy neutrons have been measured by using the accelerator-based neutron source with D-D and D-Li reactions. Four different head detectors with the same PMT (same gain) have been located on 110° and 10° against D^+ beam direction in order to investigate the abilities of gamma-ray rejection for 2.45 MeV neutron and higher-energy neutrons with induced gamma-rays, respectively. Moreover, the simulations of the detector response have been performed by using the Particle and Heavy Ion Transport code System (PHITS). The accelerator experiment and the PHITS calculation showed that four different head detectors have different properties. The function of Sci-Fi detector has been confirmed by both the accelerator experiment and the PHITS calculation. In the LHD experiment, the first decay component of the PHS in low-pulse-height region has been found to be corresponding to the signal induced by 2.45 MeV neutrons and gamma-rays. In addition, the recoil proton edge induced by triton burnup 14 MeV neutrons in high-pulse-height region has been confirmed by both the accelerator experiment and the PHITS calculation. The detection efficiency of 14 MeV neutron for the Sci-Fi detector calculated by the PHITS code agrees well with that evaluated in the LHD experiment. The Sci-Fi detector can work as a standard detector for the 14 MeV neutron measurement with a suitable threshold. By the cross-calibration with the NAS measurement, the triton burnup ratio has been evaluated shot-by-shot from the 14 MeV neutron measured by Sci-Fi detectors with a suitable threshold and calibration with the 14 MeV neutron measured by NAS.

Triton burnup ratio decreases as the magnetic axis (R_{ax}) positions shift outward, which can likely be explained by the orbit of helically trapped energetic tritons. The drift surface of helically-trapped triton tends to deviate largely from magnetic flux surfaces as the magnetic axis position is shifted outward. Meanwhile, triton burnup ratio strongly depended on magnetic field B_t at the same R_{ax}. Triton burnup ratio increases with the line-averaged electron density ($n_{\mathrm{e\_bar}}$) in the low-density region, and decreases with the electron density in the high-density region. The tendency of $n_{\mathrm{e\_bar}}$ dependence of triton burnup ratio in the high-density region agrees with the classical slowing-down model.

Time evolution of 14 MeV neutron emission rate has been evaluated from the measurement of Sci-Fi detector which was calibrated by 14 MeV neutron measured by NAS. It is observed that the time evolution of the 14 MeV neutron emission rate measured with Sci-Fi detectors lags to that of the 2.45 MeV neutrons emission rate measured with NFM. The calculation by the FBURN code was carried out for the time evaluation of triton burnup study on LHD with different diffusion coefficient of the energetic triton.

Contents

Chapter 1:

Introduction

1.1. Energy crisis

Energy is the basis for the maintenance and development of human civilization. As the population growing, human energy consumption is shown in Fig. 1.1. In addition to renewable water, wind, and tide resources, the most of energy is covered by fossil fuels such as oil, coal and natural gas, which are classified into non-renewable resource. These non-renewable resources are limited on the earth. According to the Statistical Review of World Energy June 2018, the reserve to production ratios per year of coal, oil and natural gas are approximately 134, 50.2 and 52.6 years, respectively. [1] Therefore, the most serious problems facing mankind is the energy crisis. In addition, these fossil fuels cause serious environmental problems such as global warming and air pollution, which directly affect human health. With the improvement of human living standard and population quality, people began to realize the importance of sustainable growth. The development and utilization of clean and sustainable energy has become the major theme for mankind.

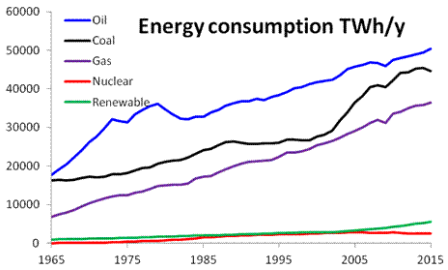

Fig. 1.1 Human energy consumption in the world. [1]

1.2. Nuclear fusion

Nuclear fusion is the energy source of the sun to keep burning for billions years. The controlled fusion could be one of the best ways to solve energy shortage in near future. Nuclear fusion is a reaction in which two or more relatively light nuclei are combined to one or more different heavy nuclei. We will use deuterium-tritium (D-T) fusion for realizing the controlled fusion on the earth because the reaction has the relatively large cross section compared with the other fusion reactions. A deuteron combines with a triton and then generate an energetic α-particle and an energetic neutron as shown in Fig. 1.2. [2] The nuclear rearrangement results in a reduction in total mass of reacted nuclei to release energy in the form of the kinetic energy of the reaction products. The mass deficit is $0.01875m_p$ in this reaction. Here, m_p represents the proton mass. According to the Albert Einstein's mass-energy equivalence, the energy equivalent to the mass with $E=mc^2$. The released energy is called reaction energy $Q=0.01875m_p\times c^2=17.59$MeV. The reaction energy will be distributed as a kinetic energy on the α-particle (3.5MeV) and the neutron (14.1MeV) according to momentum conservation. D-T of 1 g will release energy of 10^8 Wh. [3]

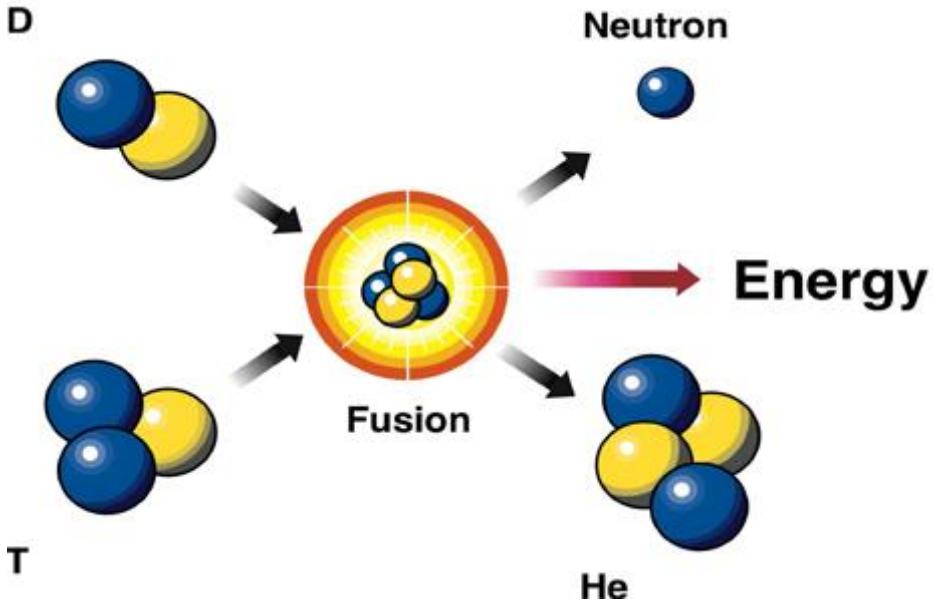

Fig. 1.2 D-T reaction [2]

In order to induce the fusion reaction, it is necessary to overcome strong electrostatic force between two nuclei and to put nuclei into the distance (~10^{15}m) of strong nuclear

force in a sufficient time. Ultra high temperature (~100 million Kelvin) is needed to overcome the electrostatic force. In such a high temperature, the fuel gas will be fully ionized. In the ionized gas, the total charge of fuel ions is equal to the total number of free electron. This highly-ionized macroscopic neutral gas is called a plasma. Any solid materials cannot be used as a container in order to confine such a high-temperature plasma because the materials are melt or evaporated in such a high temperature. Therefore, human can use magnetic field to confine the high-temperature plasma because of electrical property of a plasma. It is worth noting that in D-T fusion plasma, D-T born α-particle also can be confined by magnetic field.

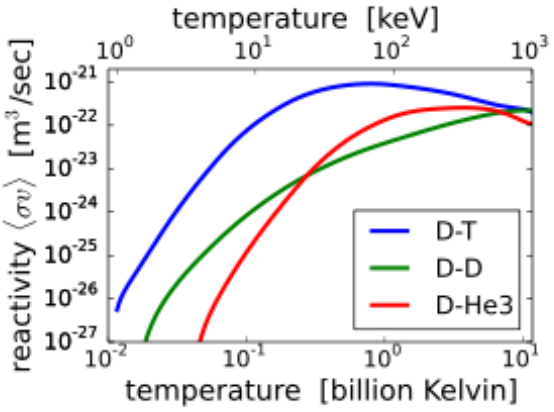

Fig. 1.3 Reactivity as a function of temperature [2]

If the plasma distributions are Maxwellian, the reaction rate of thermonuclear fusion can be write as follows:

$$R = 4\pi n_i n_j \left(\frac{m_{ij}}{2\pi KT}\right)^{3/2} \int \sigma(v_{ij}) {v_{ij}}^3 e^{-\frac{m_{ij}{v_{ij}}^2}{2KT}} dv_{ij} \tag{1.1}$$

Where, n_i, n_j, m_{ij}, v_{ij}, K, and T are the density of two nuclei i and j, reduced mass, relative velocity of two nuclei i and j $v_{ij} = v_i - v_j$, Boltzmann's constant, and plasma temperature, respectively. In laboratory experiments, the energy of incident particle i $E_i = \frac{1}{2} m_i {v_i}^2$. The EQ(1.1) can be written to be:

$$R = \left(\frac{8}{\pi}\right)^{1/2} n_i n_j \left(\frac{m_{ij}}{KT}\right)^{3/2} \frac{1}{m_i{}^2} \int \sigma(E) E \, e^{-\frac{m_{ij}E}{m_i KT}} dE \tag{1.2}$$

For D-T reaction, reaction rate can be simplified to be $R = n_D n_T \langle \sigma v \rangle$, where $\langle \sigma v \rangle$ is a function of plasma temperature as shown in Fig. 1.3. Then, the thermonuclear power per unit volume in a D-T plasma is $P_{tn} = n_D n_T \langle \sigma v \rangle E_{re}$. Here, E_{re} represents the reaction energy. The total energy of a plasma is $W = 3\overline{nT}V$, where $n = n_D + n_T$, $\bar{n}$ and $\bar{T}$ are average density and average temperature (omitting K) of plasma, V is the plasma volume. The energy-loss power $P_l = \frac{W}{\tau_E}$, where τ_E is energy confinement time. The D-T born α-particle can play an important role in self-heating. The heating power of this α-particle can be written as $P_\alpha = \frac{1}{4} n^2 \langle \sigma v \rangle E_\alpha V$, where E_α represents α-particle energy. When the overall power is balanced by using auxiliary heating with a power P_h, the power loss can be described as $P_l = P_h + P_\alpha$. Then,

$$P_h = \left(\frac{3nT}{\tau_E} - \frac{1}{4} n^2 \langle \sigma v \rangle E_\alpha\right) V \tag{1.3}$$

When $P_l < P_\alpha$ is fulfilled without auxiliary heating, a plasma achieves the self-ignition condition. The self-ignition condition is:

$$n\tau_E > \frac{12T}{\langle \sigma v \rangle E_\alpha} \tag{1.4}$$

EQ(1.4) is the famous Lawson criterion. [1] When the peak density $\hat{n}$ and temperature $\hat{T}$ are chosen, the ignition condition for D-T reaction is $\hat{n}\hat{T}\tau_E > 5 \times 10^{21}\ m^{-3} keVs$. It means that to realize the self-sustaining D-T fusion plasma, when the central density and temperature should be larger than 5×10^{20} m^{-3} and 10 keV, the energy confinement time of 1 s. [3]

1.3. Neutron

Table 1.1 shows several nuclear fusion reactions of Q>0. As shown in Table 1.1, neutrons are the one of the primary product of most fusion reactions and carry a large amount of fusion energy. Therefore, the neutron is the marker of fusion power.

Table 1.1 Nuclear fusion reaction [2]

$D + T \rightarrow {}_{2}^{4}He + n + 17.59MeV$	$D + {}_{3}^{6}Li \rightarrow {}_{4}^{7}Be + n + 3.4MeV$
$D + D \rightarrow {}_{2}^{3}He + n + 3.27MeV$	$D + {}_{3}^{7}Li \rightarrow {}_{4}^{8}Be + n + 15.03MeV$
$D + D \rightarrow {}_{2}^{3}T + p + 4.03MeV$	$D + {}_{3}^{7}Li \rightarrow 2{}_{2}^{4}He + n + 15.12MeV$
$T + T \rightarrow {}_{2}^{4}He + 2n + 11.3MeV$	$D + {}_{3}^{6}Li \rightarrow {}_{2}^{3}He + {}_{2}^{4}He + n + 2.56MeV$

The neutron has been discovered by James Chadwick in 1932. Neutrons have a mass of 1.675×10^{-27} kg or 939.56 MeV, a weak magnetic moment of -9.66×10^{-27} J/T, a spin and an isospin of 1/2, and a parity of +1. Neutrons classified by thermodynamic temperature ($E=kT$) can be divided into ultra-cold neutron (<3×10^{-7} eV), very cold neutron (0.0001~1×10^{-7} eV), cold neutron (5×10^{-5}~0.025 eV), thermal neutron (0.0253 eV), epithermal neutrons (0.025~100 eV), slow neutrons (0~1 keV), intermediate-energy neutrons (0.1~20 keV), high-epithermal neutrons (1~100 keV), fast neutrons (0.02~10 MeV), and high-energy neutrons (>10 MeV).

The most memorable characteristic of neutrons is that neutrons have no charge. It is also highly penetrable and cannot be directly observed. A free neutron is not affected by any external force until it directly collides with the nucleus. Because the nucleus is too small, there is very little chance of collisions, so the free neutrons stay the same over a very long distance. The free neutrons cause an elastic collision with nuclei. When neutrons collide with very heavy nuclei, these heavy nuclei have very little speed after collision. Whereas, the neutrons collide with light nuclei such as proton, the light nuclei and neutrons will fly out at almost the same speed. The recoiled proton method such as fast neutron organic scintillation detector is one of the most common methods for neutron detection. Other way of neutron detection is the neutron capture. Certain nuclides have a high neutron capture cross section, which is the probability of absorbing a neutron. Upon neutron capture, the compound nucleus emits more easily detectable radiation, such as an alpha particle or gamma-rays. This is the so-called neutron activation measurement.

1.4. Fusion device

There are two main approaches for controlled nuclear fusion. One is the high-density short-time scale inertial confinement fusion (ICF); the other is the low-density long-time scale magnetic confinement fusion (MCF). The most likely candidate for fusion energy is MCF. MCF devices can be morphologically divided into two types: open ended devices and toroidal devices. The open ended devices stand for magnetic mirror such as single magnetic mirror and multi-stage magnetic mirror in series. The magnetic field configuration of a toroidal device is a circular ring of toroidal topology. The helical magnetic field synthesized by poloidal magnetic field and toroidal magnetic field generates rotation transformation to avoid the loss of particle drift caused by charge separation. There are two major types of toroidal devices: tokamak and stellarator. Poloidal magnetic field is generated by the plasma current in tokamaks, whereas poloidal magnetic field are generated by external magnetic field coils in stellarator.

1.4.1. Tokamak

The word tokamak is a transliteration of the Russian word токамак, an acronym of either: toroidal chamber (kamera) with magnetic coils (kotushka). Tokamak is mainly composed of vacuum chamber, toroidal field coil, central coil and poloidal field coil as shown in Fig. 1.4. Toroidal field coils are arranged along the toroidal axis to generate a strong toroidal magnetic field, which act as a confining and stabilizing effect on the plasma. The central coil and a number of outer coils constitute an Ohmic transformer, which generates a changing magnetic flux, induces a circular electromotive force, and breaks through the gas to form a toroidal plasma. The toroidal plasma forms a toroidal plasma current to generate a poloidal magnetic field to synthesize helical magnetic field lines with a toroidal magnetic field for producing a rotational transformation of the toroidal magnetic field. The poloidal field coil produces a vertical field used to maintain the plasma equilibrium. The vacuum chamber and the pumping system maintain the purity of the gas so that the ionization (breakdown) of the gas to create a plasma which operates at a lower pressure. The flux variation of the ohm transformer is always limited and cannot maintain the plasma current consumed by the resistance for a long time. In addition, tokamak heats the plasma through an electric current, and its heating efficiency is limited. Thus, tokamak needs auxiliary heating.

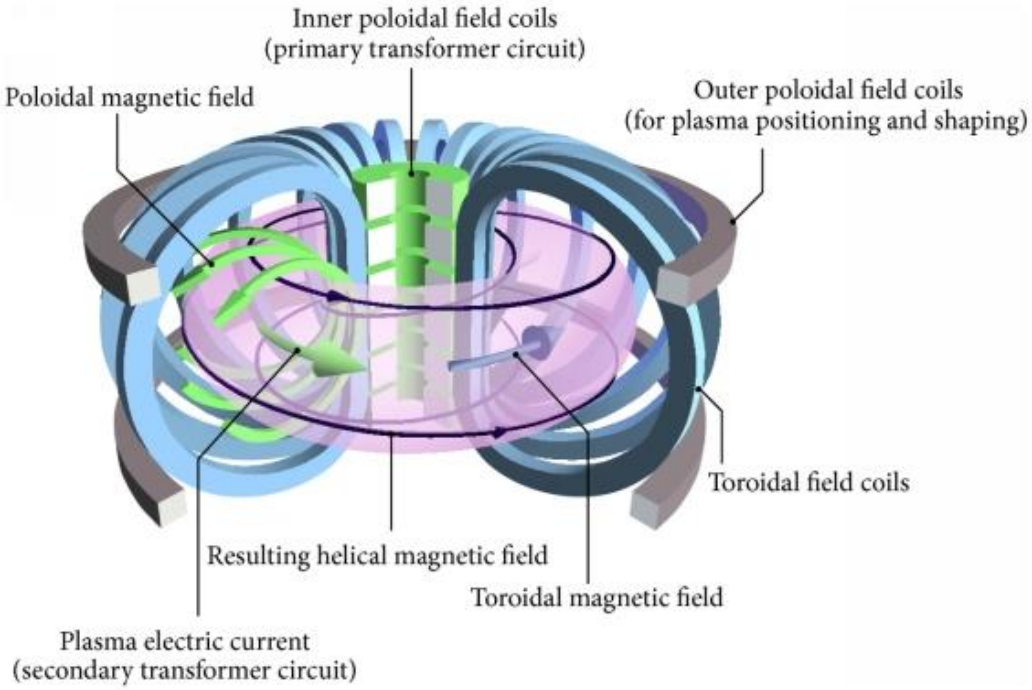

Fig. 1.4 Schematic diagram of typical tokamak and its magnetic field.

Large tokamaks currently in service or retired have the Joint European Torus (JET) from EU, the Tokamak Fusion Test Reactor (TFTR) from USA, the JAERI Tokamak-60 Upgrade (JT-60U) from Japan, and Tokamak-15 (T-15) from Russia. JET is the world's largest operational MCF device, which located at Culham Centre for Fusion Energy in Oxfordshire, UK since 1984. TFTR was built at Princeton Plasma Physics Laboratory (PPPL) and shut down in 1997. Only these two devices have been tested with D-T experiment. JET is the world record for Q at 0.67. JT-60U previously run by the Japan Atomic Energy Research Institute (JAERI) and currently run by the Japan Atomic Energy Agency's (JAEA) Naka Fusion Institute in Ibaraki Prefecture. JT-60U currently holds the record for the highest value of the fusion triple product achieved: $\hat{n}\hat{T}\tau_E = 1.53 \times 10^{21}$ keV $\cdot$ s $\cdot$ m^{-3}. The others are the mid-size tokamak such as DIII-D in USA, West Environment in Steady-state Tokamak (WEST was called Tore Supra before) in France, Experimental Advanced Superconducting Tokamak (EAST) in China, Axially Symmetric Divertor Experiment upgrade (ASDEX-U) in Germany, and so on. Then there are the little tokamaks such as several high magnetic field devices: Alcator C-Mod in USA, FTU in Italy, and TFR in France. The other is the spherical tokamak with high β such as Mega Ampere Spherical Tokamak upgrade (MAST-U) in UK, National Spherical Torus Experiment (NSTX) in USA, and Sino-UNIted Spherical Tokamak (SUNIST) in China.

The under construction device is called International Thermonuclear Experimental Reactor (ITER), which will be a largest tokamak in the world at present. Also JT-60SA will complete the assembly, which is a completely new design on the original site after the demolition of JT-60U. Another large tokamak project in the pipeline is the China Fusion Engineering Test Reactor (CFETR) in China.

High-temperature and high-density plasmas are obtained in large tokamaks. The breakeven plasmas have been achieved large tokamaks [4]-[6] One of the issues of tokamak is in order to sustain the plasma for a long time. The sustainment of high-performance plasma will be demonstrated in large tokamaks such as ITER, CFETR, and JT-60SA.

1.4.2. Stellarator

The stellarator was invented by L. Spitzer in Princeton University 1951, and early development was carried out by his team in PPPL. Plasma is confined by magnetic filed generated with winding coils in stellarator as shown in Fig. 1.5. Although the plasma performance of the stellarator does not exceed the performance achieved in tokamaks, stellarators have the advantage of steady-state operation because of the absence of disruption which occurred in tokamaks. Recently, the performance of stellarators and helical devices increased dramatically. For example, the achievement of 10 keV ion temperature in LHD [7],[8] and the stored plasma energy exceeds 6×10^{26} Celsius m^{-3} s in Wendelstein 7-X [9].

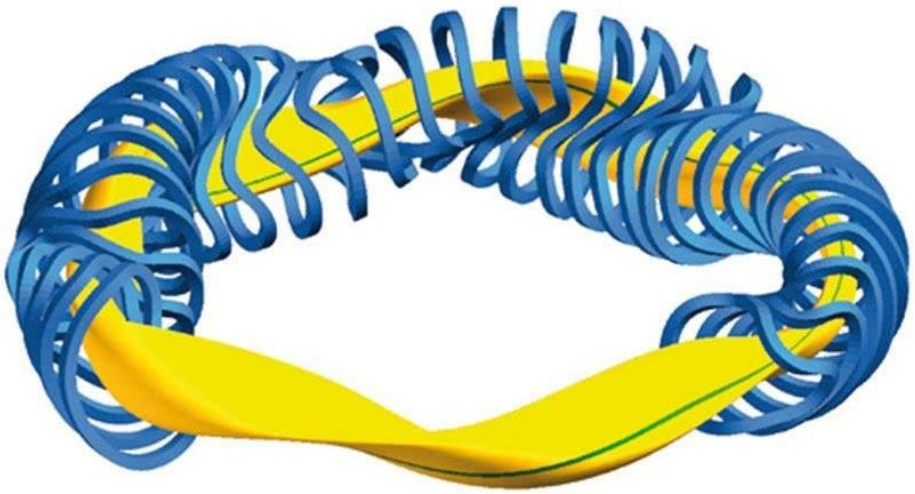

Fig. 1.5 Schematic diagram of typical stellarator and its magnetic field. [8]

1.5. Triton burnup study in tokamaks

As mentioned in previous sections, one of the most critical issues in realizing fusion burning plasma is good confinement of α-particle. To understand the α-particle behavior in deuterium plasma experiment performed in existing fusion device, confinement of D-D born 1 MeV triton have been studied because kinematic properties such as the Larmor radius and the precessional drift frequency of 1 MeV tritons are almost the same as those of D-T born 3.5 MeV alphas.

Only JET [10] and TFTR [11] have conducted D-T experiments, and most devices mainly carry out D-D experiments. In D-D plasma, there are two reactions D(d, n)^{3}He and D(d, p)T to produce 2.45 MeV neutrons and 1 MeV tritons. Here, the production rates of 2.45 MeV neutrons and 1 MeV tritons are almost the same. Energetic tritons will undergo secondary D-T reaction with background deuterons, while those tritons slow down. If 14 MeV neutrons from secondary D-T reaction can be measured selectively, confinement property of 1 MeV tritons can be studied.

In the tokamaks such as TFTR[12], JET[13], ASDEX-U[14], JT-60U[15], DIII-D[16], FT[17], and PLT[18], neutron activation systems (NAS) have been applied to measure the shot-integrated primary 2.45MeV neutron yields and secondary 14 MeV neutron yields in the deuterium plasmas. In tokamaks, the triton burnup ratio increase with plasma current (I_p), which defined by total D-T neutron yield divided by total neutron yield. This is because the banana width decreases with the increase of I_p. In large tokamaks, the maximum triton burnup ratios were evaluated to be 1% for TFTR [12], 1.25% for JT-60U [15], and over 3% for JET [23]. In middle tokamaks, the triton burnup ratios reach to 0.5%. [17]

Time-resolved measurement of triton burnup has been performed in TFTR [19] and JT-60U [20], [21] by the Scintillating-fiber (Sci-Fi) detectors developed in Los Alamos National Laboratory (LANL) as shown in Fig. 1.6(a). The buildup rate of 14 MeV neutron emission rate is slower than that of 2.45 MeV neutron emission rate due to the difference of cross section curve of D-D and D-T reactions. Also, time-resolved triton burnup has been performed the liquid scintillator detector on PLT [22], and TFTR [12] as shown in Fig. 1.6(b). The time evolution of total 14 MeV neutron emission rate has good agreement with the time evolution calculated by one-dimensional triton burnup calculation code BURNIT [12]. In addition, time evolution of total 14 MeV emission rate was measured with the silicon detector on JET [13], and TFTR [12], and with the CVD diamond detector on JET [23].

(a)

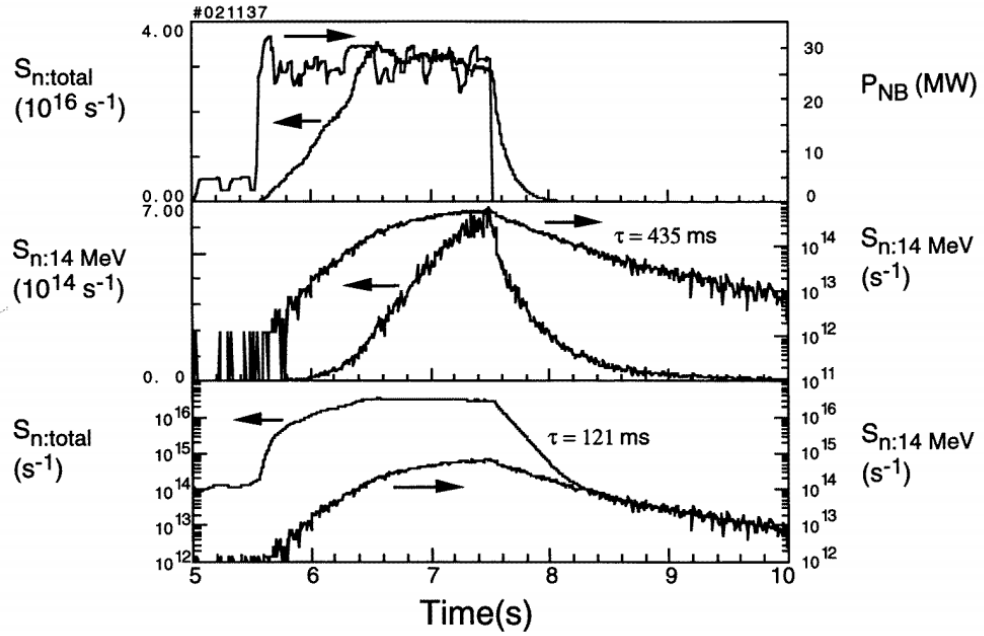

(b)

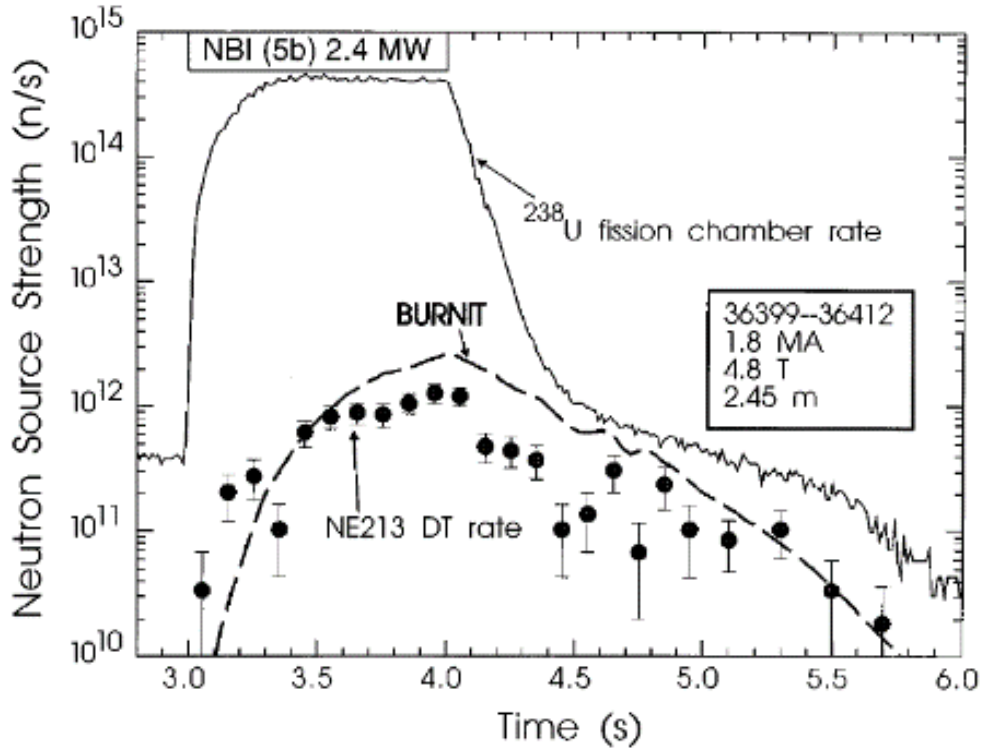

Fig. 1.6 Time evolution of triton burnup measured (a) by Sci-Fi detectors on JT-60U [20], and (b) by the liquid scintillator detector on TFTR [12].

Chapter 2:

Theories

2.1. Fusion neutron emission

Neutrons are generated with nuclear reactions of the fuel ions in fusion plasma experiments. The absolute neutron yields and the neutron energy spectra are related to the plasma where the neutrons are born. The uncharged neutrons move out of the plasma in their original emission direction promptly. Then, the most of neutrons collided with the experimental device and support structure are scattered or absorbed in materials. As a result, the initial energy spectrum and the neutron number on the initial emission-direction are changed. At last, some neutrons reach a neutron detector to produce a signal with a certain probability which is the so called the detection efficiency of a neutron detector. Those signals depend on the incident neutrons and the detection efficiency. To record those signals is the so called the neutron measurement. Based on the different neutron diagnostics, time-integrated neutron yield and time-evolution of neutron emission rate can be obtained. This is an important objective of neutron diagnostics to obtain as much information as possible on the properties of the plasma fuel ions (such as densities and temperatures) with analyzing these measured neutron signals. Another approach is the analysis for neutron emission and scattering by using computer codes. The neutron emission of plasma are simulated between reaction rate and the plasma properties to compare with measurements. The plasma densities and temperatures are measured as input parameters for the calculations of the neutron emission rate. The neutron transport calculations are needed to obtain the neutron influence from the measured neutron signals after neutron scattering and absorption. Therefore, neutron-transport simulation plays an important role for the evaluation of the different neutron diagnostics. The traditional procedure is to simulate the effects of neutron scattering and absorption on the detector

signals once, and then simple correction can be performed for the real measurement. The much effort from errors of the simulations for experimental neutron diagnostics is devoted to minimize the influence of these effects on the real measurement. [24]

2.1.1. Fusion cross section

The prediction of neutron-source intensity in present fusion experiment and the fusion power gain needs accurate fusion cross sections. Especially, the fusion rates are important on large fusion experiments. The uncertainties of the cross sections are required to be of the order or less than the errors from the measurements of the neutron-source intensity. [24]

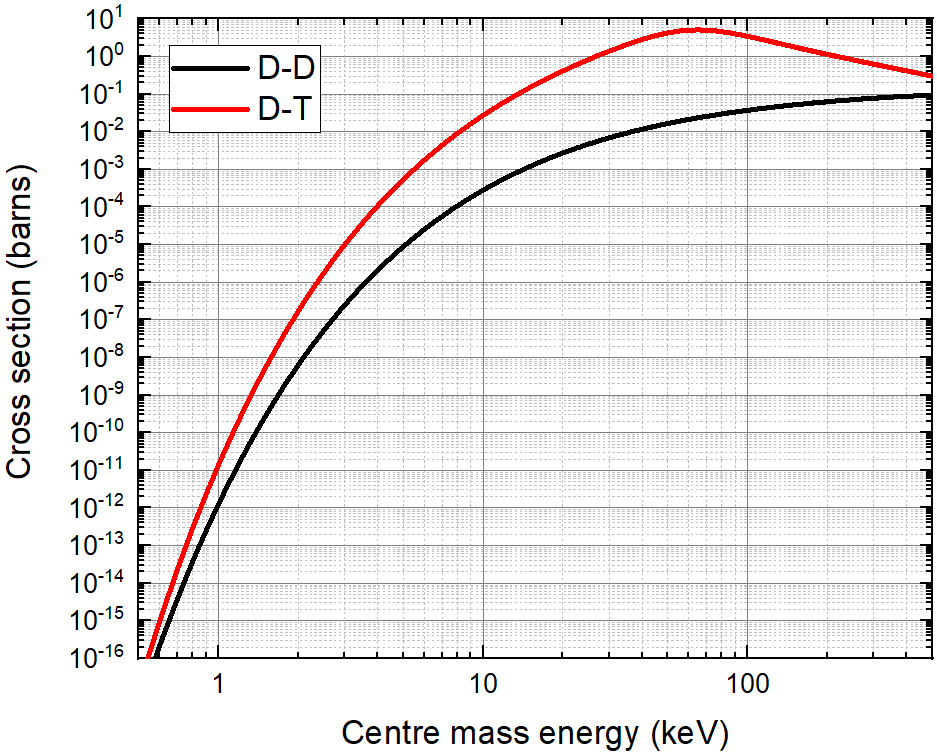

Fig. 2.1 Fusion cross sections for the fusion reactions D(D, n)^{3}He and D(T, n)^{4}He as a function of energy in the Centre-of-mass frame.

Since about 1945, the fusion cross sections have been measured in many experiments. However, reliable experimental data are not available for energy below about 10 keV and available measurements are not always in good agreement even for the limited experimental energy range. Therefore, it is necessary to use theoretical formula

for numerical extrapolation. Furthermore, analytical values of the fusion cross sections are required for calculations of fusion reaction rates. As shown in Fig. 2.1, the cross section varies over more than 10 orders of magnitude in the energy range 1~500 keV. Due to the strong dependence on the particle energy, it has been found most convenient to represent the cross section as:

$$\sigma(E) = \frac{S(E)}{E} e^{-B_G/\sqrt{E}} \tag{2.1.1}$$

where E denotes the energy in the centre-of-mass frame and $B_G = \pi\alpha Z_i Z_j \sqrt{2m_{ij}}$ is the Gamov constant for reacting particles with atomic numbers Z_i and Z_j. Here, $m_{ij} = \frac{m_i m_j}{m_{i+} m_j}$ is the reduced mass and $\alpha = \frac{1}{137}$ is the fine structure constant. The exponential term in EQ. (2.1.1) describes simply the tunneling probability and was first given by Gamov [25]. The factor 1/E results from the quantum mechanical description of the fusion probability, and S is the astrophysical S-function [26]. Thus, the cross section is factorized into terms describing the well-known and strongly energy-dependent quantum mechanical processes and a term which refers solely to nuclear processes of the fusion reaction. For energies below about 90 keV in the case of D-D reactions and about 30 keV for D-T reactions, the S-function can be written as:

$$S(E) \approx \beta e^{-\gamma E} \tag{2.1.2}$$

where β and γ are 52.6 and -5.8×10^{-3} for D-D reaction, and 9821 and -2.9×10^{-2} for D-T reaction, respectively. The improvement in the cross section representation could be achieved by fitting the S-function data obtained from R-matrix analysis [27] with a Padé polynomial. New parameterizations were given for the reactions D(D,n)^{3}He, D(T,n)^{4}He, D(D,p)T and ^{3}He(D,p)^{4}He. For the reaction T(T,2n)^{4}He, a mass-6 R-matrix analysis has also been carried out [28]. The result agrees well with new accurate measurements [29]. [24]

2.1.2. Fusion reactivity

The number of fusion reactions (the number of neutrons produced by fusion

reactions) from the fuel particles involved in the reactions per unit time and volume is called the fusion reaction rate *R* (neutron emission rate), which has a relation between the fuel ion density (n_A and n_B) involved in the reaction and the fusion reactivity $\langle\sigma v\rangle_{AB}$:

$$R = \frac{n_A n_B}{1+\delta_{AB}} \langle\sigma v\rangle_{AB} \tag{2.1.3}$$

where, the number of neutrons per reaction is 1, and δ_{AB} is the Kronecker symbol. The reactivity is in general given by the six-dimensional integral:

$$\langle\sigma v\rangle_{AB} = \iint f_A(\boldsymbol{v}_A) f_B(\boldsymbol{v}_B) \sigma(|\boldsymbol{v}_{AB}|) |\boldsymbol{v}_{AB}| d\boldsymbol{v}_A d\boldsymbol{v}_B \tag{2.1.4}$$

where f_A and f_B are the normalized velocity distributions of the reacting particles, and v_{AB} is relative velocity of the reacting particles. When fuel ions are in thermal equilibrium, ion temperature T_i presents Maxwellian velocity distribution, EQ(2.1.4) change into:

$$\langle\sigma v\rangle_{AB} = \frac{2}{\sqrt{\pi}} \left(\frac{m_{AB}}{2KT_i}\right)^{3/2} \int_0^\infty \sigma(v)\, v^3 e^{-\frac{m_{AB} v^2}{2KT_i}} dv \tag{2.1.5}$$

where $m_{AB} = \frac{m_A m_B}{m_A+m_B}$ is reduced mass of the reacting particles. The more complicated, but rather accurate parameterized form for the thermal reactivity has been given by Bosch and Hale [30]:

$$\langle\sigma v\rangle_{AB} = c_1 \theta \left[\frac{\xi}{m_{AB}(KT)^3}\right]^{1/2} e^{-3\xi}$$

$$\text{where } \theta = \frac{KT}{1-\frac{KT[c_2+KT(c_4+KTc_6)]}{1+KT[c_3+KT(c_5+KTc_7)]}} \text{ and } \xi = \sqrt[3]{\frac{{B_G}^2}{4\theta}} \tag{2.1.6}$$

Here, the reactivity is in cm^3/s and the parameters resulting from this fit are shown in

Table 2.1. [24]

Table 2.1 Parameters for the thermal reactivity fit in Hale-Bosch formula. [30]

Coefficient	D(d,n) ^{3}He	D(d,p)T	T(d,n) ^{4}He	^{3}He(d,p) ^{4}He
B_G (keV$^{1/2}$)	31.397	31.397	34.3827	68.7508
m_{ij} (keV)	937814	937814	1124656	1124572
c_1	5.43360×10^{-12}	5.65718×10^{-12}	1.17302×10^{-9}	5.51036×10^{-10}
c_2	5.85778×10^{-3}	3.41267×10^{-3}	1.51361×10^{-2}	6.41918×10^{-3}
c_3	7.68222×10^{-3}	1.99167×10^{-3}	7.51886×10^{-2}	-2.02896×10^{-3}
c_4	0	0	4.60643×10^{-3}	-1.91080×10^{-5}
c_5	-2.96400×10^{-6}	1.05060×10^{-5}	1.35000×10^{-2}	1.35776×10^{-4}
c_6	0	0	-1.06750×10^{-4}	0
c_7	0	0	1.36600×10^{-5}	0
T_i range (keV)	0.2－100	0.2－100	0.2－100	0.5－190

For D-D neutron emission rate:

$$S_{n-DD} = \int \frac{1}{2} {n_D}^2 \langle \sigma v \rangle_{DD} dV \tag{2.1.7}$$

where, n_D is deuterium density and V is plasma volume.

For triton burnup process, D-T 14 MeV neutron emission rate is:

$$S_{n-DT} = \int n_D n_T \langle \sigma v \rangle_{DT} dV \tag{2.1.8}$$

where, n_T is tritium density which is equal to D-D neutron emission rate. The integral neutron yield Y_n in one shot can be obtained by the shot time integration of the neutron emission rate.

For parameter studies it is often convenient to characterize the radial dependence of a given plasma parameter, i.e. its profile, by the so-called profile peaked-ness or peaking factor which is defined as: $\hat{Z} = \frac{Z(0)V}{\int Z(\rho)dV} = \frac{Z(0)}{\langle Z(\rho)\rangle}$. For neutron emission profiles:

$$S_n(\rho) = S_n(0)(1-\rho^2)^2 \tag{2.1.9}$$

where ρ labels the flux surface or the normalized radius for plasma cross section.

2.1.3. Neutron energy spectra

In the laboratory frame, Using classical kinematics the energy of the fusion neutron from the reaction A(B,n)a, neutron energy can be written as follow [31], [32]:

$$E_n = \frac{1}{2}m_n {v_n}^2 = \frac{1}{2}m_n V^2 + \frac{m_a}{m_n+m_a}(Q+K) + V\cos\varphi\sqrt{\frac{2m_n m_a}{m_n+m_a}(Q+K)} \tag{2.1.10}$$

where m_n is the neutron mass, v_n is its velocity in the laboratory frame, V is the centre-of-mass velocity of the colliding particles, m_a is the mass of the second reaction product, φ is the angle between the centre-of-mass velocity and the neutron velocity in the centre-of-mass frame, Q is the reaction energy, and $K = \frac{1}{2}m_{AB}{v_{AB}}^2$ is the relative energy. The neutron energy spectrum for a given direction of emission is:

$$\frac{d^2N}{d\Omega_{lab}dE} = \frac{n_A n_B}{1+\delta_{AB}}\iint f_A(\boldsymbol{v}_A) f_B(\boldsymbol{v}_B)\frac{d^2\sigma(|\boldsymbol{v}_{AB}|)}{d\Omega_{lab}dE}|\boldsymbol{v}_{AB}|\delta(E-E_n)d\boldsymbol{v}_A d\boldsymbol{v}_B \tag{2.1.11}$$

The energy spectrum of neutrons produced in fusion plasmas provides information on the production mechanisms of the emitted neutrons and the energy distributions of the reacting ions. The thermonuclear plasmas have shown analytically that the energy distribution of the emitted neutrons is approximately given by a Gaussian as:

$$\frac{d^2N}{d\Omega_{lab}dE} = \frac{1}{W\sqrt{\pi}} e^{-\frac{(E-\langle E_n\rangle)^2}{W^2}} \quad (2.1.12)$$

where $\langle E_n \rangle$ denotes averaging of Eq. (2.1.10) over the angle φ and $W^2 = \frac{4m_n\langle E_n\rangle KT}{m_n+m_a}$. Thus, the full width at half maximum (FWHM) $\Delta E = 2W\sqrt{\ln 2}$ of the spectra is a direct measure of the plasma ion temperature. The analytical results are $\Delta E_{DD} = 82.5\sqrt{KT}$ and $\Delta E_{DT} = 177\sqrt{KT}$, respectively. Maxwellian neutron spectra serve as an important test case for the numerical spectra simulation. [24]

2.1.4. Neutron transport theory

The behavior of individual neutrons emitted from fusion experiments cannot be predicted. However, the average behavior in a statistically large population of neutrons can be evaluated quite accurately by extending the concepts of neutron densities, nuclear cross sections, and reaction rates. [24]

A complete mathematical representation of the neutron population requires knowledge of seven variables, viz., position in space $\boldsymbol{r}$, velocity (usually broken into energy E and direction $\boldsymbol{\omega}$) and time t, for which the coordinates $\boldsymbol{r}$, E and $\boldsymbol{\omega}$ are appropriate. Fusion neutron transport problems are usually considered as stationary problems, i.e. time-independent. The neutron transport equation may formally be written as a Fredholm-type integral equation:

$$\psi(\boldsymbol{r}, E, \boldsymbol{\omega}) = \int d\boldsymbol{r}'\, Q(\boldsymbol{r}', E, \boldsymbol{\omega}) T(\boldsymbol{r}' \to \boldsymbol{r}|E, \boldsymbol{\omega}) + \iiint d\boldsymbol{r}' dE' d\boldsymbol{\omega}' \psi(\boldsymbol{r}', E', \boldsymbol{\omega}') C(E', \boldsymbol{\omega}' \to E, \boldsymbol{\omega}) T(\boldsymbol{r}' \to \boldsymbol{r}|E, \boldsymbol{\omega}) \quad (2.1.13)$$

Here, $\psi(\boldsymbol{r}, E, \boldsymbol{\omega})$ is commonly called "out-coming collision density" which it is a density function by the definition used in probability theory. It relates to the expected number of particles coming out of a collision in a volume element of the six-dimensional phase-space and is directly connected to the particle flux. $Q(\boldsymbol{r}', E, \boldsymbol{\omega})$ is the source term which describes the emission of particles at $\boldsymbol{r}'$ with energy E and direction $\boldsymbol{\omega}$. When interaction with matter takes place at a point $\boldsymbol{r}$, the energy and the direction of the neutron-motion will be changed if the neutron is scattered. There are also collisions which lead to absorption or multiplication of the neutron. The total effect of all types of possible

interaction is described by the collision kernel:

$$C(E', \boldsymbol{\omega}' \rightarrow E, \boldsymbol{\omega}) = \frac{1}{\sigma_{tot}(\boldsymbol{r}, E')} \sum_{i=1}^{n} \sum_{j=1}^{m} \nu_{ij} \sigma_{ij}(\boldsymbol{r} | E', \boldsymbol{\omega}' \rightarrow E, \boldsymbol{\omega}) \qquad (2.1.14)$$

where the summations are over the *n* possible elements in the material considered and the *m* possible types of interactions with ν_{ij} expected numbers of out-coming neutrons. Furthermore, σ_{ij} is the differential cross section for element *i* and interaction *j* and σ_{tot} is the total macroscopic cross section. When a neutron has just a collision, until its next interaction, its energy and direction remain unchanged. This is described by the transition kernel:

$$T(\boldsymbol{r}' \rightarrow \boldsymbol{r} | E, \boldsymbol{\omega}) = \sigma_{tot}(\boldsymbol{r}, E) e^{-\int_{r'}^{r} \sigma_{tot}(\boldsymbol{r}'', E) ds} \frac{1}{(\boldsymbol{r} - \boldsymbol{r}')^2} \delta\left(\boldsymbol{\omega} \frac{\boldsymbol{r} - \boldsymbol{r}'}{|\boldsymbol{r} - \boldsymbol{r}'|} - 1\right) \qquad (2.1.15)$$

where $\boldsymbol{r}' \rightarrow \boldsymbol{r}$ represents the integration along a straight line from $\boldsymbol{r}'$ to $\boldsymbol{r}$. [24]

Numerically, Monte Carlo methods are being effectively used for solving neutron transport problems. A comprehensive and detailed overview on the Monte Carlo particle transport methods is given in the book by Lux and Koblinger [33].

2.2. Simulations for fusion neutron emission

Interpretations of neutron signals devoted to obtain information on basic plasma parameters such as densities and temperatures, which require fast dedicated computer codes for simulations. For routine analysis of neutron signals, there are mainly two different approaches as follows.

Firstly, the anticipative neutron signals can be calculated by computer codes for various plasma properties and experimental conditions. By comparing the measured signal with the pre-calculated results, relevant plasma parameters can be deduced.

Secondly, the analysis is restricted to with employing relevant physical boundary conditions. Further restriction is obtained by choosing a set of plasma parameters which are sufficient to describe the most important properties of the plasma neutron source. Then, the neutron signal can be calculated by using this set of measured plasma data. By

comparing measured and calculated results in an iterative procedure, the values of the plasma parameters can be found for consistency between the measurement and the physical assumptions. [24]

By using the measured neutron signals directly as input in order to extract interest plasma parameters, the key assumption for calculations is that the ion velocity distribution can be modelled with sufficient accuracy. For thermal plasmas modelling, due to the ion velocity distribution is Maxwellian distributions, the prediction of plasma parameters from the neutron signals is a straightforward procedure. To treat plasmas with auxiliary heated, it is important that models can be built by non-Maxwellian velocity distributions with sufficient accuracy. For neutral-beam (NB) heated plasmas, the absolute magnitude of the fusion neutron emission has been compared in detail with calculations that assume classical beam deposition and thermalization on many tokamak devices, where it is mainly concerned with the calculation of ion velocity distributions in the presence of NB heating by means of a Fokker-Planck equation. [24]

For the simulation of the neutron emission, accurately measured basic plasma data and neutron signals are as input data. As a direct link with the plasma itself, the neutron emission rate with systematic errors in calculations for known plasma sources need to be discussed carefully. The fast ions deposition profiles must be calculated by several codes or using measured plasma data as input.

2.2.1. Calculation for neutron emission

By using test particle method, a particle with velocity v_i go into a plasma with thermal electron velocity v_e and thermal ion velocity v_{ion}, when $v_e > v_i > v_{ion}$, the kinetic equation can be linearized and the collision operator of the kinetic equation can be the linearized and approximated as:

$$\left(\frac{\partial f_i}{\partial t}\right)_c = \frac{1}{\tau_{se} v^2}\frac{\partial}{\partial v}[(v^3 + {v_c}^3) f_i] + \frac{{v_c}'^3}{4\tau_{se} v^3}\frac{\partial}{\partial \mu}\left[(1-\mu^2)\frac{\partial f_i}{\partial \mu}\right] \qquad (2.2.1)$$

where, τ_{se} is the slowing-down time of ions on electrons which will be expressed with next part. $\mu = \cos\theta$, θ is the pitch angle in a spherical coordinate system (v, θ, ϕ). $v_c = \sqrt{\frac{2E_c}{m_{bi}}}$ and ${v_c}' = {v_c}^3\sqrt{\frac{m_i}{m_{bi}}}$ are the characteristic velocities which can be obtained from the characteristic energy E_c in the next part, where m_i and m_{bi} are

mess of thermal ion and beam test particle.

In the case of NB-heated plasmas, the velocity v_b of NB fast ion obey $v_e > v_b > v_{ion}$. Then, the distribution $f_D(\boldsymbol{v})$ can be split into a thermal part $f_{th}(\boldsymbol{v})$ and a non-thermal (so-called beam) part $f_b(\boldsymbol{v})$. In many codes, a scheme is bsed where usually all slowing-down particles above $1.5v_{th}$ are classified as beam and those below $1.5v_{th}$ are classified as thermal. However, the most general way of splitting the velocity distribution is by defining an isotropic Maxwellian $f_{th}(\boldsymbol{v})$ which coincides with the distribution $f_D(\boldsymbol{v})$ as $v \to 0$:

$$f_D(\boldsymbol{v}) = f_{th}(\boldsymbol{v}) + f_b(\boldsymbol{v}) \tag{2.2.2}$$

The corresponding densities are n_D, n_{th}, and n_b. The fusion reactivity may be written as the sum of three different reactivities:

$$\langle \sigma v \rangle_{DD} = \langle \sigma v \rangle_{tt} + \langle \sigma v \rangle_{bt} + \langle \sigma v \rangle_{bb} \tag{2.2.3}$$

The first term describes the reactivity from the thermal part of the plasma, the second one describes the reactivity between the fast ions and the thermal ions, and the last one the reactivity of the fast ions among themselves. This leads to the decomposition of the neutron rate S_n into three different neutron rates, S_{n-tt} (thermal-thermal), S_{n-bt} (beam-thermal) and S_{n-bb} (beam-beam). [24]

The analytical pitch angle averaged steady-state solution of the kinetic equation with the approximate expression (2.2.1) of the collision term is for the fast particles:

$$f_b(\boldsymbol{v}) = \frac{p_{nbi}}{4\pi E_{inj}} \frac{\tau_{se}}{v^3 + {v_c}^3} \sigma\left(v_{inj} - v\right) \tag{2.2.4}$$

where p_{nbi} is the power density, E_{inj} is the injection energy, and σ is the step function. By using this expression, the following approximate scaling laws for the neutron rates can be found [34]:

$$S_{n-tt} \sim {n_{th}}^2 {T_i}^{\kappa},\ \kappa \approx \frac{6.27}{\sqrt[3]{T_i}} - \frac{2}{3} \tag{2.2.5}$$

$$S_{n-bt} \sim n_{th} \tau_{se} P_{nbi} \tag{2.2.6}$$

$$S_{n-bb} \sim \left(\frac{\tau_{se} P_{nbi}}{E_b}\right)^2 \tag{2.2.7}$$

As can be seen in the above equations, the thermal-thermal neutron rate is determined by the ion temperature and the thermal ion density. The beam-thermal neutron rate is determined by the NB power, the thermal ion density, and slowing-down properties. Here, NB power include beam energy which determine slowing-down time τ_{se} and beam density. The beam-beam neutron rate is solely dependent on the NB power and slowing-down properties. These neutron rates are not independent of each other, but are related through the different plasma parameters. For example, if the non-thermal ion density n_b is of the several orders of the total density, then the thermal density n_{th} is very small and therefore S_{n-tt} and S_{n-bt} are small, and the neutron production is given by beam-beam reactions: S_{n-bb}. With increasing plasma density and keeping the injection power and the temperatures constant, S_{n-bb} will decrease, while S_{n-bt} will reach a constant level, and S_{n-tt} increases with ${n_{th}}^2$. Therefore, for a given operational regime of a tokamak and its NB, there are mainly three approaches to achieve high neutron emission rates. Under the condition of constant energy storage, with the increase of density, the temperature will decrease, which will cause the neutron emission rate to decrease with the increase of density in the high-density area. In high-density plasmas, the thermonuclear reactions between the Maxwellian background ions dominate or are of similar order as the beam-thermal fusion reactions. The contributions due to beam-beam reactions are small or negligible. In plasmas with moderately high electron densities and moderately high temperatures the slowing-down time is relatively short and most of the fusion neutron production is due to beam-thermal reactions. For low-density plasmas with reasonable confinement properties the slowing-down time is comparatively large and the non-thermal ion fraction can exceed 0.2 s, so that a considerable fraction or even the majority of the fusion reactions are due to beam-beam reactions. Therefore, the neutron emission rates will increase with density in low-density plasma, then reach to maximum neutron emission rates, and decrease with density in high-density plasma. [24]

For the triton burnup in a deuterium plasma, the 14 MeV neutron emission rate per volume will be simplified as:

$$S_{n-DT} = n_D n_T \int_0^{t_{th}} \langle \sigma v \rangle_{DT} dt = n_D n_T \int_{E_0}^{E_{th}} \frac{\langle \sigma v \rangle_{DT} dE}{\frac{dE}{dt}} \sim 1.54 n_D n_T \tau_{se} \langle \sigma v \rangle_{DT} \quad (2.2.8)$$

where t_{th} is the time for triton slowing-down from E_0 (1 MeV) to E_{th} and τ_{se} is slowing down time for 1 MeV triton. Therefore,

$$\text{Triton burnup ratio} = \frac{S_{n-DT}}{S_{n-DD}} = n_D \tau_{se} \langle \sigma v \rangle_{DT} \approx n_e \tau_{se} \langle \sigma v \rangle_{DT} \quad (2.2.9)$$

2.2.2. Code of triton burnup calculation

Several computer codes have been developed for the triton burnup calculation on tokamaks. These codes are: a MIS code [18] (Heidbrink *et al*., 1983), a TIMEEV code [35] (Heidbrink, 1984), and a BURNIT code [12] used at TFTR, the SOCRATE [36] (Gorini *et al*., 1987), HECTOR [37] (Kovane and Core, 1988) and TRAP-T [13] (Conroy *et al*., 1988) codes used at JET, and the TBURN code [20] (Nishitani 1990) used at JT-60U. SOCRATE has also been used to analyze data from the FT Tokamak [38] (Batistoni *et al*., 1989). MIS, SOCRATE, HECTOR, and BURNIT can compute the time independent of the triton burnup for a stationary plasma. BURNIT, TIMEEV, and TBURN can calculate the time dependent of triton burnup. SOCRATE and HECTOR calculate the slowing-down along the bounced orbit, while the others assume the tritons slow down on the flux surface of birth. Previously, the JET codes HECTOR and SOCRATE have been compared to each other [39] (Gorini and Kovane, 1988) and to TRAP-T (Conroy *et al*., 1988). The comparison between the calculated neo-classical prompt losses of 1 MeV tritons and the resulting burnup probability for SOCRATE and the TFTR codes is done by P. Batistoni and C.W. Barns, 1991. [35] The comparison between the calculation for 14 MeV neutron emission by TRANSP [41] and BURNIT is done by C.W. Barnes *et al*., 1998 [12].

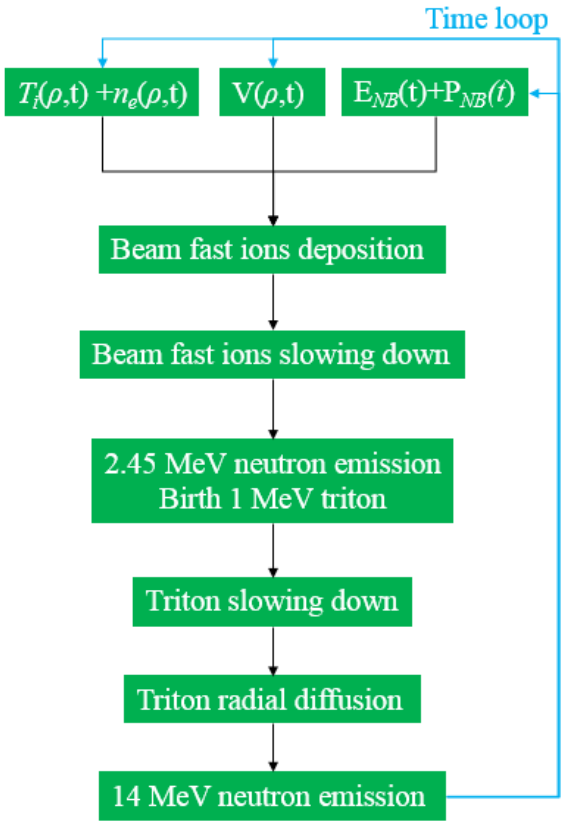

Fig. 2.2 Block diagram of FBURN.

The FBURN code was developed from the TBURN code [20] and used to calculate the triton burnup 14 MeV neutron on LHD as shown in Fig. 2.2. [42] The density and temperature profile were measured in LHD experiment and fitted for smoothness as the input data for the calculation. Z_{eff} is assumed to be 2 and hydrogen to deuterium ratio and hydrogen to helium ratio are specified from Hα, Dα, and He line ratio [43]. The neutron emission is calculated by a simple classical slowing-down model. The plasma is divided into 140 circular shells and each volume is given according to the MHD equilibrium reconstruction by VMEC2000 code [44]. The triton birth profile is calculated using the HFREYA code [45]. Triton slowing-down and D-T reaction rate are calculated by means of calculated radial profile of triton birth. The 1 MeV tritons slowed down in each shell based on the classical energy loss theory. The radial diffusion of triton is assumed to be constant in radius and unchanged in time. The 14 MeV neutron emission rate is evaluated from EQ(2.2.8).

2.3. Classical slowing-down theory

To calculate the 14 MeV neutron emission rate, one of the important process is the calculation of slowing-down for 1 MeV triton in a deuterium plasma. For fast ion velocity v_{bi} between thermal electron velocity and ion velocity $v_e > v_{bi} > v_i$, it will meet the conditions:

$$\frac{0.09m_{bi}}{m_e}KT_e > E_{bi} > \frac{4m_{bi}}{m_i}KT_i \tag{2.3.1}$$

Then, the energy-loss rate can be written as:

$$\langle\frac{dE_{bi}}{dt}\rangle \approx -\sum_i \frac{n_i Z_{bi} Z_i e^4 \sqrt{m_{bi}} \ln \Lambda_{ii}}{4\pi {\varepsilon_0}^2 m_i \sqrt{2E_{bi}}} - \frac{n_e Z_{bi} e^4 \ln \Lambda_{ie} \sqrt{m_e} E_{bi}}{3\sqrt{2} {\varepsilon_0}^2 m_{bi} (\pi K T_e)^{3/2}} = -\frac{\alpha}{\sqrt{E_{bi}}} - \beta E_{bi} \tag{2.3.2}$$

where $\alpha = \sum_i \frac{n_i Z_{bi} Z_i e^4 \sqrt{m_{bi}} \ln \Lambda_{ii}}{4\sqrt{2}\pi {\varepsilon_0}^2 m_i}$ and $\beta = \frac{n_e Z_{bi} e^4 \ln \Lambda_{ie} \sqrt{m_e}}{3\sqrt{2} {\varepsilon_0}^2 m_{bi} (\pi K T_e)^{3/2}}$. Coulomb logarithm is written as:

$$\ln(\Lambda) = 18.86 + \frac{3}{2}\ln(KT) - \frac{1}{2}\ln\left(\frac{n}{10^{19}}\right),\ KT \text{ in keV, } n \text{ in m}^{-3} \tag{2.3.3}$$

$$\ln(\Lambda)_{ei} = 17.1 + \ln(KT_e) - \frac{1}{2}\ln\frac{n_e}{10^{19}},\ KT_e \text{ in keV} \tag{2.3.4}$$

If $KT_e > 0.181\ keV$, $v_e > v_{T=1MeV} > v_i$. Therefore, EQ(2.3.2) can apply to triton burnup. The first term is the ion heating term, and the second term is the electron heating term. When two terms are same, the critical energy can be evaluated as:

$$E_c = \left(\frac{\alpha}{\beta}\right)^{2/3} = \left(\sum_i \frac{3\sqrt{\pi} n_i Z_i \ln \Lambda_{ii}}{4 n_e m_i \sqrt{m_e} \ln \Lambda_{ie}}\right)^{2/3} m_{bi} K T_e \tag{2.3.5}$$

where $n_i = n_e$, Z_i is charge number of ion in the plasma. When $E_{bi} = E_c$, ions and electrons in plasma gain the same amount of energy. When $E_{bi} > E_c$, the electrons gain more energy. When $E_{bi} < E_c$, ions gain more energy. [46]

Here, the mean time for the energy of beam particles slowing-down to the thermal energy or 0 can be calculated:

$$\tau = \int_{E_0}^{0} \frac{dE_{bi}}{\langle \frac{dE_{bi}}{dt} \rangle} = \int_{0}^{E_0} \frac{dE_{bi}}{\frac{\alpha}{\sqrt{E_{bi}}} + \beta E_{bi}} = \frac{2}{3\beta} \ln\left(1 + \frac{\beta}{\alpha} E_0^{3/2}\right) = \frac{2\tau_{se}}{3} \ln\left[1 + \left(\frac{E_0}{E_c}\right)^{3/2}\right] \quad (2.3.6)$$

where E_0 is the initial energy of beam, τ_{se} is the slowing-down time for ion beam.

$$\tau_{se} = \frac{1}{\beta} = \frac{3\sqrt{2}\varepsilon_0^2 m_{bi} (\pi K T_e)^{3/2}}{n_e Z_{bi}^2 e^4 \sqrt{m_e} \ln \Lambda_{ie}} \quad (2.3.7)$$

2.4. Single-particle orbit motions

It is necessary to analyze the orbit effect of a triton for 14 MeV neutron emission rate due to large Larmor radius of the 1 MeV triton. Because the densities of a plasma are in an intermediate range between a fluid and a rarefied gas, it is not easy to say plasma is a fluid or a rarefied gas. Fluids such as water are dense, therefore, the motions of individual molecules do not need to be considered. Collisions dominate in fluid, therefore, the simple equations of ordinary fluid dynamics are enough for analysis. In extremely low-density case, such as the synchrotron, only single-particle trajectories need to be considered, and collective behaviors of particles are often unimportant. For simplified consideration of a plasma, the first step is to understand single-particle behaviors in electric and magnetic fields. [47]

2.4.1. $\mathbf{E} \times \boldsymbol{B}$ drift

From electric field **E**=0, the cyclotron frequency and radius of the particle in a magnetic field $\boldsymbol{B}$ can be deduced:

$$\omega_c = \frac{|e|\boldsymbol{B}}{m} \text{ and } r_c = \frac{\boldsymbol{v}_\perp}{\omega_c} = \frac{m\boldsymbol{v}_\perp}{|e|\boldsymbol{B}} \quad (2.4.1)$$

where e and m are the charge and the mass of particle, and $\boldsymbol{v}_\perp$ is the velocity perpendicular to the magnetic field $\boldsymbol{B}$. The cyclotron radius r_c is a so called Larmor radius r_L. If there is an electric field, the motion will be found to be the sum of two motions: the usual circular Larmor gyration and a drift of the guiding-center which is center of Larmor radius. The equation of motion is described as follows:

$$m\frac{d\boldsymbol{v}_\perp}{dt} = e(\mathbf{E} + \boldsymbol{v}_\perp \times \boldsymbol{B}) \tag{2.4.2}$$

Therefore, the drift velocity of guiding center can be written as:

$$\boldsymbol{v}_{\perp gc} = \frac{\mathbf{E}\times\boldsymbol{B}}{\boldsymbol{B}^2} = \boldsymbol{v}_\mathbf{E} \tag{2.4.3}$$

This is the so called $\mathbf{E} \times \boldsymbol{B}$ drift. It is important to note that $\boldsymbol{v}_\mathbf{E}$ is independent of e and m. [46]

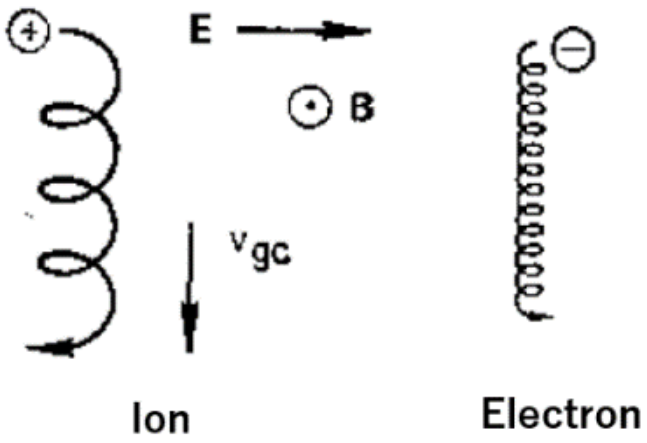

Fig. 2.3 Drifts of charged particles in crossed electric and magnetic fields. [47]

In the first-cycle of ion's orbit as shown in Fig. 2.3, it gains energy from the electric field and increases in $\boldsymbol{v}_{\perp gc}$ and r_L. In the second half-cycle, it loses energy and decrease

in $\boldsymbol{v}_{\perp gc}$ and r_L. This difference in r_L on the first and second half-cycle of orbit causes the $\mathbf{E} \times \boldsymbol{B}$ drift. A negative electron gyrates in the opposite direction but also gains energy in the opposite direction, where results that it ends up drifting in the same direction with ion. For particles of the same velocity but different mass, the lighter one will have smaller r_L and hence drift less, but, ω_c is larger, and the two effects exactly cancel. For two same particles with different energy, the slower one will have smaller r_L and gain less energy. [47]

2.4.2. $\nabla \boldsymbol{B}$ drift and curvature drift

The charged particle moves in a non-uniform magnetic field, thus, the drift will be induced by the non-uniform magnetic field. The inhomogeneity of flux density is represented by the gradient of magnetic field $\nabla \boldsymbol{B}$ as shown in Fig. 2.4. The velocity of grad $\boldsymbol{B}$ drift is:

$$\boldsymbol{v}_{\nabla \boldsymbol{B}} = \pm \frac{1}{2} \boldsymbol{v}_{\perp} r_c \frac{\boldsymbol{B} \times \nabla \boldsymbol{B}}{\boldsymbol{B}^2} \tag{2.4.4}$$

where the stands $\pm$ for the sign of electron and ion charges. This means that grad $\boldsymbol{B}$ drift for ion and electron is in opposite, and the reason is to create a current transverse to $\boldsymbol{B}$. [47]

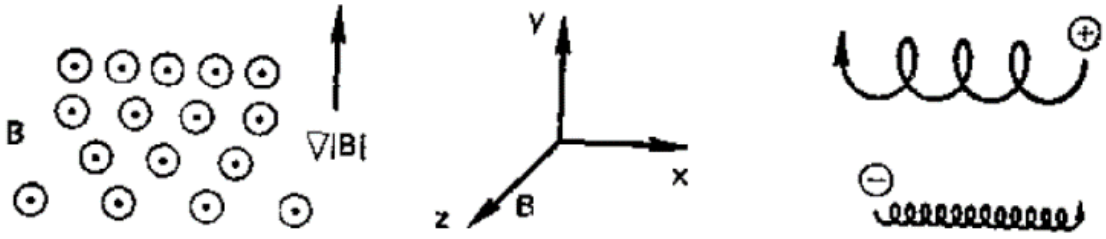

Fig. 2.4 Drift of a gyrating charged particle in a non-uniform magnetic field. [47]

A guiding-center drift increases from the centrifugal force on the particles as motion along the field lines that have a constant radius of curvature $\boldsymbol{R}_c$ as shown in Fig. 2.5. Therefore, the velocity of curvature drift is:

$$\boldsymbol{v_R} = \frac{m{v_{/\!/}}^2}{e\boldsymbol{B}^2}\frac{\boldsymbol{R_c}\times\boldsymbol{B}}{{\boldsymbol{R_c}}^2} \tag{2.4.5}$$

The curvature drift must be accompanied with the grad $\boldsymbol{B}$ drift in and out of the bending magnetic field. [46] The drift velocity is:

$$\boldsymbol{v_R} + \boldsymbol{v_{\nabla B}} = \frac{m}{e\boldsymbol{B}^2}\frac{\boldsymbol{R_c}\times\boldsymbol{B}}{{\boldsymbol{R_c}}^2}\left({\boldsymbol{v}_{/\!/}}^2 + \frac{1}{2}{\boldsymbol{v}_{\perp}}^2\right) \tag{2.4.6}$$

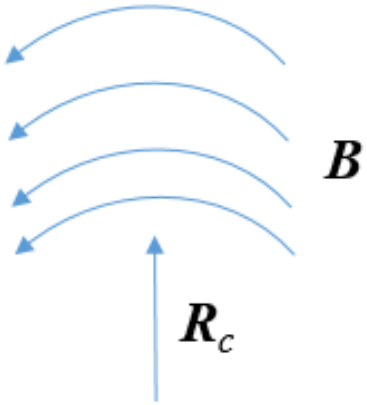

Fig. 2.5 Curved magnetic field.

2.4.3. Motion in a magnetic mirror

There is a magnetic field which is pointed primarily in the z direction and whose magnitude varies in the z direction. And the field is axisymmetric, which means that $\boldsymbol{B}_\theta = 0$ and $\frac{\partial}{\partial\theta} = 0$. Since the lines of force converge and diverge, there is necessarily a component $\boldsymbol{B}_r$, which lead to the guiding center follow the lines of magnetic force. Therefore, the average drift force can be written as $\overline{\boldsymbol{F}}_z = \mp\frac{e\boldsymbol{v}_\perp r_c}{2}\frac{\partial \boldsymbol{B}_z}{\partial z} = -\frac{m{\boldsymbol{v}_\perp}^2}{2\boldsymbol{B}}\frac{\partial \boldsymbol{B}_z}{\partial z}$, where the magnetic moment of the gyrating particle is defined as:

$$\mu = -\frac{m{\boldsymbol{v}_\perp}^2}{2\boldsymbol{B}} \tag{2.4.7}$$

μ is antiparallel to $\boldsymbol{B}$ and independent of the sign of the charge, which is called the anti-magnetism of a plasma. [47]

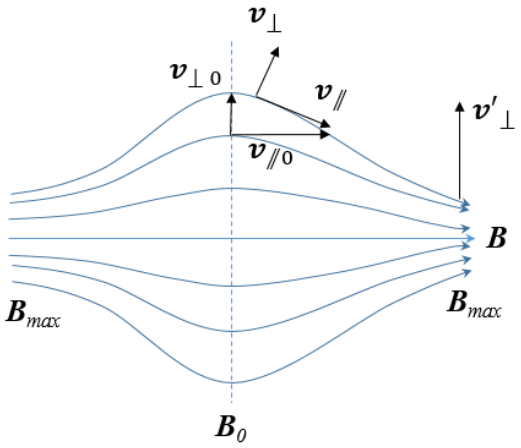

Fig. 2.6 Drift of a particle in a magnetic mirror field.

This is because the current source of a gyrating charged particle generates a magnetic field opposite to the original field $\boldsymbol{B}$. From the force parallel to the magnetic field $\boldsymbol{F}_{/\!/}\boldsymbol{v}_{/\!/} = -\mu\frac{d\boldsymbol{B}}{dt} = \frac{d}{dt}\left(\frac{1}{2}m\boldsymbol{v}_{/\!/}{}^2\right)$, $\boldsymbol{B}$ is not changing with time $\frac{d\boldsymbol{B}}{dt} = 0$, and conservation of energy $\frac{d}{dt}\left(\frac{1}{2}m\boldsymbol{v}_{/\!/}{}^2 + \frac{1}{2}m\boldsymbol{v}_\perp{}^2\right)_{-\mu\boldsymbol{B}=\frac{1}{2}m\boldsymbol{v}_\perp{}^2} = 0$, μ is not changing with time $\frac{d\mu}{dt} = 0$. It means that μ is an invariant. As the particle moves from a weak field region to a strong field region, $\boldsymbol{v}_\perp$ increase with $\boldsymbol{B}$ to keep μ constant. Since total energy is conservation, $\boldsymbol{v}_{/\!/}$ must decrease. If $\boldsymbol{B}$ is high enough in the "throat of mirror", $\boldsymbol{v}_{/\!/}$ eventually becomes 0, and the particle is reflected back to the weak field region. [47] The result is that the particle is trapped in a configuration of magnetic mirror as show in Fig. 2.6.

However, the trapping is not perfect. If $\boldsymbol{B}_m$ is not large enough, a particle with small $\boldsymbol{v}_\perp/\boldsymbol{v}_{/\!/}$ at the mid-plane ($\boldsymbol{B}$= $\boldsymbol{B}_0$) will escape. A particle with $\boldsymbol{v}_{\perp 0}$ and $\boldsymbol{v}_{/\!/0}$ at the mid-plane will have $\boldsymbol{v}_\perp = \boldsymbol{v}'_\perp$ and $\boldsymbol{v}_{/\!/} = 0$ at the turning point. Then the invariance of μ yields $\boldsymbol{v}_{\perp 0}{}^2/\boldsymbol{B}_0 = \boldsymbol{v}'_\perp{}^2/\boldsymbol{B}_m$ and conservation of energy $\boldsymbol{v}'_\perp{}^2 = \boldsymbol{v}_{\perp 0}{}^2 + \boldsymbol{v}_{/\!/0}{}^2 = \boldsymbol{v}_0{}^2$,

$$\frac{\boldsymbol{B}_0}{\boldsymbol{B}_m} = \frac{{\boldsymbol{v}_{\perp 0}}^2}{{\boldsymbol{v}'_{\perp}}^2} = \frac{{\boldsymbol{v}_{\perp 0}}^2}{{\boldsymbol{v}_0}^2} = \sin^2\theta_m = \frac{1}{R_m} \tag{2.4.8}$$

Here, θ_m is the minimum θ of a confined particle, where θ is the pitch angle of the orbit in the weak field region. If $\theta < \theta_m$, the particle can not be trapped. Therefore, a boundary of a region in velocity space in the shape of a cone θ_m is so called a loss cone. R_m is the mirror ratio. It can be seen that θ_m decrease with increase of R_m. It means that the number of loss particles decreases with the increase of R_m. The proportion of the escape cone solid angle to the total solid angle 4π is $\mathrm{P} = 1 - \cos\theta = 1 - \sqrt{R_m - \frac{1}{R_m}}$.

When $R_m \gg 1$, $\mathrm{P} \cong \frac{1}{2R_m}$. To consider the collision, there will be more and more particles going into the loss cone. [47]

2.4.4. Motion in a toroidal magnetic field

Inevitably, there is terminal loss in the magnetic mirror confinements. The terminal loss can be avoided by using closed magnetic field configuration such as the toroidal magnetic field configuration as shown in Fig. 2.7. In the toroidal magnetic field configuration, the magnetic-force lines are formed by circling around the toroidal direction for several cycles. The magnetic surfaces are nested structure. The most central magnetic surface degenerates into a magnetic-force line closed around one cycle which is called the magnetic axis. The distribution of the magnetic field is getting smaller and smaller outward, and getting larger and larger inward along the radius *R* of the device. Therefore, curvature drift will lead to charge separation to create electric filed which is perpendicular to $\boldsymbol{B}$. Then, $\mathbf{E} \times \boldsymbol{B}$ drift lead to particle loss. The simple ring magnetic field is not enough to confine the thermonuclear plasma.[48]

In tokamak and stellarator, the rotation transformation is adopted to make the magnetic field line not close after one circle and rotate form up side to down side to offset charge separation as shown in Fig. 2.8. In this magnetic field configuration, $\iota = 2\pi\frac{n}{m}$ is the rotation transformation angle, where *m* and *n* mean that it returns to its original position after going around the circle *m* times in the polar direction of a magnetic field line, which happens to go around the circle *n* times in toroidal direction. In order to realize the rotation transformation, a polar magnetic field $\boldsymbol{B}_\theta$ needs to be added to the toroidal magnetic field $\boldsymbol{B}_\varphi$ as shown in Fig. 2.8. Thus the magnetic field in the plasma is the

superposition of these two fields, and the magnetic-field lines become helical. In stellarator, $\boldsymbol{B}_\theta$ is supplied by coil. In tokamak, $\boldsymbol{B}_\theta$ is generated by plasma current. The stability factor (safety factor) of magnetohydrodynamics (MHD) is also defined as:

$$q = \frac{\boldsymbol{B}_\varphi}{\boldsymbol{B}_\theta}\frac{r}{R} = \frac{2\pi}{\iota} \tag{2.4.9}$$

where R is the radius of magnetic axis, r is the small radius of the helical magnetic-field line. [48]

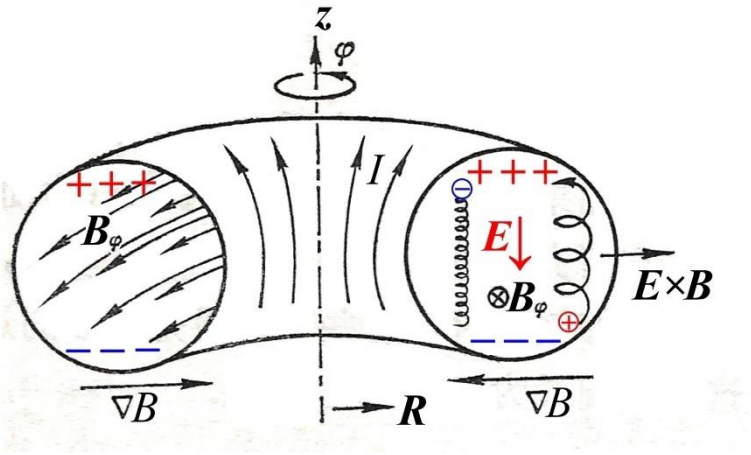

Fig. 2.7 Drift in a toroidal magnetic field.

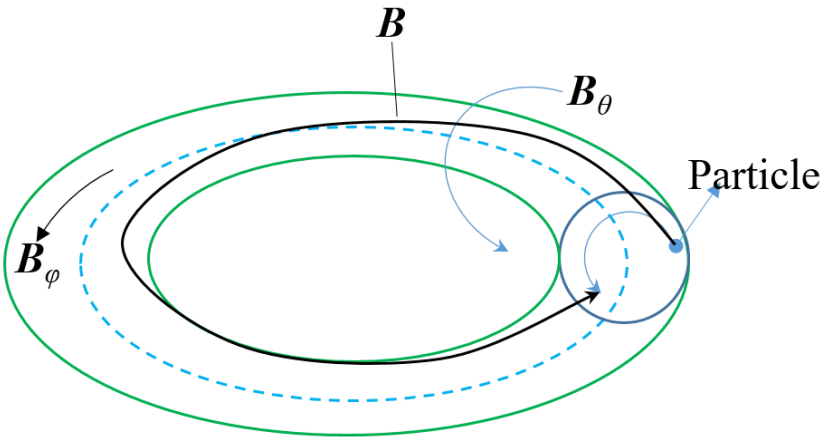

Fig. 2.8 The rotation transform of magnetic field line.

In this kind of magnetic-field configurations, the motion of charged particles can be divided into two categories. One is a passing particle whose angle between the particle velocity and the magnetic field $\boldsymbol{B}$ is small, that is the parallel component $\boldsymbol{v}_{/\!/}$ is larger. The result is that the particle can pass through the strong field without being bounced back. The other type is the trapped particle. This kind of particles with a small $\boldsymbol{v}_{/\!/}$ cannot pass through a region of strong magnetic field, but can only bounce back and forth between two adjacent regions of strong magnetic field. Its orbit is like the shape of a banana. Therefore, it is also called a banana particle. [48]

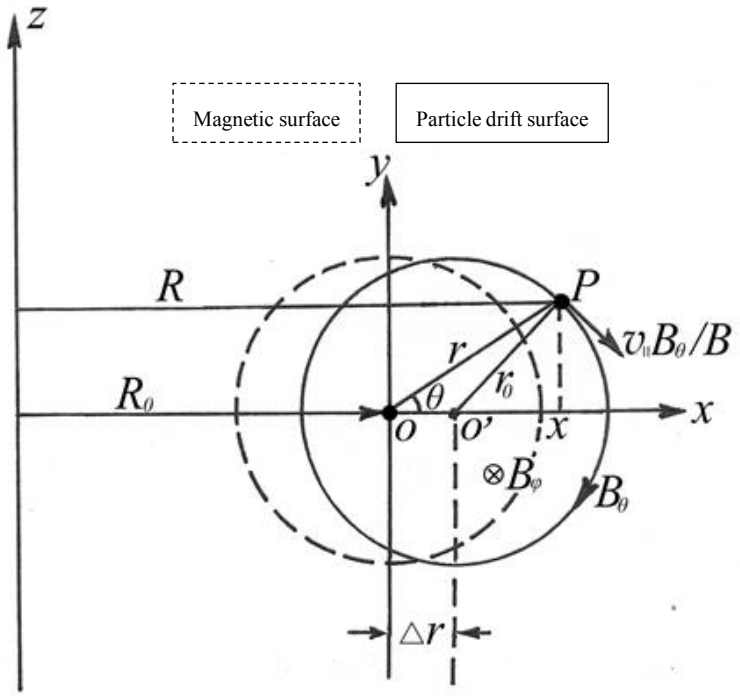

Fig. 2.9 Passing particle cyclotron motion.

If there is no drift, the passage particle moves only along the magnetic surface. Fig. 2.9 shows that a passing particle moves along with a magnetic surface centered at O and drift. The motion of a particle guiding-center is decomposed into the motion along the magnetic-field line and the drift caused by the non-uniform magnetic field $\boldsymbol{B} = \boldsymbol{B}_\varphi \boldsymbol{e}_\varphi + \boldsymbol{B}_\theta \boldsymbol{e}_\theta$, where $\boldsymbol{B}_\varphi = \boldsymbol{B}_0 \frac{R_0}{R}$.

$$\boldsymbol{v}_D = m\frac{2\boldsymbol{v}_{/\!/}{}^2+\boldsymbol{v}_{\perp}{}^2}{2e\boldsymbol{B}_{\varphi}R}\boldsymbol{e}_y \tag{2.4.10}$$

The motion equation of the projection on the *xy* plane of the guiding center is:

$$\begin{cases} \frac{dx}{dt} = \boldsymbol{v}_{/\!/}\frac{\boldsymbol{B}_\theta}{\boldsymbol{B}}\frac{y}{r} \\ \frac{dy}{dt} = -\boldsymbol{v}_{/\!/}\frac{\boldsymbol{B}_\theta}{\boldsymbol{B}}\frac{x}{r} + \boldsymbol{v}_D \end{cases} \tag{2.4.11}$$

By using $dr = \frac{1}{r}(xdx + ydy)$, EQ(2.4.11) change to $\frac{dr}{dx} = \frac{\boldsymbol{v}_D\boldsymbol{B}}{\boldsymbol{v}_{/\!/}\boldsymbol{B}_\theta} = a_0$ (for passing particles $a_0 \ll 1$) whose solution is $r = r_0 + a_0 x$. Therefore, $(x - a_0 r_0)^2 + y^2 \approx {r_0}^2$, which means that the entire drift surface of the co-going (clockwise) particle orbit moves a distance Δr to the right relative to the magnetic field.

$$\Delta r = a_0 r_0 \approx q r_c \tag{2.4.12}$$

Similarly, the center of the entire drift surface of a counter-going (counterclockwise) particle orbit is shifted a distance Δr to the left relative to the magnetic surface. [48]

If drift is not taken into account, the trapped particle only moves back and forth in two local magnetic-mirror fields of the rotating transformation-magnetic-field configuration, where the projection of its guiding-center on the *xy* plane is only an arc between two reflection points *M1* and *M2* on the magnetic surface as shown in Fig. 2.10. After considering the drift, the orbit projection of the guiding center is $\frac{dr}{dx} = \pm\frac{\boldsymbol{v}_D\boldsymbol{B}}{\boldsymbol{v}_{/\!/}\boldsymbol{B}_\theta}$. Due to $\boldsymbol{v}_0{}^2 = \boldsymbol{v}_\perp{}^2 + \boldsymbol{v}_{/\!/}{}^2 = \boldsymbol{v}_{\perp M}{}^2$ and $\mu = \frac{m\boldsymbol{v}_\perp{}^2}{2\boldsymbol{B}} = \frac{m\boldsymbol{v}_0{}^2}{2\boldsymbol{B}_M}$, $\boldsymbol{v}_{/\!/} = \boldsymbol{v}_0\sqrt{1-\frac{\boldsymbol{B}}{\boldsymbol{B}_M}} \cong \boldsymbol{v}_0\sqrt{\frac{x-x_M}{R_0}}$, where $\boldsymbol{v}_{\perp M}$ is perpendicular velocity at the maximum magnetic field $\boldsymbol{B}_M$. Therefore, the maximum deviation between the particle drift surface and the magnetic surface is:

$$\Delta r_T = \frac{2\boldsymbol{v}_D\boldsymbol{B}_0}{\boldsymbol{v}_0\boldsymbol{B}_\theta}\sqrt{R_0 r_0(1-\cos\theta_M)} \approx \frac{2qr_c\sqrt{\varepsilon(1-\cos\theta_M)}}{\varepsilon} < \frac{2qr_c}{\sqrt{\varepsilon}} \tag{2.4.13}$$

where θ_M is the angle between r_0 and the x-axis when the particle returns to the magnetic surface. Δr_T is half Banana orbit width.

$$\varepsilon = \frac{r_0}{R_0} \approx \frac{a}{R_0} \tag{2.4.14}$$

ε^{-1} is a ratio of transverse and longitudinal. [48]

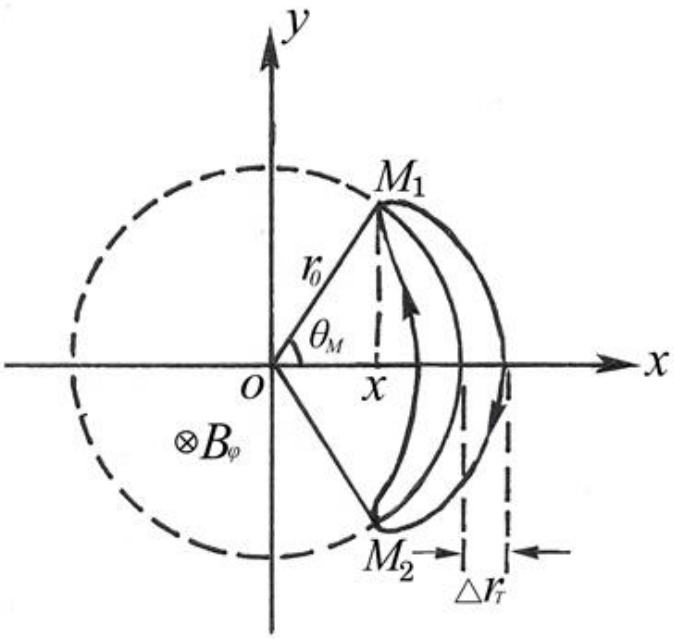

Fig. 2.10 Banana orbit.

When the guiding center of the particle rotates clockwise along the magnetic field line, $r > r_0$, it drift outward; When the guiding center of the particle rotates counterclockwise along the magnetic field line, $r<r_0$, it drift inward.

The critical angle θ_c of the toroidal magnetic field can be obtained by the loss cone similar to the magnetic mirror. The minimum and maximum values of the magnetic field are $\boldsymbol{B}_m \cong \boldsymbol{B}_0(1-\varepsilon)$ and $\boldsymbol{B}_M \cong \boldsymbol{B}_0(1+\varepsilon)$, respectively.

$$\sin\theta_c = \sqrt{\frac{\boldsymbol{B_m}}{\boldsymbol{B_M}}} = \sqrt{\frac{1-\varepsilon}{1+\varepsilon}} \tag{2.4.15}$$

According to the proportion of the escape cone solid angle to the total solid angle 4π is $\mathrm{P} = 1 - \cos\theta_c$. The ratio of trapped particles to total particles is:

$$f_T = 1 - P = \sqrt{\frac{2\varepsilon}{1+\varepsilon}} \approx \sqrt{2\varepsilon} \tag{2.4.16}$$

Therefore, when $\boldsymbol{v}_{/\!/}/\boldsymbol{v}_{\perp} > \sqrt{2\varepsilon}$, and $\theta < \theta_c$, the particle is passing particle. When $\boldsymbol{v}_{/\!/}/\boldsymbol{v}_{\perp} < \sqrt{2\varepsilon}$, and $\theta > \theta_c$, the particle is trapped particle. [48]

Chapter 3:

Neutron diagnostics for triton burnup study on LHD[1]

The fusion products of nuclear reactions occurring within the plasma can be used as a convenient diagnostic for the ions. For this purpose, the neutron is the reaction product of most interest since, being uncharged, it is able to escape immediately from the plasma and, hence, can be detected. Neutron diagnostics involve the experimental neutron detection techniques and the (computational) techniques for extracting relevant information about the velocity functions of the fusing ions out of the measured neutron signals.

3.1. Large Helical Device

The Large Helical Device (LHD) is a fusion research device in Toki, Gifu, Japan, belonging to the National Institute for Fusion Science, which is the first largest superconducting stellarator in the world, with major radius of 3.9 m, plasma minor radius of 0.6 m, plasma volume of 30 m^3, and toroidal magnetic field 3 T as shown in Fig. 3.1. Its mode number l/n is 2/10. The total heating power is 36 MW. The maximum neutron rate reached 3.3×10^{15} n/s. The ion temperature, the electron temperature (T_e), and the density reached 12 keV at density of 1.3×10^{19} m^{-3}, 23 keV at density of 0.2×10^{19} m^{-3} or 12 keV at density of 1.6×10^{19} m^{-3}, and 1.2×10^{21} m^{-3} at T_e of 0.3 keV, respectively. The maximum plasma sustaining time reached 54 min. operated with hydrogen plasma since

[1] This chapter is written by:
N. Pu, *et al*, "*In situ calibration of neutron activation system on the large helical device*", Rev. Sci. Instrum., **88** 113302 (2017).
N. Pu, *et al*, "*Scintillating fiber detectors for time evolution measurement of the triton burnup on the Large Helical Device*", Rev. Sci. Instrum., **89** 10I105 (2018).

1998 and the deuterium plasma operation was conducted from March 2017. [8]

(a)

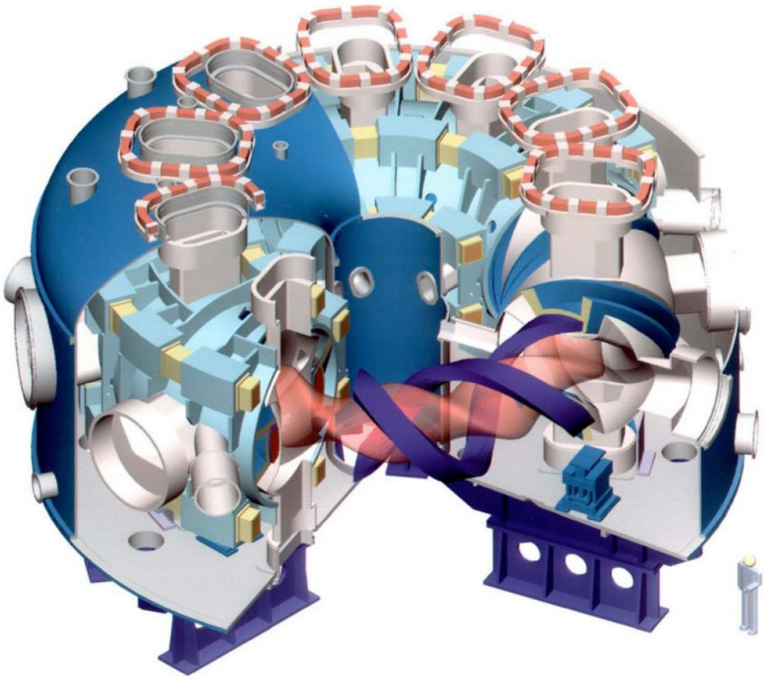

(b)

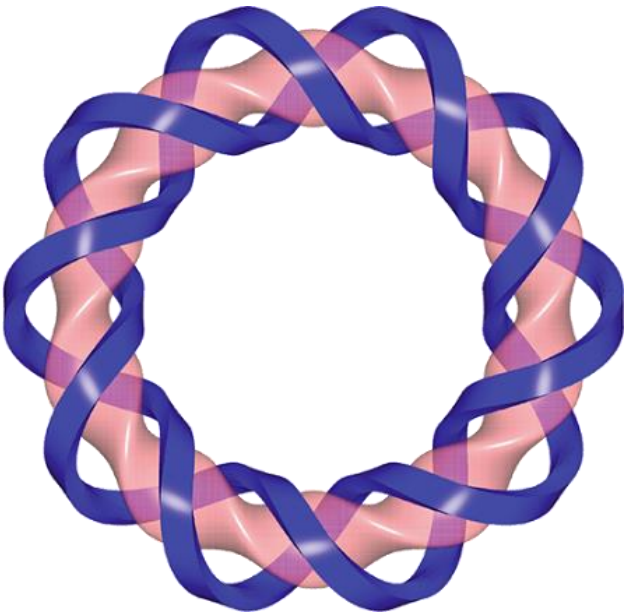

Fig. 3.1 (a) The Large Helical Device, and (b) the shape of LHD plasma and helical coils.[50]

3.2. Neutron flux monitor

Neutron flux monitor (NFM) is the most important neutron diagnostics for measuring the absolute total neutron emission rate from the plasma and essential in the LHD operation in addition to physics purposes since annual neutron budget permitted by the Nuclear Regulation Authority of Japan is set to be 2.1×10^{19}. [51] Uranium fission chambers are widely used in present fusion devices and also ITER [52]. A wide dynamic range NFM based on leading-edge digital technologies has been developed for LHD deuterium experiment. [53] Fig. 3.2 shows the schematic view of the NFMs on LHD. The NFMs consist of three ^{235}U fission chambers and additional high sensitive neutron detectors of a ^{10}B proportional counter or two ^{3}He proportional counters. The thermal neutron sensitivity of the ^{10}B proportional counter is about 1/5 of that of the ^{3}He proportional counter. The NFMs are positioned at three locations outside the cryostat: on the top of the center axis, and two large outside ports, which are the 4-O port and the 10-O port. Thermal neutron sensitivities of the ^{235}U fission chamber, the ^{10}B proportional counter, and the ^{3}He proportional counter are 0.1, 6.5, and 39 cps/nv, respectively. Those detectors are mounted in the 50 mm-thick polyethylene moderators, which have an almost flat response function in the neutron energy range of 0.5 eV-14 MeV. [54]

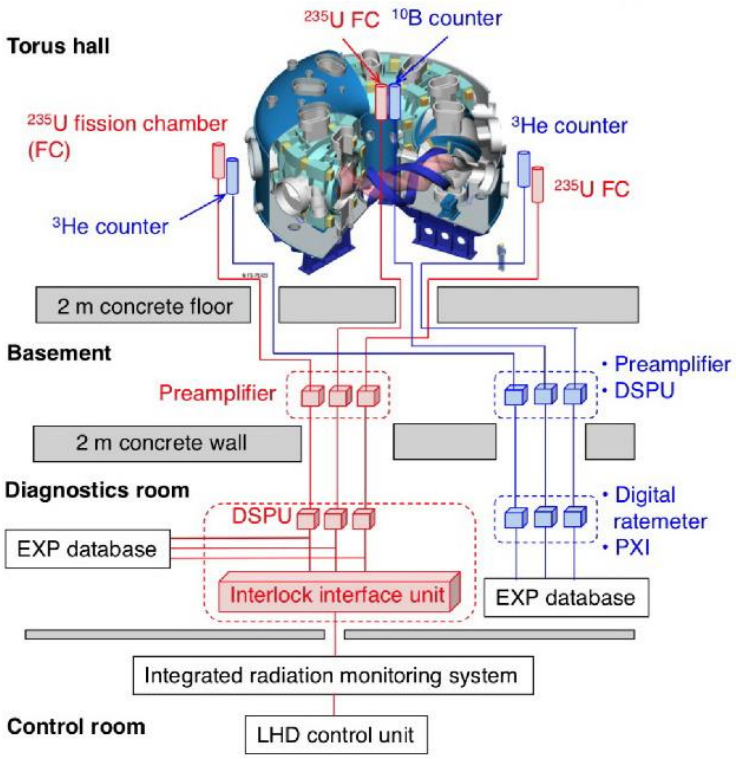

Fig. 3.2 Schematic view of the LHD neutron flux monitors. [51]

These detectors measure neutrons by $^{10}B(n, \alpha)^{7}Li$ reaction, $^{3}He(n, p)T$ reaction, and neutron induced fission reaction $^{235}U(n, f)$. The secondary particles or fission fragments from the reactions carry a larger reaction which can ionize in the detector gas to produce a detectable electrical signal. These signals are therefore easily distinguishable from low-ionized gamma ray signals. By setting suitable threshold, the neutron signal can discriminate from back gamma-rays.

The preamplifiers and the digital data processing modules are located in the basement and the diagnostic room, respectively, in order to avoid irradiation damage on those electronic components. A digital data processing module is used for fission chambers, which operates in both pulse counting mode and Campbell (Mean Square Voltage: MSV) mode with Field-Programmable Gate Arrays (FPGAs). By using this digital data processing (DDP), a wide dynamic ranges up to 5×10^{9} cps equivalent is obtained for one fission chamber [53]. The FC line (red line in Fig. 3.2) is responsible for middle- to high-neutron yield shots when NBs are injected. [51] The detection efficiencies of ^{10}B and ^{3}He proportional counters are larger than those of the fission chamber. Those detectors operate only in the pulse counting mode whose typical pulse width is several μs. The maximum counting rates are up to 1×10^{5} counts/s or less. [54] Therefore, the usage of ^{10}B and ^{3}He proportional counters is limited in the low neutron emission rate plasma discharges such as plasmas heated by electron-cyclotron-resonance wave without NB injection.

3.3. Neutron activation system

The neutron activation system (NAS) on the LHD is a so-called rabbit system, consisting of the activation foils, the capsule, pneumatic system (control systems, two irradiation ends, pneumatic tubes, air compressor, and launching/collecting station), and two high-purity germanium (HPGe) gamma-ray detectors. The system design of the NAS is based on that used in JT-60U.[15] The activation foil is mounted on a capsule made of polyethylene. The capsule loaded with the activation foils is transferred through a pneumatic tube from the station to the irradiation end.[56]

Although the NAS does not provide time evolution of the neutron emission rate, it is completely insensitive to the gamma ray and is of great value for performing cross check of the neutron yield evaluated by the NFM. [57], [58] The NAS also performs an important role in the triton burnup study through measurements of the secondary 14.1 MeV neutron yield.

3.3.1. Principle of activation measurement

The neutron activation techniques have been used to measure neutron flux on different occasions. For an activated sample, the reaction rate is *R*. The number of radioactive nuclei can be written as;

$$N(t) = \frac{R(1-e^{-\lambda t})}{\lambda} \tag{3.1}$$

here $\lambda = \frac{1}{t_{1/2}}$ is the decay constant of activated nuclide in the sample ($t_{1/2}$) and t is the end of irradiation time from the start of irradiation ($0 \sim t_0$) [s], where the activity of the sample just after irradiation time t_0 is $A(t_0) = \lambda N(t_0) = A_0$. [59]

The gamma-ray counts of under the specific gamma-ray peak measured in a measurement time $\Delta t = t_2 - t_1$ can be written as:

$$C = S_n \alpha_\gamma \varepsilon \int_{t_1}^{t_2} A_0 e^{-\lambda t} dt = \frac{S_n \alpha_\gamma \varepsilon R}{\lambda}\left(1 - e^{-\lambda t_0}\right)\left(e^{-\lambda t_1} - e^{-\lambda t_2}\right) \tag{3.2}$$

where α_γ is gamma ray abundance, t_1 is start time of the gamma-ray measurement from the start of the irradiation [s], t_2 is end time of the gamma-ray measurement from the start of the irradiation [s], and ε is the efficiency of the HPGe detector in the specific gamma-ray peak. The reaction rate *R* and the total number of reactions from the irradiation can be evaluate from Eq(3.2) by assuming the irradiation time is much shorter than the half-life of the radioactive nucleus $t_0 \ll \frac{1}{\lambda} = t_{1/2}$. [59]

The averaged neutron emission rate S_n [s^{-1}] can be calculated by the expression:

$$S_n = \frac{\lambda \cdot C}{N \cdot \alpha_\gamma \cdot \varepsilon \cdot \left(e^{-\lambda t_1} - e^{-\lambda t_2}\right) \cdot \left(1 - e^{-\lambda t_0}\right) \cdot \sum_E \sigma(E) \cdot \Phi(E)} \tag{3.3}$$

here the reaction rate *R* is given by $\sum_E \sigma(E) \cdot \Phi(E)$, where $\sigma(E)$ is cross section of the reaction [b], $\Phi(E)$ is neutron spectrum in the irradiation end for unit source neutron [cm^{-}

$^{2}\cdot s^{-1}]$, E is neutron energy, which means reaction number of sample for unit source neutron and unit sample nuclei number. $N = \frac{\alpha_{is} \cdot m \cdot N_A}{M}$ is the number of sample nuclei, α_{is} is the isotopic fraction of the sample nuclide, m is the mass of the sample [g], N_A is Avogadro's constant [mol^{-1}], and M is the molar mass of the nuclide [g/mol]. [56]

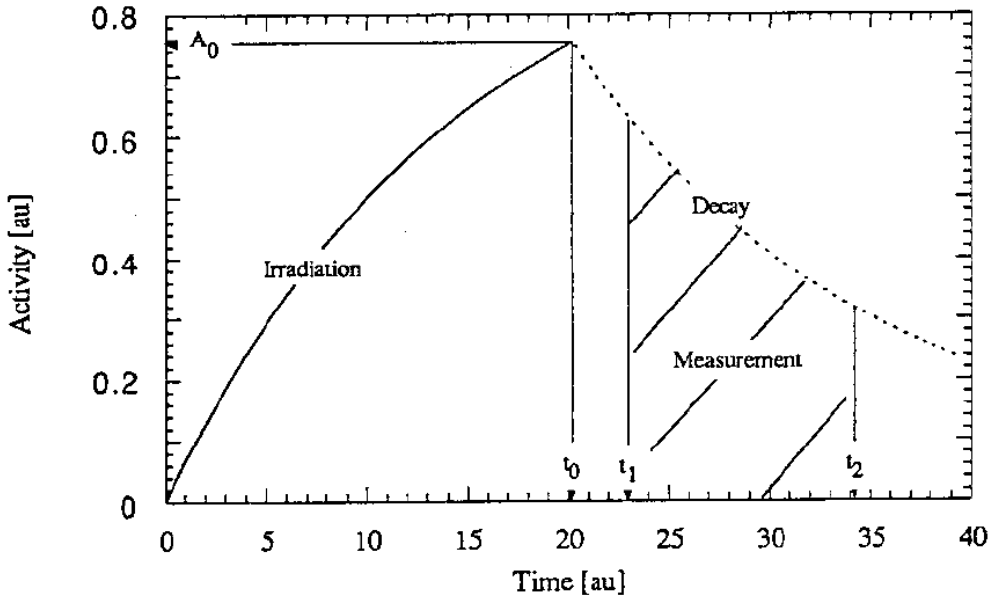

Fig. 3.4 Irradiation and the decay for a neutron activated sample. The activity after irradiation is A_0 at time t_0. The gamma-ray measurement starts from t_1 to t_2. [59]

In addition, total neutron yield can be obtained:

$$Y_n = S_n \cdot t_0 \tag{3.4}$$

Thus the activation response coefficients (the reaction rate R) per unit source neutron and unit target nuclei can be expressed as follows:

$$\sum_E \sigma(E) \cdot \Phi(E) = \frac{\lambda \cdot C}{N \cdot S_n \cdot \alpha_\gamma \cdot \varepsilon \cdot \left(e^{-\lambda t_1} - e^{-\lambda t_2}\right) \cdot \left(1 - e^{-\lambda t_0}\right)} \ [s^{-1}] \tag{3.5}$$

3.3.2. Activation foils

Table 3.1 shows several activation reactions for fast neutron measurement. The activated samples are made to be the thin foils to decrease the self-shielding effect for neutron from sample itself. The foil size is 10 mm in diameter and 1 mm in thickness as shown in Fig. 3.5(a). The indium foil is employed for the 2.45 MeV neutron measurements by utilizing ^{115}In(n, n')^{115m}In reaction. This reaction has a threshold of 336 keV which can exclude the influence of scattering neutrons below the threshold. A suitable half-life of 4.486 hours will be good for the cooling down ^{115}In(n, γ)^{116}In reaction, where half-life of ^{115}In(n, γ)^{116}In reaction is about 54 min. In addition to this, the ^{115}In(n, n')^{115m}In reaction has a rather large and flat (from 0.336 to 3 MeV) cross section as shown in Fig. 3.6(a), which will be suitable for fusion D-D neutron measurement. The mass for one-piece indium foil is 0.59±0.015 g. [56]

Table 3.1 The activation reactions for fast neutron measurement

Reaction	Isotopic abundance	Half-life	Gamma energy (MeV)	Gamma abundance	Threshold (MeV)
^{58}Ni(n,2n)^{57}Ni	67.9%	36h	1.37	86%	13
^{63}Cu(n,2n)^{62}Cu	69.1%	9.8 min	0.511	195%	11.9
^{65}Cu(n,2n)^{64}Cu	30.9%	12.7 h	0.511	37.8%	11.9
^{19}F(n,2n)^{18}F	100%	109.7 min	0.511	194%	11.6
^{127}I(n,2n)^{126}I	100%	13 d	0.667	33%	9.3
^{197}Au(n,2n)^{196}Au	100%	6.18 d	0.33, 0.35	25%, 94%	8.6
^{24}Mg(n,p)^{24}Na	78.7%	15 h	1.368	100%	6
^{59}Co(n,α)^{56}Mn	100%	2.56 h	0.84	99%	5.2
^{56}Fe(n,p)^{56}Mn	91.7%	2.56 h	0.84	99%	4.9
^{27}Al(n,α)^{24}Na	100%	15 h	1.368	100%	4.9
^{27}Al(n,p)^{27}Mg	100%	9.46 min	0.84,1.01	100%	3.8
^{28}Si(n,p)^{28}Al	92.2%	2.24 min	1.78	100%	3.9
^{64}Zn(n,p)^{64}Cu	48.8%	12.7 h	0.511	37.8%	2
^{58}Ni(n,p)^{58}Co	67.9%	71.6 d	0.81	99%	1.9
^{115}In(n,n')^{115m}In	95.7%	4.5 h	0.336	48%	0.336

The silicon foil and the aluminum foil are used with ^{28}Si(n, p)^{28}Al, ^{27}Al(n, p)^{27}Mg, and ^{27}Al(n, α)^{24}Na reactions to measure the secondary 14.1 MeV neutrons with same size

of indium foil as shown in Fig. 3.5(a). Because those reactions have large cross section with threshold energy about 4 MeV, 2.5 MeV, and 5.5 MeV as shown in Fig. 3.6(b) and (c), respectively. The mass for one-piece silicon foil and aluminum foil are 0.166±0.001 g and 0.21±0.001 g, respectively. The triton burnup ratio can be evaluated by the measurements of indium, silicon, and aluminum. [56]

The capsule for loading the foils is made by polythene in large outside diameter of 1.8 cm, inside diameter of 1.1 cm, outside length of 4 cm, inside length of 3 cm, and thickness of 1 mm which is also for decrease the neutron shielding effect from capsule itself. Each capsule can load 30-piece foils as shown in Fig. 3.4(b). [56]

(a)

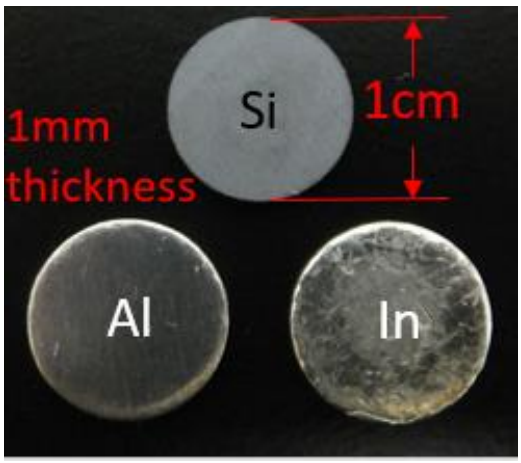

(b)

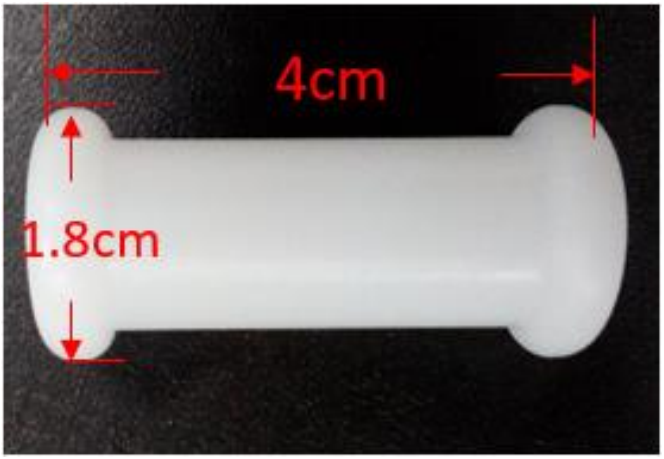

Fig. 3.5 Photographs of (a) the foils, and (b) the capsule.

(a)

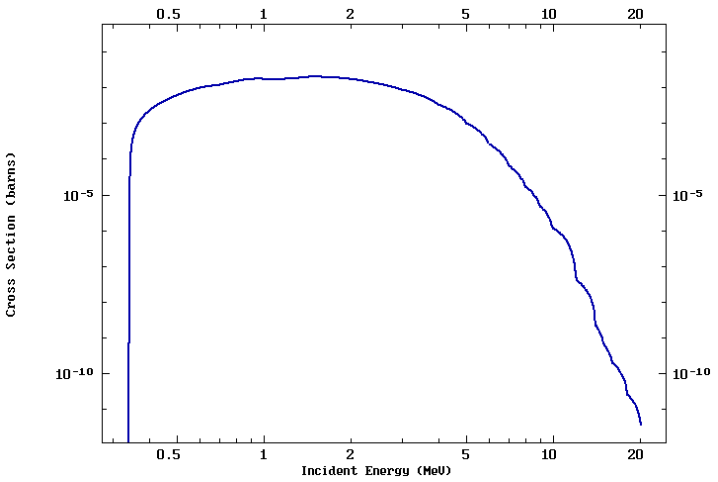

(b)

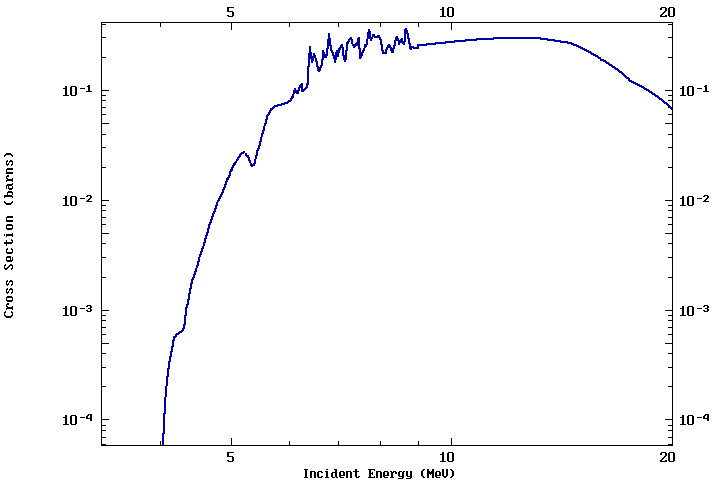

(c)

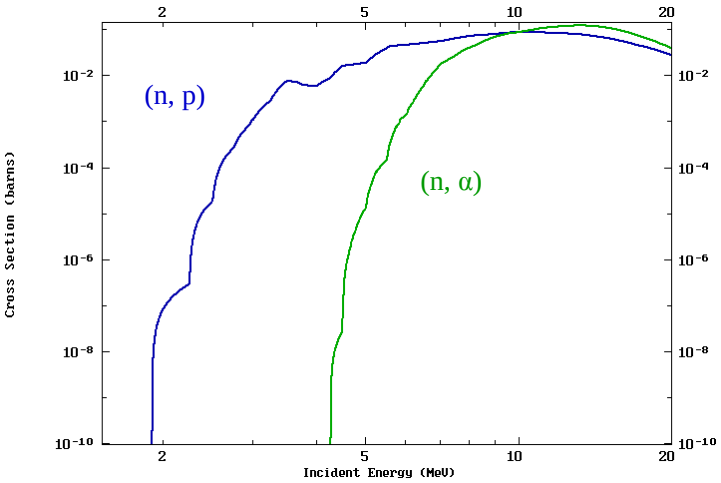

Fig. 3.6 The cross section for ^{115}In(n, n')^{115m}In reaction (a), ^{28}Si(n, p)^{28}Al reaction (b), ^{27}Al(n, p)^{27}Mg, and ^{27}Al(n, α)^{24}Na reactions (c). [60]

3.3.3. High-purity germanium detector

The HPGe detector is essentially required to identify nuclides of interest through gamma-ray spectroscopy with high energy resolution as shown in Fig. 3.7. The HPGe detector used in this work is manufactured by Canberra Industries, Inc. (Model: GX3018/CP5-PLUS-U). The detector has a very thin window made of carbon composites on the front surface, which reduces the gamma-ray shielding effect of the window and extends the useful energy range down to 3 keV. The effective diameter and thickness of the germanium crystal of the HPGe detectors are 61.80 mm and 39.80 mm, respectively. The distance from the window to the surface of the HPGe detectors is 5.00 mm. Because the detector is in a lead shield having the thickness of 100 mm, the background pulse counting rate due to external sources is low enough for our purpose. Output pulses from the preamplifier are fed into the multichannel analyzer, the DSA-LX produced by Canberra Industries, Inc., based on advanced digital signal processing techniques, and data are analyzed on a personal computer. [56]

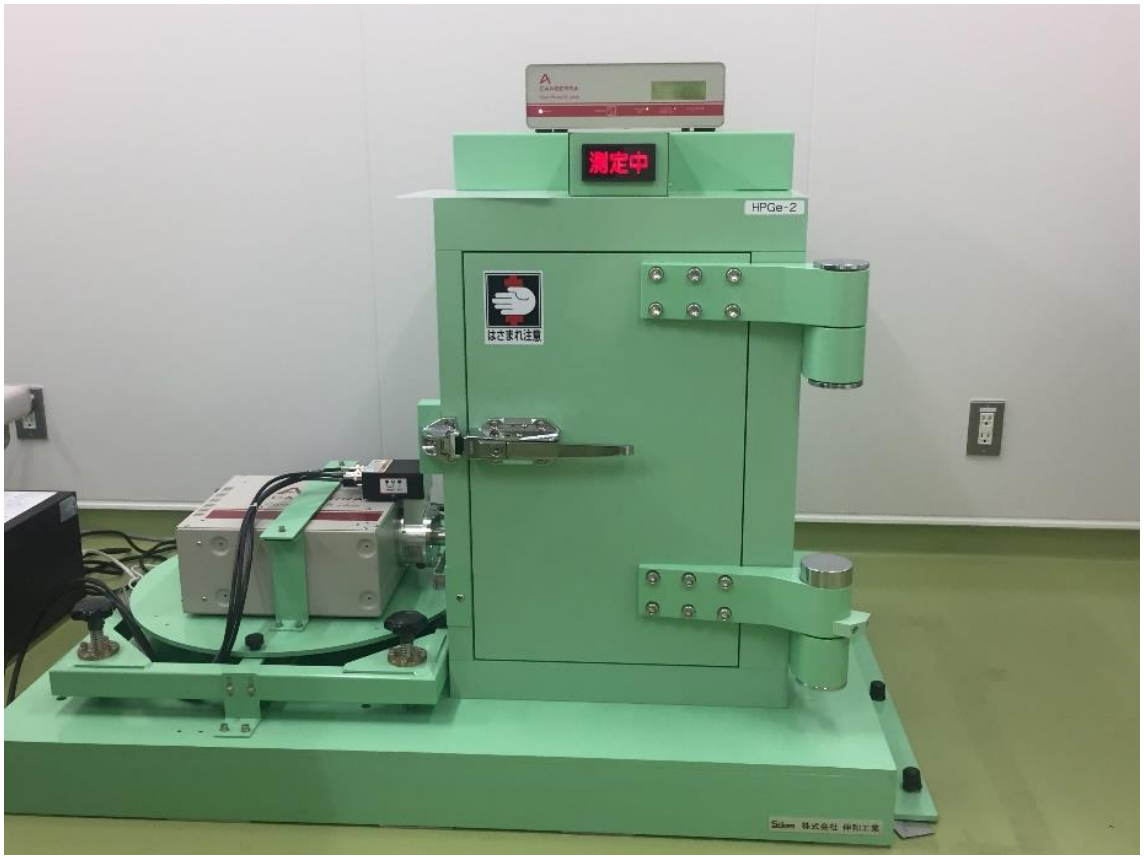

Fig. 3.7 HPGe detector for LHD experiment.

3.3.4. Pneumatic system

The pneumatic system consists of the control systems, pneumatic tubes, air compressor, launching/collecting station, and two irradiation ends as shown in Fig. 3.8. There are two irradiation ends: one is at the 8-O horizontal port, which is located at the outboard side of the horizontally elongated poloidal cross section of the plasma, and the other is located at the 2.5-L lower port, which is under the vertically elongated cross section of the plasma as shown in Fig. 3.9. Each irradiation end is made of stainless steel with a coaxial structure. Outside the port flange, the inner tube of the irradiation end is connected to a capsule transfer tube made of acrylonitrile-butadiene-styrene resin and the outer tube is connected to a vinyl chloride resin tube for compressed air supply and exhaust. The length of the pneumatic tubes in the 8-O port line and the 2.5-L port line is 93 m and 80 m, respectively. [56]

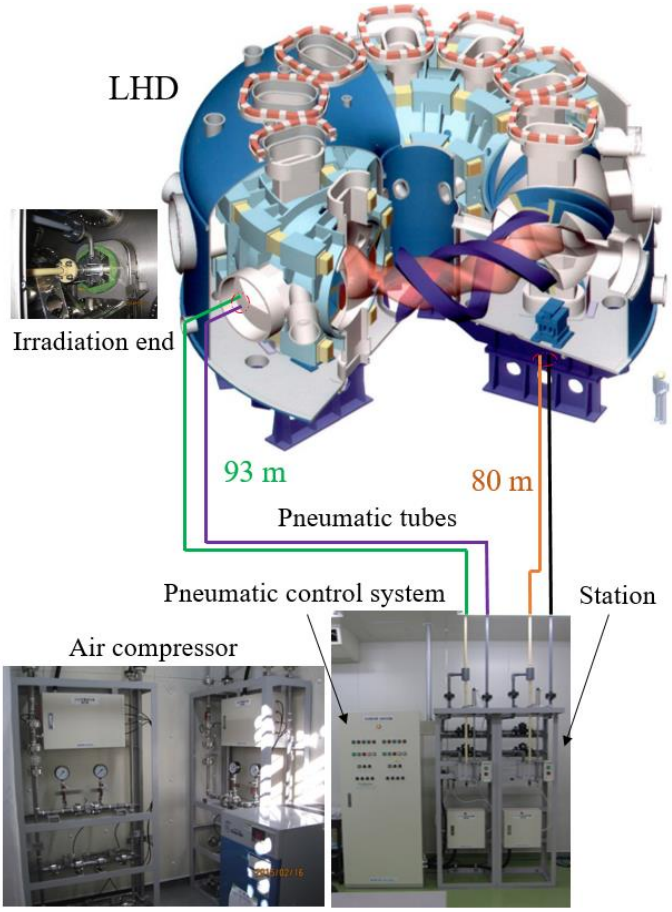

Fig. 3.8 The pneumatic system of neutron activation system on the LHD

During the LHD experiment, the capsule will be transferred to the irradiation end

before discharge initiation by receiving a trigger pulse before the discharge. After the discharge, the capsule will be transferred to the station for the measurement of gamma-ray spectroscopy within the specified time. In the automatic control mode, this specified time can be set in the pneumatic control system by hand according to the discharge duration. In the manual control mode, a capsule can be launched and transferred back at any time. The transfer time from the irradiation end to the station is about 20 s, which depends on the pressure of compressed air. Each tube has a manometer to monitor the air pressure. [56]

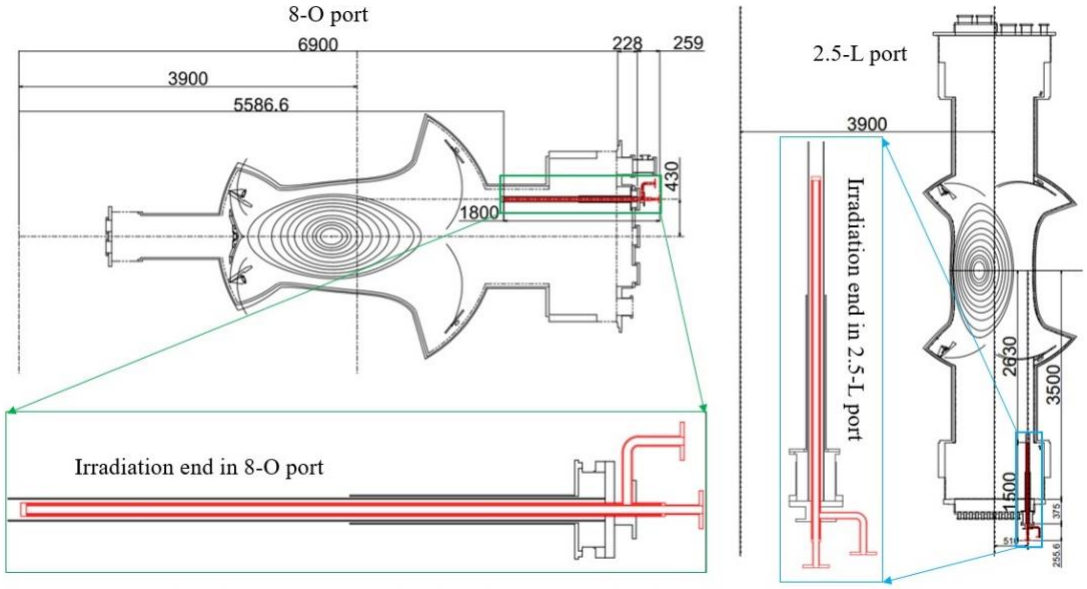

Fig. 3.9 Two irradiation ends of neutron activation system at two poloidal cross sections of 8-O and 2.5-L ports. [56]

3.4. Scintillating-fiber detector

For fast neutron measurement, the plastic scintillator has good temporal resolution, but higher gamma-ray sensitivity. Therefore, the scintillating-fiber (Sci-Fi) detector is developed with gamma-ray rejection based on the fast temporal response of plastic scintillator. The neutrons response and the rejection properties of gamma-ray and background for square fiber kind of Sci-Fi detector have been investigated by EGS4 code and TRACE code by Y. Yariv, *et al*. in 1990 [61], and a comparison of square fibers and cylindrical fibers in different diameter was carried out by the McSUB V2.0 code by S. Singkarat, *et al*. in 1997 [62]. Then, the responses of 2.6 MeV and 14 MeV were measured

in angular effect, and the gamma-ray responses were measured for ^{137}Cs and ^{60}Co gamma-rays source by S. Singkarat, *et al*. [63]. In addition, Sci-Fi like detectors have been used for a particles tracking detector in high-energy physics. [64]

(a)

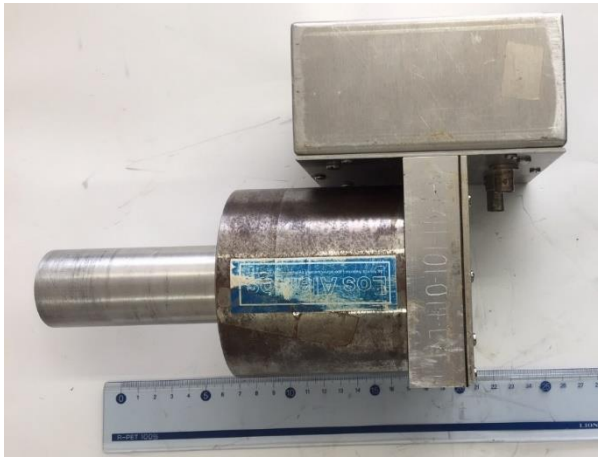

(b)

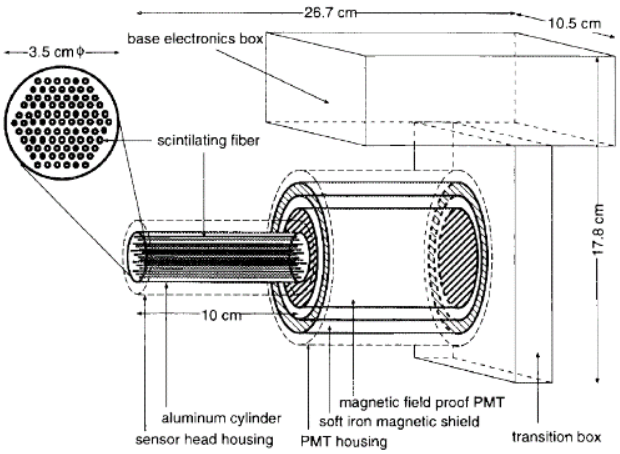

(c)

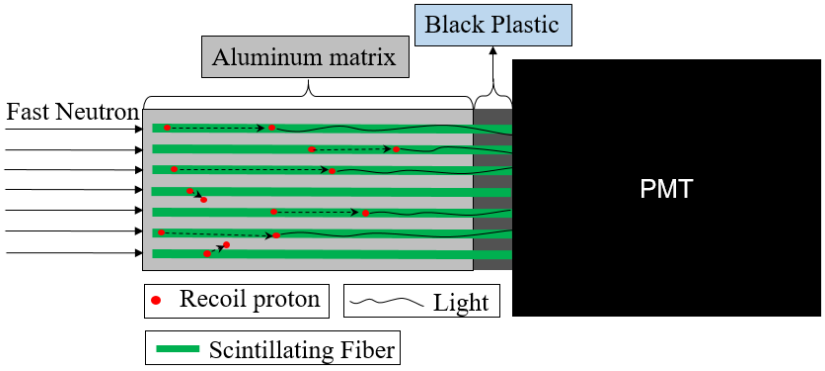

Fig. 3.10 (a) Photograph of LANL Sci-Fi detector, (b) Schematic view of the LANL Sci-

Fi detector, and (c) function of LANL Sci-Fi detector.

A Sci-Fi detector with over 10^7 counts per second (cps) counting ability was developed by 91 fibers of 1 mm in diameter and 10 cm in length embedded in an aluminum (Al) matrix in the Los Alamos National Laboratory (LANL) as shown in Fig. 3.10(a) and (b). [19], [65] A black plastic matrix was used to connect to a Hamamatsu R2490-5 magnetic field resistant photo-multiplier tube (PMT). The PMT of 50 mm in diameter with an active high-voltage (HV) divider network enables high-current output capability. Also, a soft iron housing is used for magnetic field shielding. The large area PMT is to reduce the influence from the non-uniform light collection at the PMT edge on the pulse height. A plastic matrix was used to make fibers to directly connect PMT and to maintain electrostatic standoff to the PMT windows glass. [66]

(a)

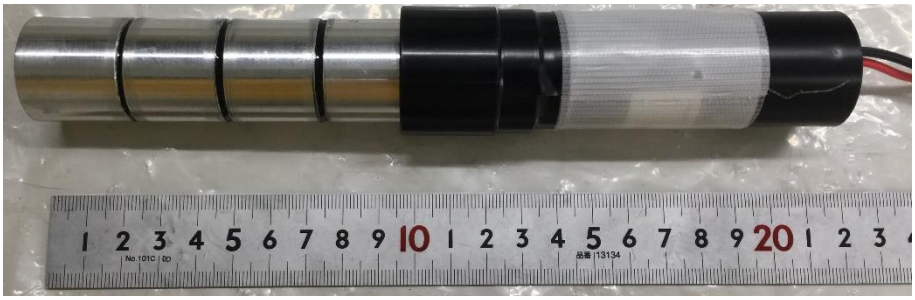

(b)

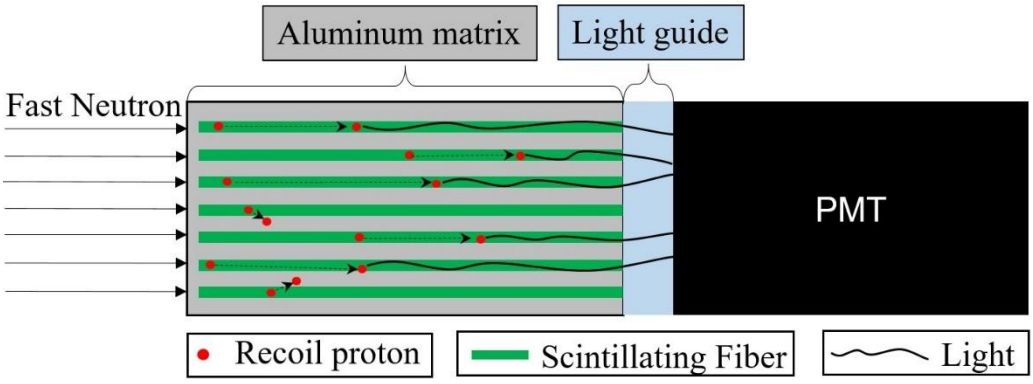

Fig. 3.11 (a) Overview of the NIFS Sci-Fi detector, and (b) Principle of the NIFS Sci-Fi detector. [66]

A newly designed Sci-Fi detector was developed in NIFS as shown in Fig. 3.11(a).

The NIFS Sci-Fi detector is a compact detector consisting of 109 fibers with a diameter of 1 mm and a length of 10 cm. The fibers were embedded into an aluminum matrix for stopping recoil protons and electrons induced by 2.45 MeV neutrons and gamma-rays passing into the adjacent fiber to reduce the contribution from low-energy neutrons and gamma-rays, as shown in Fig. 3.10(c) and Fig. 3.11(b). The acryl plastic plate of 10 mm thickness is a light guide for the fiber and is an insulation layer for an aluminum matrix and a PMT window. The light output of the plastic plate induced by 2.45 MeV neutrons and gamma-rays is negligible which is confirmed by experiment using a 14 MeV neutron generator. A magnetic resistant PMT assembly H6152-70 with a maximum divider current of 0.41 mA is used for signal output. H6152-70 consists of a magnetic resistant PMT R5505-70 and RC divider base. The gain of PMT R5505-70 is constant (5×10^5) at magnetic field of 0-0.25 T in the HV of 2000 V. [66]

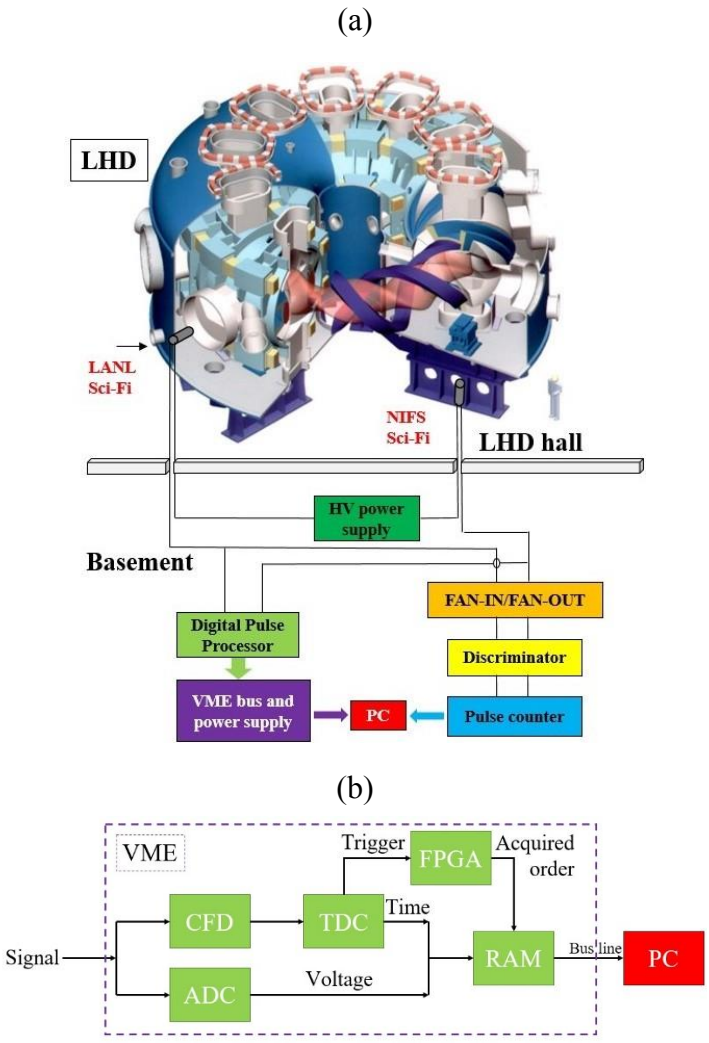

Fig. 3.12 (a) Experimental setup of Sci-Fi detectors and the block diagram of electronics

and the data acquisition system and (b) the logic diagram of the DPP. [66]

In the LHD experiment, a soft iron collar with 5 mm thickness is around the PMT and a perm-alloy collar is placed inside the PMT assembly of the NIFS Sci-Fi detector to improve magnetic resistance. The total length of the detector is less than 22 cm. This compact Sci-Fi detector will be helpful for the development of a 14 MeV neutron camera. [66]

The setup of detectors is shown in Fig. 3.12(a). The LANL Sci-Fi detector is located on the outside of the 8-O port, and the NIFS Sci-Fi detector is located on the outside of the 2.5-L port. The distance from the two detectors to the plasma center is around 4 m. The block diagram of electronics and Digital Pulse Processor (DPP) is also shown in Fig. 3.12(b). In the LHD experiment, the ORTEC 556 was used as a high voltage direct current power supply for Sci-Fi detectors. The anode signals of PMT are divided into two channels, which are directly fed into the DPP and the nuclear instrument module (NIM) in the basement by coaxial cables of 10 m and 20 m with an input impedance of 50 Ω or each detector, as shown in Fig. 3.12(a). The NIM module is employed for online measurement with a fixed threshold, which consists of a FAN-IN/FAN-OUT module, a discriminator of 300 MHz bandwidth, and a pulse counter. [66]

The DPP (model no. APV8102-14MWPSAGb) with 1 Mcps data throughput consists of two channel digitizers which include two analog/time-to-digital converters (ADC/TDC) of 1 GHz sampling with 14-bit resolution and two constant fraction discriminators (CFD), a flash memory RAM of 1 GB (512 MB for each channel) for data storage, and the field-programmable gate array (FPGA) module for signal processing. The raw data (the shaping information of each pulse) have been used for offline analysis. The pulse height spectrum and time evolution of integral counts can be obtained. Full pulse shape information for each pulse is recorded by the DPP, as shown in Fig. 3.12(b). A low level threshold was set in the digitizer to discriminate lower pulse height signals and noise. A pulse higher than this low threshold comes into the digitizer, and FPGA receives a trigger to start to record this pulse in 64 sampling points with 1 ns time bin, where 10 sampling points are before the trigger and 54 sampling points are after the trigger. Also the time stump of the trigger time is recorded. Here, the pulse width of the anode signal from the Sci-Fi detectors is 10–20 ns. The maximum voltage value of the pulse is picked up for pulse amplitude analysis, and pulse counts integrated in 1 ms where the pulse height is larger than the specific threshold can be picked for the time-resolved measurement. [66]

Chapter 4:

Calibration for neutron diagnostics on LHD[2]

The absolute neutron yield is one of the most important parameter for the deuterium or deuterium-tritium plasma experiment in fusion study, which provides information on the plasma performance such as the total fusion power and the energetic ion behaviors. Also it is important for the radiation control, the evaluation of activation and damage for the fusion machine, and the peripheral equipment. Therefore, it is necessary to obtain the neutron yield more accurately.

In the neutron measurement, the detector can only give a limited response count based on its own response function. In order to give accurate neutron yield, it is necessary to calibrate the neutron detector. In addition, due to the complicated structures of fusion devices such as first wall, magnetic coils, and vacuum vessel between the volumetric plasma and the neutron detector, the neutron scattering effect is different in different devices. Therefore, it is necessary to calibrate neutron in situ for different devices. However, in reality, there is no volumetric source as plasma. The absolute calibration between the neutron detector output and the total neutron emission rate in the whole plasma is the most important issue. Therefore, the in situ calibration is rather difficult work. Much effort and time are devoted to the in situ calibration at many tokamak using a ^{252}Cf neutron source or a compact neutron generator [67]-[79]. [54]

The machine structure of the LHD is extremely complicated in comparison with tokamaks, and the efficiencies of NFM and the activation response coefficients of the

[2] This chapter is written by:
T. Nishitani, *et al*., "*Calibration experiment and the neutronics analyses on the LHD neutron flux monitors for the deuterium plasma experiment*", Fusion Eng. Des., **136** 210 (2018).
N. Pu, *et al*, "*In situ calibration of neutron activation system on the large helical device*", Rev. Sci. Instrum., **88** 113302 (2017).

NAS should be obtained from the experiment in addition to the simulation. The LHD has enough space to install a railway, support structures, and a train loaded with the neutron source running along the magnetic axis position inside the vacuum vessel to simulate a ring-shaped neutron source. In November 2016, the *in situ* absolute calibration of the NFM and NAS was carried out in the LHD by using an approximately 800 MBq ^{252}Cf neutron source. [56]

4.1. Calibration tools

To simulate the toroidal plasma neutron source, the ring-shaped source must be created. Fig. 4.1 shows the source transport system by using a toy train rail with 36 mm rail width, which so-called O-gauge rail as shown in Fig. 4.2(a). Basically the train loading the ^{252}Cf neutron source as shown in Fig. 4.2(b) rotated on the rail track continuously. The train-passing sensor is located on one position near the rail track in order to monitor the rotation speed of the train, which is typically 40 s/turn. The train is loaded with a neutron source to circulate on the magnetic axis position at the major radius of 3.744 m inside the LHD vacuum chamber for generating a ring-shaped neutron source. The rail is fixed on the Bakelite plate which is installed on the maintenance stage made of aluminum frames as shown in Fig. 4.2(b). [56]

An approximately 800 MBq ^{252}Cf neutron source by spontaneous fission was chosen for the *in situ* calibration because the mean neutron energy of neutrons emitted from ^{252}Cf is approximately 2.1 MeV, which is close to that of neutrons produced by D–D reaction. The ^{252}Cf neutron source releases 3.7 neutrons on average per spontaneous fission event, which is almost 3.1% of the decay. The half-life is approximately 2.646 years. The precise birth neutron emission rate was $(1.34\pm0.014)\times10^{8}$ n/s at 12:00 GMT on April 27, 2015, which was calibrated at National Physics Laboratory, United Kingdom. Therefore, the birth neutron emission rate was calculated to be $(8.95\text{-}8.91)\times10^{7}$ n/s day by day during the in situ calibration period. [56]

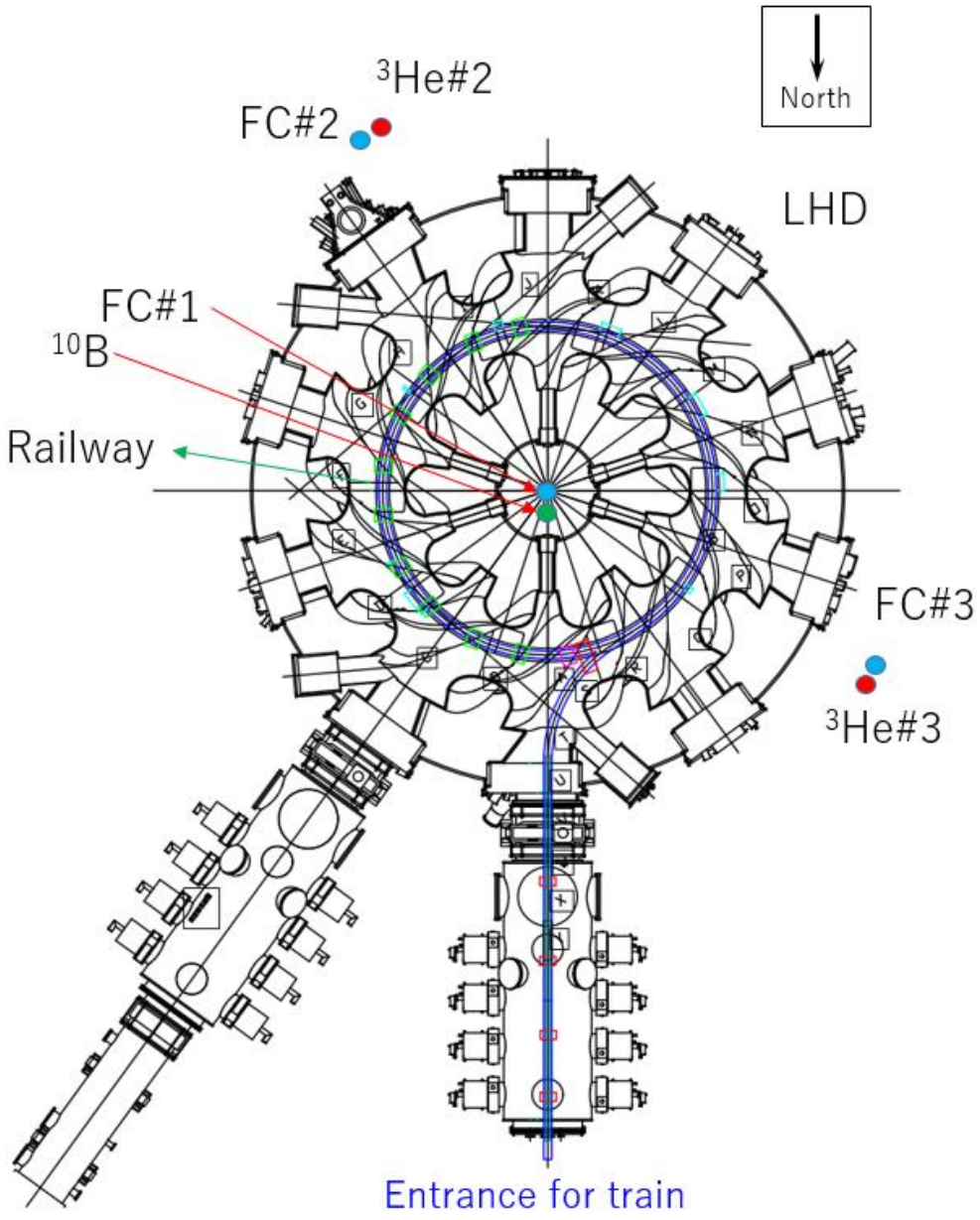

Fig. 4.1 Neutron source transfer system for the *in situ* calibration experiment on LHD. Horizontal layout diagram of *in situ* calibration experiment by using ^{252}Cf neutron source.

(a)

(b)

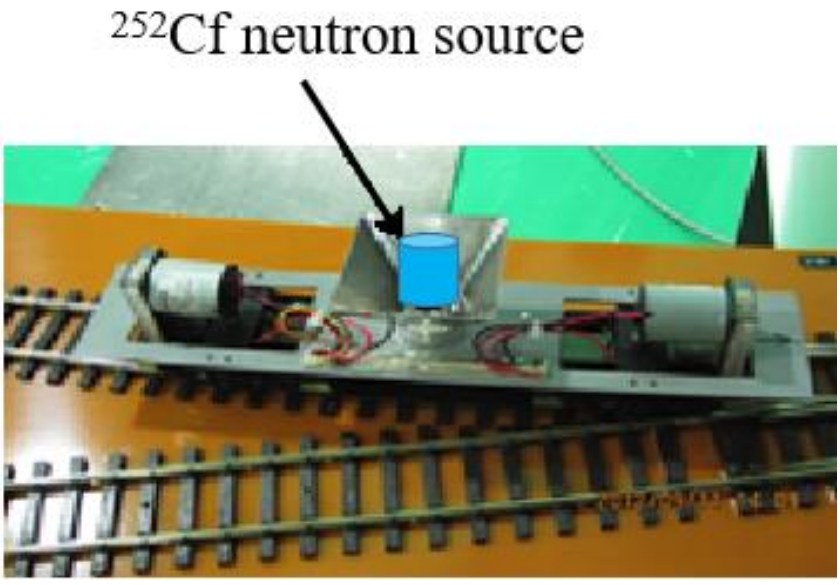

4.2 (a) the photograph of the railway inside the LHD vacuum vessel, and (b) the photograph of the specially designed toy train.

4.2. *In situ* calibration of neutron flux monitor on LHD

4.2.1. Experimental results

The counts of each detector during the continuous rotation of the neutron source are typical 5 hours or more, where total counts were obtained to be of 10000 or more for ^{235}U fission chamber (FC). The absolute detection efficiency for the ^{252}Cf ring source of NFM detectors in the detector positions is defined as:

$$\varepsilon_{^{252}Cf} = \frac{cps}{S_{n(^{252}Cf)}} \tag{4.1}$$

where cps is the detector counts per second and $S_{n(^{252}Cf)}$ is the average neutron emission rate during the measurement period. The time history of counts for each detector was stored with a time bin of 1 ms. The position of the neutron source was derived from the time after the time when the train passed at the train passing monitor assuming the rotation speed was constant during one turn. Fig. 4.3 shows counts accumulated during the continuous rotation as a function of the source toroidal position. It is clearly seen that the detector at the top of the center axis is almost insensitive to the source toroidal position. The detection efficiency of each detector for the point ^{252}Cf neutron source (so-called point efficiency) on the rail track can be derived from the count time history of each detector divided by the total neutron number emitted at each toroidal point. [54]

In addition to this, the tendency for each position detectors are almost the same as shown in Fig. 4.3(a) and (b). It is clear that ^{3}He detectors can be a reference for FC#2 and FC#3 in this in situ calibration experiment. Because the position for FC#2 (FC#3) and ^{3}He#2 (^{3}He#3) are almost the same, but the efficiency of FC is smaller than ^{3}He detectors, which leads to that counts error of FC is larger. The difference between ^{10}B detector and FC#1 may come from the position of ^{10}B detector. Because the position of ^{10}B detector is not strictly at the center of the device, which lead to the counts of ^{10}B detector have small angle effect comparing with FC#1 as shown in Fig. 4.3(a) and (b).

(a)

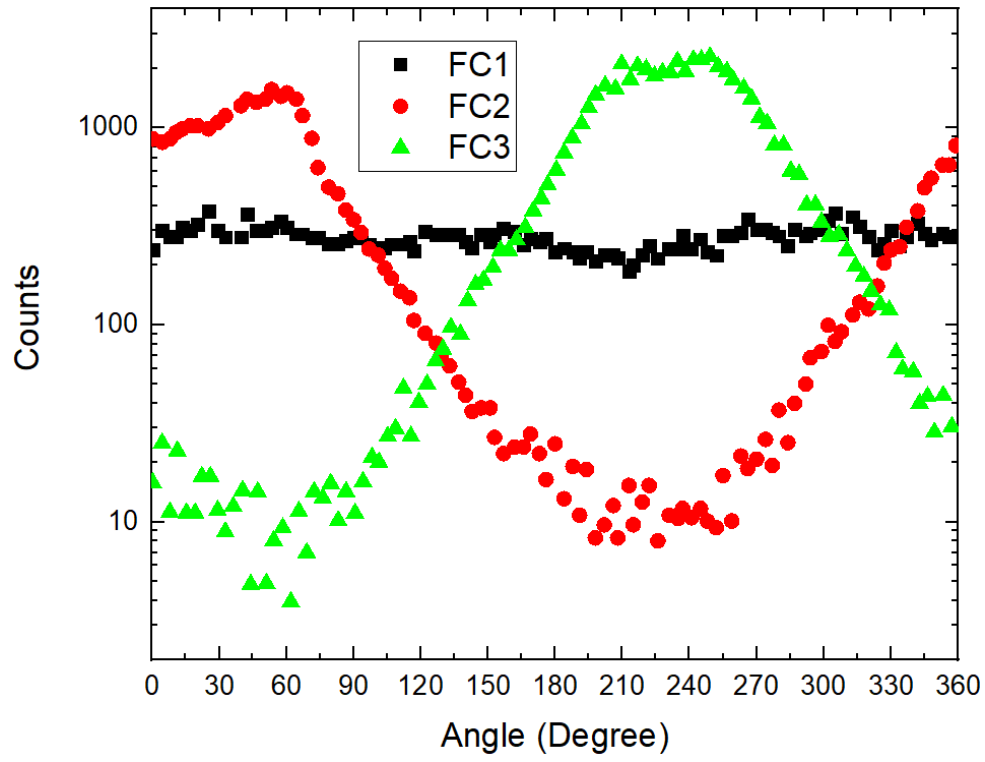

(b)

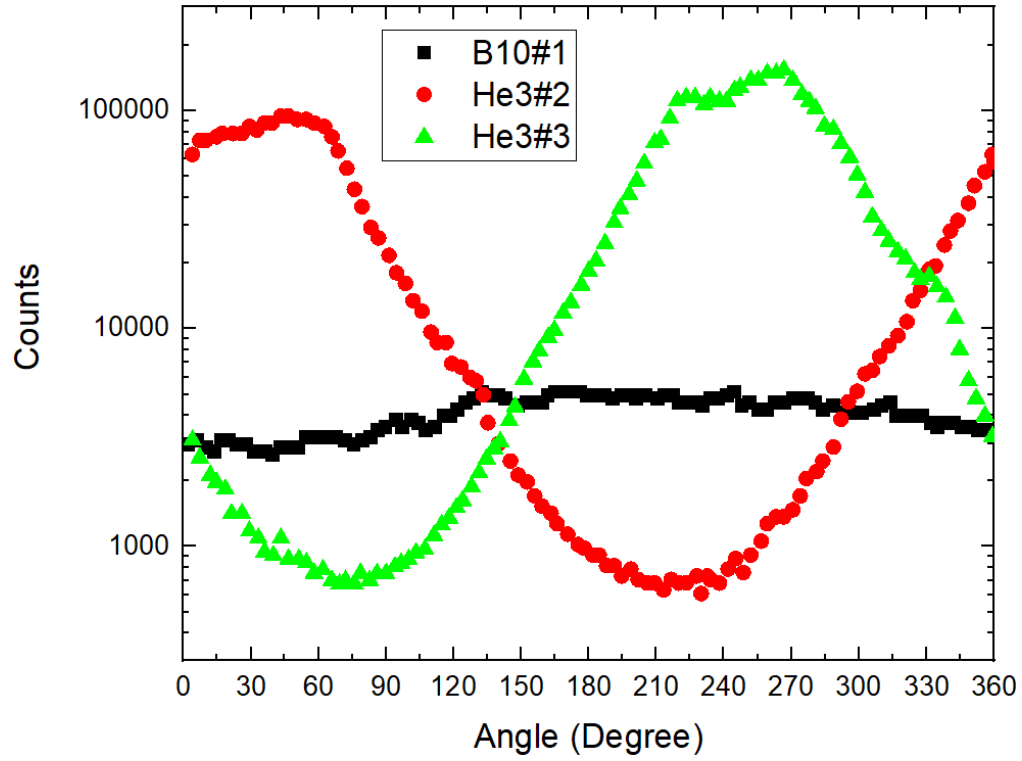

Fig. 4.3 Counts of fission chambers(a), ^{10}B, and ^{3}He detectors (b) as a function of the neutron source toroidal position.

4.2.2. Neutron transport analyses

In the D-D plasma, the neutron source is volumetric with source profile in the poloidal cross-section. The source neutron energy is almost mono-energy of 2.45 MeV. Thus, detection efficiencies of the ^{235}U fission chambers have been corrected for the condition deference effects between the in situ calibration and the real plasma by using the Monte Carlo N-Particle transport code MCNP-6 [80] and the cross-section library of FENDL-3.0 [81]. [54]

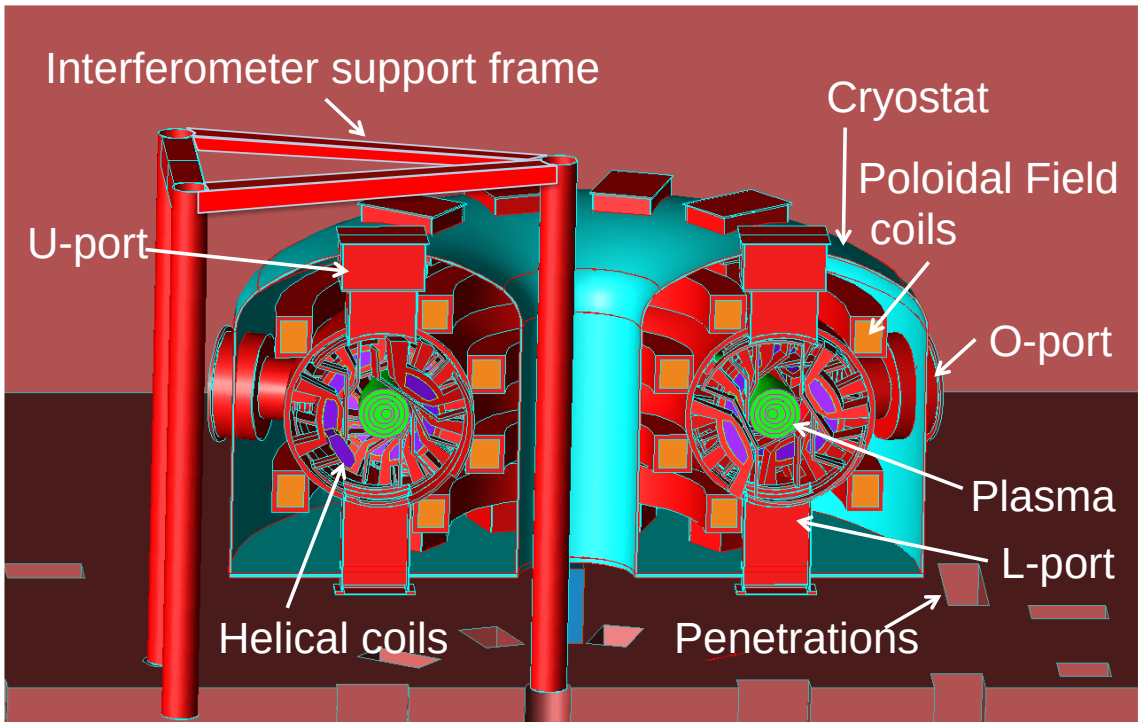

Fig. 4.4 Schematic view of the MCNP calculation model for LHD and the experimental building. [55]

In order to take account of neutrons scattered by the torus hall walls, not only LHD but also the LHD experimental building is modeled in the MCNP calculations. Fig. 4.4 shows the schematic view of the MCNP calculation model, which is drawn with SuperMC code [82]. The torus hall was modeled as a rectangular concrete box of 47×77×41.6 m. In the torus hall, LHD and the interferometer support are also modeled. This is because the interferometer support is very close to the FC#1. MCNP can not treat helical surfaces, thus the helical coils and the case structures are divided by 6° toroidal angle pitch, and those components are assumed to be toroidally symmetric in a toroidal pitch angle [83]. [54]

(a) (b)

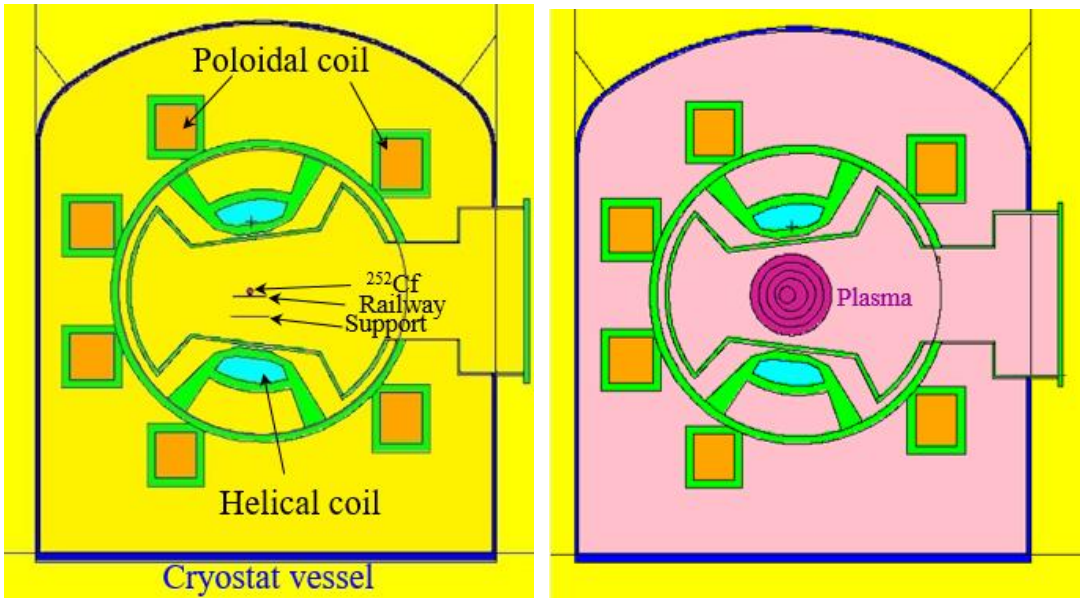

Fig. 4.5 Poloidal cross-sections of the MCNP calculation model for LHD in the cases of (a) in situ calibration and (b) the real plasma. [56]

(a) (b)

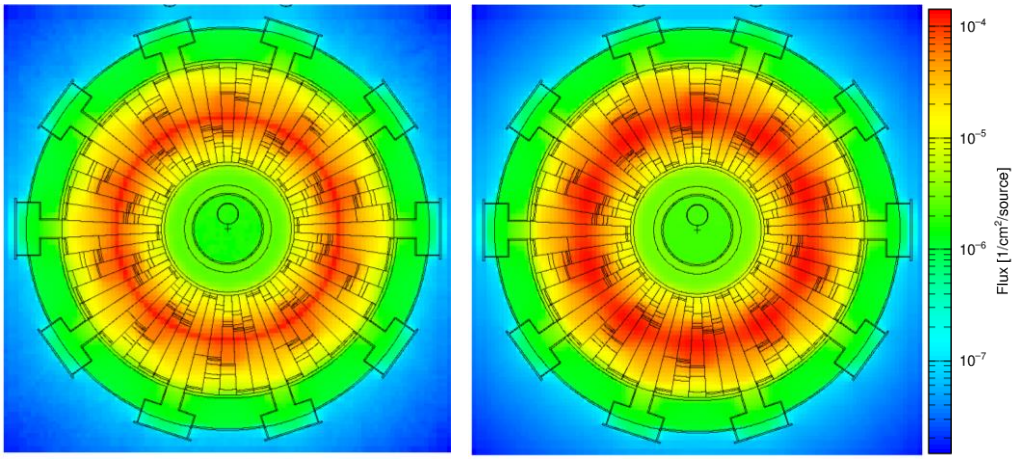

Fig. 4.6 The neutron flux distribution for ^{252}Cf ring source (a) and plasma toroidal source (b).

Fig. 4.5(a) and (b) show the poloidal cross-section of the LHD in the MCNP model for the *in situ* calibration case and the real plasma case, respectively. The rail track and

the support structure are simply modeled. Liquid helium is not included in the model for the in situ calibration, but the model of inside LHD for the real plasma. Also, the air is filled in the model of inside LHD for the *in situ* calibration, but is in the model for the real plasma is vacuum. The LHD plasma is modeled by a simple circular torus with the major radius of 3.8 m and the minor radius of 0.5 m. The plasma is divided into five regions in minor radius whose neutron emission rates are determined to be a neutron source profile expected by a plasma simulation. The source neutron energy is assumed to be 2.45 MeV. [54] The neutron flux distribution on x-y plane for ^{252}Cf ring source and plasma toroidal source were calculated as shown in Fig. 4.6, which show the different intensity in source shape distribution. The ^{252}Cf ring source is a clear ring shape distribution, and plasma toroidal source has a clear neutron emission profile, which will lead to the difference in calibration experiment and plasma experiment from those two shape source.

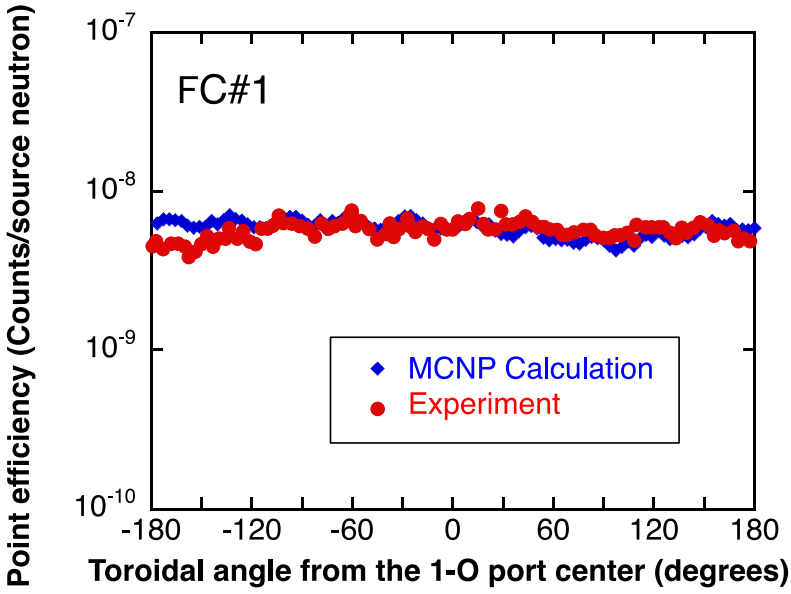

Fig. 4.7 Comparison of the point efficiencies between the experiment and the MCNP calculation for FC#1. [54]

At first, the point efficiency is calculated in order to confirm the modeling validity as shown in Fig. 4.7 and Fig. 4.8. Here 0° of toroidal angle is normalized by the center of each detector. [54] Because the FC#1 is in the center of LHD. Angle effect of toroidal source on the FC#1 is confirmed to be negligible by the *in situ* calibration and MCNP calculation as shown in Fig. 4.7. This means that neutron emission for FC#1 is seen as

isotropy.

(a)

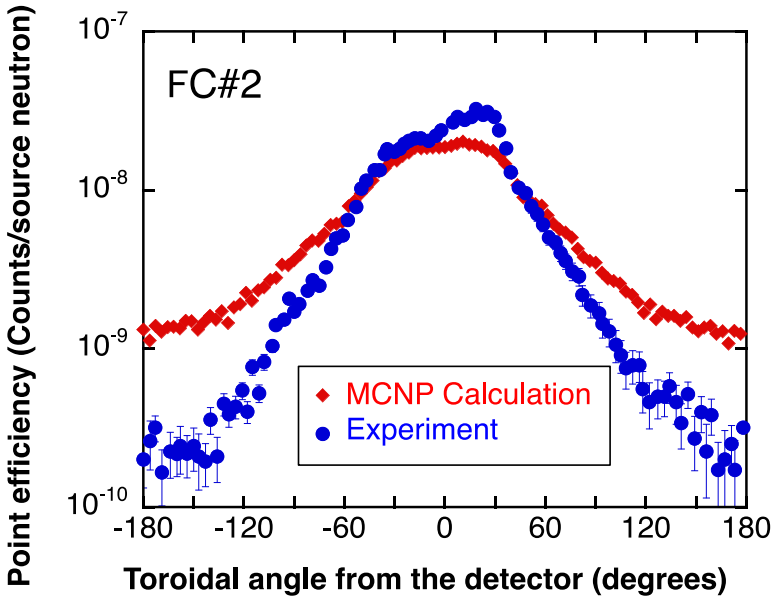

(b)

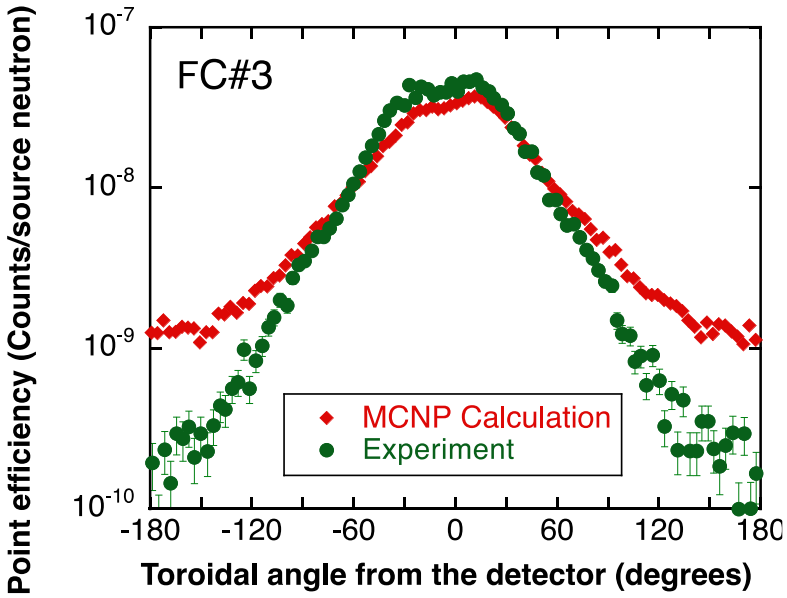

Fig. 4.8 Comparison of the point efficiencies between the experiment and the MCNP calculation for (a) FC#2, and (b) FC#3. [54]

In the cases of FC#2 and FC#3 as shown in Fig. 4.8(a) and (b), the MCNP calculation

overestimates the point efficiencies for the source positions on the opposite side of the detector, which is considered to be due to the modeling inaccuracy. The point efficiency of FC#2 has large asymmetry around 0°, which is probably due to the effect of large sub-port structure at the 10-O port. The statistical error of the MCNP calculation is ±3% or less, which is smaller than the symbol size in Fig. 4.7 and Fig. 4.8. The detection efficiency for the plasma (ε_{plasma}) is evaluated from the measured one for the ring ^{252}Cf neutron source ($\varepsilon_{^{252}Cf}$) listed in Table 4.1 as:

$$\varepsilon_{plasma} = \varepsilon_{^{252}Cf(exp.)} \frac{\varepsilon_{plasma(MCNP)}}{\varepsilon_{^{252}Cf(MCNP)}} \tag{4.2}$$

where $\varepsilon_{plasma(MCNP)}$ and $\varepsilon_{^{252}Cf(MCNP)}$ are calculated efficiencies for the plasma and the ring ^{252}Cf neutron source, respectively. Fig. 4.9 shows the calculated neutron spectra at the position of FC#3 for the plasma and the ring ^{252}Cf neutron source. Those neutron spectra are almost identical in the energy range lower that 1 MeV, which suggests that the difference between $\varepsilon_{plasma(MCNP)}$ and $\varepsilon_{^{252}Cf(MCNP)}$ is sufficiently small. [54]

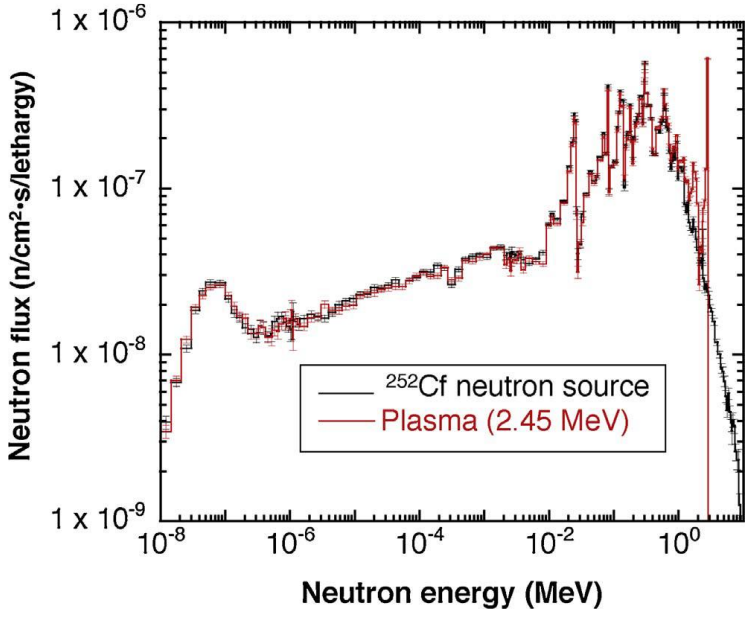

Fig. 4.9 Calculated neutron spectra at the position of FC#3 for the ring-shaped ^{252}Cf neutron source and the plasma with unit intensity. [54]

The measured $\varepsilon_{^{252}Cf(exp.)}$, calculated $\varepsilon_{^{252}Cf(MCNP)}$, $\frac{\varepsilon_{plasma(MCNP)}}{\varepsilon_{^{252}Cf(MCNP)}}$, final ε_{plasma} for LHD D-D experiment are listed in Table 4.1, where the uncertainties of the MCNP calculation results are statistical errors. It is clearly found that MCNP calculations agree well with the measured detection efficiencies for the ring ^{252}Cf neutron source. Also, the ratio of $\frac{\varepsilon_{plasma(MCNP)}}{\varepsilon_{^{252}Cf(MCNP)}}$ is close to unity. The error of ε_{plasma} in Table 4.1 is evaluated from the statistical error of the in situ calibration and the MCNP calculations. [54]

Table 4.1 Measured and calculated efficiencies of the fission chambers with a factor of 1×10^{-9} for the ^{252}Cf ring source, and evaluated detection efficiencies for the plasma. [54]

Detector	$\varepsilon_{^{252}Cf(exp.)}$	$\varepsilon_{^{252}Cf(MCNP)}$	$\varepsilon_{plasma(MCNP)}$	$\frac{\varepsilon_{plasma(MCNP)}}{\varepsilon_{^{252}Cf(MCNP)}}$	ε_{plasma}
FC#1	5.6±0.03	6.17±0.09	6.14±0.10	0.995±0.02	5.57±0.11
FC#2	6.83±0.04	7.03±0.03	7.42±0.03	1.06±0.005	7.24±0.06
FC#3	11.4±0.05	10.7±0.03	11.1±0.03	1.04±0.006	11.9±0.09

The uncertainty of $\frac{\varepsilon_{plasma(MCNP)}}{\varepsilon_{^{252}Cf(MCNP)}}$ is evaluated to be ±6% including statistical error by MCNP calculations. The uncertainties of the neutron source profile and the plasma position are both ±2% [83]. LHD has intensive tangential neutral beam (NB) injectors. The uncertainty of ^{252}Cf neutron source is 1%. The of neutron source profile is estimated to be 2%. Finally, total uncertainty in the pulse counting mode of NFM is evaluated to be ±7%. In the NB-heated plasma, all the NFM detectors in the pulse counting mode are saturated due to high neutron flux. Therefore, the neutron emission rate is measured with the FC in the Campbell mode, where the cross calibration between the pulse counting mode and the Campbell mode is necessary. The uncertainty of the cross calibration is evaluated to be ±5% [73]. The fluctuation of the Campbell mode depends on the time constant of the Campbell circuit. In the LHD, the time constant of 0.5 ms is employed, which results in the fluctuation level of ±2%. Taking account of those factors, total uncertainty of the neutron emission rate measurement with the fission chambers in the Campbell mode is evaluated to be ±9%. [54]

4.3. *In situ* calibration of neutron activation system on LHD

In tokamaks such as TFTR [12], JET [84], ASDEX-U [14], and JT-60U [15], neutron activation techniques have been applied to measure the neutron yield from deuterium plasmas. The activation response coefficients of NASs were evaluated from the MCNP calculation in those devices. Limited points of *in situ* calibration experiments for NASs were performed in TFTR [85], JET [86], and FTU [87] by using neutron sources, but not by toroidal shape sources. The machine structure of the LHD is extremely complicated in comparison with tokamaks, and the activation response coefficients of the NAS should be obtained from the experiment in addition to the simulation. The LHD has enough space to install a railway, support structures, and a train loaded with the neutron source running along the magnetic axis position inside the vacuum vessel to simulate a ring-shaped neutron source. In November 2016, the *in situ* absolute calibration of the NFM and NAS was carried out in the LHD by using an approximately 800 MBq ^{252}Cf neutron source. This *in situ* calibration of the NAS was performed for the first time in the world on a fusion device. [56]

4.3.1. Efficiencies of the HPGe detector

Before the *in situ* calibration, the detection efficiencies of the HPGe detector were calibrated by using the standard gamma-ray sources placed on the surface of the HPGe detector. The standard sources are the volumetric gamma-ray sources made by mixed powder gamma-ray sources of different types of nuclides in the U-8 container. In the *in situ* calibration experiment, thirty pieces of activated foils ware placed on the surface of the HPGe detector as shown in Fig. 4.10. The geometry of the standard gamma-ray sources and the activated foil source are significantly different. Therefore, it is necessary to evaluate the detection efficiencies of the HPGe detector for foil sources. [56]

The efficiencies of the HPGe detector for 336 keV (^{115m}In), 843 keV (^{27}Mg), 1368 keV (^{24}Na), and 1779 keV (^{28}Al) gamma rays of the activated foils were evaluated with the assistance of the simulation calculation using the Particle and Heavy Ion Transport code System (PHITS) [88] as shown in Fig. 4.11. The thirty pieces of foil stack was uniformly distributed on the surface of the HPGe detector in the model of the PHITS code as shown in Fig. 4.12. The different distributions of gamma-ray flux for thirty pieces of foil stacks and one-piece foil around the HPGe detector is shown in Fig. 4.13(a) and (b), which indicate that the detection efficiencies for both two case will be different. In addition to this, the detection efficiencies of the thirty pieces of indium foil, silicon foil,

and aluminum foil were calculated to be without the self-absorbed effect, which is the absorption of gamma rays by the foil material itself, where the foil density is assumed to be the same as the air density. Then, the detection efficiencies of thirty pieces of indium foil, silicon foil, and aluminum foil were calculated to be with the self-absorbed effect by using the actual density of the foil, where self-absorbed effect on the detection efficiency is clearly observed in Fig. 4.11. [56]

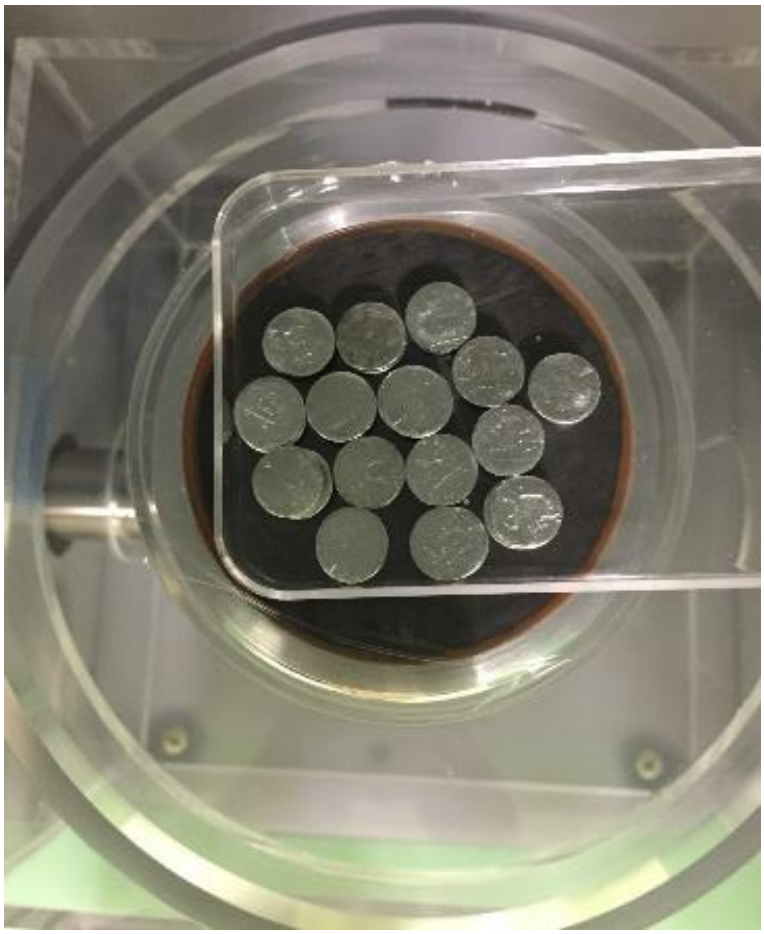

Fig. 4.10 The thirty pieces of foil stack in 15 group of two pieces on the on the surface of the HPGe detector.

In the case with the self-absorbed effect, the self-absorbed effect of thirty pieces of indium foils for 336 keV is larger than the self-absorbed effect of thirty pieces of silicon foils and aluminum foils for high-energy gamma rays. Thus, the detection efficiency with the self-absorbed effect is used for measurement. Moreover, the efficiencies of one piece of indium foil, silicon foil, and aluminum foil on the center of the surface of the HPGe detector with self-absorbed effect also was evaluated by the PHITS code for plasma

experiments. In the one-piece case model, the actual sizes of the HPGe detector and foil were also considered. Note that, the detection efficiencies of indium foil and silicon foil in different case were calculated by photo-electrical peak as shown Fig. 4.14(a) and (b), respectively, which indicate the different self-absorbed effect for both two foil in different case. [56]

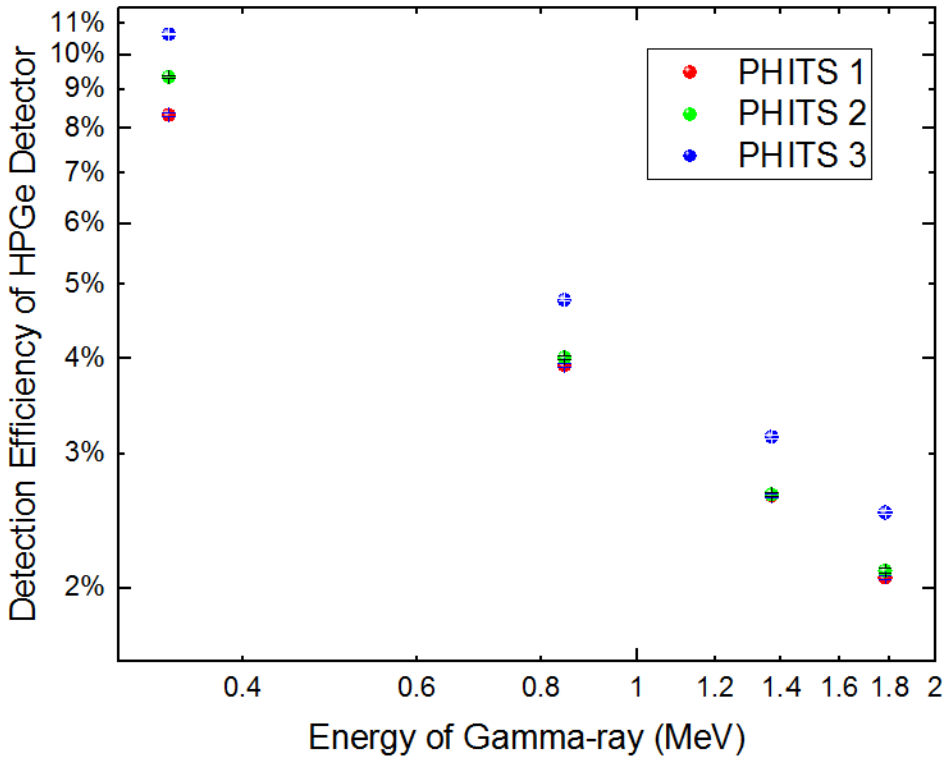

Fig. 4.11 Detection efficiencies of the HPGe detector. Red, blue, and green dots stand for the efficiencies of the HPGe detector for 336 keV (^{115m}In), 843 keV (^{27}Mg), 1368 keV (^{24}Na), and 1779 keV (^{28}Al) gamma-rays of the activated foils calculated by the PHITS code. “PHITS 1” represents calculation results of the case of thirty pieces of foil with self-absorbed effect. “PHITS 2” stands for the calculation results of the case of thirty pieces of foil without self-absorbed effect. “PHITS 3” is the calculation results for the case of one piece of foil with self-absorbed effect. [56]

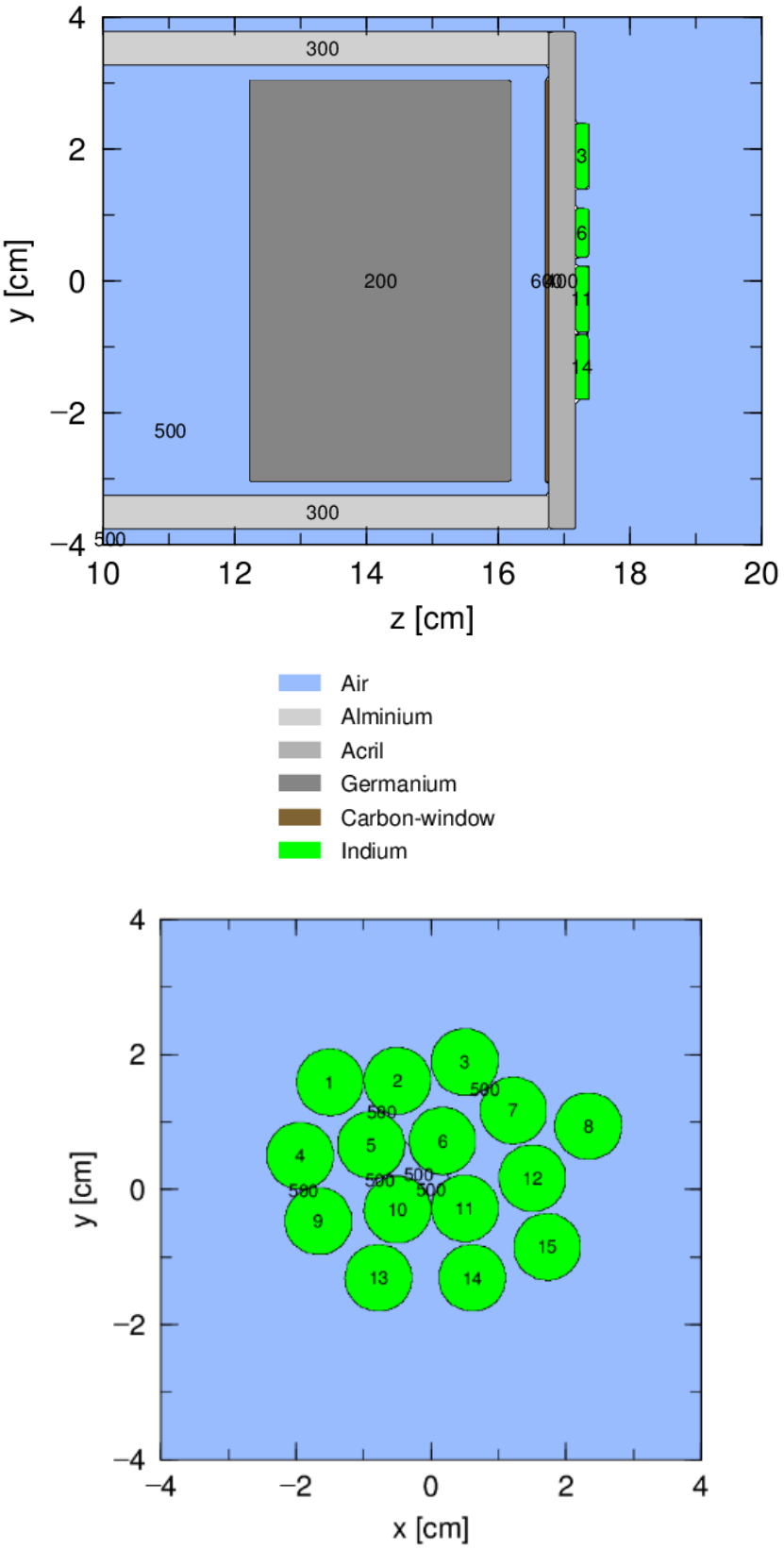

Fig. 4.12 The model of thirty-pieces foil stack on the surface of the HPGe detector.

(a)

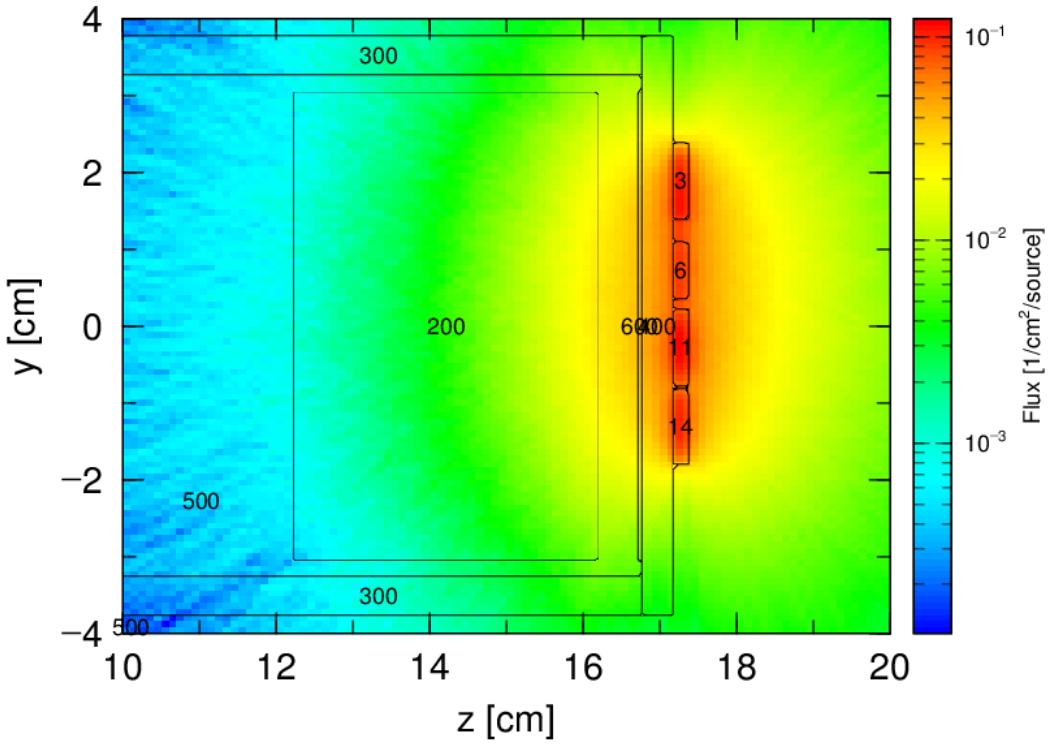

(b)

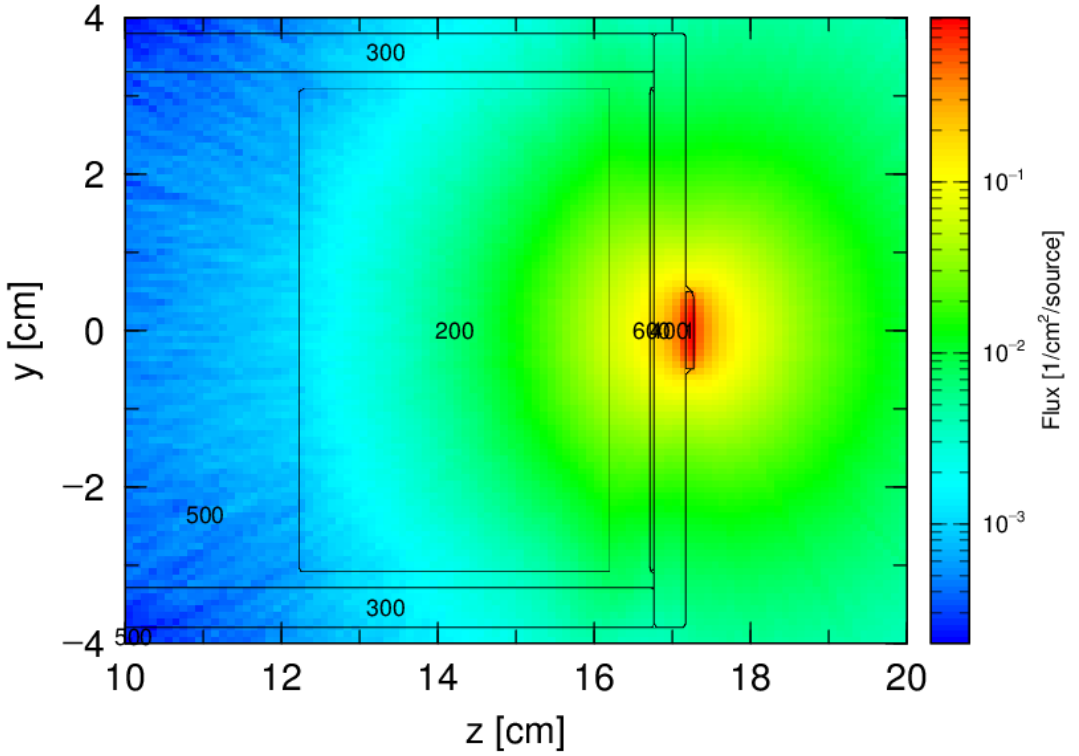

Fig. 4.13 Gamma-ray flux distribution for thirty pieces of foil stacks (a) and one-piece foil (b) around the HPGe detector.

(a)

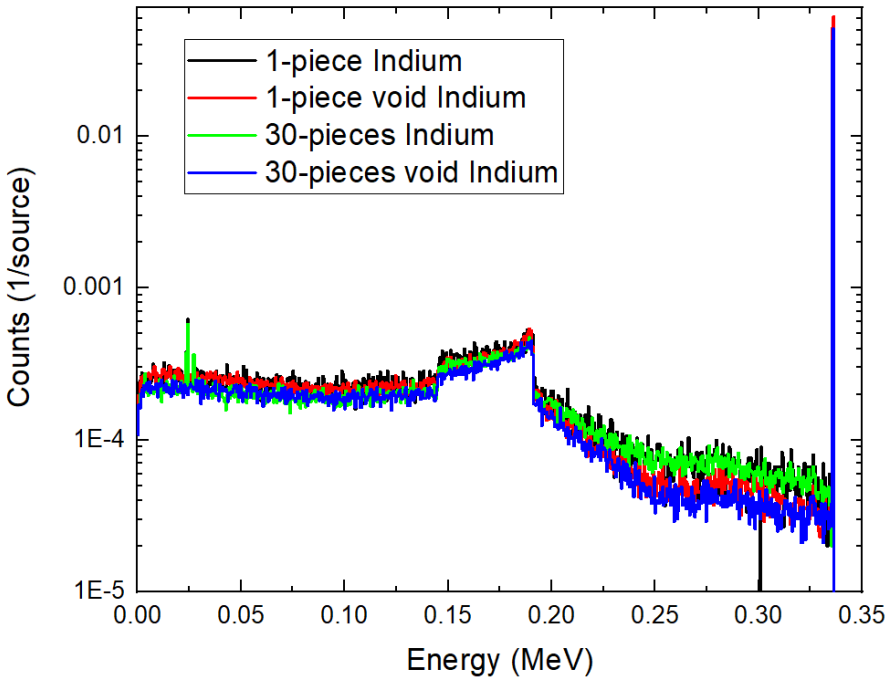

(b)

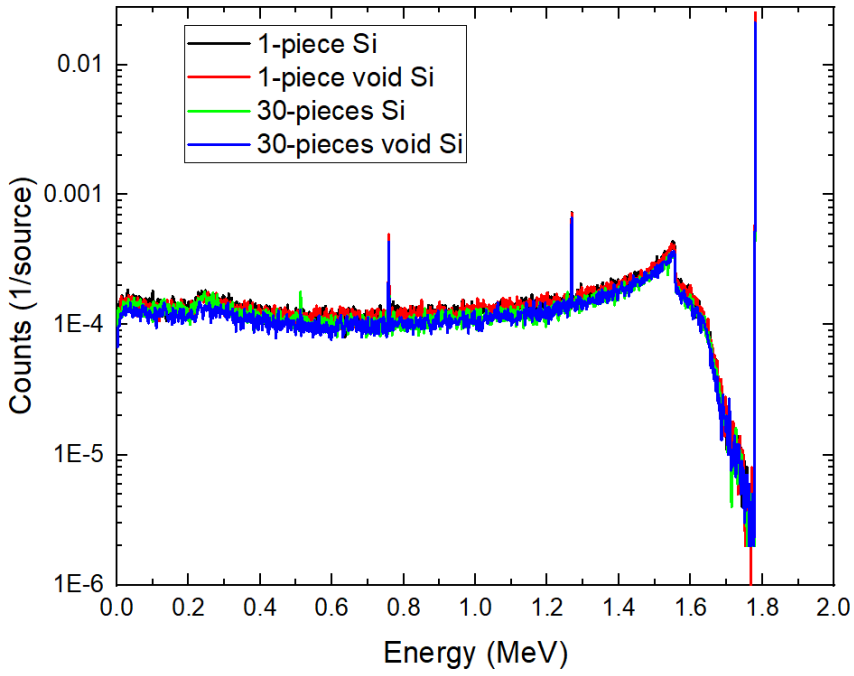

Fig. 4.14 Gamma-ray response calculated by PHITS for indium foil (a) and silicon foil in the case of 1-piece and 30-pieces with and without the self-absorbed effect.

4.3.2. Experimental results

In the *in situ* calibration experiment, three capsules were irradiated over 15 h at the 8-O port. Each capsule has thirty pieces of indium foils inside and the total mass of indium is approximately 18 g. The capsule cannot be transferred by using the NAS pneumatic tube due to insufficient air pressure. The neutron flux of irradiation end in the 2.5-L port is lower than that in the 8-O port because the irradiation end in the 2.5-L port is far from the plasma compared with the distance from the irradiation end in the 8-O port to the plasma. In addition to this, it is not easy to support the capsule inside the irradiation end in the 2.5-L port. Therefore, the capsule was placed inside the 8-O port and removed by hand. Immediately after the irradiation, the capsule was removed for gamma-ray measurement. The irradiation times of capsule #1, capsule #2, and capsule #3 are 15.217 h, 15.583 h, and 46.283 h, respectively. [56]

Multiple measurements were performed to improve the statistical error and to eliminate the effect of the gamma rays from $^{115}In(n, \gamma)^{116}In$ reactions. Each measurement time of the gamma rays ranged from 3000 s to 10000 s in order to ensure that there are sufficient statistics of the photoelectric peak counts for the gamma ray of interest. The integrated photoelectric peak pulse counts of 336 keV gamma ray are evaluated by Gaussian fitting as shown in Fig. 4.15. [56]

The thirty pieces of irradiated indium foils were uniformly distributed on the surface of the HPGe detector and were measured simultaneously. The detection efficiencies of the HPGe detector for thirty pieces of indium foil measurement are evaluated by the PHITS code. In Table 4.2, the activation response coefficients obtained by multiple gamma-ray measurements of each capsule are listed and those are plotted for each run number in Fig. 4.16. The standard deviation of each counting is 13%. The error of the detection efficiencies of the HPGe detector from the PHITS calculation is 0.98%. Also, there is an error in irradiation time because it took approximately 2 min to place the capsule and to remove the capsule at the irradiation end. This error is considered to be 0.22% for total irradiation time of each capsule. The error of ^{252}Cf neutron source neutron emission rate is 1%. The total error of the calibration experiment is estimated to be approximately 13%. Thus the mean activation response coefficients of $^{115}In(n, n')^{115m}In$ reaction is evaluated to be $(9.40\pm1.2)\times10^{-8}$. [56]

(a)

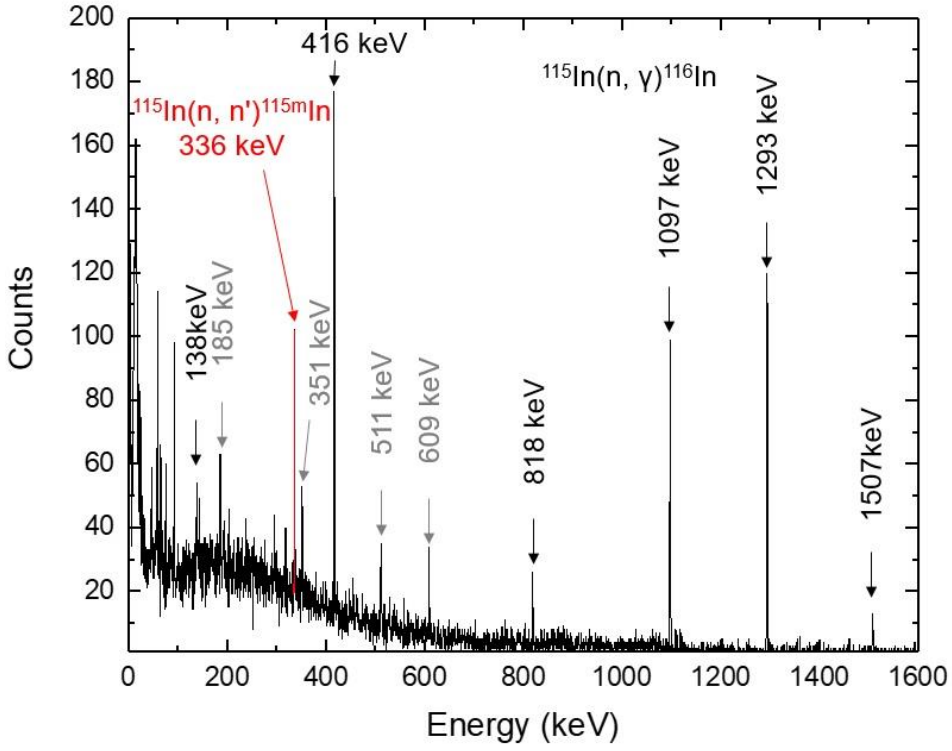

(b)

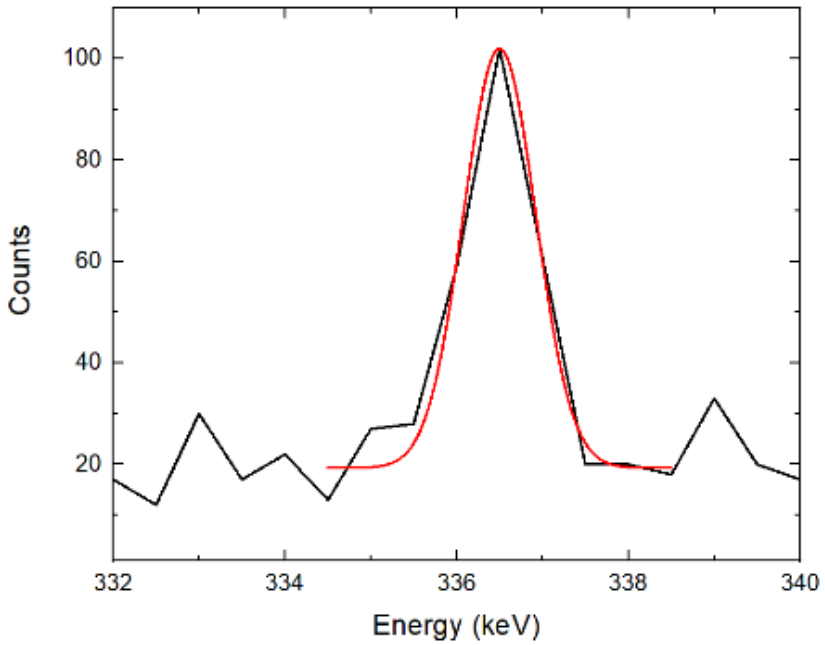

Fig. 4.15 (a) The gamma-ray spectrum for thirty pieces of indium foils was obtained from 10,000 s measurement by the HPGe detector. Here, red font stands for ^{115}In(n, n')^{115m}In reaction, black font stands for ^{115}In(n, γ)^{116}In reactions, and gray font is not a gamma ray from indium, and (b) enlarged 336 keV peak with a Gaussian fitting. [56]

Table 4.2 Activation response coefficients (ARC) (with a factor of 1 ×10^8) of the ^{252}Cf ring-shaped neutron source. [56]

	Capsule #1			Capsule #2			Capsule #3		
Mass (g)	17.785			17.717			17.678		
Irradiation time (h)	15.217			15.583			46.283		
Run number	Count time	Counts	*ARC*	Count time	Counts	*ARC*	Count time	Counts	*ARC*
1st	3000s	29.8[a]	9.15	3000s	85.6	11.3	3000s	71.1	8.52
2nd	3000s	56[a]	8.83	10000s	164.9	8.69	3000s	63.7	8.70
3rd	10000s	162	9.82	10000s	85	7.06	10000s	171.2	9.23
4th	10000s	111	10.4	3000s	22.375	8.34	10000s	121	11.0
5th							10000s	64.5	9.06
6th							40000s	115	11.4

[a]Note that in the run number 1 measurement for the capsule #1, the gamma-ray was measured for thirty pieces of indium foils with the capsule. In the run number 2 measurement for the capsule #2, the gamma-ray was measured for twenty-nine pieces of indium foils without the capsule. In the other measurements, gamma-ray measurements were performed for the thirty pieces of indium foils without the capsule.

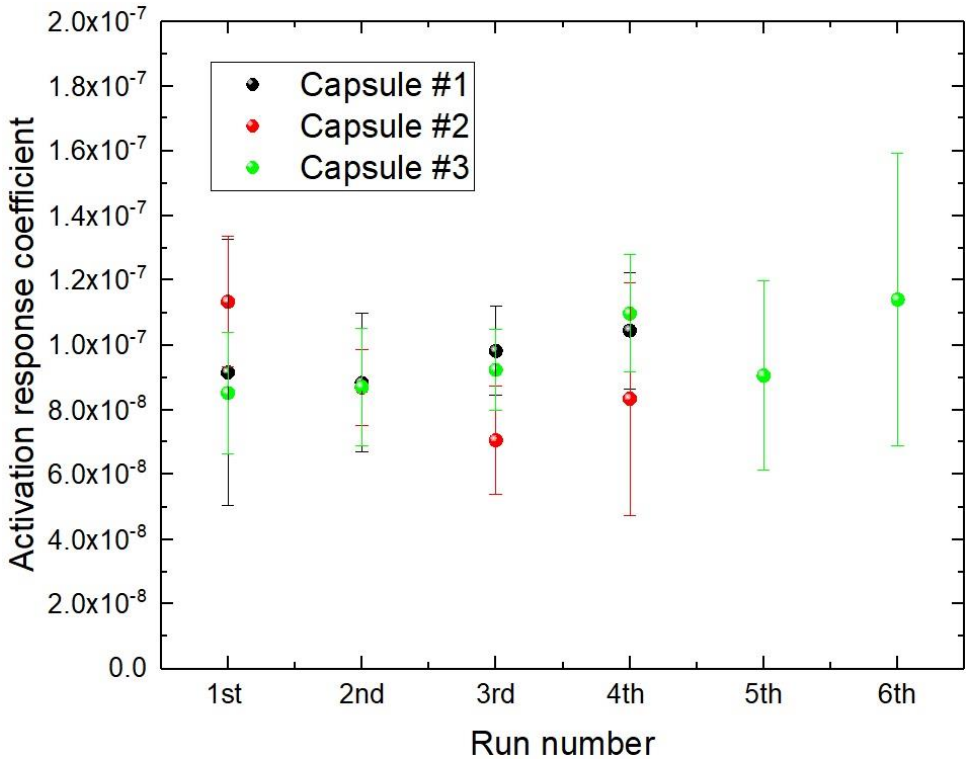

Fig. 4.16 Activation response coefficients of the ^{252}Cf ring-shaped neutron source for run number of each capsule were obtained from the *in situ* calibration experiment. [56]

4.3.3. Discussion based on MCNP simulation

The neutron spectrum Φ(E) in the irradiation end normalized for unit source neutron is obtained from MCNP simulation. Activation response coefficients ∑σ(E)·Φ(E) also can be obtained from MCNP simulation. Here, MCNP6 code[89] and nuclear data library FENDL 3.0[90] are used for the Φ(E) calculation, and JENDL 99 Dosimetry file [91] is used for the reactivity calculation. The rotation time, about 40 s, of the calibration neutron source on the magnetic axis is sufficiently shorter than the half-life of ^{115m}In. Therefore, this source can be regarded as a toroidal ring-shaped source by averaging a long-time effect. [56]

Actually, the neutron source in the plasma has poloidal distribution. The ^{252}Cf neutron source is a point source and is nearly isotropic in neutron emission. The model for ^{252}Cf ring-shaped source is shown in Fig. 4.17(a), where detailed components are considered carefully, such as the irradiation end (enlarged part of Fig. 4.17(b)), the train, the railway, the maintenance support, and the model of superconducting coils without liquid helium. In the ^{252}Cf ring-shaped source case, source neutron energy has fission neutron spectrum represented by the Watt formula [89] of $\frac{dN}{dE} \propto e^{(-E/a)} \cdot Sinh(bE)^{1/2}$, where a=1.18, and b=1.03419. Meanwhile, foil stack of thirty pieces inside the capsule is modeled to estimate the self-shielding effect of the foil stack. The activation response coefficients of ^{115}In(n, n')^{115m}In reaction for ^{252}Cf ring-shaped source case was evaluated to be 8.8×10^{-8} (statistical error 4.2%) by MCNP calculation. It is in good agreement with the result of the calibration experiment within 7% difference. This indicates that the MCNP calculation taking account of the self-shielding effect of the foil stack is sufficiently accurate. [56]

In order to obtain the activation response coefficients for the plasma source, differences between the plasma source and the ^{252}Cf ring-shaped source have been evaluated by MCNP. In the model for plasma, neutron source is a volumetrically mono-energetic neutron with a neutron emission density profile which is the structure of five coaxial torus geometry, as shown in Fig. 4.17(b). The neutron emission probability of five coaxial torus regions is determined to fit the typical neutron emission profile estimated in the LHD deuterium plasma. Meanwhile, only one piece of activation foil is modeled to simulate the measurement at the plasma experiment. The model of superconducting coils has liquid helium. Other main structures of LHD are the same. The neutron spectra normalized by unit source in the capsule without and with foil for the neutron from ^{252}Cf neutron, 2.45 MeV neutron, and 14.1 MeV neutron are shown in Fig.4.18(a) and (b), respectively. [56]

(a)

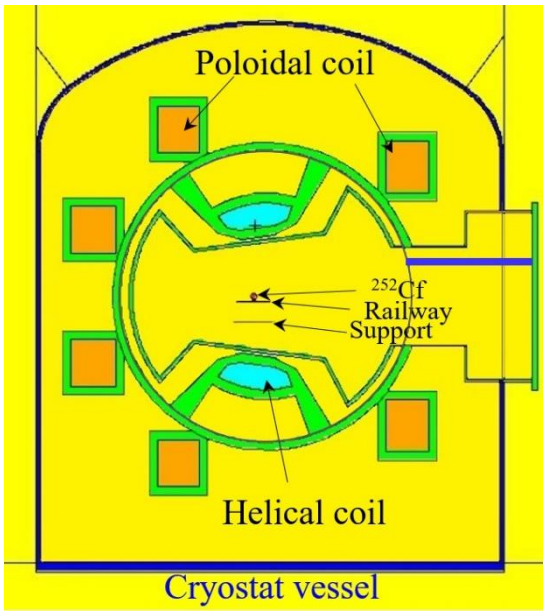

(b)

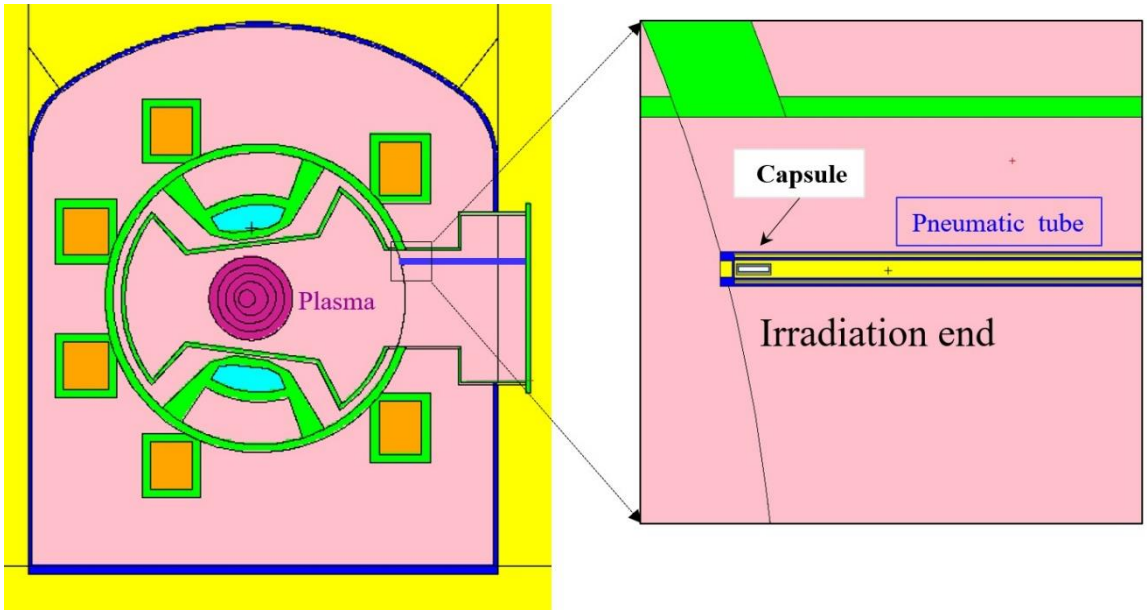

Fig. 4.17 (a) MCNP model for ^{252}Cf source, and (b) MCNP model for plasma source and enlarged irradiation end. [56]

(a)

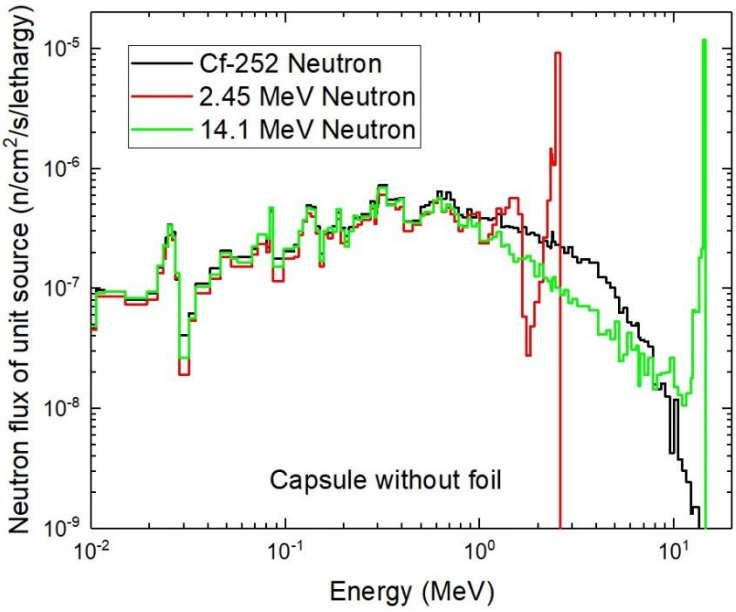

(b)

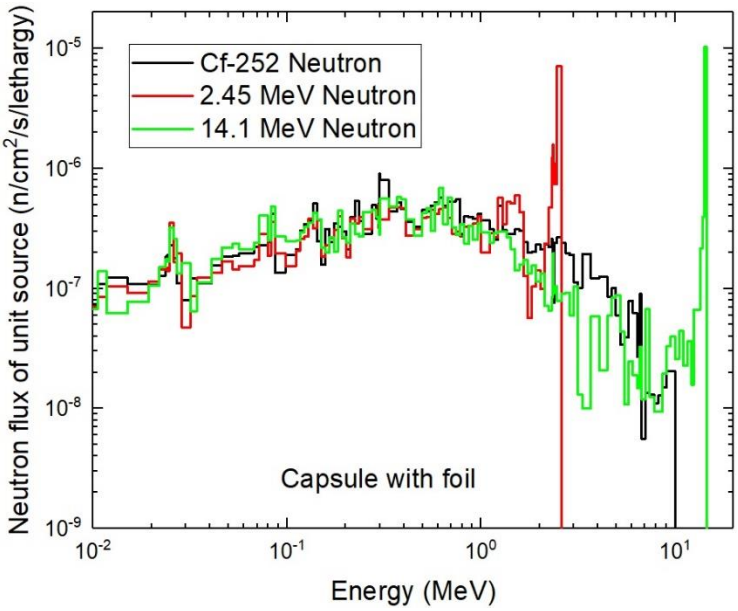

Fig. 4.18 (a) The neutron spectra normalized by unit source in the capsule without the foil in the ^{252}Cf neutron case and two plasma source cases, and (b) the neutron spectra normalized by unit source in the capsule with thirty pieces of indium foils in the ^{252}Cf neutron case and one piece of foil in two plasma source cases. [56]

In the incoming neutron spectra for the capsule without foil case shown in Fig. 4.18(a), there are significant differences in three spectra above 1 MeV. ^{252}Cf fission neutron spectrum has high-energy component, while the neutron is mono-energetic in the

plasma case. The low energy parts of the spectra are almost the same. This means that scattered neutrons from LHD models for ^{252}Cf ring-shaped source and plasma of volume neutron emission are almost the same. In other words, the difference of activation response constants should mainly come from the difference of high energy neutron spectra. However, due to the number and type of foils, the self-shielding effect on neutrons should be different. Therefore, it is necessary to investigate the differences in the neutron spectra of different numbers and types of foils. [56]

By comparing to Fig. 4.18(a) and (b), there are several differences in the neutron spectra of ^{252}Cf neutron, 2.45 MeV neutron, and 14.1 MeV neutron for the capsule without and with foil cases, respectively. Here, thirty pieces of the indium foil inside the capsule were modeled in the MCNP calculation for ^{252}Cf ring-shaped source in the case of capsule with foil. Meanwhile, one piece of indium foil, silicon foil, and aluminum foil in the capsule was modeled for 2.45 MeV and 14.1 MeV plasma neutron source in the case of capsule with foil. In the case of capsule without foil, there is only air in the capsule. Thus, the self-shielding effect of the foil for neutron was calculated by MCNP in the case of capsule with foil. Those reasons would lead to the differences in the activation response coefficients for each reaction in the ^{252}Cf ring-shaped source case and the plasma case. [56]

Thus, the correction factor of MCNP F_{cor} between experiment and MCNP can be obtained as follows:

$$F_{cor} = \frac{[\sum_E \sigma(E)\cdot\Phi(E)]_{exp.}}{[\sum_E \sigma(E)\cdot\Phi(E)]_{MCNP}} \quad (4.3)$$

$[\sum\sigma(E)\cdot\Phi(E)]_{exp.}$ is activation response coefficient which is obtained from calibration experiment or activation response coefficients for plasma experiment, and $[\sum\sigma(E)\cdot\Phi(E)]_{MCNP}$ is activation response coefficient which was obtained from MCNP6. Therefore, F_{cor} is evaluated to be 1.07.

4.3.4. Correction for the LHD experiment

The difference of 7% between the in situ calibration and the MCNP calculation in the ^{252}Cf ring-shaped source case is mainly due to the modeling error in the MCNP calculation. Therefore, 7% is assumed to be a modeling error in the MCNP calculation not only for ^{115}In(n, n')^{115m}In reaction but also other reactions in plasma case to be used

in the NAS measurement on LHD. By this assumption, F_{cor} obtained from in situ calibration experiment and MCNP calculation can be applicable not only for 2.45 MeV neutrons but also for 14.1 MeV neutrons from the triton burnup process, and not only for ^{115}In(n, n')^{115m}In reaction also for other reactions. Note that, the difference in energy of ^{252}Cf ring-shaped source, D-D plasma source, and D-T plasma source included device scattering effect is evaluated by MCNP calculation. The activation response coefficients for plasma case can be obtained as follow:

$$[\sum\sigma(E)\cdot\Phi(E)]_{plasma} = [\sum\sigma(E)\cdot\Phi(E)]_{Exp.(^{252}Cf)} \times \frac{[\sum\sigma(E)\cdot\Phi(E)]_{MCNP(plasma)}}{[\sum\sigma(E)\cdot\Phi(E)]_{MCNP(^{252}Cf)}}$$

$$= F_{cor} \times [\sum\sigma(E)\cdot\Phi(E)]_{MCNP(plasma)} \quad (4.4)$$

The error 12.92% from in situ calibration should be taken in account to the activation response coefficients in plasma case. The statistical error of the activation response coefficient of ^{115}In(n, n')^{115m}In reaction for ^{252}Cf ring-shaped source case was evaluated to be 4.23% by MCNP calculation. Here, we assumed error from cross section is less than 5%. By using those errors and the statistical error from MCNP calculation for other reactions, we can evaluate the total error for each reaction in the plasma case. The activation response coefficients for 2.45 MeV neutron from the D-D plasma case and for secondary 14.1 MeV neutron are evaluated by using the MCNP calculation and F_{cor} in Table 4.3.

Table 4.3 Activation response coefficients for plasma case calculated by both the MCNP code and the correction factor F_{cor} for all reactions in plasma case.

Reaction (neutron source)	ARC from MCNP	MCNP statistical error	ARC after correction	Total error
^{115}In(n, n')^{115m} In (^{252}Cf)	8.80×10^{-8}	4.23%	9.40×10^{-8}	12.92%
^{115}In(n, n')^{115m}In (2.45 MeV)	1.53×10^{-7}	3.4%	1.64×10^{-7}	14.88%
^{28}Si(n, p)^{28}Al (14.1 MeV)	8.42×10^{-8}	5.7%	8.99×10^{-8}	15.58%
^{27}Al(n, p)^{27}Mg (14.1 MeV)	2.36×10^{-8}	5.6%	2.52×10^{-8}	15.54%
^{27}Al(n, α)^{24}Na (14.1 MeV)	3.57×10^{-8}	5.8%	3.82×10^{-8}	15.61%

Chapter 5:

Neutron measurement on LHD

The LHD started deuterium plasma experiments in March 2017. The neutron diagnostic is one of the most important diagnostics on the deuterium experiment, not only for understanding the plasma performance but also for the radiation safety. In the LHD deuterium plasma experiment, the neutron emission rate and the shot-integrated neutron yield are measured with the NFM and the NAS, respectively. At the same time, the shot-integrated 14 MeV neutron was measured by NAS and the time evolution of 14 MeV neutron was measured by Sci-Fi detectors.

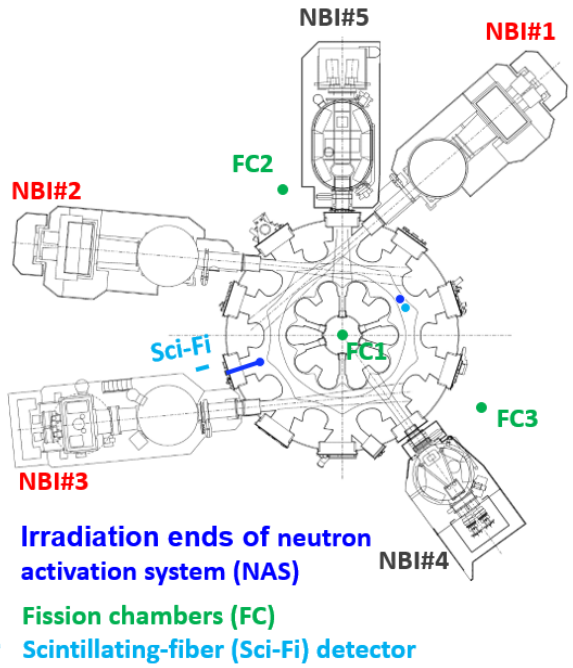

Fig. 5.1 The arrangement of NBIs, NFM, and irradiation ends of NAS on LHD.

LHD has two perpendicular neutral beam injectors (NBIs) (NBI#4, and #5) with the typical energy of 60–80 keV and three tangential NBIs (NBI#1, #2, and #3) with the typical energy of 180 keV as shown in Fig. 5.1. The normal direction of the toroidal magnetic field is counterclockwise as seen from the top of device. Therefore, NBI#1 and #3 are co-direction injections to the toroidal magnetic field, and NBI#2 is a counter-direction injection to the toroidal magnetic-field directions. NBI is an important heating method for fusion plasma. In NBI heating, the neutron yield is significantly higher than that in the plasma only with electron-cyclotron resonance heating (ECRH). In the perpendicular-NBI (P-NBI) phase, the neutron yield is relatively low around 1×10^{12}~7×10^{14} n/s. In the full D-D phase, three tangential NBIs were injecting to the plasma, where the neutron yield reached to 4×10^{15} n/s which was recorded by NFM.

NAS can not realize time-resolved measurements, but provides shot-integrated neutron fluence. Neutron measurements are often affected by gamma-rays and scattered neutrons. Activation measurement accurately evaluates the flux of irradiated neutrons by measuring the gamma-rays emitted from the nucleus activated by neutrons. Generally, the energy of gamma-rays emitted from different reactions is different, thus it is easy to identify the required reaction through the measurement using a HPGe detector with the high energy resolution. Furthermore, the activation reactions, such as (n, n'), (n,p), and (n,α) reactions, are usually accompanied by a neutron energy threshold, therefore, the influence of scattered neutrons can be eliminated by selecting the appropriate reaction.

Neutron measured by NFM can provide both integral measurement and time evolution information. Under the condition of low neutron flux, the ^{10}B and ^{3}He proportional counter can work normally and are almost imperceptible to gamma-rays. Selecting the appropriate amplifier integration time, these detectors with suitable threshold can provide absolute neutron flux. At high neutron flux, these detectors become saturated and do not work properly. At this point, the less sensitive FC will enter counting mode. As the neutron flux increases, FC will work in the Campbell mode. However, these detectors are thermal neutron detectors, thus the influence of scattering neutrons cannot be excluded.

The Sci-Fi detector is designed as a 14 MeV neutron detector. It eliminates the effects of low-energy neutrons and gamma rays and provides time resolved and integrated measurements.

5.1. Shot-integrated neutron yield on LHD

5.1.1. NAS measurement on 8-O port

The shot-integrated neutron yield in LHD experiment was evaluated by the gamma-ray intensity emitted from the activated foil after irradiation. Fig. 5.2(a) shows the typical gamma-ray spectrum of an In foil measured with the HPGe detector, where the gamma-ray intensity is derived from the peak area by Gaussian fitting as shown in Fig. 5.2(b). The gamma-ray spectrum in Fig. 5.2 is the long time measurement results subtracted background. Since the cross section of ^{115}In(n, γ)^{116}In reaction is relatively larger than that of ^{115}In(n, n')^{115m}In reaction and the gamma-ray intensity from ^{116}In reaction is relatively stronger than that from ^{115m}In, the activated In foil usually needs to be cooled for 1 hour or more for ^{115}In(n, n')^{115m}In reaction measurement in order to suppress the effect of ^{116}In. Note that, the half-life of ^{116}In is about 54 min. If the sample is not cooled sufficiently, 336 keV peak of ^{115}In(n, n')^{115m}In reaction will be superimposed on Compton continuum of ^{116}In gamma-rays as shown in Fig. 5.2(b). Therefore, the Compton continuum will increase the error in Gaussian fitting, and will reduce the measurement accuracy. Moreover, the neutron yield is not the same in the different shot, and the difference is several orders of magnitude. Fig. 5.3 (a) and (b) show the gamma-ray spectrum measured in different cooling time and measurement time Δt for two different neutron yield shots, which show that 336 keV peak affected by Compton continuum is different for different neutron yield shots. In order to provide measurement accuracy, multiple measurements with different cooling time were performed for one irradiation shot. Fig. 5.4(a) and (b) show the counts per second (cps) with different cooling time for one irradiation measurement fitted by decay equation $y = y_0 + A_1 e^{-\frac{x-x_0}{t_1}}$, respectively. Theoretically, *y0* is 0, but due to the measurement error from Compton continuum, *y0* will be around 0 as shown in Fig. 5.5(a). In the case of the close cooling times, the exponential decay law is not obvious, and the fitting curve is close to a straight line, then, the deviation of *y0* is large. Fig. 5.5(b) shows the factor *A0* evaluated from the exponential decay equation as a function of the shot-integrated neutron yield, as $A_0 = A_1 e^{\frac{x_0}{t_1}}$ which is the cps on the end of irradiation time t_0. Therefore, there are over cps difference of 25 times with the neutron yield from 1.5×10^{14} to 4.5×10^{15}. Fixed measurement time and fixed cooling time are obviously not suitable for this kind of measurement across 1 magnitude. Therefore, if at least over statistics of 100 counts or larger one were obtained, the measurement time would change from 1,000 s to 300 s. In fact, a measurement in a long time and the average of multiple measurements are the equivalent. It can be chosen the

lazy way that a single long time measurement, but the accuracy of the data will be relatively reduced. Single long time measurement is often concentrated in a short time period, and multiple measurements can be dispersed in different cooling time. Multiple measurements can reduce the activation gamma-ray emission randomness and interference from other reactions, and is good for multiple irradiations of LHD discharge within close shots for each irradiation, but just increases the workload of measurement.

(a)

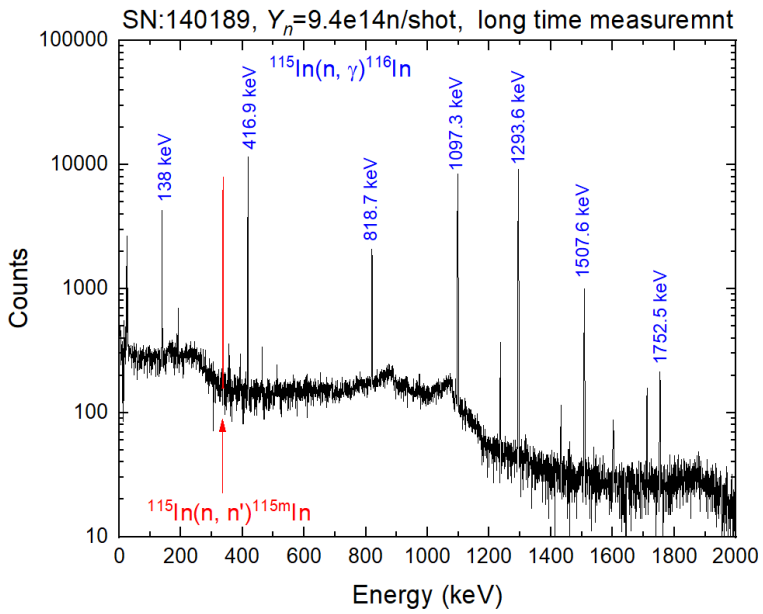

(b)

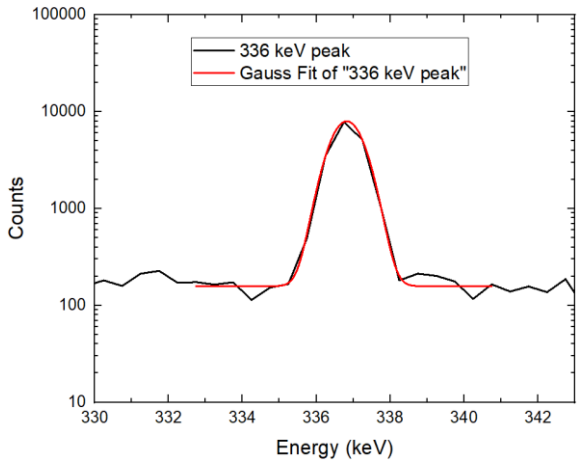

Fig. 5.2(a) The gamma-ray spectrum without background for SN: 140189 in LHD experiment, where the neutron yield in this shot is 9.4×10^{14}, and (a) Gaussian fitting for 336 keV form ^{115}In(n, n')^{115m}In reaction.

(a)

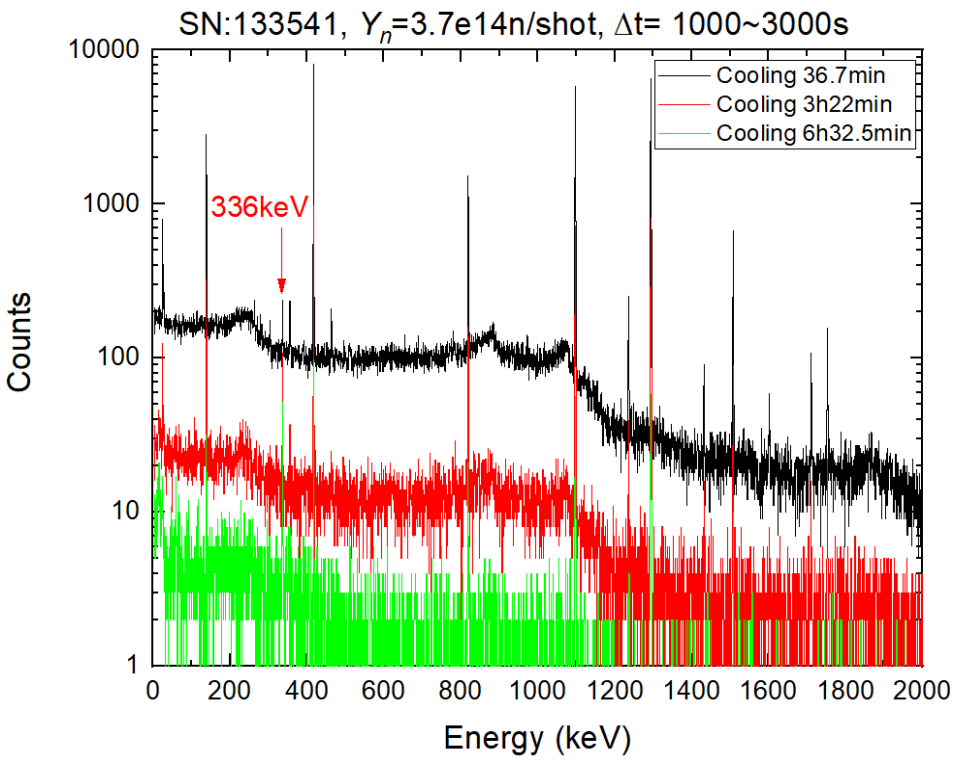

(b)

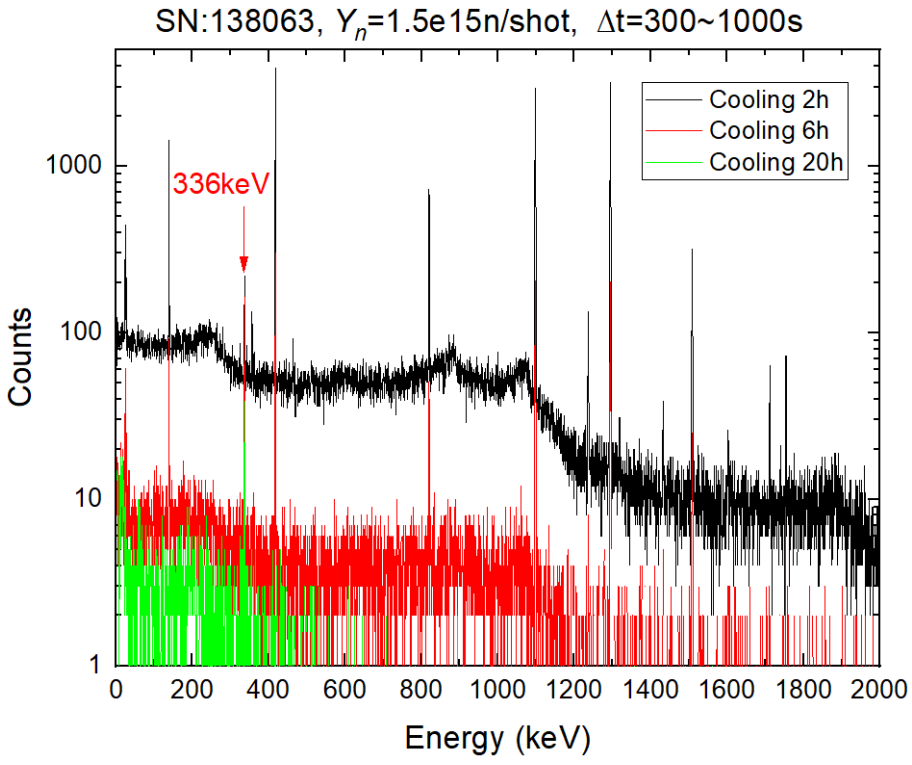

Fig. 5.3 The gamma-ray spectrum measured in different cooling time and measurement time in low neutron yield shot (a) and high neutron yield shot.

(a)

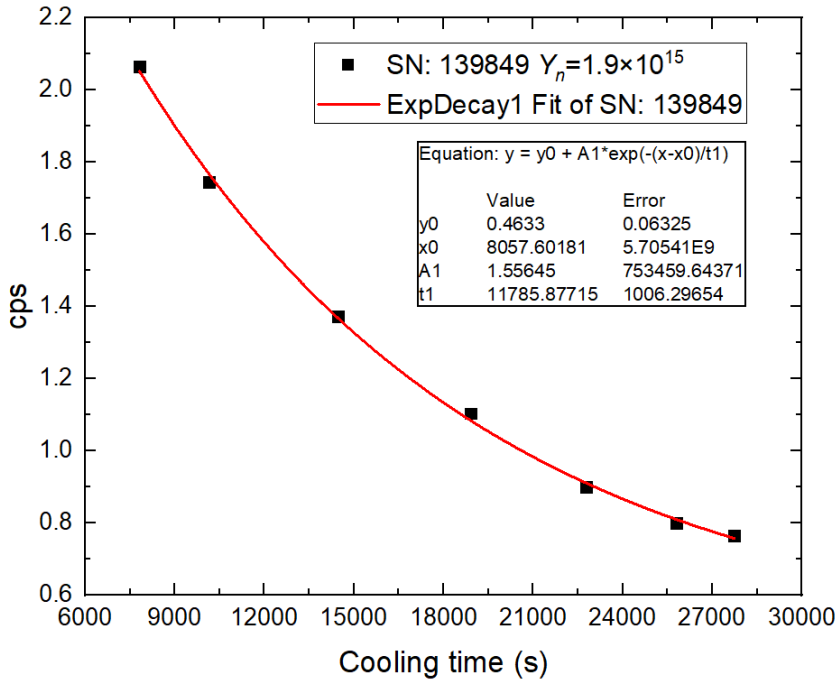

(b)

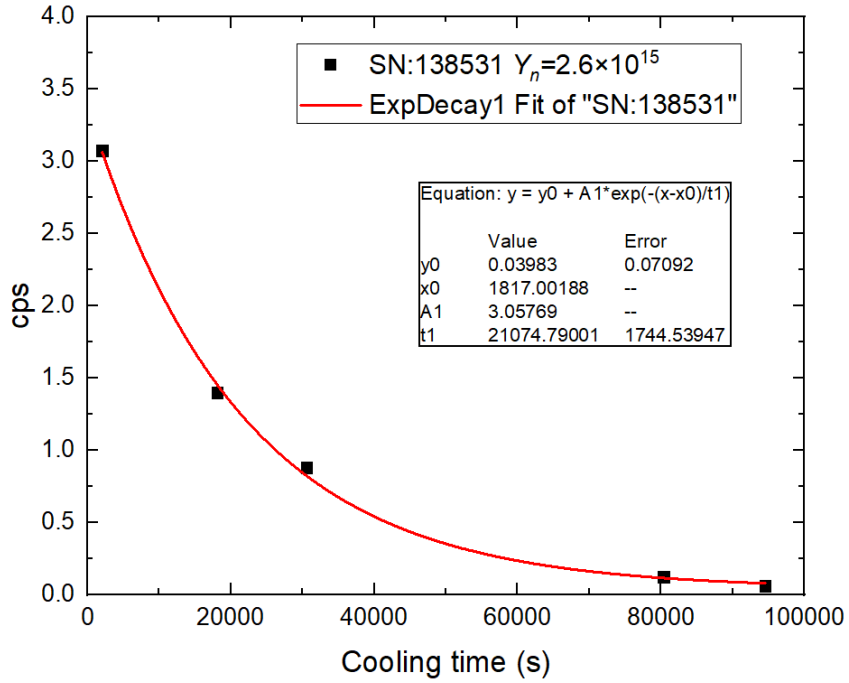

Fig. 5.4 The exponential decay fitting of cps for one irradiation on (a) SN: 139849 and (b) SN: 138531.

(a)

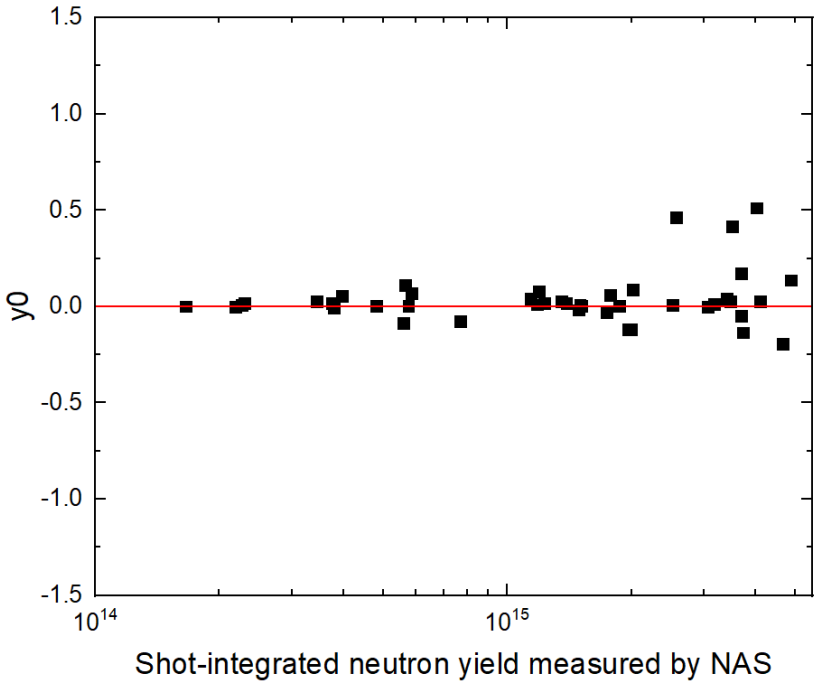

(b)

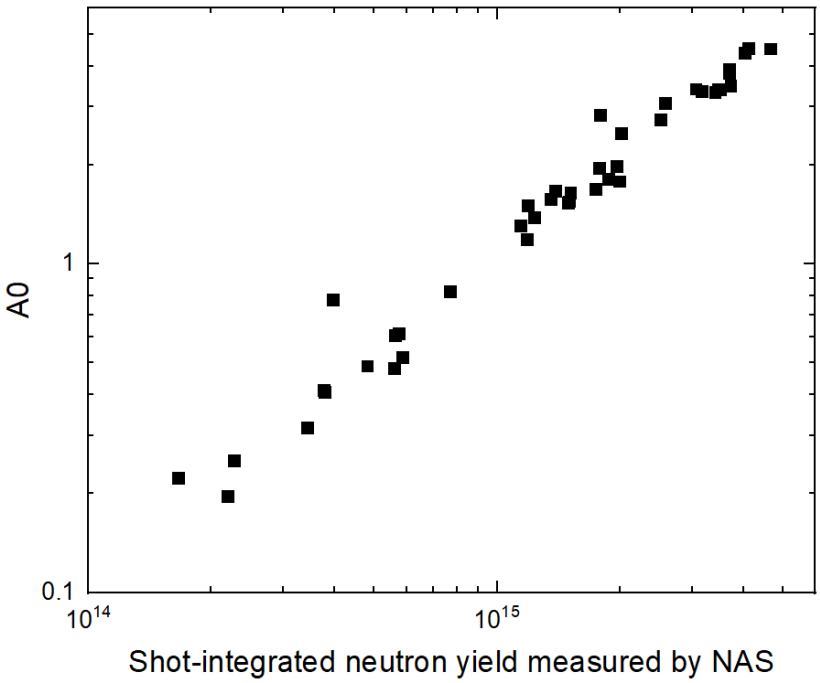

Fig. 5.5 (a) *y0* in the exponential decay equation as a constant of shot-integrated neutron yield, and (b) *A0* evaluated from the exponential decay equation as a function of Shot-integrated neutron yield.

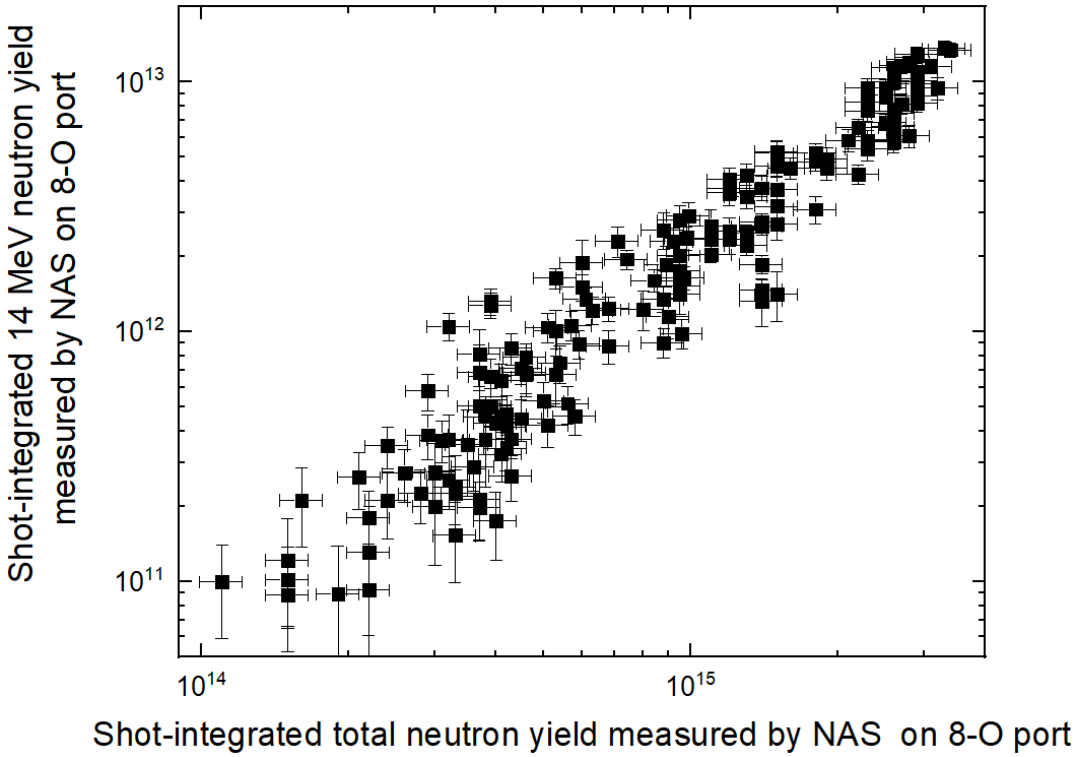

Fig. 5.6 14 MeV neutron yield measured by ^{28}Si(n, p)^{28}Al reaction as a function of total neutron measured by ^{115}In(n, n')^{115m}In reaction.

The shot-integrated neutron yield is evaluated by the average of multiple measurements for gamma-rays from ^{115}In(n, n')^{115m}In reaction measurements in each irradiation, where the activation response coefficient is obtained in the calibration experiment with the correction for D-D plasma of LHD by the MCNP calculation. At the same time, shot-integrated 14 MeV neutron yield is measured by ^{28}Si(n, p)^{28}Al reaction. Fig. 5.6 shows the 14 MeV neutron yield measured by NAS as a function of the total neutron yield measured by NAS. Basically, the shot-integrated 14 MeV neutron yield increase with the total neutron yield. Note that the activation response coefficient for ^{28}Si(n, p)^{28}Al reaction is calculated by MCNP for D-T plasma with the correction factor as shown in Table 4.3. Here, the correction factor only means the model error between experiment and MCNP calculation. The difference in energy of 2.45 MeV neutron and 14 MeV neutron spectra from device scattering effect is evaluated by the MCNP. The scattering data is coursed by different triton burnup ratio in different plasma conditions.

5.1.2. Comparison of NFM and NAS on 8-O port

The neutron yield across three orders of magnitude measured by NAS is in good agreement with that by NFM as shown in Fig. 5.7.

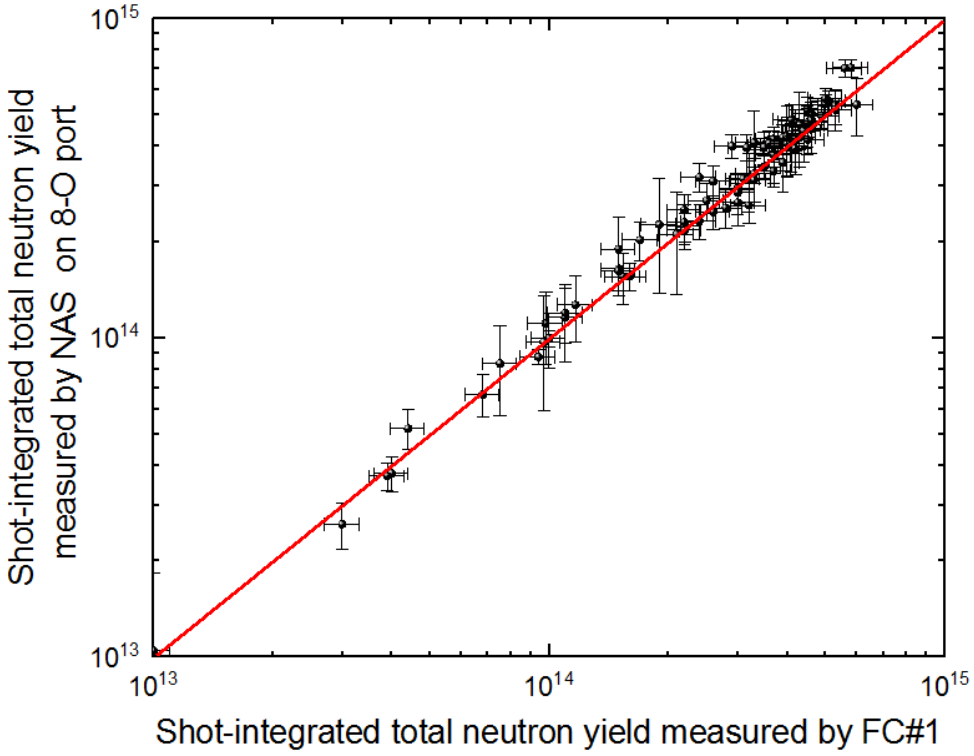

Fig. 5.7 Comparison of neutron yield measured by FC#1 and NAS on 8-O port.

The difference of NAS measurement from NFM measurement in perpendicular NBI phase is almost lower than 10%. The difference of the activation response coefficients coursed by the neutron profile shift with magnetic axis (R_{ax}) shift is calculated by MCNP as shown in Fig. 5.8. In the MCNP calculation, all calculations take account into same plasma radius, same neutron emission profile, and same LHD model, but only change in R_{ax} shift. The changes in the activation response coefficients were evaluated from the MCNP calculation as the differences of 1.3% between R_{ax} of 3.55 m and R_{ax} of 3.60 m, 1.1% between R_{ax} of 3.60 m and R_{ax} of 3.75 m, and 2.4% between R_{ax} of 3.75 m and R_{ax} of 3.90 m. Therefore, the changes in neutron yield measured by NAS from the neutron profile shift with R_{ax} is negligible. In other words, it just proves that the activation response coefficient evaluated by MCNP and corrected by *in situ* calibration is accurate.

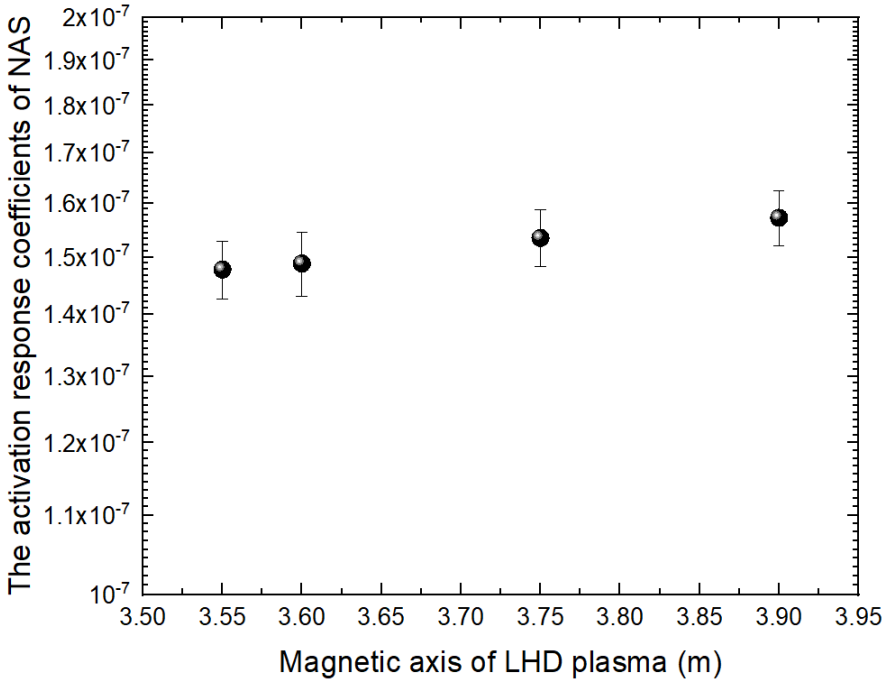

Fig. 5.8 The activation response coefficients for ^{115}In(n, n')^{115m}In reaction of NAS change with magnetic axis shift.

5.1.3. Cross-calibration of NAS on 2.5-L port with NFM

In several shots neutron yields was measured by NAS on the 2.5-L port as shown in Fig. 5.9. The activation response coefficient of ^{115}In(n, n')^{115m}In reaction for NAS on the 2.5-L port is evaluated by MCNP calculation without in situ calibration to be 4.98×10^{-8}. By using activation response coefficients in Table 4.3, neutron yields measured by NAS on the 2.5-L port are lower than those by NFM around 18%.

The *in situ* calibration was only performed on the 8-O port. Therefore, the correction factor evaluated from *in situ* calibration and MCNP calculation for ^{252}Cf ring-shape source only indicated the model error for the irradiation end of NAS on the 8-O port. It is clear that this correction factor can not be used for the irradiation end of NAS on the 2.5-L port. Therefore, the activation response coefficient calculated by MCNP for the irradiation end of NAS on the 2.5-L port is cross-calibrated by the center FC#1 measurement of NFM. After the cross calibration, the neutron yields measured by NAS on the 2.5-L port agree with those by NFM. Note that the activation response coefficient for the irradiation end of NAS on the 2.5-L port is corrected to be 4.24×10^{-8} after cross calibration, where the correction factor is evaluated to be 1.18. This correction also represents the model error for irradiation end on 2.5-L port between the MCNP

calculation and experiment.

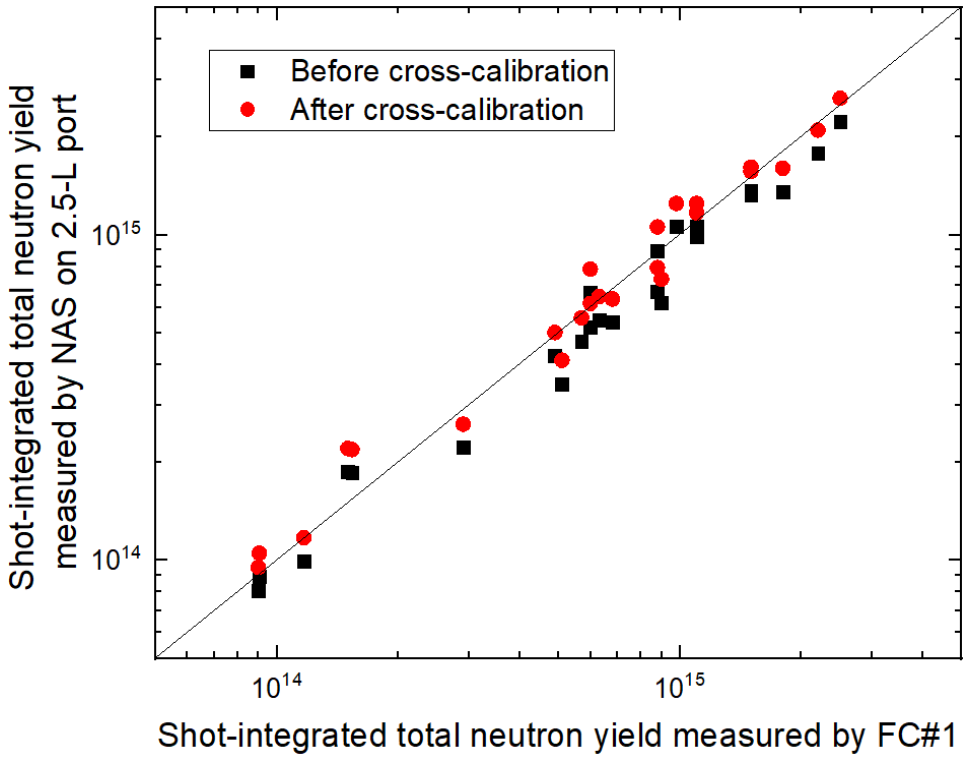

Fig. 5.9 Comparison of neutron yield measured by NFM and NAS on the 2.5-L port.

5.2. Time evolution of neutron emission rate on LHD

Before the LHD experiment, the threshold dependence of Sci-Fi detector counts has been measured at HV of -1800 V by using a ^{60}Co gamma-ray source in the laboratory as shown in Fig. 5.10, which indicates that the counts of gamma-ray and background decrease with increasing the threshold level.

In the beginning of the LHD experiment, the stability of the PMT gain was confirmed in LHD experiment by using a plastic scintillator and a ^{60}Co gamma-ray source with and without magnetic field as shown in Fig. 5.11. The pulse height of Compton electron edges did not change significantly, which indicates that PMT gain does not change in the LHD magnetic field environment, where the maximum magnetic field around detector position is about 0.025 T. Fig. 5.12 shows that LANL Sci-Fi detector with the threshold of 50 mV can work in the linear region of close to 7×10^{6} cps below the neutron emission rate of 1.5×10^{15} n/s in LHD deuterium experiment.

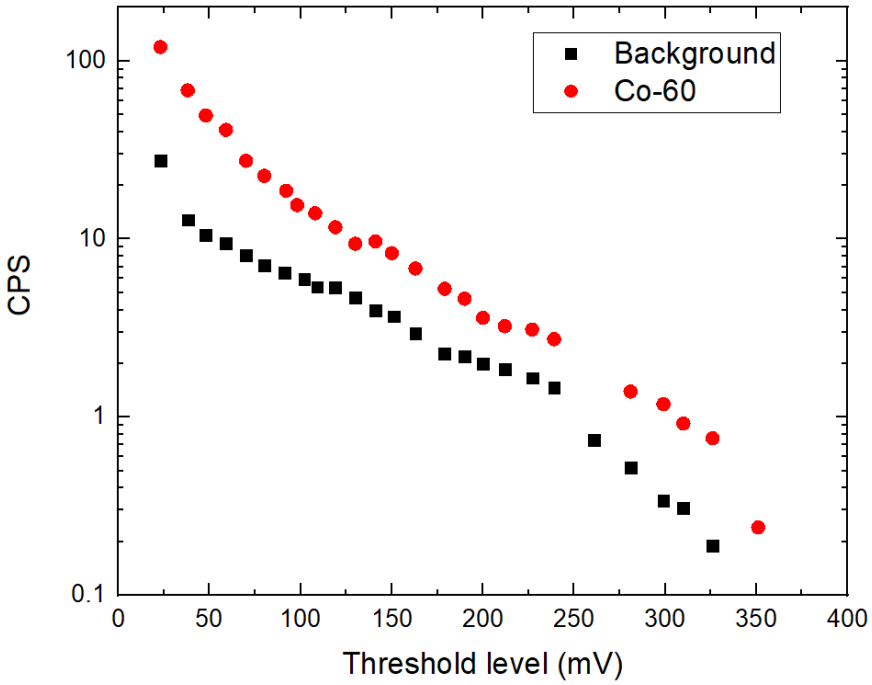

Fig. 5.10 The threshold dependence of LANL Sci-Fi detector for background and gamma-rays with the HV -1,800 V.

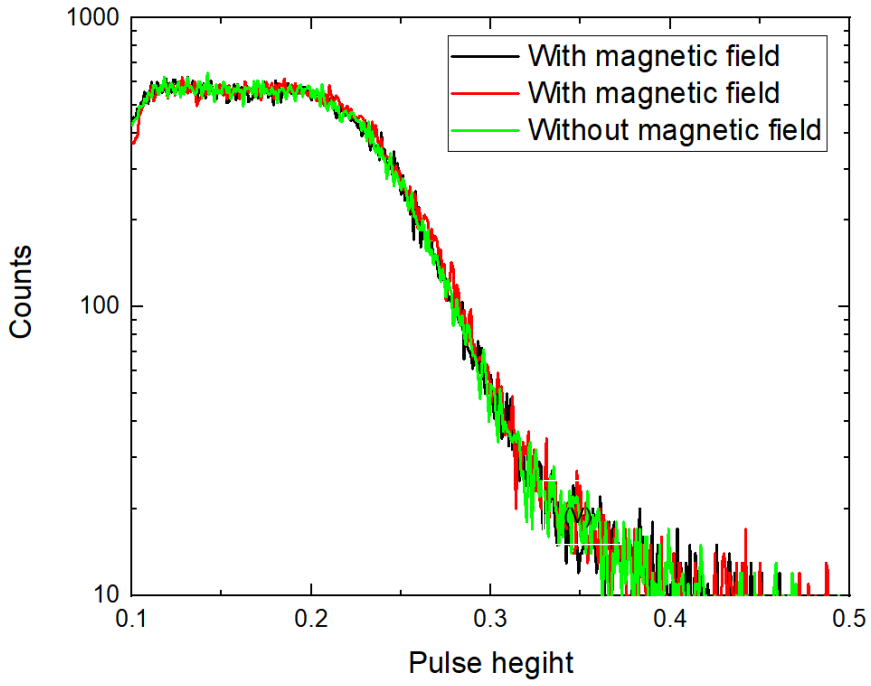

Fig. 5.11 Pulse height spectra of a plastic scintillator for a ^{60}Co gamma-ray source with and without magnetic field in LHD experiment.

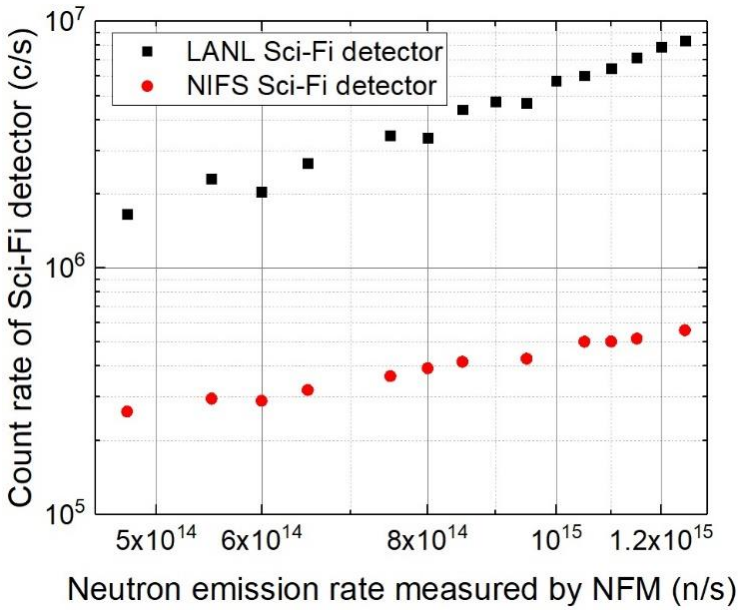

Fig. 5.12 Pulse counting rate linearity of the LANL Sci-Fi detector and NIFS Sci-Fi detector.

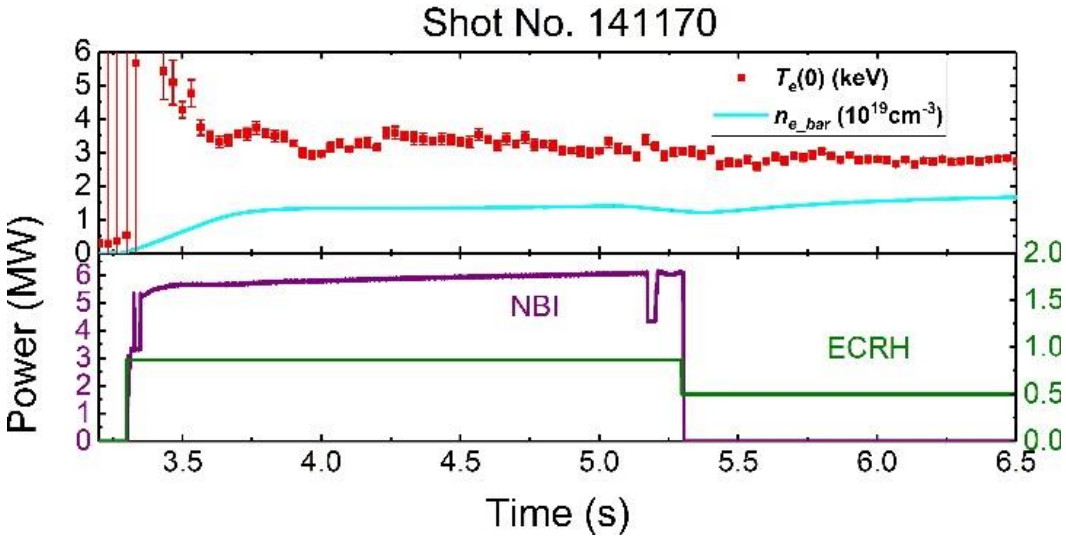

Fig. 5.13 Plasma parameter of shot No. 141170. [66]

(a)

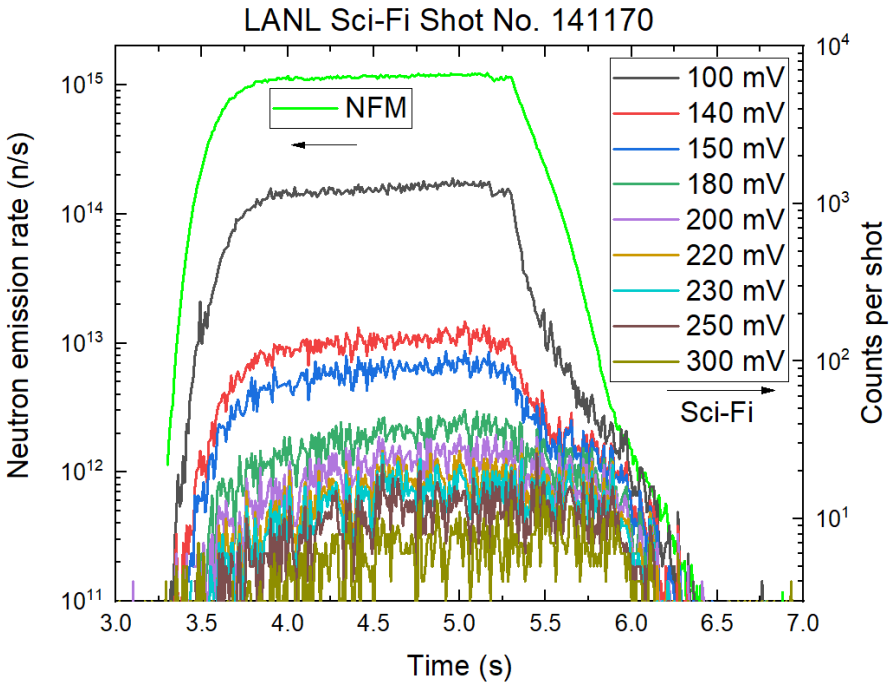

(b)

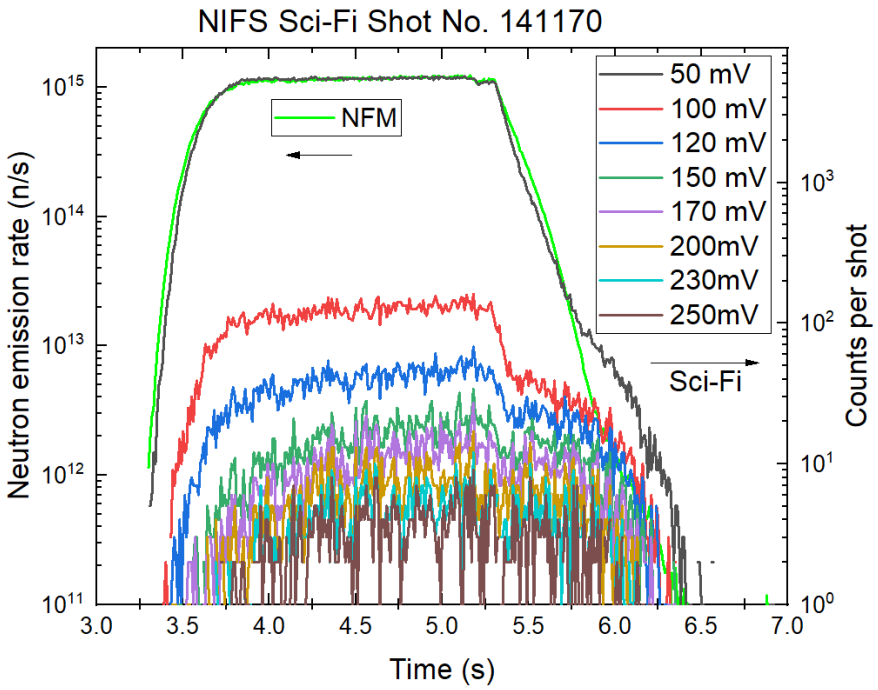

Fig. 5.14 (a) Comparison of the 14 MeV neutron emission rate measured by using the LANL Sci-Fi detector with different thresholds at PMT HV of -17,00 V and the total neutron emission rate measured by using NFM, and (b) comparison of the 14 MeV neutron emission rate measured by using the NIFS Sci-Fi detector with different thresholds at PMT HV of 2000 V and the total neutron emission rate measured by using

NFM.

(a)

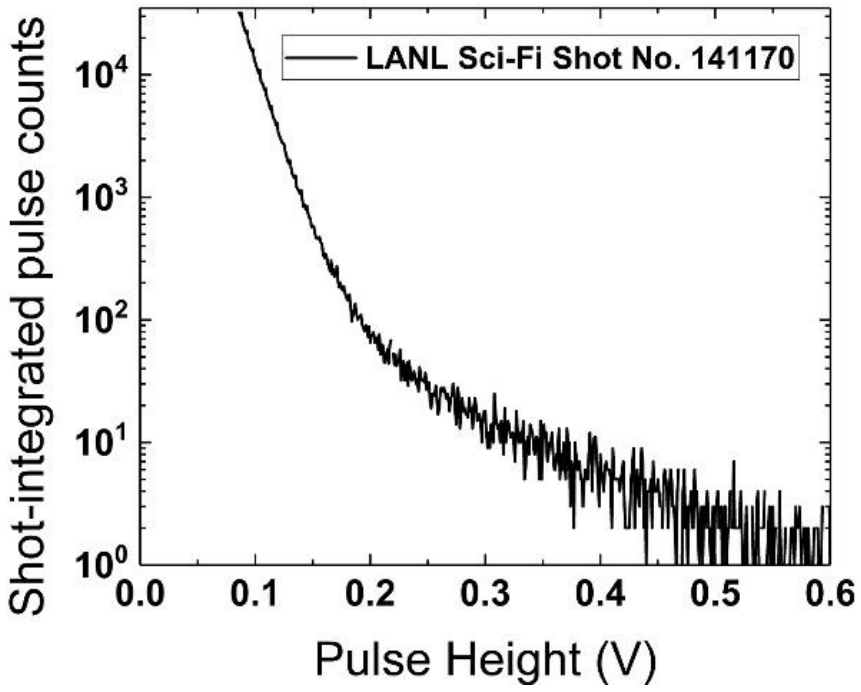

(b)

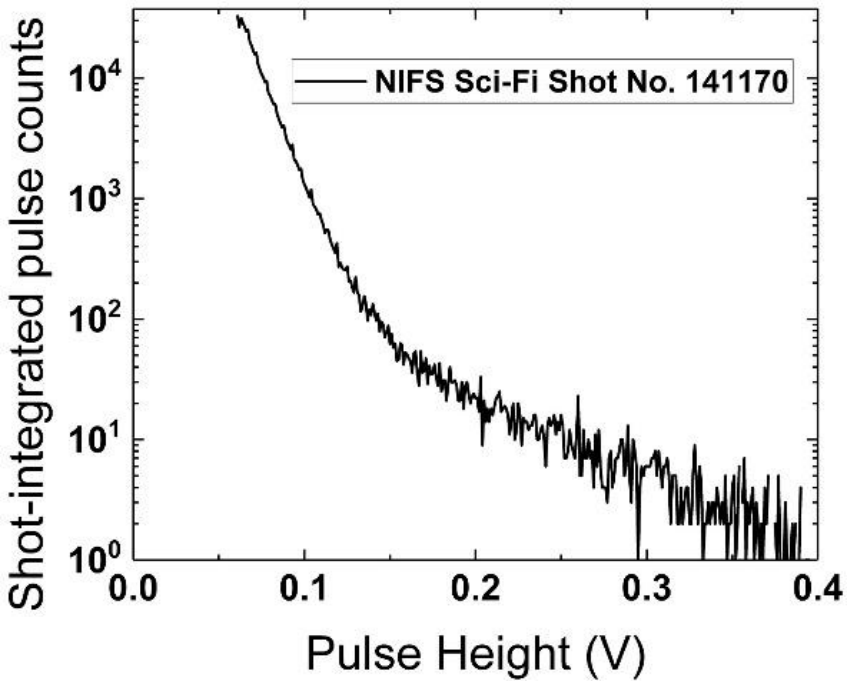

Fig. 5.15 The PHS of (a) the LANL Sci-Fi detector and (b) the NIFS Sci-Fi detector.

[66]

Fig. 5.13 shows the time evolutions of line-averaged electron density and electron temperature at the plasma center, and the power of the NBIs and ECRH for shot#141170. The time evolution of the total neutron emission rate was measured by NFM and the Sci-Fi detector as shown in Fig. 5.14 (a) and (b). The time evolution of NIFS Sci-Fi detector measurements with the threshold of 50 mV is almost the same with that time evolution of NFM measurements. When the thresholds increase, this part is significantly reduced. The two Sci-Fi detectors have shown the same time evolution of 14 MeV neutrons with in the case of high threshold levels and the same influence by 2.45 MeV neutrons and gamma-rays in the case of the low threshold levels in this shot. [66]

The pulse height spectra (PHS) of the two Sci-Fi detectors have been obtained to choose suitable threshold for discrimination in order to reject lower-energy neutrons and gamma-rays. Those PHSs have the same characteristic, i.e. two decay components, in a high-neutron-yield shot, as shown in Fig. 5.15. In shot no. 141170, the neutron emission rate reaches 1.15×10^{15} n/s, where the line-averaged electron density is 1.5×10^{19} m^{-3}, and the central electron temperature is about 3 keV. The first decay of both spectra in the low pulse height region corresponds to the detector signal induced by 2.45 MeV neutrons and gamma-rays. The second decay in the higher pulse height region corresponds to the signal induced by 14 MeV neutrons. [66]

Chapter 6:

Evaluation of response for Sci-Fi detector[3]

6.1. Objective

In the LHD deuterium plasma campaign, the scintillating-fiber (Sci-Fi) detectors have been successfully used to measure secondary 14 MeV neutrons for the triton burnup study by using a fast digitizer to record the pulse shape. The time evolution of the counting rate and the pulse height spectrum (PHS) for the Sci-Fi detector were evaluated by the off-line data analysis of the recorded pulse shapes. The PHS of the Sci-Fi detector is used to determine the appropriate threshold for the time evolution measurement of 14 MeV neutrons. The PHS of the Sci-Fi detector have two components with different decay slope in the LHD experiment. To study the PHS property of the Sci-Fi detector, the PHS for different-energy neutrons have been measured by using the accelerator-based neutron source with D-D and D-Li reactions in the fast neutron laboratory (FNL) of Tohoku University in August, 2017. Previously, the 14 MeV neutron response of the Sci-Fi detector was measured by using a D-T neutron generator in the Fusion Neutronics Facility (FNS) at JAERI Tokai 1996. [92] Meanwhile, the calculations have been performed to evaluate response function of the Sci-Fi detector by PHITS code.

[3] This chapter is written by:
N. Pu, *et al*., "*Evaluation of scintillating-fiber detector response for 14 MeV neutron measurement*" *JINST,* **14** P10015 (2019).
N. Pu, *et al*., "*Evaluation for gamma-ray rejection ability affecting neutron discrimination property in scintillating-fiber type of fast neutron detector*" Nucl. Instrum. Meth. Phys. Res., A **969** 164000 (2020).

6.2. Principle of Sci-Fi detector

6.2.1. Edge effect

An incident fast-neutron in a plastic scintillator produces a proton recoiled in the plastic scintillator, which is the so-called recoil proton. Energy of recoil proton in the center-of-mass (*COM*) system $E_{n,com}$ is represented by

$$E_{p,com} = \frac{1-\cos\Theta}{2} \tag{6.1}$$

where Θ is the scattering angle against the neutron incident direction in the COM system. The recoil proton energy in the laboratory (LAB) system E_p is represented by

$$E_p = E_n \cos^2\theta \tag{6.2}$$

where, θ is the scattering angle against the neutron incident direction in the LAB system. In the COM system, the scattering provability to the Θ direction with a width $d\Theta$ is

$$P(\Theta)d\Theta = P(E_p)dE_p \tag{6.3}$$

where, $P(E_p)\,dE_p$ is the production provability of the recoil proton with the energy of E_p with a width dE_p. Therefore,

$$P(E_p) = 2\pi \sin\Theta \frac{\sigma(\Theta)}{\sigma_s}\frac{d\Theta}{d(E_p)} \tag{6.4}$$

where, σ_s is the total scattering cross-section. The n-p scattering is regarded to be isotropic in the COM system, $\sigma(\Theta)$ is represented by $\sigma_s/4\pi$. Finally,

$$P(E_p) = \frac{\sin\Theta}{2}\frac{d\Theta}{dE_p} = \frac{1}{E_p} \tag{6.5}$$

When the scintillator size is small, a large number of high-energy recoil protons from neutrons or high-energy Compton electron from gamma-rays can not deposit the energy fully in the scintillator and escape from the scintillator as shown in Fig. 3, then pulse heights are small. This is the so called edge effect of scintillators. In other words, only fast neutrons on a same axis as the fiber (an incident angle of the 0 degree against the fiber length direction) can produce recoil protons with the full energy deposition (trajectory). Therefore, the directivity of smaller diameter scintillators (scintillating-fibers) will be better than that of larger diameter scintillators.

(a)

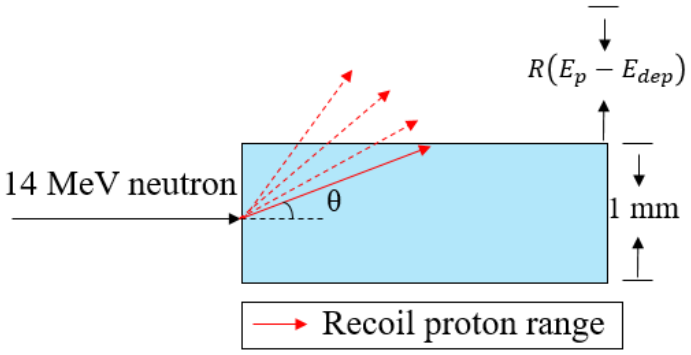

(b)

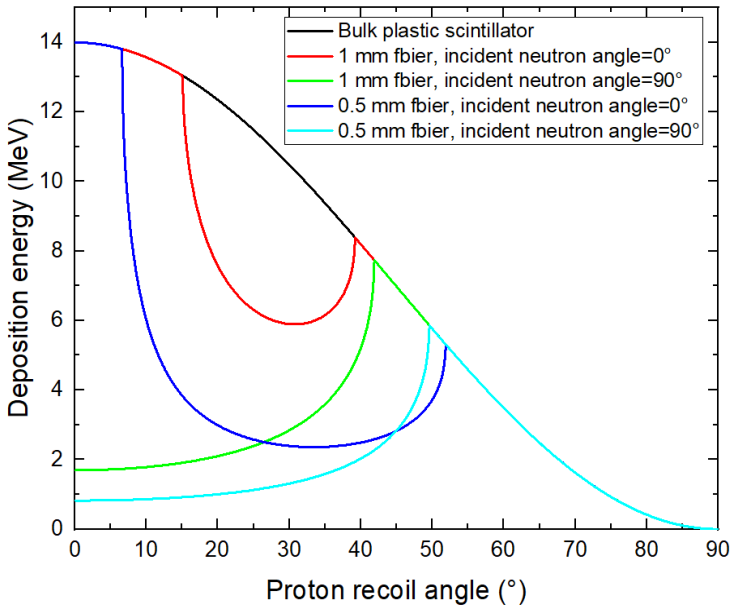

Fig. 6.1(a) Schematic diagram of recoil protons in and out a fiber of 1 mm in diameter, and (b) comparison of deposition energy of recoil proton in a bulk plastic scintillator and

in the 1 mm Sci-Fi detector for 14 MeV neutron. Note that, the incident 14 MeV neutron is assumed to enter the fiber center.

Range of a proton with E_p in MeV in a bulk plastic scintillator is approximately represented by $E_p^2/89.1$ (mm). Therefore, the relationship between the range R and the scattering angle θ of a recoil proton in a plastic scintillator can be obtained:

$$R(\theta) = \frac{{E_p}^2}{89.1} \tag{6.6}$$

For the neutron incident at the angle of θ in the center of fiber, s shown in Fig. 6.1(a), the maximum deposition distance of the recoil proton is:

$$R_f(\theta) = \frac{r}{\sin\theta} \tag{6.7}$$

where, r is the radius of fiber. When $R_f(\theta) < R(\theta)$, $R_f(\theta) = R(E_p) - R(E_p - E_{dep})$, in the case of neutron normally incident to the fiber center, the recoil protons will be likely to escape the scintillator as shown in Fig. 6.1(a). Therefore, the energy deposited by the recoil proton in the scintillator is:

$$E_{dep} = E_p - \sqrt{{E_p}^2 - \frac{89.1}{\sin\theta}} \tag{6.8}$$

Fig. 6.1(b) shows the comparison of the deposition energy of the recoil proton in a bulk plastic scintillator, in 1 mm diameter Sci-Fi detector, and in 0.5 mm diameter Sci-Fi detector for a 14 MeV neutron. Ranges of 14 MeV protons are approximately 2.2 mm in a bulk plastic scintillator. Protons of recoil angles within 15 degrees for 1 mm Sci-Fi detector and 7 degrees for 0.5 mm Sci-Fi detector deposits full energy in the scintillating fiber where neutron incident angle is 0 degree against the fiber axis. This means that the directivity of 0.5 mm Sci-Fi detector is better than that of 1 mm Sci-Fi detector. In other words, the edge effect of 0.5 mm Sci-Fi detector is larger than that of 1 mm Sci-Fi detector.

Protons of the recoil angle of 15 - 40 degrees for 1 mm Sci-Fi detector and 7 - 52 degrees for 0.5 mm Sci-Fi detector, respectively, are not able to fully deposit energy and go out of the fiber. Recoil protons with an angle larger than 40 degrees for 1 mm Sci-Fi detector and 52 degrees for 0.5 mm Sci-Fi detector can deposit energy completely in the fiber due to their low energy.

6.2.2. Gamma-ray rejection and neutron discrimination

Sci-Fi relies on scintillation from a small core of scintillating plastic, inside of a fiber-optic. Therefore, the Sci-Fi has almost the same optical and scintillation characteristics as a bulk plastic scintillator. Because the proton recoil event is a uniform distribution in an organic scintillator, the detection efficiency is proportional to the length of the scintillator for on fiber-axis neutron source. Therefore, the equation of the detection efficiency normalized by the solid angle of the scintillator for an organic scintillator is simply reviewed as

$$\varepsilon = nh\sigma\left(1 - \frac{T}{E_n}\right) \tag{6.9}$$

where n is the number of hydrogen atoms per unit volume, h is the path-length through the scintillator detector for incident neutrons (max h is the thickness of the scintillator for an incident angle of 0 degree), σ is the cross-section of the n-p elastic scattering, T is the discrimination threshold, and E is the neutron energy. When a scintillator is chosen, n is fixed. Detection efficiency is simply approximate to be a function of h and T. Therefore, the detection efficiencies of the plastic scintillator and the scintillating-fiber with the same cross-section area and the same length for neutrons are basically the same in the case of the sufficiently lower threshold T.

Gamma-rays produce electrons in an organic scintillator via Compton scattering mainly. Those electrons deposit energy in the plastic scintillator. The effective trajectory length of an electron is much larger than the range of a proton with the same energy. In other words, the proton energy must be larger than the electron energy, when the deposited energies of a proton and an electron in a scintillator are the same. Furthermore, trajectories of electron in a plastic scintillator are not straight lines but are very complicated due the large angle scattering with electron in the plastic scintillator. In the case of the scintillating fibers embedded in an Al matrix, electrons generated by gamma-

rays will easily escape from fibers and will be absorbed by the Al matrix. Therefore, it is expected that the Sci-Fi detector with an Al matrix has lower gamma-ray detection efficiency than the bulk plastic scintillator detector.

On one hand, gamma-ray rejection abilities are defined as the different the gamma-ray detection efficiency of scintillation detectors in the same (or normalized) neutron detection efficiencies. For Sci-Fi and a plastic scintillator, they have the same sensitive length of scintillator, the same scintillator material, and the same threshold level with the same PMT gain, but different diameters of scintillator or with/without stopping material such as Al matrix, under an irradiation of directional source against the direction of scintillator length. Therefore, the gamma-ray rejection (*GR*) factors are defined as the ratio of the counting efficiency normalized by neutron flux ϕ_n for the two different diameter scintillators which have the same neutron detection efficiencies and different gamma-ray detection efficiencies:

$$GR = \frac{\varepsilon_{small}}{\varepsilon_{ref.}} = \frac{\varepsilon_n^{small} + C_{small}\varepsilon_\gamma^{small}}{\varepsilon_n^{ref} + C_{ref}\varepsilon_\gamma^{ref.}}. \quad (6.10)$$

Here, a plastic scintillator has been used as a standard reference-scintillator to compare the property with a small diameter scintillator such as a Sci-Fi. Therefore, ε_{ref} and ε_{small} are the counting efficiency of a reference scintillator and a small diameter scintillator. ε_n^{ref} is the neutron detection efficiency of a reference scintillator which is the same with the neutron detection efficiency of a small diameter scintillator ε_n^{small}. Gamma-ray detection efficiencies of a reference scintillator and a small diameter scintillator are ε_γ^{ref} and $\varepsilon_\gamma^{small}$. C_{ref} and C_{small} are ratios of gamma-ray flux to neutron flux for a reference scintillator and a small diameter scintillator, which are $\phi_\gamma^{ref} = C_{ref}\phi_n$ and $\phi_\gamma^{samll} = C_{small}\phi_n$ and depend on the source property. For the detectors in the same gamma-rays and neutrons mix field ($C_{ref} = C_{small}$), this means that $\phi_\gamma^{ref} = \phi_\gamma^{samll}$. When neutron detection efficiencies are the same ($\varepsilon_n^{ref} = \varepsilon_n^{samll}$), ratios of counting efficiency normalized by neutron flux for a reference scintillator and a small diameter scintillator will only indicate the difference of gamma-ray detection efficiency, which is the so called gamma-ray rejection factor. $C_{ref} = C_{small} \gg 1$ means

that gamma-ray flux is larger than neutron flux, $GR \approx \frac{\varepsilon_\gamma^{small}}{\varepsilon_\gamma^{ref}}$ will directly show the gamma-ray rejection ability of small diameter scintillator compared with a plastic scintillator. When $\varepsilon_n^{ref} = \varepsilon_n^{samll} \leq C_{ref} = C_{small} \leq 1$, GR still shows the gamma-ray rejection ability of a small diameter scintillator compared with a plastic scintillator with a fix coefficient of $\frac{C_{ref}}{\varepsilon_n^{ref}} = \frac{C_{small}}{\varepsilon_n^{samll}}$. The small *GR* factor means a good gamma-ray rejection ability. When $C_{ref} = C_{small} \ll \varepsilon_n^{ref} = \varepsilon_n^{samll}$, this is not easy to discuss gamma-ray rejection ability with a low gamma-ray flux and high neutron flux. This means that gamma-ray rejection effect is not clear in this kind of neutrons and gamma-rays mix fields.

On the other hand, the neutron discrimination (*ND*) factor is defined with comparing counting efficiencies normalized by neutron flux ϕ_n of a scintillator in mix fields of high-energy (E_h) neutrons with gamma-rays and low-energy (E_l) neutrons with gamma-rays as follows:

$$ND = \frac{\varepsilon_h}{\varepsilon_l} = \frac{\varepsilon_n^h + C_h\varepsilon_\gamma^h}{\varepsilon_n^l + C_l\varepsilon_\gamma^l} \tag{6.11}$$

where ε_h is the counting efficiency for high-energy neutrons with gamma-rays, ε_l is the counting efficiency for low-energy neutrons with gamma-rays, and ε_n^h, ε_n^l, ε_γ^h, and ε_γ^l are detection efficiencies of high-energy neutrons, low-energy neutrons, and gamma-rays in two different energy neutron mix fields, respectively. C_h and C_l are ratios of gamma-ray flux to neutron flux, which are $\phi_\gamma^h = C_h\phi_n$ and $\phi_\gamma^l = C_l\phi_n$. When $C_h\varepsilon_\gamma^h \gg \varepsilon_n^h$ and $C_l\varepsilon_\gamma^l \gg \varepsilon_n^l$, the *ND* factors will depend on the contribution from gamma-rays mainly. When $C_h\varepsilon_\gamma^h \sim \varepsilon_n^h$ and $C_l\varepsilon_\gamma^l \sim \varepsilon_n^l$, the *ND* factors will depend on the contribution from both neutrons and gamma-rays. When $C_h\varepsilon_\gamma^h \ll \varepsilon_n^h$ and $C_l\varepsilon_\gamma^l \ll \varepsilon_n^l$, the *ND* factors will depend on the contribution from neutrons mainly.

6.3. Accelerator experiment

6.3.1. Experimental setup

There is an accelerator-based neutron source facility using a Dynamitron accelerator with the maximum acceleration voltage of 4.5 MV and the maximum beam current of 3 mA in FNL (see Fig.6.1(a)).[93] The accelerator experiment has been performed for the Sci-Fi detectors by different energy neutrons in the FNL. The experiment setup and the Sci-Fi detector arrangement are shown in Fig. 6.2(b) and (c). The detectors, a power supply, a data acquisition system (DAQ), and a PC for the data record were located in the FNL experiment hall, where the data can be read in the control room by a network. A ^{3}He proportional counter is located on the 15° against with the beam direction of accelerator to monitor the neutron flux.

The D-D reaction was used to generate 2.45 MeV neutrons and higher-energy neutrons on 10° and 110°. Moreover, the neutrons generated by ^{7}Li(d, n)^{8}Be reaction was a happenchance coursed by Li target misused for D target, where the neutron response has been found similar with 14 MeV neutron response in LHD experiment.The beam energy is 3 MeV. The D target is a deuterium absorbed by 0.1 mm thick titanium disk. Neutron energy on 110° against the D^{+} beam direction is around 2.45 MeV. On the other hand, the neutron energy on 10° around 6.2 MeV with a lower-energy tail due to the beam energy slowing down in a D_2Ti solid target for D-D reaction. The distance of from target to detectors on 10° and 110° were 50 cm and 13 cm, respectively.

Four different-head detectors were located at 110° and 10° against D^{+} beam direction to investigate each property of gamma-ray rejection and neutron discrimination for 2.45 MeV neutron and higher-energy neutrons with both induced gamma-rays and target photons, respectively. Four different-head detectors are fibers of 0.5 mm in diameter with an Al matrix (0.5 mm Sci-Fi), fibers of 1 mm in diameter with an Al matrix (1 mm Sci-Fi), fibers of 1 mm in diameter without an Al matrix (1 mm Sci-Fi w/o Al), and a bulk plastic scintillator (PS) of 0.5×1.5×10 cm^{3}. Here, all fiber lengths are 10 cm. They used the same PMT with the same gain (on the HV of -1800 V) and have the same sensitive length of 10 cm, which means that four different-head detectors have the same detection efficiency normalized by the solid angle of the scintillator for the same energy neutrons.

The fibers with and without an Al matrix are used to investigate Al matrix effect on the gamma-ray rejection and neutron discrimination ability. A plastic scintillator is as a standard detector or an equivalent larger diameter fiber for the reference. Sci-Fi detectors with different diameter fiber are used to investigate fiber diameter effect on the gamma-ray rejection and neutron discrimination ability.

(a)

(b)

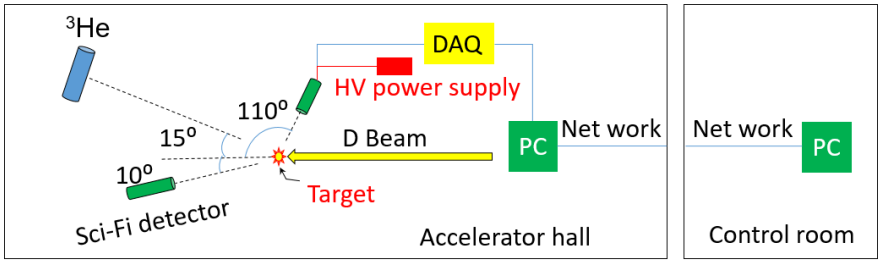

(c)

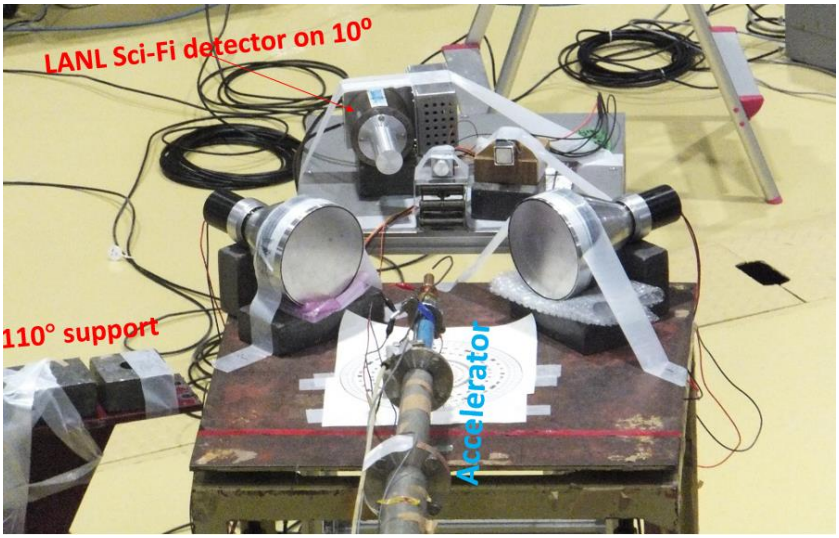

Fig. 6.2 (a) Overall arrangement of accelerator experiment in FNL, and (b) picture of Sci-Fi detector arrangement and vicinity of target of accelerator.

6.3.2. Experimental results

Fig. 6.3 shows the normalized PHS measured by using the D-D neutron source for four different heads detectors which is placed on the 110° and 10° against D^+ beam direction, respectively. The pulse counting rate per second (CPS) of four different heads detector nomalized by a reference detector and areas of scintillator itself. Note that, the detection efficiency of a reference detector is uncertainty, thus, the normalized CPS here means relative detection efficiency of four different heads detectors. The pulse height (PH) of the 0.5 mm Sci-Fi are lower than those of the 1 mm Sci-Fi as shown in Fig. 6.3(a) and (b). The PH of the 1 mm Sci-Fi are lower than those of the 1 mm Sci-Fi w/o Al as shown in Fig. 6.3 (b) and (c). The PH of the 1 mm Sci-Fi w/o Al are lower than those of a plastic scintillator as shown in Fig. 6.3 (c) and (d). The PH of the 0.5 mm Sci-Fi on the 110° is lower than that on the 10° as shown in Fig. 6.3(a). The PH of the 1 mm Sci-Fi on the 110° is lower than that on the 10° as shown in Fig. 6.3 (b). The PHS of the 1 mm Sci-Fi w/o Al on the 110° and 10° are almost the same as shown in Fig. 6.3(c). The PHS of the plastic scintillator on the 110° and 10° are almost the same as shown in Fig. 6.3(d).

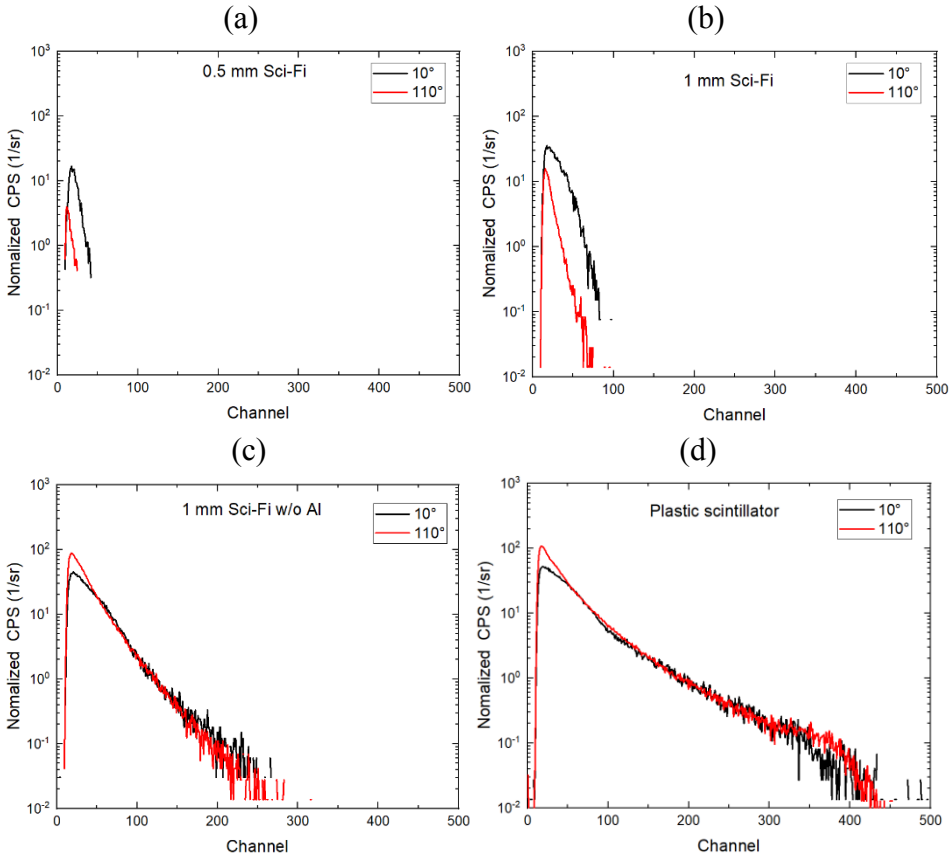

Fig. 6.3 The PHS of four different heads detectors on the HV of -1800 V located on the110° and 10° against D^+ beam direction were measured by using D-D reaction, respectively.

Table 6.1 summarizes the total CPS normalized by the solid angle of the scintillators, the *GR* and *ND* factors, and ratio of *GR* at 110° and 10° for four different-head detectors. Gamma-ray rejection and neutron discrimination ability of the 0.5 mm Sci-Fi is the best. Gamma-ray rejection and neutron discrimination ability of the 1 mm Sci-Fi is the second best. Note that the normalized *ND* factors are equal to the ratio of *GR* at 110° and 10° as mentioned in the equation (11). *ND* factors of the 0.5 mm Sci-Fi is larger than the *ND* factors of the 1 mm Sci-Fi. *ND* factors of the 0.5 mm Sci-Fi and the 1 mm Sci-Fi are larger 6.6 - 10 times than those of 1 mm Sci-Fi w/o Al. *ND* factors of the 1 mm Sci-Fi w/o Al and the PS are almost the same, and the normalized *ND* factors of them are equal to 1, which is caused by the same *GR* of the 1 mm Sci-Fi w/o Al (or the PS) at 110° and 10°.

Table 6.1 The gamma-ray rejection and neutron discrimination factors for four different heads detector

Sci-Fi head status	**0.5 mm Sci-Fi**	**1 mm Sci-Fi**	**1 mm Sci-Fi w/o Al**	**PS**
Normalized CPS (10°)	197	812.2	1655.4	2512.2
***GR* (10°)**	0.0784	0.3233	0.6589	1
Normalized CPS (110°)	26.8	169.6	2324.3	3459.6
***GR* (110°)**	0.0077	0.049	0.6718	1
Ratio of *GR* (10°) to *GR* (110°)	10.12	6.59	0.98	1
***ND* (10°/ 110°)**	7.36	4.79	0.712	0.726

Figure 6.4(a) shows the 14 MeV neutron response for the 1 mm Sci-Fi has been measured by using the FNS D-T neutron generator in JAERI Tokai on 1996. When the incident neutron is on the axis with the fiber, a proton edge from 300 channel to 900 channel caused by the 14 MeV neutron. The pulse height larger than 900 channel might be caused by the high energy gamma-rays of on-axis. However, the FNS accelerator was shut down after the earth quake in 2011, the measurement for 14 MeV neutron response could not be performed again in FNS.

(a)

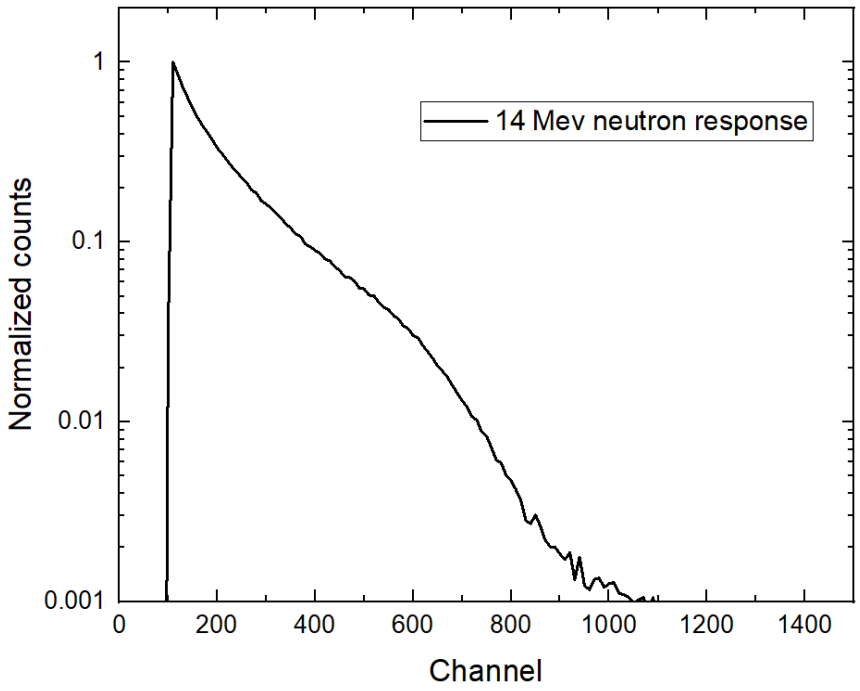

(b)

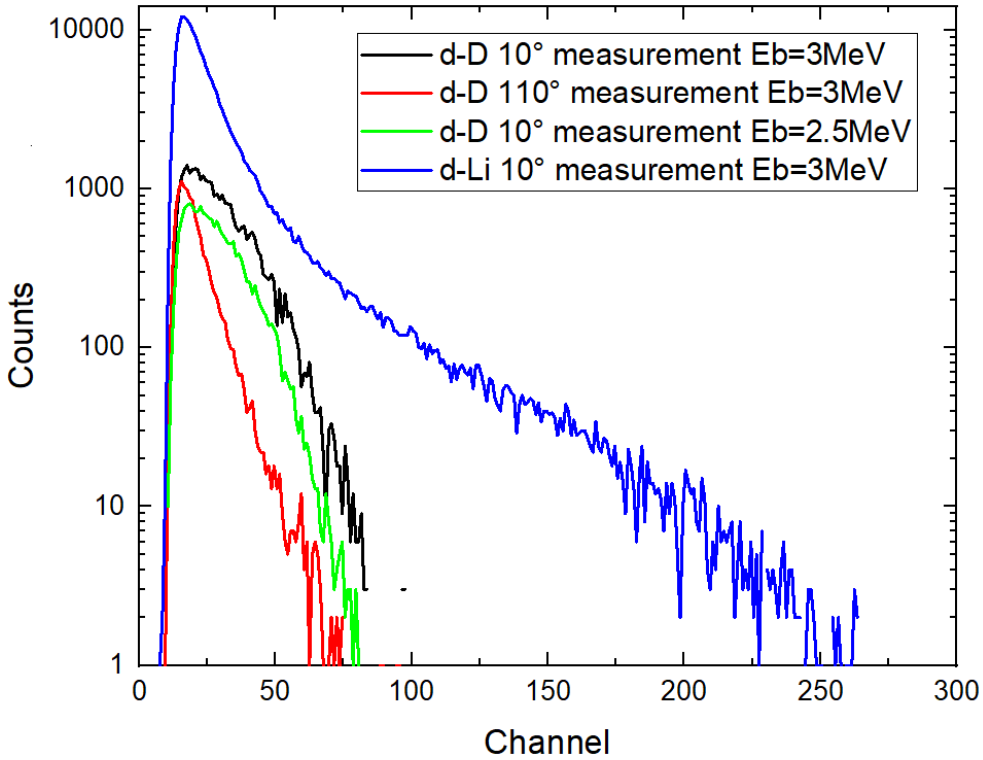

Fig. 6.4 (a) The 14 MeV neutron response for the 1 mm Sci-Fi measured by using the FNS DT neutron generator with the incident neutron angle of 0 degree, and (b) the PHS of the 1 mm Sci-Fi measured by D-Li reaction and D-D reaction in FNL experiment.

In the FNL experiment, tritium target can not be used in order avoid the tritium contamination of the beam line. Instead of the 14 MeV neutron from D-T reactions, 13 MeV neutron generated by D-Li reaction was used to test the response of the 1 mm Sci-Fi. The PHS of the 1 mm Sci-Fi detector were measured with neutrons in different energies and gamma-rays as shown in Fig. 6.4(b). The PHS of the 1 mm Sci-Fi measured by D-Li reaction shows a unconspicuous recoil proton edge generated by D-Li neutron. The pulse height (PH) of the 1 mm Sci-Fi from D-Li neutrons is obviously larger than that from D-D neutrons, and close to that of the 1 mm Sci-Fi w/o Al in Fig. 6.3(c), but different in the recoil proton edge, where there is no the recoil proton edge observed in the high PH part of the 1 mm Sci-Fi w/o Al, but in low PH part of the 1 mm Sci-Fi w/o Al by D-D reaction on 10° as shown in Fig. 6.3(c). The much larger pulse-height response has been found by neutrons generated by D-Li reaction at 10°, which is the same as the second decay slope in the LHD experiment.

6.4. Calculation of D-D neutron response for four different-head detectors

6.4.1. Calculation for neutron spectra of D-D reaction

The neutrons generated by D-D reaction in FNL have been calculated by PHITS code. Figure 6.5(a) shows the picture of the D-D target used at the FNL accelerator. The target of accelerator is modeled as real structure as shown in Fig. 6.5(b). D_2Ti solid target is modeled as real density of 4.581 g/cm^3 by using the mass of Ti and adsorbed D in thickness of 0.1 mm to calculate 3 MeV deuteron slowing-down in the target.

Arrangement of detectors in the FNL accelerator experiment has been shown in Fig. 6.5(c). D^+ beam in 3 MeV energy is incident along with z-axis. Birth neutrons scattering with the air is ignored in this calculation. Detectors at 10° and 110° are modeled as the cell 101 and 111 for the calculation of neutron spectra and target photon spectra. Scattering neutrons from those two large light-guide detectors (cell 119 and 121) were calculated by placing the large light guide detectors at 45°.

Figure 6.6 shows the neutron flux map in the FNL accelerator experiment, where the scattering neutrons from two large light-guide detectors were clearly observed. Therefore, those parts of scattering neutrons have been taken account in calculations. Figure 6.7 shows the deuterium spectrum calculated by deuteron slowing-down in the solid target with input D^+ beam energy of 3 MeV.

(a)

(b)

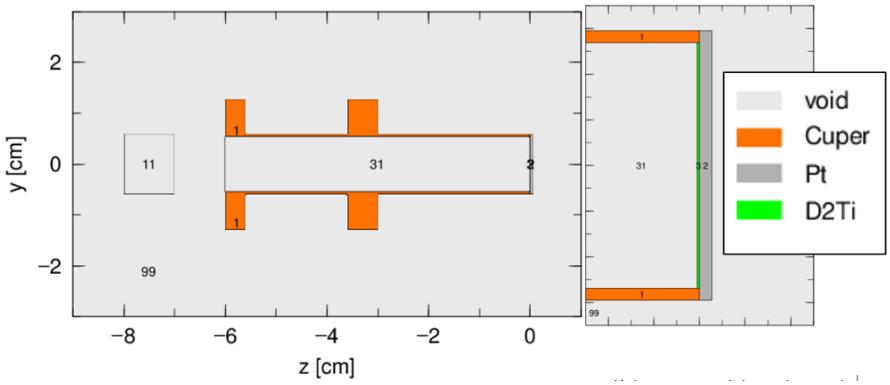

(c)

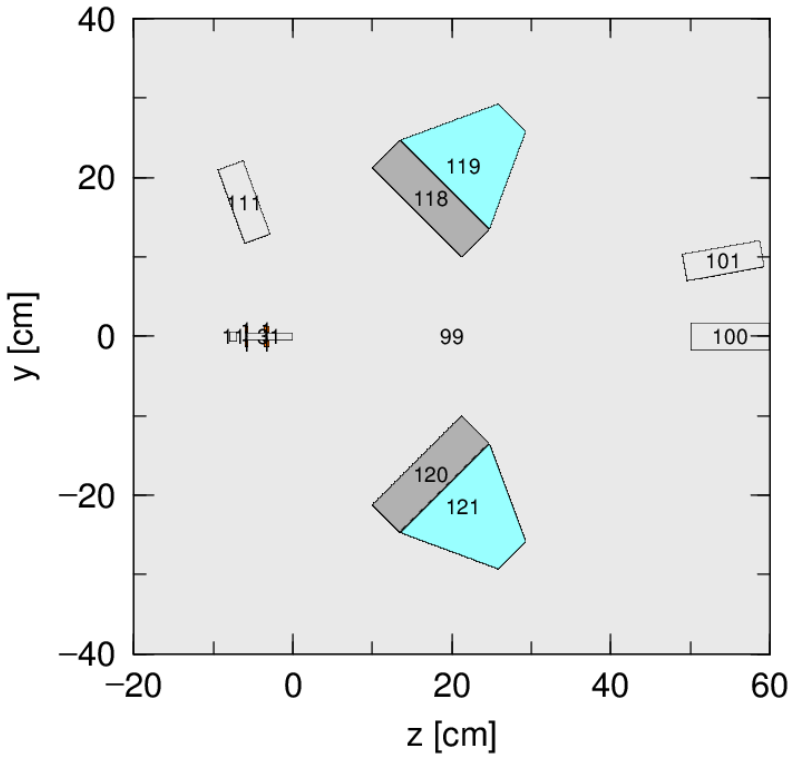

Fig. 6.5 (a) Picture of accelerator target, (b) model of accelerator target, and (c) the arrangement of detectors in the FNL accelerator experiment.

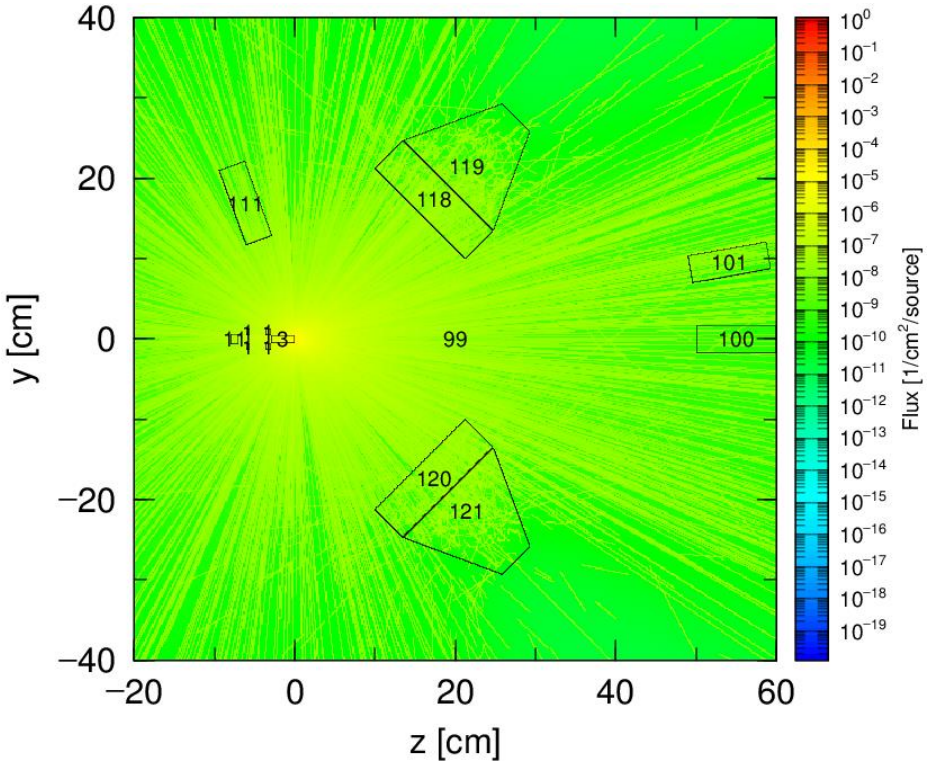

Fig. 6.6 Neutron flux map in the vicinity of FNL accelerator target.

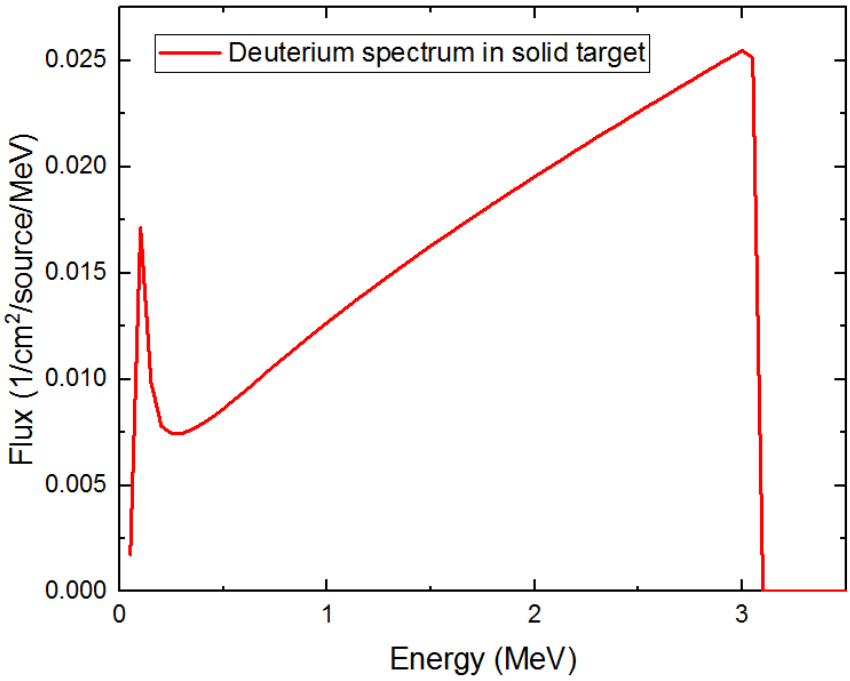

Fig. 6.7 The deuteron spectrum slowing-down in a solid target.

(a)

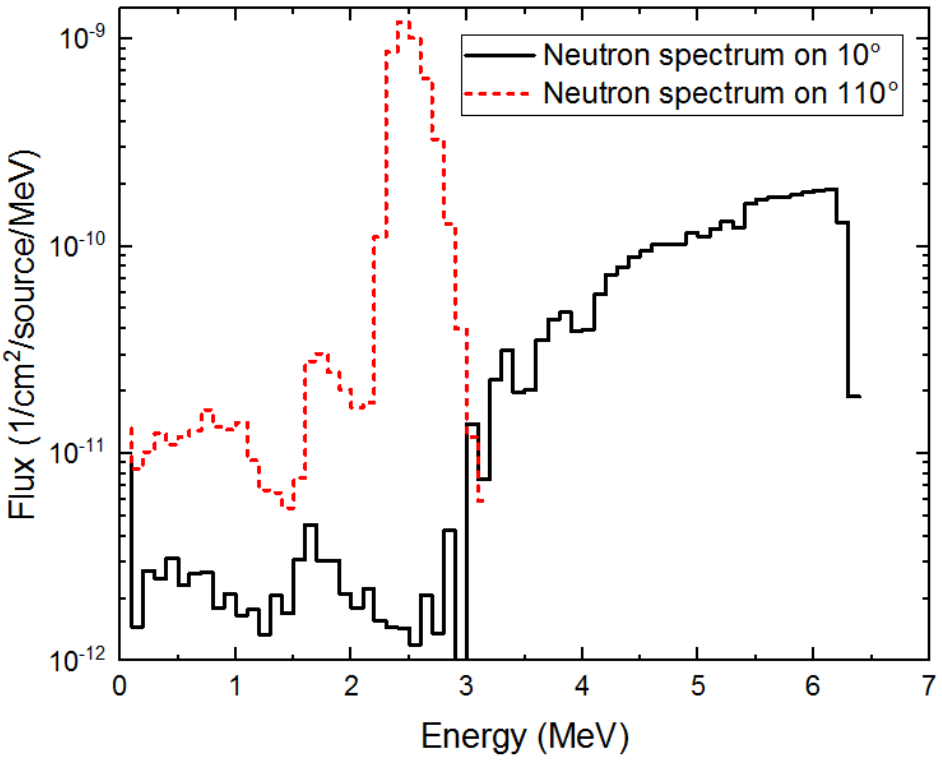

(b)

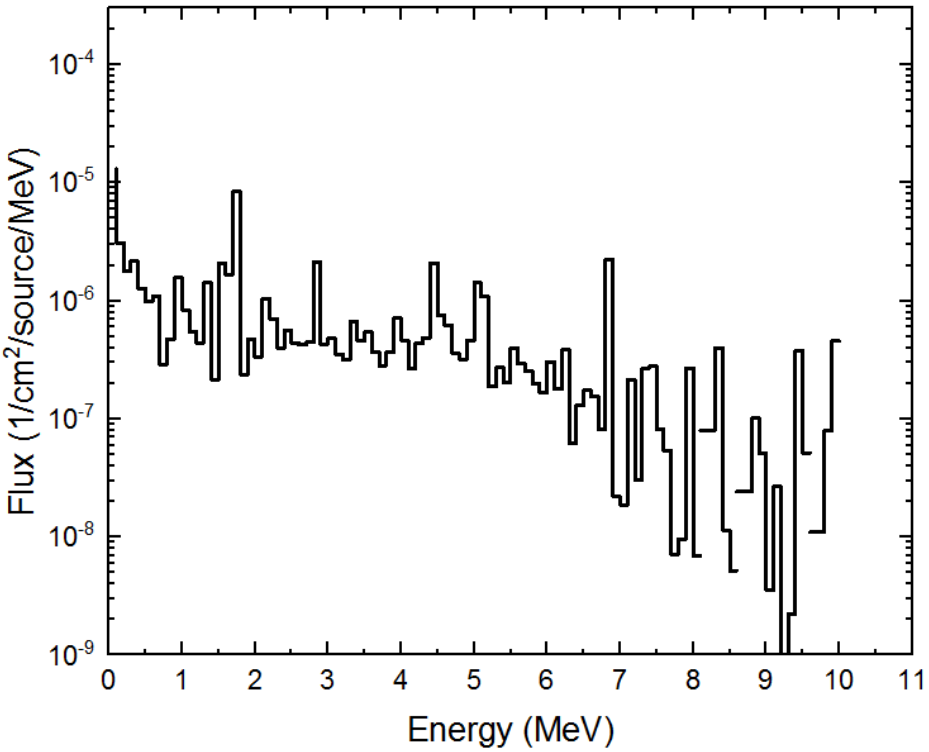

Fig. 6.8 (a) Calculated neutron spectra on 10° and 110°, and (b) the photon spectrum on 10°.

Fig. 6.8(a) shows that the calculated neutron spectra at 10° and 110°. Note that the flux of neutron spectrum at 110° is larger than that at 10°, which is caused by the distance of detector to target at 110° is smaller than that at 10°. Due to the deuteron slowing-down in a solid target, the neutron spectrum at 10° is broadened. Neutron at 110° was also not quasi-mono-energetic, where there is a neutron energy peak around 2.45 MeV. Neutron energy at 10◦ is broadened from 3 MeV to 6.2 MeV by the deuteron slowing-down in a solid target. In addition to this, the target bremsstrahlung and the gamma-ray spectrum is calculated by PHITS as shown in Fig. 6.8(b). Here, the normalized photon spectra are isotropy at 10◦ and 110◦.

6.4.2. Response calculation for D-D reactions

Four different heads in the FNL accelerator experiment are modeled to calculate the responses of four different head detectors by using the PHITS code. The 91 fibers of 1 mm or 0.5 mm in diameter and 10 cm in length are embedded in an Al matrix of 3.5 cm in diameter and 10 cm in length as shown in Fig. 6.8 and 6.9. Fibers of 1 mm in diameter without Al matrix and a plastic scintillator are placed in an Al housing as shown in Fig. 6.11 and 6.12. The density of fibers or plastic scintillator is 1.05 g/cm^3. Also, the atomic composition of the fiber and the plastic scintillator is assumed to be carbon (C) and hydrogen (H) with ratio H/C of 1.

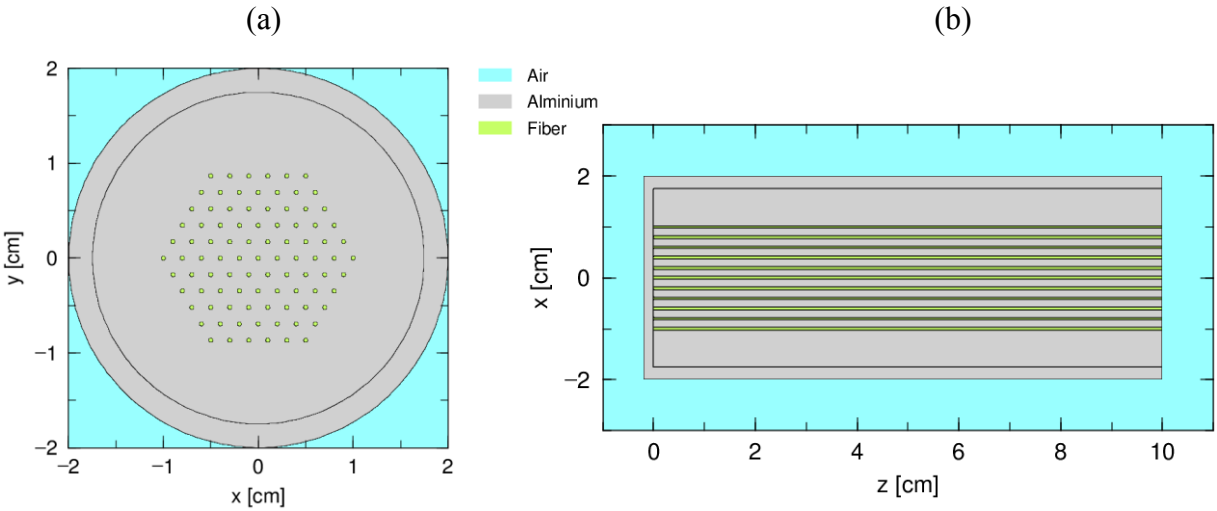

Fig. 6.9 Model for 0.5 mm Sci-Fi on (a) the x-y plane and (b) the x-z plane.

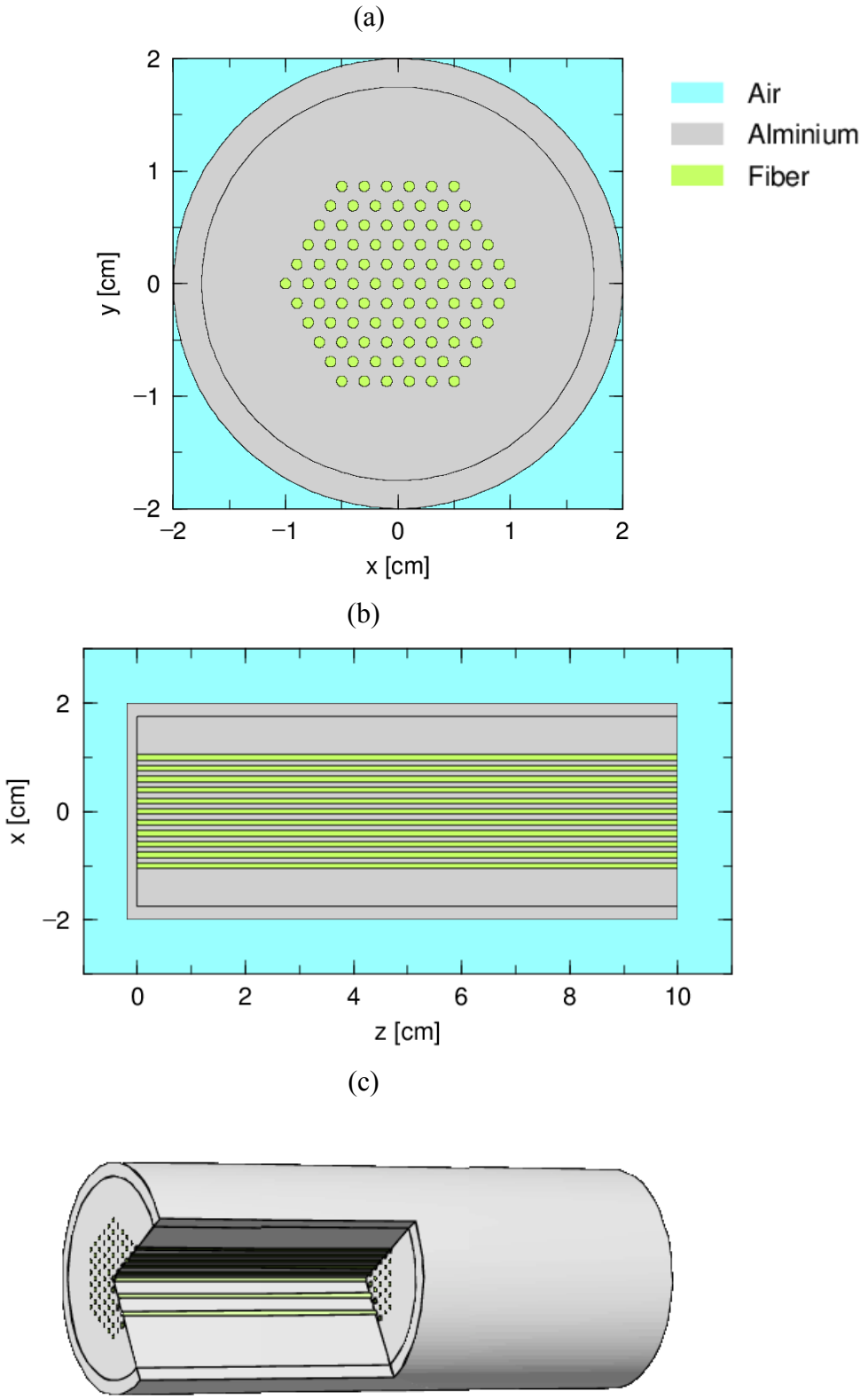

Fig. 6.10 Model for 1 mm Sci-Fi on (a) the x-y plane, (b) the x-z plane, and (c) 3 D angle cutting model.

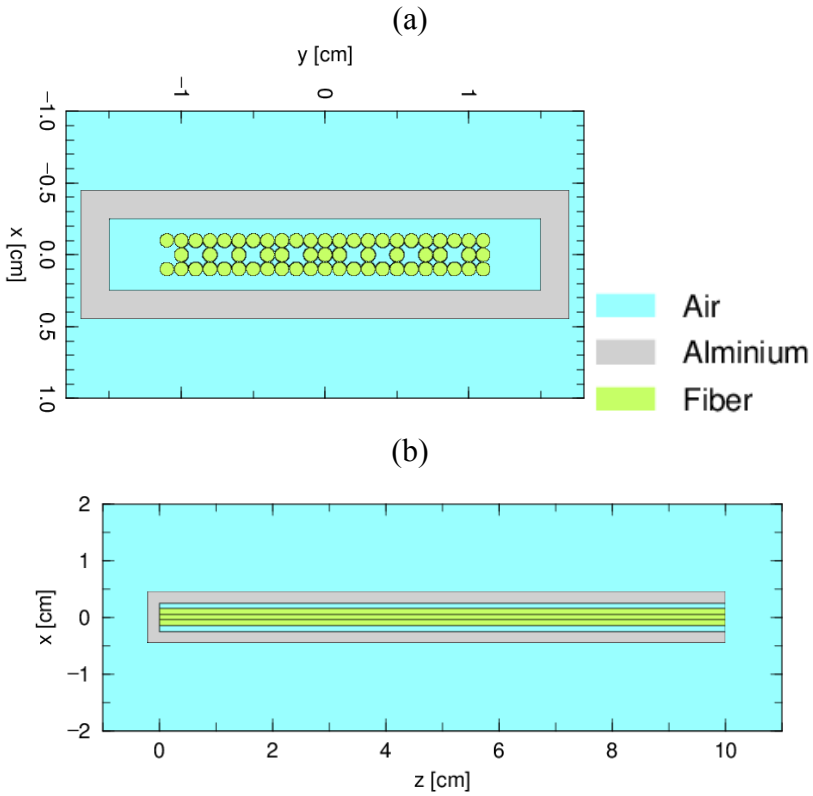

Fig. 6.11 Model for 1 mm Sci-Fi wo Al matrix on (a) the x-y plane, (b) the x-z plane.

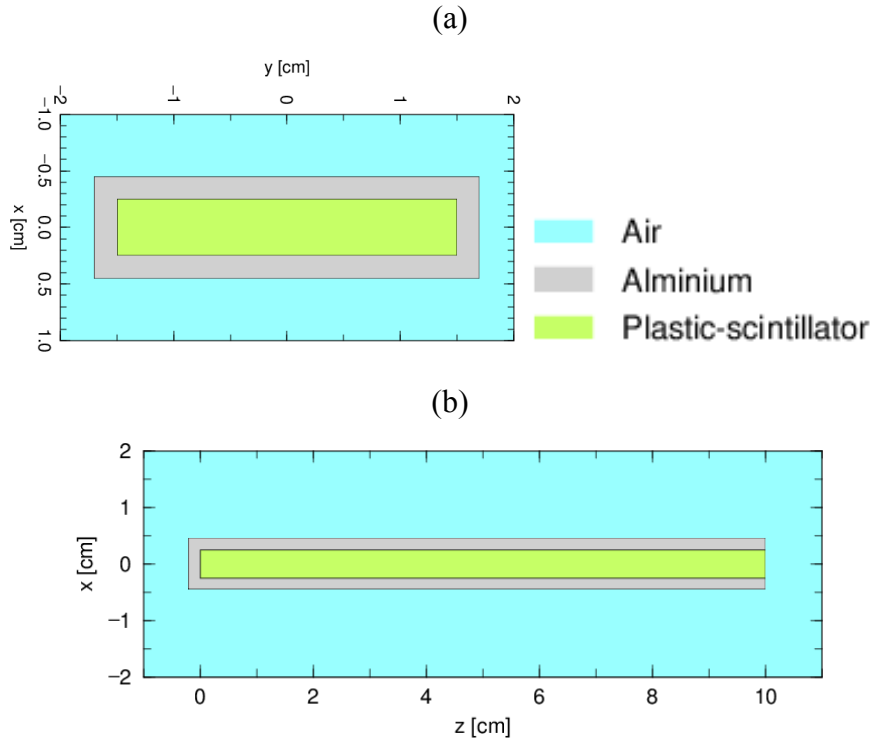

Fig. 6.12 Model for plastic scintillitor on (a) the x-y plane, (b) the x-z plane.

Neutron response of four different-head detectors were calculated by using the neutron spectra in Fig. 6.8(a) for D-D neutron in the FNL accelerator experiment, the neutron source is assumed to be a conical source along the z-axis, where the scattering neutron effect were taken account into neutron spectra. Fig. 6.13 shows the normalized neutron responses of four different head detectors at 10° in the FNL experiment.

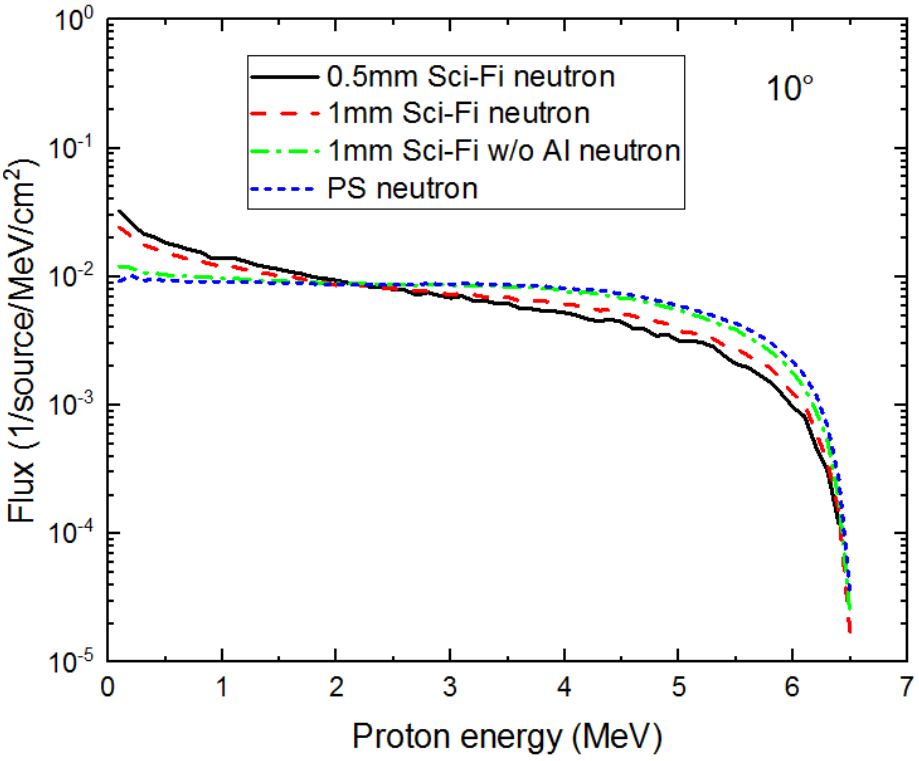

Fig. 6.13 Neutron responses for four different head detectors on 10° in the FNL experiment.

The part of low-energy neutrons below 3 MeV increases in the smaller size scintillator, which is caused by the edge effct of the recoil proton in the detector of smaller size scintillator. Here, the sensitive lengths are the same for four different head detector. This means that detection efficiencies of the same energy neutron with the same threshold are almost the same as calculations. Also, the maximum pulse heights do not change significantly. Small differences in detection efficiencies are only from the edge effect of scintillator/Sci-Fi themselves. To compare the 0.5 mm Sci-Fi with the 1 mm Sci-Fi, the neutron responses are almost the same. To compare the 1 mm Sci-Fi w/o Al with a PS, the neutron responses are almost the same. The recoil protons can move from one fiber

to others to deposit large energy in the 1 mm Sci-Fi w/o Al. To compare the 1 mm Sci-Fi with the 1 mm Sci-Fi w/o Al, the enhanced edge effects by Al matrix are clearly observed in the 1 mm Sci-Fi. Low-energy (below 2 MeV) part increases observably in the Sci-Fi caused by the edge effect of the recoil proton scattering (off-axis) neutrons. The recoil protons can not move from one fiber into others in the 1 mm Sci-Fi. This results in increasing the counts of low pulse height part and decreasing the counts of high pulse height part. Therefore, the Al matrix works for enhancing the directionality of the Sci-Fi for the fast neutron measurement. In other words, the function of the Sci-Fi detector is to reduce the contribution to the signal of the high PH from scattered neutrons which is main off-axis. By this way, the PH of off-axis neutrons can be reduced by using edge effect of the small-diameter Sci-Fi, but maximum PH does not change significantly as shown in Fig. 6.13.

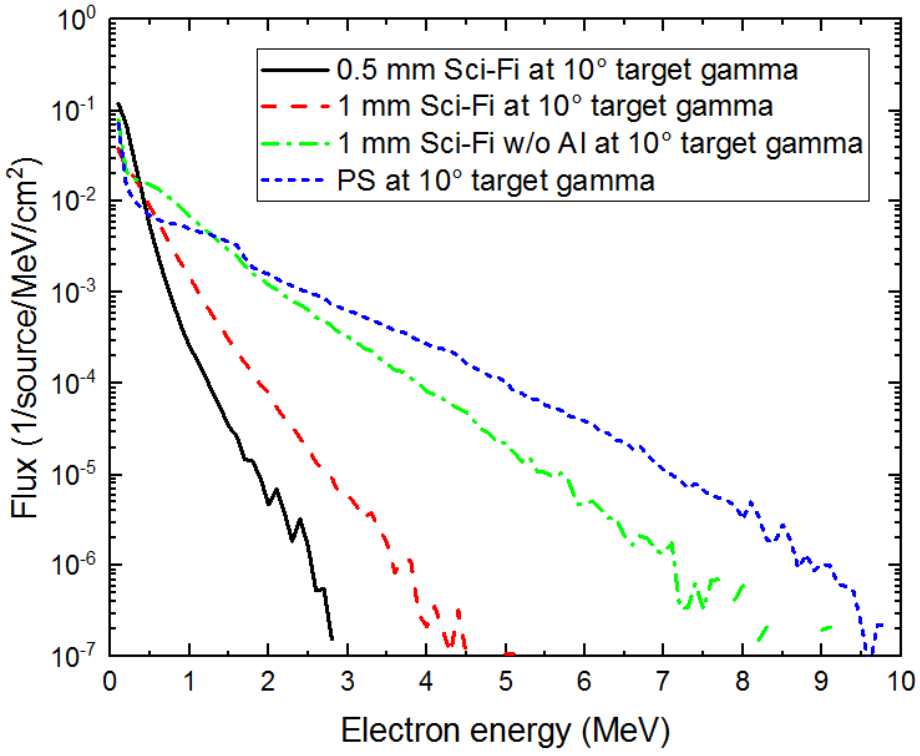

Fig. 6.14 The calculation of photon response for four different heads detector.

Fig. 6.14 the photon responses of four different-head detectors calculated by using photon spectrum in Fig. 6.8(b). From the calculation, the deposition energy of gamma-rays in a plastic scintillitor is largest, the following one is in the 1 mm Sci-Fi w/o Al, and the lowest is in the 0.5 mm Sci-Fi. This tendency of four different heads was consistent

with the measurement in the FNL accelerator experiment as shown in Fig. 6.3. Equivalent electron energy (E_{ee}) for 6.2 MeV neutrons is close to 3 MeVee. [94] Based on almost the same the neutron detection efficiencies and maximum deposition energy of neutrons for four different-head detectors, the difference in PHS is seen mainly in the gamma-ray response.

The deposition energy of gamma-rays in the 0.5 mm Sci-Fi is calculated to be lower than that in the 1 mm Sci-Fi. For the 1 mm Sci-Fi w/o Al and the plastic scintillitor, it is clearly found that the PH of gamma-rays are significantly larger than that of neutrons at 10°. Therefore, the PHS of the 1 mm Sci-Fi w/o Al and the plastic scintillator in Fig. 6.2(c) and (d) are gamma-ray dominant. Deposition energy of gamma-rays in the 1 mm Sci-Fi is significantly lower than that in the 1 mm Sci-Fi w/o Al, which means that the function of the Al matrix for Sci-Fi detector is beneficial to enhance the edge effect of the Sci-Fi for gamma-ray rejection.

6.4.3. Analyses for the experimental results based on the calculations

Due to the difference of the fiber diameter between the 0.5 mm Sci-Fi and the 1 mm Sci-Fi, the edge effect of the 0.5 mm Sci-Fi is more remarkable than that of the 1 mm Sci-Fi, which means that the lost part of protons recoiled by neutrons and the Compton electrons generated by gamma-rays in the 0.5 mm Sci-Fi is larger than that in the 1 mm Sci-Fi as shown in Fig. 6.14. Therefore, the PH and GR factor of the 0.5 mm Sci-Fi are lower than those of the 1 mm Sci-Fi as shown in Fig. 6.3(a), (b), and Table 6.1.

Diameter of the fiber in the 1 mm Sci-Fi is the same with that in the 1 mm Sci-Fi w/o Al, which means that the edge effect for single fiber is the same. Difference in pulse height is from the Al matrix. For the bundle of fibers without an Al matrix, the recoil protons can go into a neighboring fiber. At the same time, the Compton electron from gamma-ray also can go into a neighboring fiber to generate large pulse height in the bundle of fibers during a response time of PMT. Therefore, the measured PH and GR factor of the 1 mm Sci-Fi w/o Al are larger than that of the 1 mm Sci-Fi as shown in Fig. 6.3 (b), (c), and Table 6.1. It is concluded that Al matrix is beneficial to enhance the edge effect on the Sci-Fi for gamma-ray rejection and neutron discrimination.

On the other hand, the PH of the 1 mm Sci-Fi w/o Al is lower than that of the plastic scintillator as shown in Fig. 6.3 (c) and (d), which means that a part of protons and electrons lose from the 1 mm Sci-Fi w/o Al coursed by the edge effect comparing with a bulk plastic scintillator. Therefore, pulse height and *GR* factors of the 1 mm Sci-Fi w/o Al are lower than that of the PS as shown in Fig. 6.3 (c), (d), and Table 6.1.

Because the Sci-Fi with Al matrix has the enhance the edge effect, the PH of gamma-rays will be lower than that of high energy neutrons. This is the reason that the PH of the 0.5 mm Sci-Fi or the 1 mm Sci-Fi on the 110° is lower than that on the 10° as shown in Fig. 6.3 (a) and (b). If the gamma-ray rejection ability is perfect ($\varepsilon_\gamma^{small}$=0), the ratio of the total counts at 10° against that at 110° should be the ratio of neutron detection efficiency. However, gamma-ray response can not be negligible, which means that there is also a little part of gamma-ray response to contribute to the *ND* factors. In this case, the *ND* factors will larger than 1 as measurement in Table 6.1 coursed by $C_h\varepsilon_\gamma^h \sim \varepsilon_n^h$ and $C_l\varepsilon_\gamma^l > \varepsilon_n^l$ or $C_h\varepsilon_\gamma^h < \varepsilon_n^h$ and $C_l\varepsilon_\gamma^l < \varepsilon_n^l$. Here it is considered that gamma-rays are generated at the target mainly and the angular distribution is almost isotropic $C_h\varepsilon_\gamma^h = C_l\varepsilon_\gamma^l$ for the same detector. Therefore, the neutron discrimination ability of the 0.5 mm Sci-Fi is better than that of the 1 mm Sci-Fi. Note that, the detection efficiency for 10° neutrons is larger than that for 110° neutrons ($\varepsilon_n^h > \varepsilon_n^l$), when the threshold in proton energy is larger than 2 MeV as shown in Fig. 6.25(a) of appendix.

For the 1 mm Sci-Fi w/o Al and the plastic scintillator, the PHS and the GR factors of the 1 mm Sci-Fi w/o Al or the plastic scintillator on the 110° and 10° are almost the same as shown in Fig. 6.3 (c) or (d) and Table 6.1. As described in 6.2.1, the detection efficiency normalized by the solid angle of the scintillator for neutron would be same among the 1 mm Sci-Fi w/o Al and the plastic scintillator. Therefore, the total counting efficiency of the 1 mm Sci-Fi w/o Al and the plastic scintillator are contributed by photons mainly, where the photons are mainly from target bremsstrahlung and induced gamma-rays. This means that gamma-ray rejection factors will depend on the contribution from gamma-rays mainly by $C_h\varepsilon_\gamma^h \gg \varepsilon_n^h$ and $C_l\varepsilon_\gamma^l \gg \varepsilon_n^l$. Here, it is considered that gamma-rays are generated at the target mainly and the angular distribution is almost isotropic. The ratio of the total counts at 10° against that at 110° might be close to unity as measurement. There is no significant difference over 100 channel between measured PHSs on the 110° and that on 10° for the 1 mm Sci-Fi w/o Al and the plastic scintillator, respectively. This is the reason that the ND factors of the 1 mm Sci-Fi w/o Al and plastic scintillator are almost the same as shown in Table 6.1. It is concluded that the property of the 1 mm Sci-Fi w/o Al is almost the same as that of a plastic scintillator.

6.5. Comparison of calculation and experiment for the 1 mm Sci-Fi detector

6.5.1. Comparison for accelerator experiment

The neutron response of the Sci-Fi detector for D-Li reaction is analyzed as follows. The calculated neutron and photon spectra was used to calculate response for D-D reaction in the FNL accelerator experiment. The E_{ee} of proton employs that in a plastic scintillator BC-408 in J. Zhang's paper and data sheet of Organic Scintillation Materials from Saint-Gobain Crystals. [94]-[95]

(a)

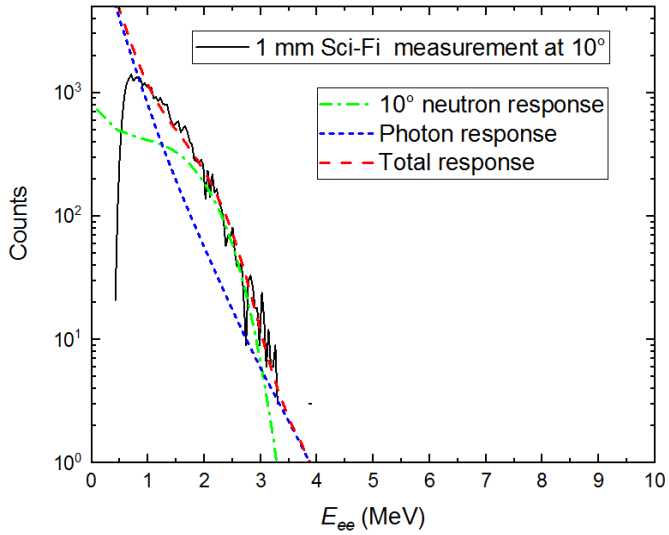

(b)

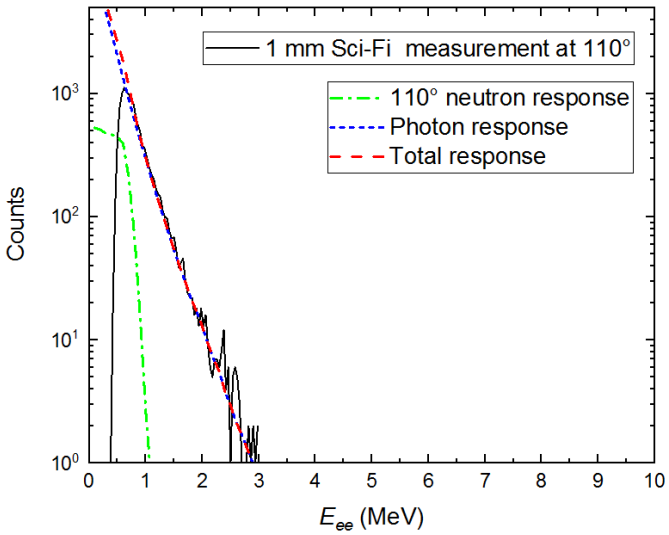

Fig. 6.15 Measured PHS and calculated response of the 1 mm Sci-Fi for D-D reaction at

10° (a) and 110° (b) in the FNL accelerator experiment.

(a)

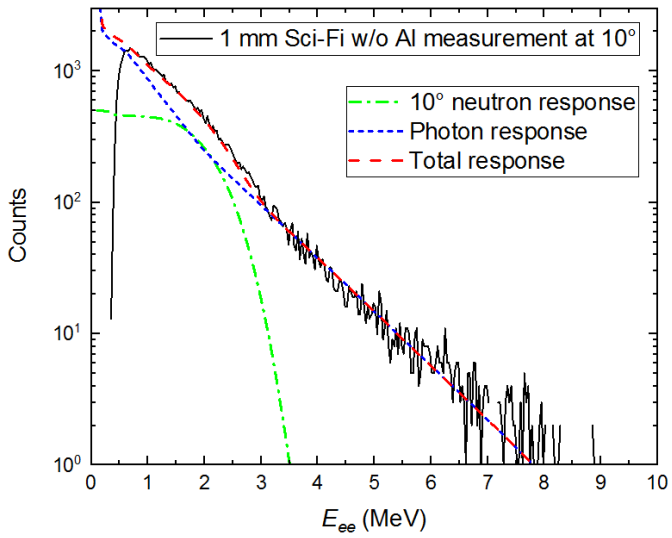

(b)

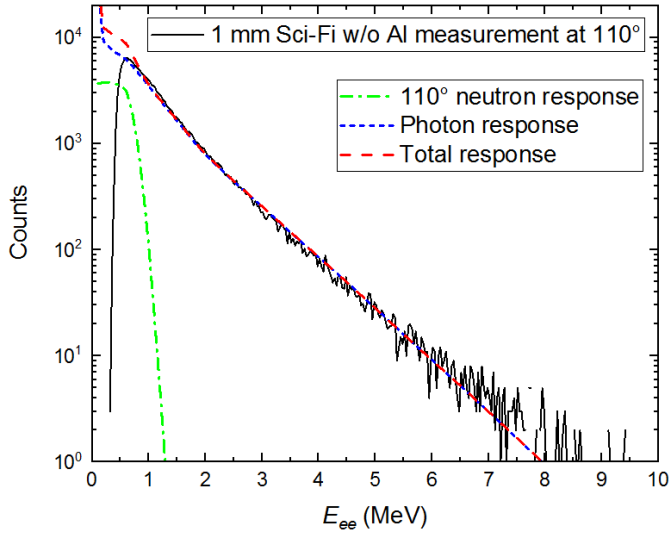

Fig. 6.16 Measured PHS and calculated response of the 1 mm Sci-Fi w/o Al for D-D reaction at 10° (a) and 110° (b) in the FNL accelerator experiment.

The responses of the Sci-Fi detector for D-D reaction on 10° and 110° with an energy resolution of 20% Gaussian broadening agree well with the measurement as shown in Fig. 6.15. Here, the threshold E_{ee} of 0.5 MeVee corresponds to about the proton energy of 2

MeV. For the 110° D-D neutron case, edges induced by recoil proton were confirmed by the PHITS calculation for the response at 10°as shown in Fig. 6.15(a) and 6.16(a). The signal of the Sci-Fi detector was almost induced by gamma-rays because the E_{ee} of 2.45 MeV neutron is lower than the gamma-ray energy as shown in Fig. 6.15(b) and 6.16(b). Gamma-ray response is significantly reduced in the 1 mm Sci-Fi comparing with that in the 1 mm Sci-Fi w/o Al. Neutron responses in both the 1 mm Sci-Fi and the 1 mm Sci-Fi w/o Al are almost the same. Different responses in both the 1 mm Sci-Fi and the 1 mm Sci-Fi w/o Al are from gamma-ray responses. Therefore, the recoil-proton edge in the 1 mm Sci-Fi is clearer than that in the 1 mm Sci-Fi w/o Al caused by the enhanced gamma-ray rejection ability of the 1 mm Sci-Fi with Al matrix. Note that the high-energy responses induced by gamma-rays are almost the same in the 1 mm Sci-Fi w/o Al at 10° and 110°. This is the reason that the normalized PHS are almost the same as shown in Fig. 6.3(c). Therefore, the PHS of Sci-Fi detector on 110° is almost induced by gamma-rays.

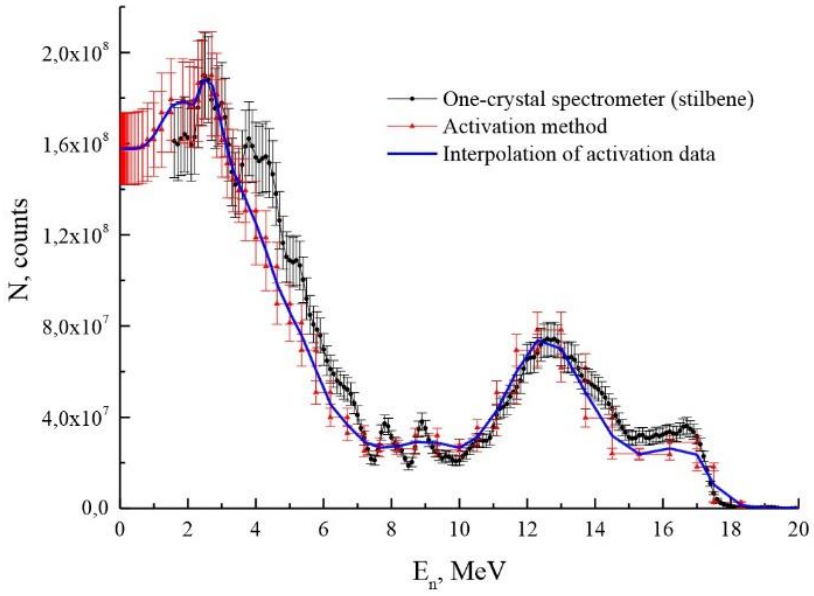

Fig. 6.17 The neutron spectrum of D-Li reaction with D^+ beam energy of 2.9 MeV was measured by an activation method in the K. V. Mitrofanov's paper. [96]

The energy spectrum of neutrons from D-Li reaction with D^+ beam energy of 2.9 MeV was measured by an activation method in the K. V. Mitrofanov's paper as shown in Fig. 6.17. [96] This neutron energy spectrum was used to calculate neutron response for D-Li reaction in the FNL accelerator experiment. The neutron response of the Sci-Fi detector for D-Li reaction has been calculated by measured neutron spectrum with an

energy resolution of 20% Gaussian broadening as shown in Fig. 6.18, where the target hard X-rays and induced gamma-rays were not taken account into this calculation. The neutron response in high-energy parts agree well with a measurement in the FNL accelerator experiment. It is found from the calculation that the inconspicuous recoil proton edge around E_{ee} of 6 MeV corresponds to the response of 13 MeV neutron peak as measurement in the K. V. Mitrofanov's work.

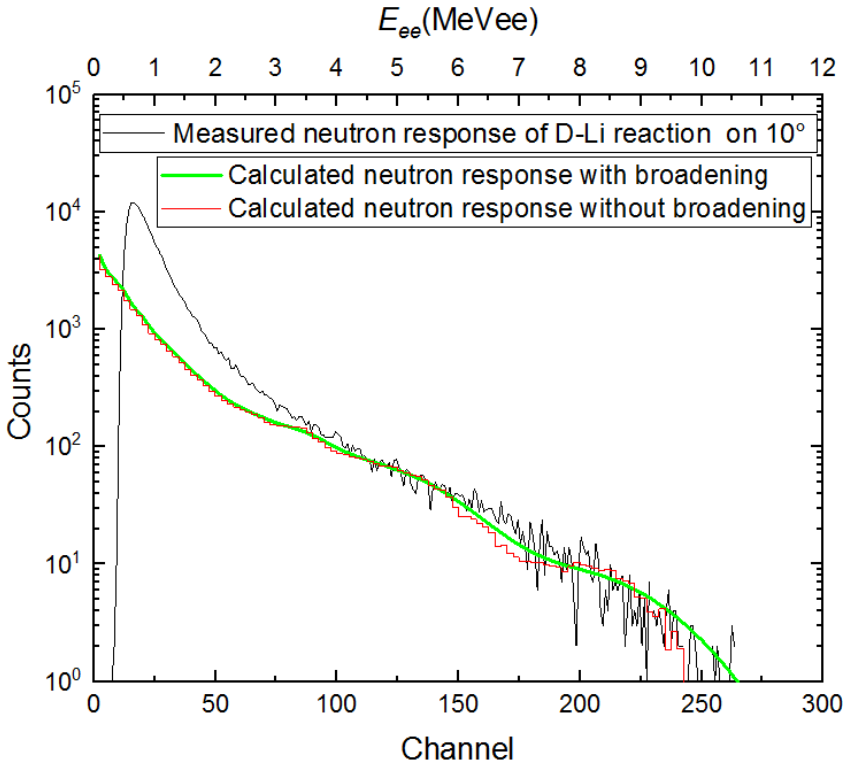

Fig. 6.18 Measured PHS and calculated neutron response for D-Li reaction in the FNL accelerator experiment.

The mono-energy 14 MeV neutrons was used to calculated the response for D-T reaction in the FNS accelerator experiment as shown in Fig. 6.19. The recoil proton edge induced by 14 MeV neutron is observed in both calculation and measurement, where the E_{ee} of the recoil proton edge corresponds to around 6.5 MeV.

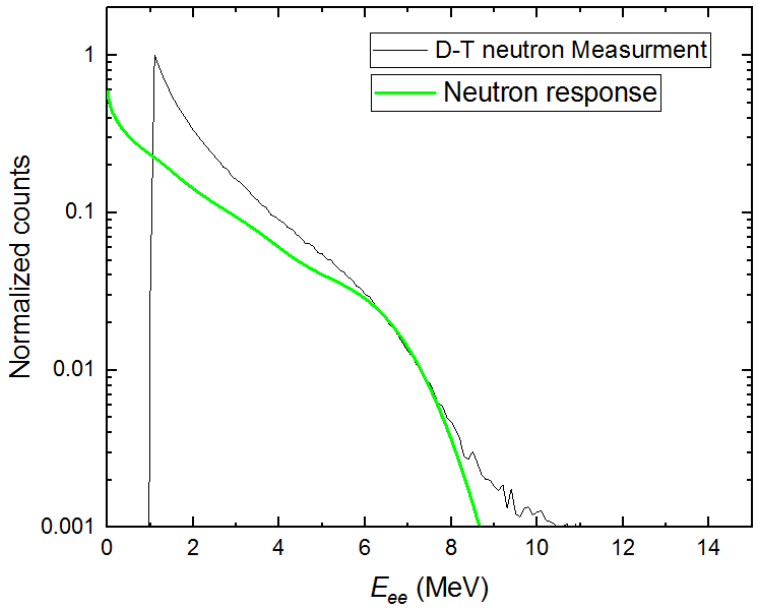

Fig. 6.19 Measured PHS and calculated response for D-T reaction in the FNS accelerator experiment.

6.5.2. Comparison for LHD experiment

The neutron response of the Sci-Fi detector on the LHD deuterium plasma experiment is analyzed. The energy spectrum of neutrons just outside the 8-O horizontal ports of LHD was calculated by MCNP6 assuming the triton burnup ratio of 0.5% as shown in Fig. 6.20. [97] Based on this neutron spectrum, the neutron response and the induced gamma-ray response for the LHD experiment were calculated. Note that the induced gamma-ray response is only from Sci-Fi detector itself in the LHD experiment. The calculated response agrees with the LHD measurement as shown in Fig. 6.21. The pulse-height of 0.7 V equal to E_{ee} of 7 MeVee as shown in the up and down x-axis. Therefore, the pulse height in voltage is calibrated by calculated response to be a conversion coefficient E_{ee}/V of 10, where the high voltage for the Sci-Fi detector on the LHD experiment was -1700 V. This would be consistent with previous measurements in Fig. 5.10.

The recoil proton edge in high pulse height part of spectrum from 0.5 V to 0.67 V is corresponding 14 MeV neutron as shown in Fig. 6.21. The calculated E_{ee} of around 6.5 MeV for this edge is slightly larger than the calculated E_{ee} of around 6 MeV for 13 MeV neutron from D-Li reaction in FNL as shown in Fig. 6.18 and the same with 14 MeV neutron measured in FNS as shown in Fig. 6.19.

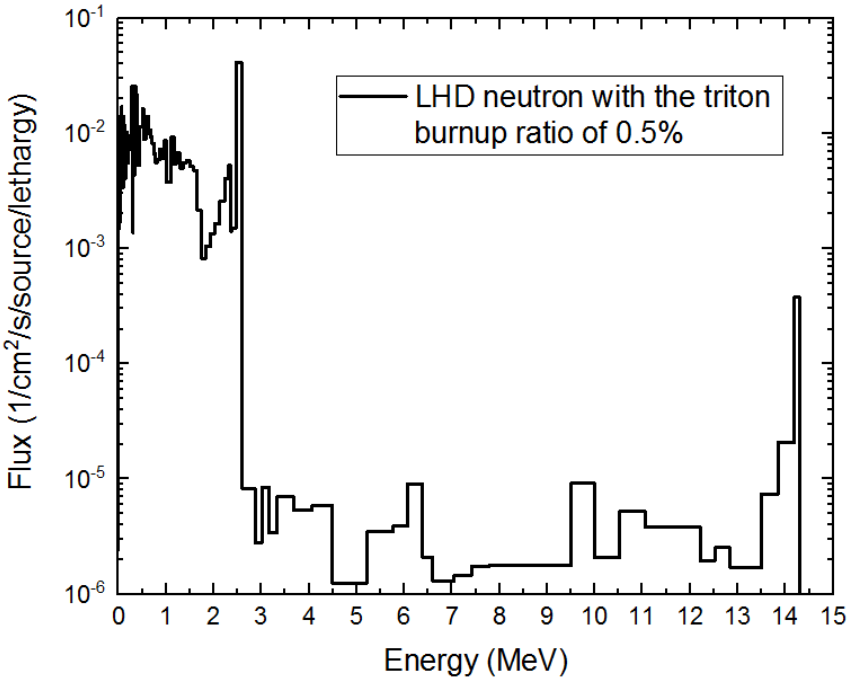

Fig. 6.20 Neutron spectrum near the LHD horizontal port was calculated by MCNP6 assuming the triton burnup ratio of 0.5%.

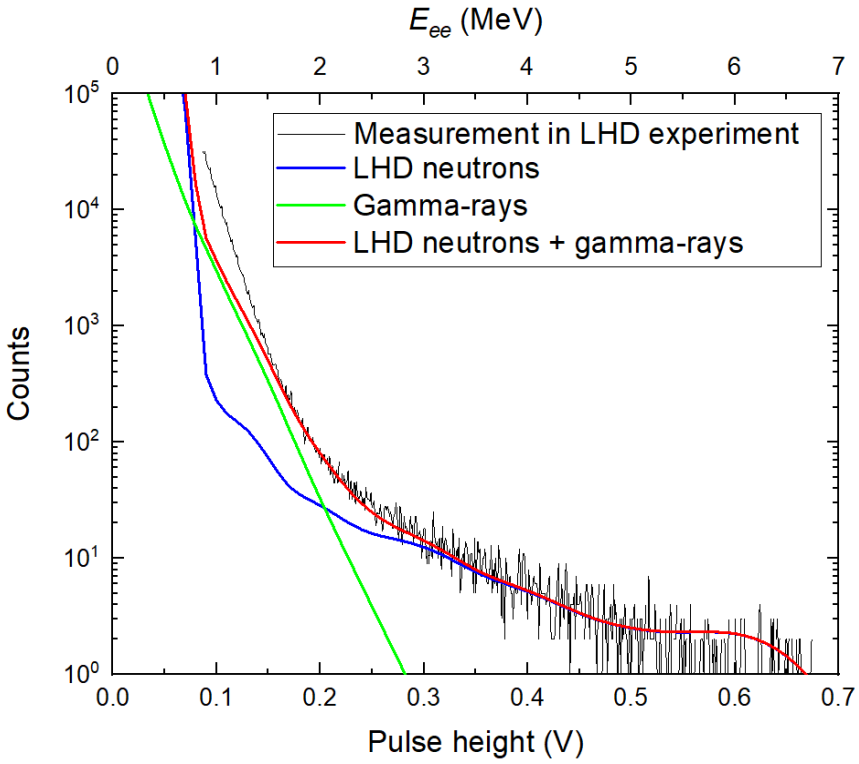

Fig. 6.21 Measured PHS and calculated response in LHD experiment.

The discrepancy in low pulse height might come from that a large number of hard X-rays and gamma-rays in LHD experiment which is not taken into account. The gamma-ray response is calculated to be lower than 3 MeV as shown in Fig. 6.21. The E_{ee} of 3 MeV corresponds to approximately the proton energy of 7 MeV. Therefore, if the threshold of 300 mV (E_{ee} =3 MeV) is applied to discriminate 14 MeV neutron, the 2.45 MeV neutron and gamma-rays can be eliminated in the LHD experiment as shown in Fig. 6.21.

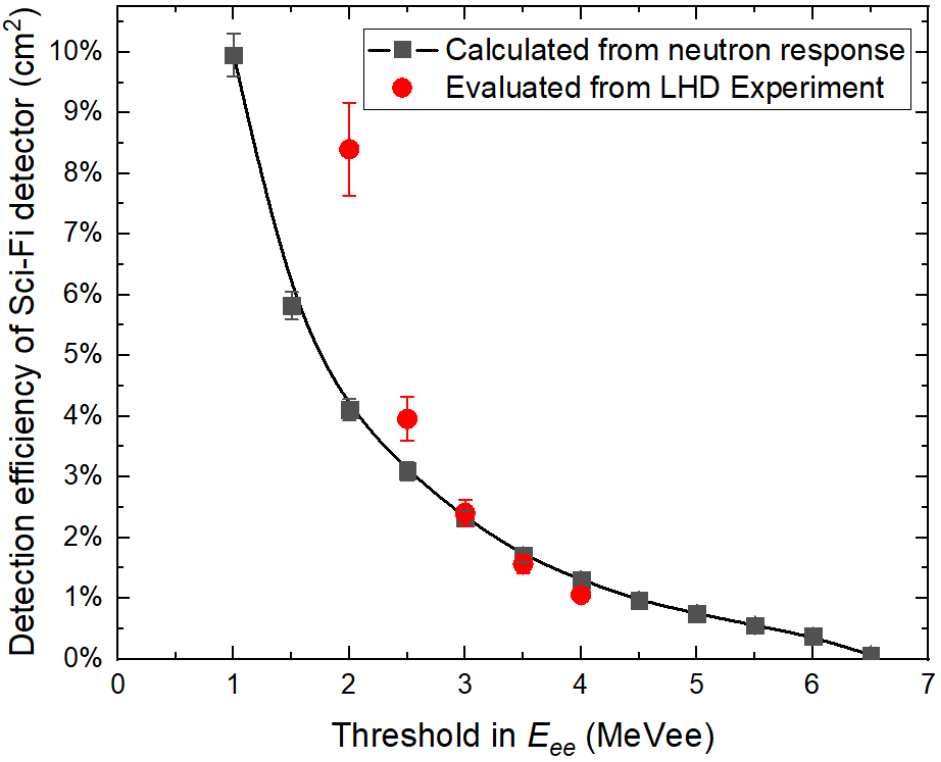

Fig. 6.22 Detection efficiencies of the 1 mm Sci-Fi detector for 14 MeV neutron with different threshold in proton energy.

Finally, the detection efficiencies of the Sci-Fi detector have been evaluated from the calculated neutron response and the LHD experiment as shown in Fig. 6.22. Here, the threshold is evaluated to correspond to E_{ee} by the calibration done in Fig. 6.21. Note that, the detection efficiency of Sci-Fi detector for 14 MeV neutron in the LHD experiment (the experimental detection efficiency) is evaluated from the relationship among the shot-integrated 14 MeV neutron yield measured by NAS, the shot-integrated counts of Sci-Fi detector with the thresholds, and the neutron fluence in the detector position calculated by MCNP6. The error of the shot-integrated 14 MeV neutron yield measured by NAS is

about 7.5%. The error of the neutron flux in the detector position calculated by MCNP6 is 5%. Therefore, the error of the experimental detection efficiencies is evaluated from those errors and the standard error of the shot-integrated counts of Sci-Fi detector with the thresholds. The error of the calculated detection efficiencies is a statistical error of the calculation. The experimental detection efficiencies with the thresholds of 3 MeVee and 3.5 MeVee agree well with the calculation. The experimental detection efficiency with the threshold of 4 MeVee close to the calculation. There is a small difference which may come from statistical error of counts with such high threshold. In addition to this, the experimental detection efficiency with the threshold of 2.5 MeVee and 2 MeVee are higher than the calculations as shown in Fig. 6.22. This is because gamma-rays are taken into account in the low-threshold case. The higher threshold should be chosen to evaluate the triton burnup ratio by using data of Sci-Fi detector which is calibrated by the NAS measurement.

Table 6.2 Uncertainties of the experimental detection efficiencies and the calculated detection efficiencies

Threshold (MeVee)	*2*	*2.5*	*3*	*3.5*	*4*
Uncertainty of Experimental Detection Efficiencies	9.1%	9.2%	9.2%	9.4%	9.5%
Uncertainty of Calculated Detection Efficiencies	4.3%	4.7%	5.3%	6.0%	6.7%

6.6. Conclusion

In the accelerator experiment, the gamma-ray rejection and neutron discrimination ability of the 0.5 mm Sci-Fi detector has been confirmed to be higher than that of the 1 mm Sci-Fi detector, but the detection efficiency of the 0.5 mm Sci-Fi detector is lower than that of the 1 mm Sci-Fi detector. Obviously, for experiments with a higher 14 MeV neutron flux, the 0.5 mm Sci-Fi detector will give a better performance advantage. The function of the Sci-Fi detector has been confirmed by comparing the measured and calculated responses of the 0.5 mm Sci-Fi detector, the 1 mm Sci-Fi detector, the 1 mm Sci-Fi w/o Al detector, and the plastic scintillator detector. PHITS calculations show that the neutron responses of four different-head detectors are almost the same as an expectation. Different PHS of four different heads are from gamma-rays mainly. Al matrix for the Sci-Fi like detector is beneficial for enhancing the edge effect on Sci-Fi for gamma-ray rejection and neutron discrimination ability. It is also found that the neutron

discrimination property of the Sci-Fi without the Al matrix is the same as that of a plastic scintillator.

For the measurement of the Sci-Fi detector in the LHD experiment, the first decay component of the pulse-height spectra in low-pulse-height region has been found to correspond to the signals induced by 2.45 MeV neutrons and gamma-rays by the PHITS calculation. The recoil-proton edge induced by triton burnup 14 MeV neutrons in the LHD deuterium experiment has been confirmed by both the accelerator experiment and the PHITS calculation. The threshold level of the Sci-Fi detector with a high voltage of -1700 V is evaluated to correspond to E_{ee}. The detection efficiencies of the Sci-Fi detector evaluated from the LHD experiment with higher threshold agree well with the detection efficiencies of the Sci-Fi detector calculated by PHITS code. By setting a suitable threshold, the gamma-rays and low-energy neutrons can be completely eliminated which allows to discriminate 14 MeV neutrons from a mixed-radiation field of low-energy neutrons and gamma-rays. Therefore, the Sci-Fi detector can be a standard 14 MeV neutrons detector for future D-T experiments.

6.7. Appendix

Aluminum has a large cross-section of ^{27}Al(n, p)^{28}Si reaction by higher energy neutrons, therefore, protons from the Al matrix might hit the Sci-Fi and induce signals. In the PHITS calculation, the Al matrix was replaced to be a Teflon matrix to investigate the contribution of protons from ^{27}Al(n, p)^{28}Si reaction by 14 MeV neutron. Fig. 6.23(a) and (b) show the two dimensional distributions of proton on the 1 mm Sci-Fi detector with the Al matrix and with the Teflon matrix by 14 MeV neutron, respectively. Figure. 6.24 shows the recoil proton spectra on the Sci-Fi with an Al matrix and with a Teflon matrix for 14 MeV neutron.

It is found that about 4.5% protons above the threshold of 0.01 MeV proton energy are generated from Al matrix by ^{27}Al(n, p)^{28}Si reaction for 14 MeV neutrons enter into fibers unit comparing with recoil protons generated by fibers themselves, but the energy deposition of those protons in fibers is small as shown in Fig. 6.24. In the case of Teflon matrix, there is no proton produced from the Teflon matrix by14 MeV neutrons, but the range of recoil proton in Teflon matrix is larger than that in the Al matrix. There is no proton generated from the Al matrix by the 2.45 MeV neutrons as shown in Fig. 6.23(c). Therefore, the part of protons from the Al matrix is negligible.

(a)

(b)

(c)

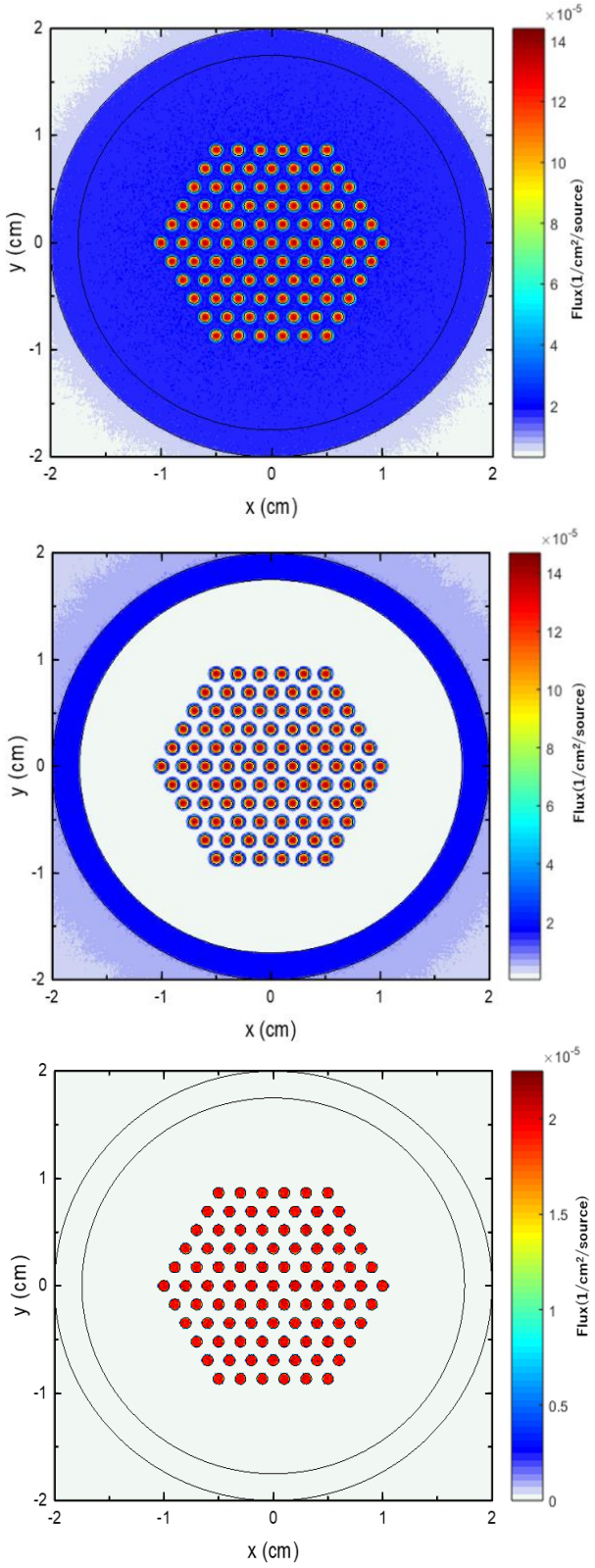

Fig. 6.23 Proton flux 2-D distributions for mono-energetic 14 MeV neutron in the 1 mm Sci-Fi with the Al matrix (a), in the 1 mm Sci-Fi with the Teflon matrix (b), and for mono-

energetic 2.45 MeV neutron in the 1 mm Sci-Fi with Al matrix (c).

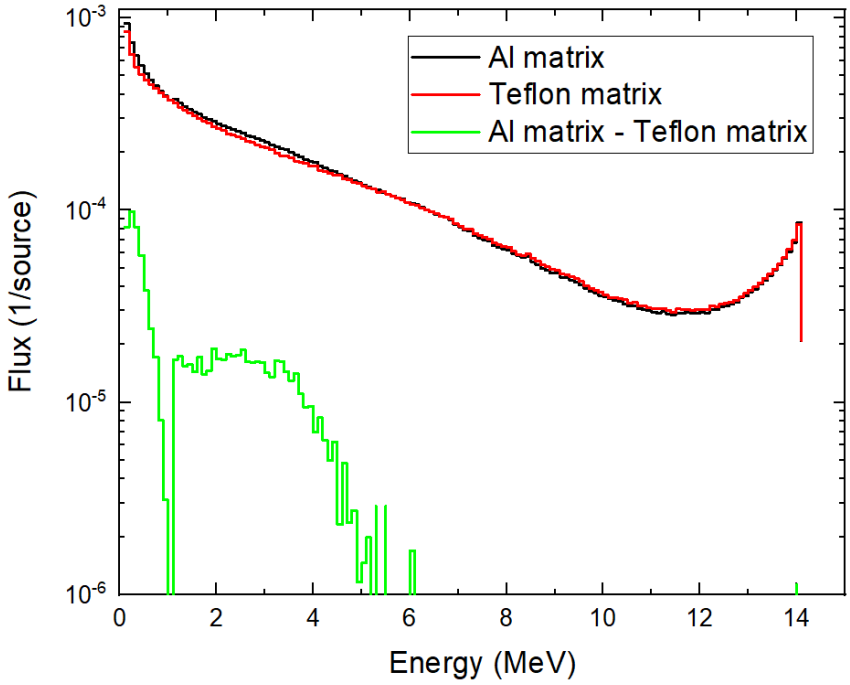

Fig. 6.24 Recoil proton of Sci-Fi with an Al matrix (black line) and a Teflon matrix (red line) by 14 MeV neutron, and the difference between Sci-Fi with an Al matrix and a Teflon matrix (green line).

Detection efficiencies of the 1 mm Sci-Fi detector contributed by protons have been evaluated by PHITS calculations with the different threshold of the proton energy as shown in Fig. 6.24(a). Fig. 6.24(b) shows the detection efficiencies of the 1 mm Sci-Fi detector which is the contribution from carbon elastic scattering by different energy neutron with different threshold of carbon energy for the contribution from the recoiled carbon by n-C elastic scattering. The equivalent energy to electron light output E_{ee} of 1 MeV proton in a plastic scintillator is almost the same as that of 13 MeV carbon. [93] In addition, the energy deposited on the carbon by 14 MeV neutron elastic scattering is about 4.1 MeV. Therefore, when the proton energy threshold is set to 1 MeV, the contribution of carbon for detection efficiency is negligible.

(a)

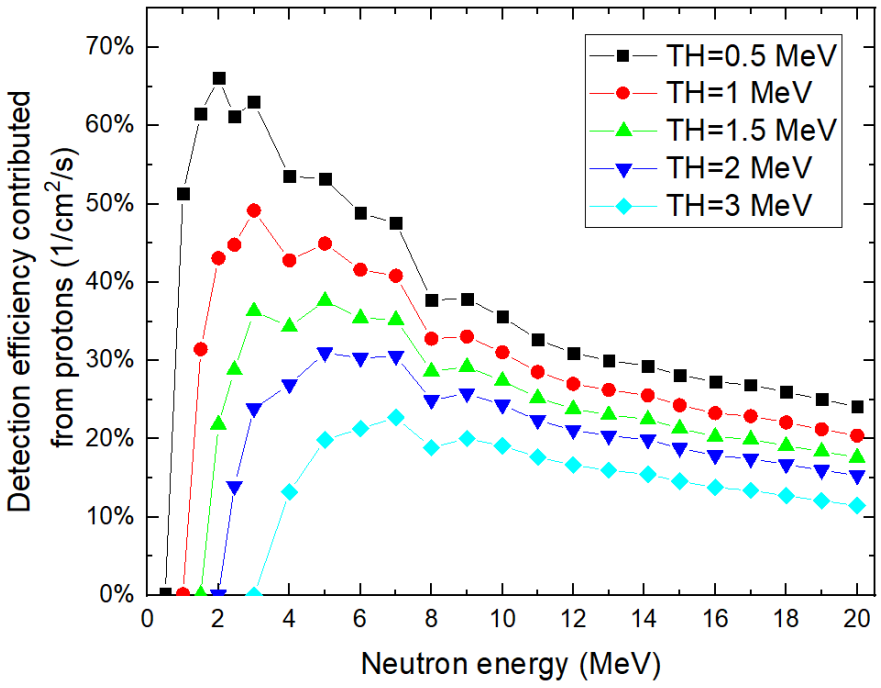

(b)

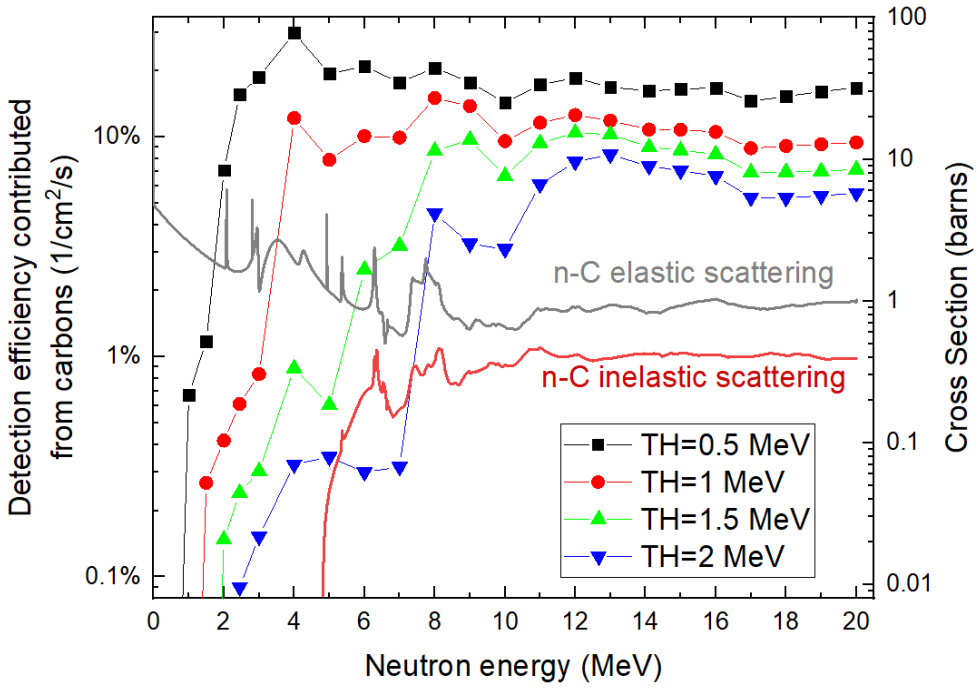

Fig. 6.25 Detection efficiencies of the 1 mm Sci-Fi detector from proton with different threshold of proton energy (a) and that from carbon with different threshold of carbon energy (b).

As can be seen from Fig. 6.24(a) and (b), the detection efficiency contributed from protons drops remarkably around 8 MeV neutron in the different threshold and the detection efficiency contributed from carbons increases slightly in low threshold and remarkably in high threshold around 8 MeV neutron. Obviously, the decreased detection efficiency comes from the competition between n-p and n-C elastic scattering around 8 MeV neutron. This is because the cross section of n-C elastic scattering has a peak around 8 MeV. Also, the cross section of n-C inelastic scattering has a maximum peak around 8 MeV. The decrease of detection efficiencies in low proton threshold case at 4 MeV also have same reason.

Chapter 7:

Triton burnup study on LHD[4]

In the near future, the fusion research will enter the D-T operational era, where the plasma will be maintained by the self-heating of energetic D-T born alpha particles. Therefore, the research on energetic-particle confinement and self-heating of alpha particles will be particularly important.

In deuterium plasmas, 2.45 MeV neutrons and 1 MeV tritons are produced by D-D reaction with almost the same production rate. Energetic tritons will undergo secondary D-T reaction with background deuterons while those tritons slow down in a plasma. If the secondary 14 MeV neutrons can be measured selectively, we can study the confinement of 1 MeV tritons. Kinematic properties such as the Larmor radius and the precessional drift frequency of 1 MeV tritons are almost the same as those of 3.5 MeV alphas. Therefore, the triton burnup study can be regarded as a simulation of alpha particle confinement.

[4] This chapter is a revised by
N. Pu, *et al*., "*Initial Results of Triton Burnup Study by Using Neutron Activation System in the Large Helical Device",* A3 proceeding (2017). (non-refereed)
N. Pu, *et al*, "*Scintillating fiber detectors for time evolution measurement of the triton burnup on the Large Helical Device*", Rev. Sci. Instrum., **89** 10I105 (2018).
N. Pu, *et al*, "*Initial results of triton burnup study in the Large Helical Device*", Plasma and Fusion Research, **13** 3402121 (2018).

7.1. Triton burnup ratio measured in various plasma conditions using NAS

In the LHD first deuterium plasma campaign, the triton burnup ratio was measured with NAS on 8-O port in various magnetic configurations. The triton burnup ratios in R_{ax} from 3.55 m to 3.90 m are plotted in Fig. 7.1. The triton burnup ratio tends to decrease as the plasma column is shifted outwardly. As can be seen in Fig. 7.1, the highest triton burnup ratio is obtained in the inwardly shifted configuration (R_{ax}/B_t=3.55 m/2.89 T). [98] The magnetic field strength dependence on triton burnup ratio was obtained in R_{ax}= 3.6 m. Figure 7.2 shows that triton burnup ratio strongly depended on magnetic field B_t. When B_t decreased to 1.375 T, triton burnup ratio was close to 0.

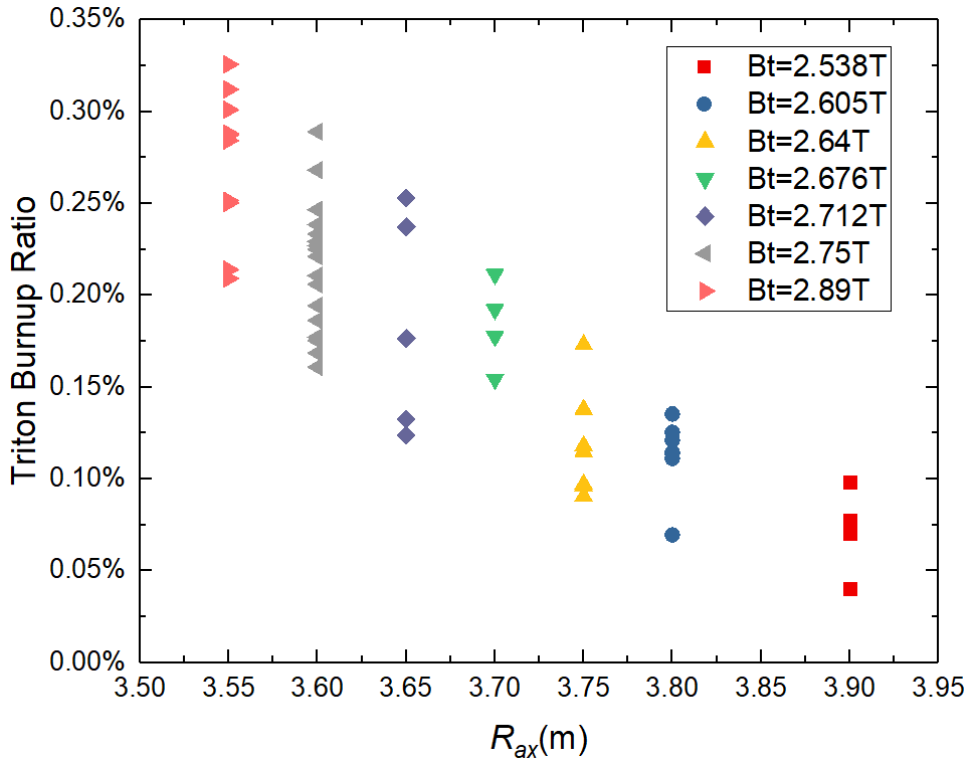

Figure 7.1. The triton burnup ratio in different magnetic axis position.

The confinement property of helically-trapped energetic ions largely depends on magnetic axis positions. Collisionless orbits of helically-trapped energetic ions in R_{ax} of 3.55 m, 3.6 m, 3.75 m, and 3.9 m are shown in Fig. 7.3. The drift surface of helically-trapped energetic ion in R_{ax} of 3.55 m matches with magnetic flux surfaces. It tends to deviate largely from magnetic flux surfaces as the magnetic axis position is shifted outward. [99] Higher triton burnup ratio in inward shifted configuration obtained in

experiment is consistent with the improvement of helically-trapped energetic ion orbit by inward shift of R_{ax}.

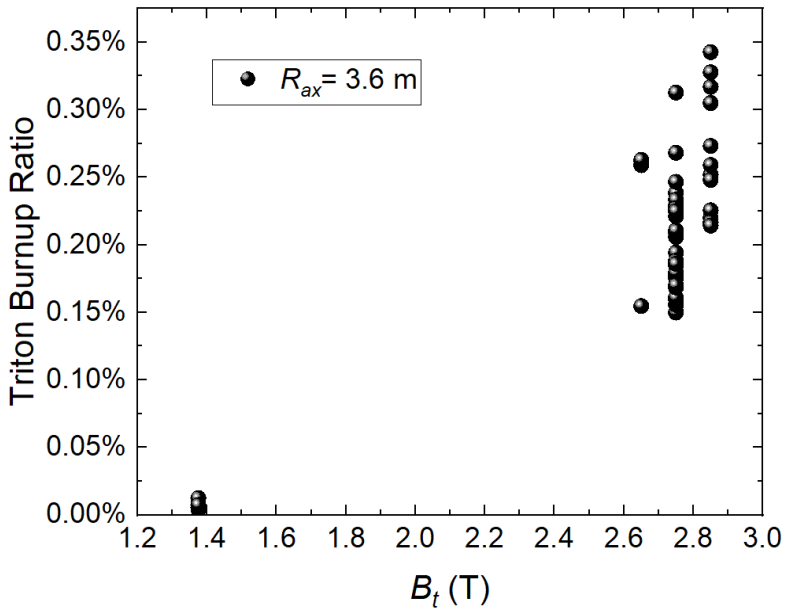

Fig. 7.2 Magnetic field strength dependence of triton burnup ratio at R_{ax} of 3.6 m.

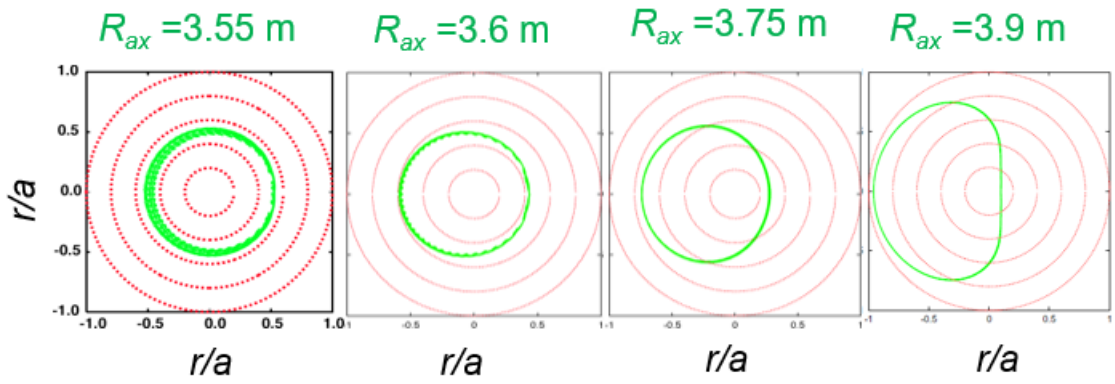

Figure 7.3. Collisionless orbits of helically-trapped energetic ions in the Boozer coordinates in R_{ax} of 3.55 m, 3.6 m, and 3.75 m. [98]

Dependence of triton burnup ratio on electron density was obtained in R_{ax} of 3.55 m, 3.60 m, 3.75 m, and 3.90 m as shown in Fig. 7.4. Here a heating pattern and heating power of plasmas are almost the same. The triton burnup ratio increased with n_{e_bar} below about 2.5×10^{19} m^{-3}, and decreased about that density in R_{ax} of 3.55 m, 3.60 m, and 3.75 m. It seems that more data points are needed in order to show the dependence in R_{ax} of 3.90 m.

From Eq (2.2.8), triton burnup ratio is proportional to $n_e \times \tau_{se} \sim T_e^{3/2}$, because $\tau_{se} \propto$

$T_e^{3/2}/n_e$. The right downward slope appeared in $n_{e\_bar} > 2.5\times10^{19}$ m^{-3} shown in Fig. 7.4 can be understand by the decrease of T_e due to the increase of n_e. If the effect of triton loss is included, EQ (2.2.8) can be modified by

$$\text{Triton burnup ratio} \approx n_e \tau_{eff} \langle \sigma v \rangle_{DT} \tag{7.1}$$

where,

$$\frac{1}{\tau_{eff}} = \frac{1}{\tau_p} + \frac{1}{\tau_{se}} \tag{7.2}$$

Here, τ_p and τ_{eff} represent confinement time of tritons and effective confinement time of tritons, respectively. The right upward slope of triton burnup ratio shown in Fig. 7.4 below n_{e_bar} of 2.5×10^{19} m^{-3} might be due to the effect of triton confinement. In low-n_{e_bar} region, effect of confinement can be dominant because of relatively long slowing down time. The effect of confinement on triton burnup ratio will be discussed in Section 7.3.

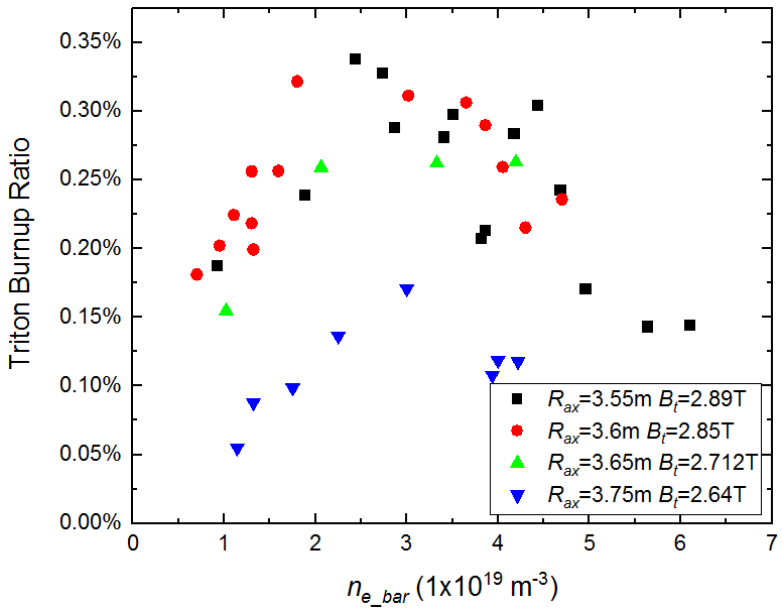

Figure 7.4. Line-averaged electron density dependence of triton burnup ratio in different magnetic axis positions.

7.2. Time-evolution measurement of triton burnup

7.2.1. Cross-calibrated Sci-Fi counts with total 14 MeV neutron yield

To measure the total 14 MeV neutron emission rate by using Sci-Fi detector, the conversion factor from 14 MeV neutron pulse counting rate measured by Sci-Fi detectors to total 14 MeV neutron emission rate was obtained by comparing shot-integrated 14 MeV neutron pulse counts and shot-integrated 14 MeV neutron yield measured using NAS on 8-O port. As shown in Fig. 7.5, shot-integrated 14 MeV neutron pulse counts of two Sci-Fi detectors shows good linearity to shot-integrated 14 MeV neutron yield measured by NAS on 8-O port. Here, the threshold level/high voltage of LANL Sci-Fi detector and NIFS Sci-Fi were set to be 300 mV/-1700 V and 170 mV/2000 V, respectively. Thus, the absolute detection efficiencies of 14 MeV neutron at the detector position in the LHD experiment are evaluated to be 2.3×10^{-10} counts per 14 MeV neutron for the LANL Sci-Fi detector and 3.9×10^{-10} counts per 14 MeV neutron for the NIFS Sci-Fi detector, respectively. The absolute detection efficiencies can be used to be the conversion factors for Sci-Fi detectors, therefore, the 14 MeV neutron emission rate can be measured as 2.5 MeV neutron emission rate changing in time by using both Sci-Fi detectors. [66]

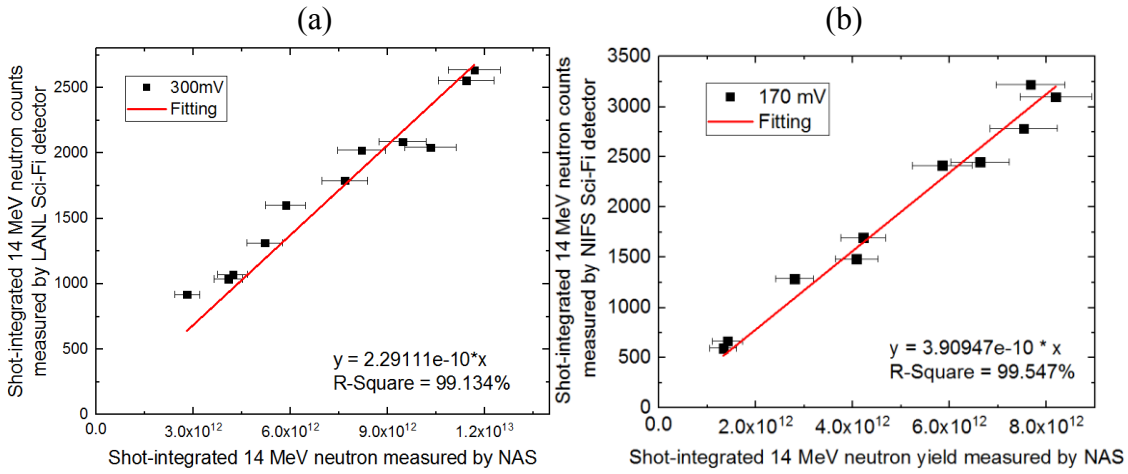

Fig. 7.5 Shot-integrated 14 MeV neutron pulse counts measured with (a) LANL Sci-Fi detector and (b) NIFS Sci-Fi detector as a function of shot-integrated 14 MeV neutron yield measured with NAS. [66]

7.2.2. Time evolution of triton burnup 14 MeV neutron

Time trace of 14 MeV neutron emission rate can be measured by using the two Sci-Fi detectors with the absolute detection efficiencies as shown in Fig. 7.6. In this shot, all NBs are terminated at t=5.3 s. Two Sci-Fi detectors have shown almost the same time evolution. It is worth note that the rise time and decay time of D-T neutrons are much longer than that of D-D neutrons. This is because the 1 MeV triton needs time to slow down to around 100 keV in order to cause secondary D-T reactions. Note that the cross-section of D(t,n)^{4}He reaction have a peak around 170 keV in center mass energy as shown in Fig. 2.1.

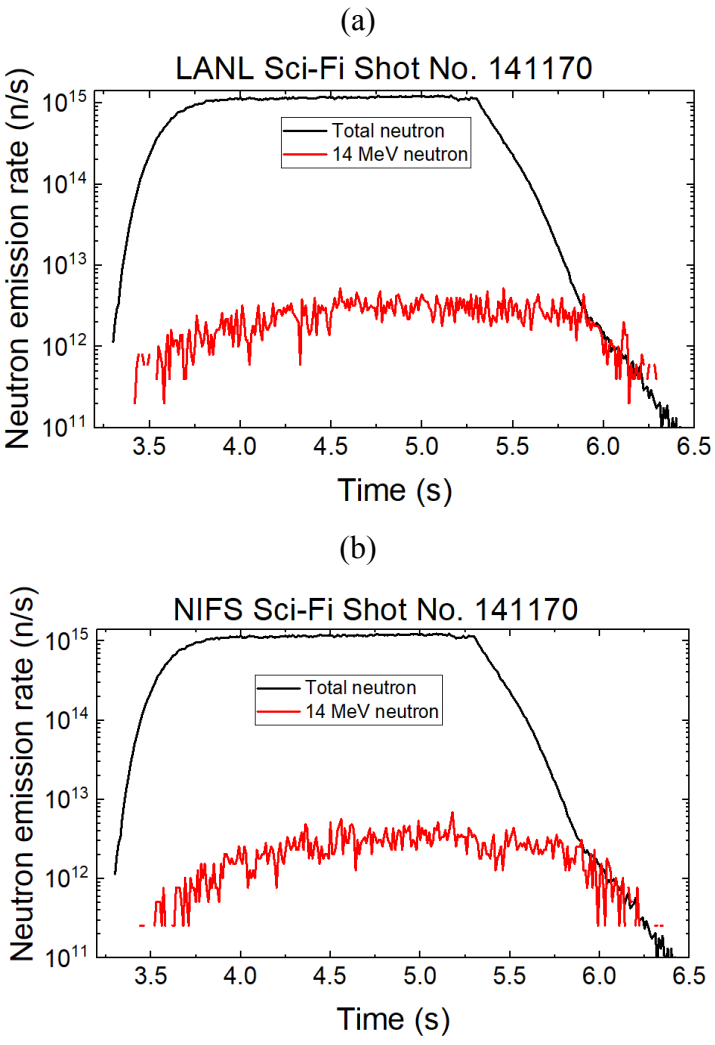

Fig. 7.6 Time traces of total neutron emission rate measured by NFM and the 14 MeV neutron emission rate measured using (a) LANL Sci-Fi detector and (b) NIFS Sci-Fi detector.

7.2.3. Comparison of triton burnup ratio evaluated with NAS and Sci-Fi detector

As verification in the last of Chapter 6 with Fig. 6.21 and 6.22 that the Sci-Fi detector can work as a standard 14 MeV neutrons detector with suitable threshold, triton burnup ratio also can be evaluated shot by shot with Sci-Fi detector. In Fig. 7.7, triton burnup ratios are evaluated by shot-integrated Sci-Fi counts with threshold voltage of 300 mV and calibration factor of 2.3×10^{-10} counts per 14 MeV neutron for the LANL Sci-Fi detector as shown in Fig. 7.5(a), and NAS measurements. It can be seen that density dependence of triton burnup ratio evaluated from Sci-Fi is almost the same with that from NAS. Therefore, it is demonstrated again that the Sci-Fi detector can work as complementary 14 MeV neutron diagnostic to NAS and will play important role in triton burnup study.

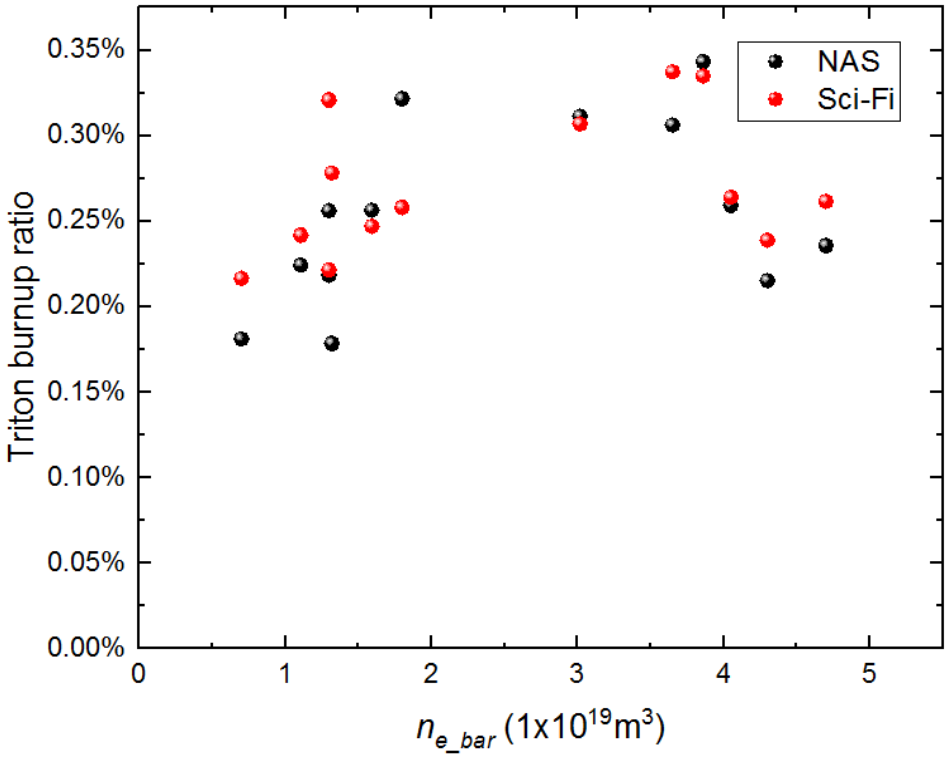

Fig. 7.7 Triton burnup ratio evaluated by NAS and Sci-Fi detector.

7.3. Time-evolution calculation of 14 MeV neuron emission rate

Time trend of secondary D-T neutron rate has been calculated using the FBURN code as shown in Fig. 7.8 [42]. In this experiment, NB1, NB2, and NB3 were injected from t=3.3 s to 5.3 s. In the FBURN calculation, radial diffusion coefficient of triton (D_T) is changed from 0.0 to 0.5 m^2/s. Here, the D-T neutron emission rate by the calculation is normalized at NB turn off (t of 5.3 s). It is found that the rise time and decay time becomes shorter as the increase of D_T. By comparing decay of D-T neutron emission rate after NB turn off, radial diffusion coefficient is estimated to be around 0.2 m^2/s.

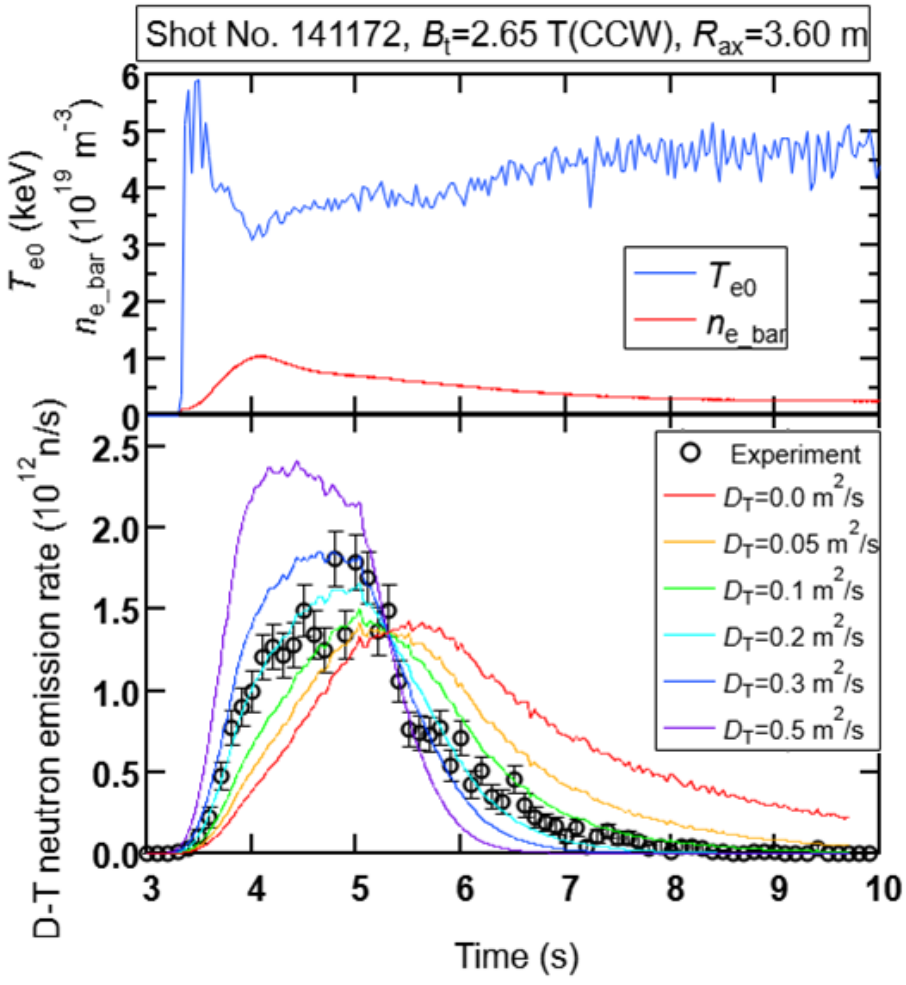

Fig. 7.8 Time evolution of central electron temperature, n_{e_bar}, D-T neutron emission rate measured by Sci-Fi detector, and calculated by the FBURN code. Here, calculated D-T neutron emission rate is normalized at t =5.3 s.

Chapter 8:

Summary

The deuterium plasma experiments have been conducted since March 2017 on LHD. This is the first time D-D experiment in a large Stellarator in the world. Neutrons are the primary product of the D-D reaction and carry the most energy of the fusion reaction. To evaluate the accurate data of neutron yield, *in situ* calibrations was performed by using an intense ^{252}Cf neutron source for NFM and NAS on the LHD before the D-D experiment. To simulate a ring-shaped neutron source, a railway was installed inside the LHD vacuum vessel, where a train loaded with the ^{252}Cf source run along a typical magnetic axis position continuously.

The detection efficiencies of NFM for the ^{252}Cf ring source are derived from the total counts in the continuous rotation of the neutron source. The detection efficiencies for the plasma neutron source are evaluated from detection efficiencies for the ^{252}Cf ring source with assistance of the MCNP calculations. The final uncertainty in the neutron emission rate measurement is evaluated to be ±7% and ±9% in the pulse counting mode and the Campbell mode, respectively.

On the other hand, the activation response coefficients for the ^{252}Cf neutron source, where the detection efficiency of the HPGe detector which was evaluated by the PHITS code, were in good agreement with the MCNP result. The activation response coefficients for 2.45 MeV neutrons and secondary 14.1 MeV neutrons from the D-D plasma were evaluated from the MCNP calculation with correction by using the *in situ* calibration results. This is the first time to evaluate the activation response coefficients of the NAS for a toroidal source on a fusion device in the world. The difference of the activation response coefficients between the *in situ* calibration and the MCNP calculation for the ^{252}Cf neutron ring-source is only 7%. This *in situ* calibration will be a good reference for

future calibration experiments of fusion devices such as ITER.

In the LHD experiment, NAS has been utilized to perform cross checking of the absolute total neutron yield measured by NFM. By using the activation response coefficients evaluated by the MCNP calculation with correction by the *in situ* calibration results, the neutron yield evaluated by NAS on 8-O port is consistent with that measured with FC#1 of NFM. Most relative deviations between the measurement of NAS on 8-O port and FC#1 are less than 10%. The 14 MeV neutron yields is the first time measured by NAS from stellarators in the world.

The triton burnup ratios were evaluated by the NAS measurement for the triton burnup study. Triton burnup ratio increases with line-averaged electron density in the low-density region, and decreases with electron density in the high-density region. Meanwhile, the triton burnup ratio decreases as the magnetic axis (R_{ax}) positions shift outward, which can likely be explained by the orbit of helically trapped energetic tritons. And the triton burnup ratio strongly depended on the magnetic field B_t at the same R_{ax}.

Two Sci-Fi detectors successfully worked to measure the time evolution of the 14 MeV neutron emission rate for the triton burnup study on LHD. By using a fast digitizer, the shaping information of each pulse was obtained for the off-line analysis on the pulse height spectrum and the time evolution of 14 MeV neutrons. By the cross calibration of the shot integrated counts of Sci-Fi detectors with the absolute 14 MeV neutron measured by NAS, the triton burnup ratio has been evaluated shot-by-shot by the measurement of Sci-Fi detectors. In addition to this, the compact design for the NIFS Sci-Fi detector will be helpful for the development of a 14 MeV neutron camera in the future.

The accelerator experiment and PHITS calculation have been carried out to study the pulse height property of Sci-Fi detector. In the accelerator experiment, the gamma-ray rejection ability of the 0.5 mm Sci-Fi detector has been confirmed to be higher than that of the 1 mm Sci-Fi detector, but the detection efficiency of the 0.5 mm Sci-Fi detector is lower than that of the 1 mm Sci-Fi detector. Obviously, for experiments with a higher 14 MeV neutron flux, the 0.5 mm Sci-Fi detector will give a better performance advantage. The function of the Sci-Fi detector has been confirmed by using the measurement of the 0.5 mm Sci-Fi detector, the 1 mm Sci-Fi detector, the 1 mm Sci-Fi w/o Al detector, and the plastic scintillator detector. It is found that the property of Sci-Fi without the Al matrix is the same as that of plastic scintillator. The Al matrix for the Sci-Fi detector is beneficial to enhance the edge effect of Sci-Fi and gamma-ray rejection ability of the Sci-Fi detector.

For the measurement of the Sci-Fi detector in the LHD experiment, the first decay component of the PHS in low-pulse-height region has been found to be corresponding to

the signal induced by 2.45 MeV neutrons and gamma-rays by the PHITS calculation. The recoil proton edge induced by triton burnup 14 MeV neutron in the LHD deuterium experiment has been confirmed by both the accelerator experiment and the PHITS calculation. The threshold level of the 1 mm Sci-Fi detector with HV of -1700 V is evaluated to be corresponding to the proton energy. The detection efficiencies of the 1 mm Sci-Fi detector for 14 MeV neutron are obtained with different threshold for the LHD experiment. By setting suitable threshold, the Sci-Fi detector can completely eliminate gamma-rays and low-energy neutrons. Therefore, the Sci-Fi detector can be a standard 14 MeV neutron detector for future D-T experiment.

The calculation by the FBURN code was carried out for the triton burnup study on LHD. The diffusion coefficient of the energetic triton was evaluated by the calculation of the time evolution of the secondary D-T reactivity with different diffusion coefficients to obtain a good agreement with the measured by Sci-Fi detectors. Also, the shot-integrated triton burnup ratios were calculated by the FBURN code, which decrease with diffusion coefficients of the energetic triton.

References

[1] Statistical Review of World Energy 67th edition June 2018, https://www.bp.com/en/global/corporate/energy-economics/statistical-review-of-world-energy.html

[2] D-T reaction, https://interestingenergyfacts.blogspot.com/2010/04/nuclear-fusion-facts.html

[3] J. Wesson, "Tokamaks", Clarendon press – Oxford (2004).

[4] D. L. Jassby, *et al* Physics of Fluids B: Plasma Physics, **3** 2308 (1991).

[5] M. Keilhacker and the JET Team, Physics of Fluids B: Plasma Physics, **2** 1291 (1990).

[6] T. Nishitani, *et al*, Nucl. Fusion, **34** 1069 (1994).

[7] T. Morisaki, *et al*, IAEA Fusion Energy Conference, Gandhinagar, India, (2018).

[8] Y. Takeiri, IEEE T. Plasma Sci., **46** 1141 (2018).

[9] A. Dinklage, *et al*, Nature Physics, **14** 855 (2018).

[10] JET Team, Nucl. Fusion, **32** 187 (1992).

[11] J. D. Strachan, et al., Phys. Rev. Lett., **72** 3526 (1994).

[12] C. W. Barnes, *et al*., Nucl. Fusion, **38** 597 (1998).

[13] S. Conroy, *et al.*, Nucl. Fusion, **28** 2127 (1988).

[14] M. Hoek, *et al*., IPP-Report IPP-1/320 (1999).

[15] M. Hoek, *et al*., Nucl. Instrum. Methods Phys. Res. A, **368** 804 (1996).

[16] H. H. Duong and W. W. Heidbrink, Nucl. Fusion, **33** 211 (1993).

[17] P. Batistoni *et al*., Nucl. Fusion, **27** 1040 (1987).

[18] W. W. Heidbrink, R. E. Chrien and J. D. Strachan, Nucl. Fusion, **23** 917 (1983).

[19] G. A. Wurden, *et al*., Rev. Sci. Instrum., **66 (1)** 901 (1995).

[20] T. Nishitani, *et al*., Plasma Phys. Control. Fusion, **38** 355 (1996).

[21] T. Nishitani, *et al*., Fusion Eng. Des., **34-35** 563 (1997).

[22] H. H. Duong and W. W. Heidbrink, Nucl. Fusion, **33** 211 (1993).

[23] G. Nemtsev, *et al*., Rev. Sci. Instrum., **87** 11D835 (2016).

[24] B. Wolle, Physics Reports **312** 1-86 (1999).

[25] G. Gamov, Z. Phys., **51** 204 (1928).

[26] D. D. Clayton, Principles of Stellar Evolution and Nucleosynthesis, McGraw-Hill, New York, 1968.

[27] A. M. Lane, R. G. Thomas, Rev. Mod. Phys., **30** 57 (1958).

[28] G. M. Hale, D. C. Dodder, Nuclear Cross Sections for Technology, in: J.L. Fowler, C. H. Johnson, C. D. Bowman (Eds.), Special Publications, vol. 594, National

Bureau of Standards, Washington DC, 650 (1980).
[29] N. Jarmie, Requirements for charged-particle reactions cross sections in the D-T, D-D, T-T and D-^{3}He fuel cycles, Report LA-UP 86-3705, Los Alamos National Laboratory, Los Alamos, NM, 1986.
[30] H. S. Bosch, G. M. Hale, Nucl. Fusion, **32** 611 (1992).
[31] T. J. Murphy, Nucl. Instr. and Meth. A **267** 520 (1988).
[32] H. Brysk, Plasma Physics, **15** 611 (1973).
[33] I. Lux, L. Koblinger, Monte Carlo Particle Transport Methods: Neutron and Photon Calculations, CRC Press, Boston, 1990.
[34] J. D. Strachan, *et al*., Nucl. Fusion, **33** 991 (1993).
[35] W. W.Heidbrink, Tokamak diagnostics using fusion products. Ph.D. thesis, Princeton Univcrsity (1984).
[36] G. Gorini, *et al*., Calculation of the classical triton burn-up in JET deuterium plasmas. Technical Report JET-P(87)35. JET, Culham, U.K (1987).
[37] M. A. Kovanen, and W. G. F. Core, HECTOR: A code for the study of high energy charged particles in axisymmetric Tokamak plasmas. Technical Report JET-R(88)01, JET, Culham, U.K (1988).
[38] P. Batistoni, E. Bittoni and M. Haegi, Nucl. Fusion, **29** 673(1989).
[39] G. Gorini, and M. A. Kovanen, A comparison study of the I MeV triton burn-up in JET using the HECTOR and SOCRATE *codes.* Technical Report JET-R(88)09, JET, Culham, U.K (1988).
[40] P. Batistoni and C. W. Barnes, Plasma Phys. Control. Fusion, **33** 1735 (1991).
[41] D. V. Srvukhin, "*Reviews of Plasma Physics*" (M. A. Leontovich Ed.) Consultants Bureau, New York, **4** 93 (1966).
[42] K. Ogawa, *et al*., Nucl. Fusion, **58** 034002 (2018).
[43] M. Goto, *et al*., Fusion Sci. Technol., **58** 394 (2010).
[44] S.P. Hirshman and O. J. Betancourt, Comput. Phys., **96** 99 (1991).
[45] S. Murakami, *et al*., *Trans.Fusion Technol.*, **27** 256 (1995).
[46] D. V. Sivukhin, *Reviews of Plasma Physics* (M. A. Leontovich Ed.) Consultants Bureau, New York, Vol. **4** (1966).
[47] F. F. Chen, "Introduction to Plasma physics and Controlled Fusion", Springer (2015).
[48] K. Miyamoto, Plasma Physics for Controlled Fusion, Springer (2016).
[49] F. L. Hinton, Plasma Phys. **19** 082516 (2012).
[50] NIFS wed page
[51] M. Isobe, *et al*., Nucl. Fusion, **58** 082004 (2018).
[52] G.L. Yuan, *et al*., Plasma Sci. Technol., **16** 168 (2014).

[53] M. Isobe, *et al*., Rev. Sci. Instrum., **85** 11E114 (2014).
[54] T. Nishitani, *et al*., Fusion Eng. Des., **136** 210 (2018).
[55] T. Nishitani, *et al*., Prog. Nucl. Sci. Technol., **6** 48 (2019).
[56] N. Pu, *et al*., Rev. Sci. Instrum., **88**, 113302 (2017).
[57] L. C. Johnso, *et al*., Rev. Sci. Instrum., **66**, 894 (1995).
[58] C.W. Barnes, *et al*., Rev. Sci. Instrum., **61**, 3190 (1990).
[59] M. Hoek, *et al*., JAERI-M-94-002 (1994).
[60] ENDF/B-VIII.0 released February 2, 2018
[61] Y. Yariv, *et al*., Nucl. Instrum. Meth. Phys. Res., A **292** 351 (1990).
[62] S. Singkarat, *et al*., Nucl. Instrum. Meth. Phys. Res., A **335** 248 (1993).
[63] S. Singkarat, *et al*., Nucl. Instrum. Meth. Phys. Res., A **384** 463 (1997).
[64] R. Greim on behalf of the LHCb collaboration, JINST, **12** C02053 (2017).
[65] W. C. Sailor, *et al*., Rev. Sci. Instrum., **66** 898 (1995).
[66] N. Pu, *et al*., Rev. Sci. Instrum., **89**, 10I105 (2018).
[67] E. B. Nieschmidt, *et al*., Rev. Sci. Instrum., **56** 1084 (1985).
[68] H.W. Hendel, *et al*., Rev. Sci. Instrum., **59** 1682 (1988).
[69] C.W. Barnes, *et al*., Rev. Sci. Instrum., **61**, 3151 (1990).
[70] H.W. Hendel, *et al*., Rev. Sci. Instrum., **61** 1900 (1990).
[71] O.N. Jarvis, *et al*., Rev. Sci. Instrum., **61** 3172 (1990).
[72] J, D. Strachan, *et al*., Rev. Sci. Instrum., **61** 3501 (1990).
[73] T. Nishitani, *et al*., Rev. Sci. Instrum., **63** 5270 (1992).
[74] L.C. Johnson, *et al*., Rev. Sci. Instrum., **66** 894 (1995).
[75] J, D. Strachan, *et al*., Rev. Sci. Instrum., **66** 1247 (1995).
[76] M. J. Loughlin, *et al*., Rev. Sci. Instrum., **70** 1126 (1999).
[77] P. Batistoni, *et al*., Rev. Sci. Instrum., **88** 103505 (2017).
[78] Z. Ghani, *et al*., Fusion Eng. Des., **136** 233 (2018).
[79] P. Batistoni, *et al*., Nucl. Fusion, **58** 026012 (2018).
[80] D.B. Pelowits (Ed.), MCNP6 User's Manual, LA-CP-13-00634, Los Alamos National Laboratory, Los Alamos, 2013.
[81] R. Forrest, *et al.*, FENDL-3 Library – Summary Document, IAEA Report INDC(NDS)- 628, IAEA, Vienna, 2012.
[82] Y. Wu, F.D.S. Team, Fusion Eng. Des., **84** 1987 (2009).
[83] T. Nishitani, *et al*., Fusion Eng. Des., **123** 1020 (2017).
[84] J. Källne, *et al*., Nucl. Fusion, **28** 1291 (1988).
[85] E. B. Nieschmidt, *et al*., Rev. Sci. Instrum., **59** 1715 (1988).
[86] D. B. Syme, *et al*., Fusion Eng. Des., **89** 2766 (2014).
[87] M. Angelone, *et al*., Rev. Sci. Instrum., **61**, 3157 (1990).

[88] T. Sato, *et al*., J. Nucl. Sci. Technol., **55** 684 (2018).
[89] D.B. Pelowits (Ed.), MCNP6 User's Manual, LA-CP-13-00634, Los Alamos National Laboratory, Los Alamos, 2013.
[90] R. Forrest, *et al.*, FENDL-3 Library – Summary Document, IAEA Report INDC(NDS)- 628, IAEA, Vienna, 2012.
[91] K. Kobayashi, *et al*., JAERI 1344 (2002).
[92] M. Baba, *et al*., Nucl. Instrum. Methods Phys. Res. A, **376** 115 (1996).
[93] F. D. Becchett, *et al*., Nucl. Instrum. Meth., **138** 93 (1976).
[94] Organic Scintillation Materials, https://www.crystals.saint-gobain.com.
[95] J. Zhang, *et al*., Chinese Phys. C, **34(7)** 988 (2010).
[96] K. V. Mitrofanov, *et al*., EPJ Web of Conferences, **146** 11041 (2017).
[97] T. Nishitani, *et al*., Fusion Eng. Design, **123** 1020 (2017).
[98] S. Murakami, *et al*., J. Plasma Fusion Res. SERIES, 620 **5** (2002).
[99] M. Isobe, *et al*., IEEE T. Plasma Sci., **46** 6 (2018).

Publications

[1] N. Pu, *et al*., "*In situ* calibration of neutron activation system on the large helical device", Review of Scientific Instruments, **88** 113302 (2017).

[2] N. Pu *et al*., "*Initial Results of Triton Burnup Study by Using Neutron Activation System in the Large Helical Device",* Proc. of A3 Foresight Program Seminar, 11-14 July, 2017, Sapporo, **NIFS-PROC-109** Jan. 12, 2018, p243-248.

[3] N. Pu, *et al*., "*Scintillating fiber detectors for time evolution measurement of the triton burnup on the Large Helical Device*", Review of Scientific Instruments, **89** 10I105 (2018).

[4] N. Pu, *et al*., "*Initial results of triton burnup study in the Large Helical Device*", Plasma and Fusion Research, **13** 3402121 (2018).

[5] N. Pu, *et al*., "*Evaluation of scintillating-fiber detector response for 14 MeV neutron measurement*", Journal of Instrumentation, **14** P10015 (2019).

[6] N. Pu, *et al*., "*Evaluation for gamma-ray rejection ability affecting neutron discrimination property in scintillating-fiber type of fast neutron detector*", Nuclear Instruments and Methods in Physics Research Section A, **969** 164000 (2020).

Presentations

[1] N. Pu *et al*., "*Initial Results of Triton Burnup Study by Using Neutron Activation System in the Large Helical Device*", 11th A3 Foresight Program Workshop on Critical Physics Issues Specific to Steady State Sustainment of High-Performance Plasmas, July 11-14, 2017, Sapporo, Japan. (Oral)

[2] N. Pu *et al*., "*Initial results of triton burnup study in the Large Helical Device*", 21st International Stellarator-Heliotron Workshop (ISHW2017), October 2-6, 2017, Kyoto, Japan. (Poster)

[3] N. Pu *et al.,* "*Initial results of triton burnup study in the Large Helical Device*", 26th International Toki Conference (ITC-26) and 11th Asia Plasma and Fusion Association Conference, December 5-8, 2017, Toki, Japan. (Poster)

[4] N. Pu *et al.,* "*Scintillating fiber detectors for time evolution measurement of the triton burnup on the Large Helical Device*", the 22nd Topical Conference on High Temperature Plasma Diagnostics, April 16-19, 2018, San Diego, USA (Poster)

Acknowledgements

This thesis is accomplished according to the work on measurement of 14 MeV neutron for triton burnup study by using neutron diagnostics on LHD in National Institute for Fusion Science (NIFS) and the Graduate University for Advanced Studies, SOKENDAI, Toki, Japan. I have obtained a mass of helps from many people during this work. I would like to express my sincere thnaks and appreciations to all of these people.

At first, I wish to express my earnest and most sincere gratitude to Prof. Mitsutaka Isobe. I am very grateful to have the chance to learn 14 MeV neutron diagnostics and energetic particle physics from Isobe-sensei. Actually, he did not only guide me on science, but also taught me to overcome my weakness in my daily life in NIFS. I think that this will be significantly valuable for my future. I am deeply affected with his scrupulously and seriously scientific attitude as an experimental physicist, which will be great fortune for my future research. There are a lot of knowledge and skills in this field, which I have learned from his insightful suggestions and guidance. Those are remarkably helpful for my study. He also guided me on the scientific English writing. This made me to be more careful in my study. Looking around those years I lived in Japan, Isobe-sensei helped me to settle myself in Japan at the beginning I came. With his generous help in my personal life, I can start to study and live in Japan. With his strict guidance, I can finish my study smoothly. With his patience, I can obtain a good result. I wish to thank everything what he did for me.

I feel extremely grateful to Prof. Takeo Nishitani for his professional and considerable supports in experiments and data analyses during my study in Japan. In the beginning I came, Nishitani-sensei took me into the hall of Monte Carlo simulation with MCNP code. This is a useful method for me to analyze the measurement data from the beginning to the end of my study here. He also guided on the triton burnup in a deuterium plasma and help me a lot on the code understanding and the calculations with different codes. There are a large amount of valuable suggestions and comments from him not only in experiments, but also in simulations and the scientific English writing, which are significantly helpful for my research. In addition to this, I deeply appreciate for his encouragement and moral support to me in my every hard moment. This kind of powerful support enabled me to complete my study. I wish to thank his every help not only in my study, but also in my daily life in NIFS.

I wish to thank Dr. Kunihiro Ogawa to develop NIFS Sci-Fi detector and allow me to use his digitizer for Sci-Fi measurement in LHD experiment, and his help for moving house in the beginning I came Japan and the end I left Japan. Without his permission and help, I can not carry out experiment on LHD. I also want to thank for his help on FBURN code to calculate time-evolution of triton burnup 14 MeV on LHD.

I am deeply grateful to Prof. Liqun Hu from Institute of Plasma Physics, Chinese Academy of Sciences (ASIPP) for his forceful encouragement and moral support. Each conversation is significantly useful for me in the rest of my life, which let me to finish my study here. I would like to thank every help from him and everything he did for me not only when I worked in ASIPP, but also when he visited NIFS those years.

I heartily wish to express my thanks to Prof. Yasuhiko Takeiri, Prof. Satoru Sakakibara, and Prof. Shigeru Morita for their helps to make me to go on study in NIFS.

I devoutly appreciate Prof. Masaki Osakabe and Dr. Teruya Tanaka for reviewing this thesis and their valuable suggestions and comments on this thesis, which help me to improve this thesis. I wish to thank Teruya Tanaka-sensei to discuss the response calculation of Li glass detector, the reaction rate of neutron activation foil, the fusion blanket neutronics, and to share his data of Li glass detector to help me to understand detector response and study by using PHITS code.

I would like to thank Prof. Katsuji Ichiguchi for the discussion of particle confinement time, Dr. Shinsuke Satake for the discussion of neo-classical transport physics and neo-classical diffusion for energetic particles in helical plasma, Dr. Akihiro Shimizu for code checking and first lecture of plasma physics, and Prof. Takeo Muroga for his comments on the *in situ* calibration experimental results.

I wish to express my thanks to Prof. G.A. Wurden for discussion of the design of the Sci-Fi detector from E-mail and his colleagues for the development of the Sci-Fi detector in LANL.

I wish to express my thanks to a mass of assistances from radiation works in NIFS for *in situ* calibration experiment, LHD Experiment Group in NIFS for LHD experiment, and Prof. Shigeo Matsuyama in Tohoku University for accelerator experiment. In addition, I wish to thank Prof. Yuri Kashchuk and Dr. Vitaly Krasilnikov from ITER organization, Prof. Mamiko Sasao from Tohoku University for their discussions during the *in situ* calibration experiment, and Prof. Tieshuang Fan and Dr. Mr. Lijian Ge from Peking University for the comments on the *in situ* calibration experiment when they visited NIFS. I also wish to thank Miss T. Tanaka and Mr. Siyuan Li from Nagoya University to join the *in situ* calibration experiment and their useful discussion on the detection efficiency

of HPGe detector in the activation measurement together with Dr. S. Yoshihashi and Prof. A. Uritani in Nagoya University.

I wish to express my thanks to Prof. William W. Heidbrink from University of California in Irvine to give comments and questions on triton burnup study on LHD during my post presentation in the post section of the 22nd Topical Conference on High Temperature Plasma Diagnostics, Prof. Kazuo Toi from NIFS and Prof. Jiangang Li from ASIPP to give me comments and questions on triton burnup study on LHD during my presentation in the 11th A3 Foresight Program Workshop, and Prof. Yasushi Todo from NIFS, Prof. Ralf König from IPP, Prof. R. Wolf from IPP, Prof. Guoyong Fu from Zhejiang University in China, Prof. David Gates from PPPL, and Prof. Sadayoshi Murakami from Kyoto University to give me comments and questions on triton burnup study on LHD during the post section of the 21st International Stellarator-Heliotron Workshop (ISHW2017). I would like to thank Prof. Katsumi Ida from NIFS to explain neo-classical transport physics for me in the free discussion time of ISHW2017.

I would like to thank Masaki Osakabe-sensei, Katsuji Ichiguchi-sensei, and Toshiyuki Mito-sensei to give a lecture on Fundamentals of Fusion Science, Hiroshi Yamada-sensei to give a lecture of plasma physics, Ryuichi Sakamoto-sensei to give a lecture of advances in plasma science, and Nakamura-sensei to give a lecture of Japanese language in SOKENDAI/NIFS. Those lecture gave me the first impression of fusion science, plasma physics, engineering, fusion materials science, and Japanese.

I wish to thank Matsunaga-san for a lot of his daily helps and also helping me to move house together with Isobe-sensei and Dr. Kunihiro Ogawa in the end I left Japan. I wish to thank SOKENDAI students: Matsunaga-san, Fujita-san, and Sakamoto-san who study and stay with me in a some room in NIFS, and Indian student Nilam-san and Vietnamese student Trang-san to share their gift and happiness with me for a long time. I also wish to thank Mr. Junki Morimoto for his helps in the beginning I came Japan. In addition, I wish to thank Mr. Siyuan Li for each his help on my daily life when I live in Japan.

I heartily appreciate Dr. Hao Wang, Dr. Jie Huang, Dr. Jun Chen, Dr. Yang Liu, Dr. Hongming Zhang, Dr. Henjun Chen, Dr. Yue Xu, Dr. Xianqu Wang (SJU), Dr. Jie Huang (SJU), Dr. Haifeng Liu (SJU), Dr. Bo Huang, Dr. Gaowei Zhang, Dr. Qilai Zhou, Dr. Jingjie Shen, Mr. Bing Ma, Dr. Shaoning Jiang, Dr. Shuyu Dai, Dr. Xiaodi Du, Dr. Haiying Fu, Dr. Hailin Bi, and Dr. Botz Huang for their helps and friendships during the different phases which I live in NIFS. Special thanks to Dr. Hao Wang, Dr. Jie Huang, Dr. Jun Chen, Dr. Yang Liu, Dr. Hongming Zhang, Dr. Henjun Chen, Dr. Yun Xu for their every help, concern, and talking out with them on my dark time in NIFS.

I wish to thank Mr. Shiyao Lin, Dr. Jiafeng Chang, Dr. Yanmin Duan, Dr. Yang Zhang, Dr. Liqing Xu, Dr. Yi Yuan, Mr. Min Xiao, Mr. Jizong Zhang, Mr. Songtao Mao, Dr. Kaiyun Chen, Dr. Hongrui Cao, Miss Luying Niu, Mr. Jinlong Zhao, Miss Xiuli Sheng, Miss Zijun Zhang, Miss Caiyun Fang, Dr. Juan Huang, Dr. Guoqiang Zhong from ASIPP for their helps and concern about my study in NIFS. I also wish to thank Prof. Yanguo Li, Dr. Yong Chen, Dr. Yifei Zhang from Institute of High Energy Physics, Chinese Academy of Sciences, and Dr. Xi Yuan, Dr. Xin Zhang, Dr. Xufei Xie, Dr. Zhongjing Chen, Dr. Xingyu Peng, Dr. Zhimeng Hu, Dr. Tengfei Du, Dr. Yimo Zhang, and Dr. Jiaqi Sun from Peking University.

I would like to express my gratitude to all staffs of NIFS and SOKENDAI for their kind supports, and special thanks to Masuda-san and Ando-san from SOKENDAI for so many daily assistances not only in my study, but also in daily life in NIFS.

I wish to thank NIFS Associate Research (RA) and Kakuyugo Kagaku KenkyuKai (YUKWAI) in Japan support for my work. Without supports from RA and YUKWAI, I even can not survive in Japan. I also wish to thank SOKENDAI Travel budget to travel to FNL experiment and international conference, and support from the JSPS-NRF-NSFC A3 Foresight Program to attend A3 conference.

I also wish to thank PHITS group in JAEA, Tokai, Japan to fund me for travelling to Tokai to attend PHITS 14th tutorial in Tokai, and give me many comments and helps on my calculations.

Finally, I would like to thank my parents to be a most powerful spiritual pillar for me, which made me to accomplish this work and my study in Japan.